Volume 19 | Number 1 | January-December 2025

DTI | Drug Target Insights

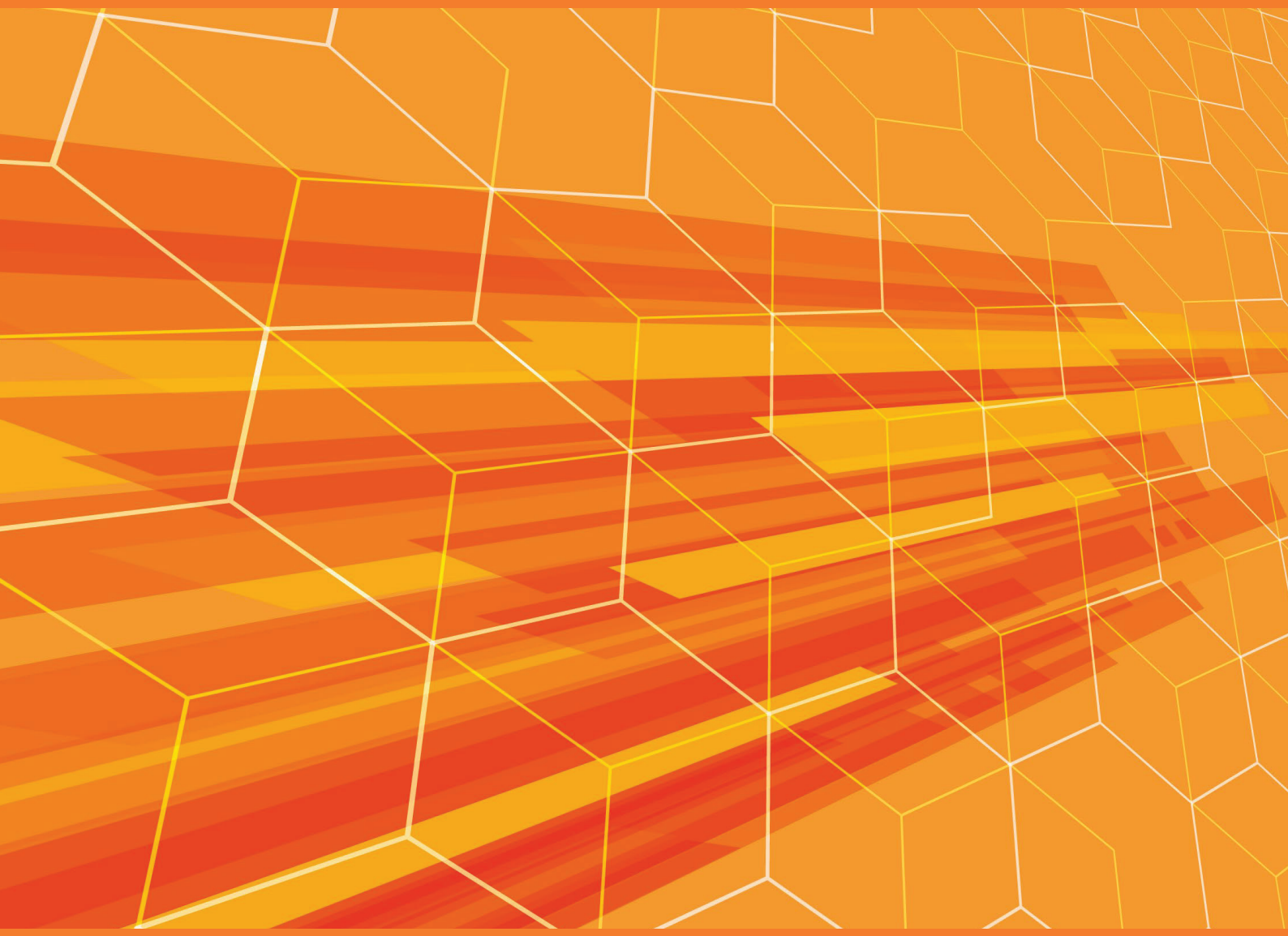

ABOUTSCIENCE

Aims and Scope
Drug Target Insights covers current developments in all areas of the field of clinical therapeutics and focusing on molecular drug targets which include disease-specific proteins, receptors, enzymes, and genes. The journal seeks to elucidate the impact of new therapeutic agents on patient acceptability, preference, satisfaction and quality of life.

Abstracting and Indexing
CNKI Scholar
CrossRef
DOAJ
Ebsco Discovery Service
Embase
Emerging Sources Citation Index (ESCI)
Google Scholar
J-Gate
OCLC WorldCat
Opac-ACNP (Catalogo Italiano dei Periodici)
Opac-SBN (Catalogo del servizio bibliotecario nazionale)
PubMed Central
ROAD (Directory of Open Access Scholarly Resources)
Scilit
Scimago
Scopus
Sherpa Romeo
Transpose
Web of Science

Publication process
Peer review
Papers submittied to DTI are subject to a rigorous peer review process, to ensure that the research published is valuable for its readership. DTI applies a single-blind review process and does not disclose the identity of its reviewers.

Lead times
Submission to final decision: 6-8 weeks
Acceptance to publication: 2 weeks

Publication fees
All manuscripts are submittied under Open Access terms. Article processing fees cover any other costs, that is no fee will be applied for supplementary material or for colour illustrations. Where applicable, article processing fees are subject to VAT.

Open access and copyright

Author information and manuscript submission
For full author guidelines and online submission visit www.aboutscience.eu

ABOUTSCIENCE

Aboutscience Srl
Piazza Duca d'Aosta, 12 - 20124 Milano (Italy)

Editorial and production enquiries
dti@aboutscience.eu

Supplements, reprints and commercial enquiries
Lucia Steele - email: lucia.steele@aboutscience.eu

Publication data
eISSN: 1177-3928
Continuous publication
Vol. 19 is published in 2025

DTI
Drug Target Insights 2025; 19: 1-10
ISSN 1177-3928 | DOI: 10.33393/dti.2025.3171
ORIGINAL RESEARCH ARTICLE

Characterization and enhanced antibiofilm activity of *Annona muricata* extract in combination with fluconazole against *Candida albicans*

Abhay P. Mishra[1,2], Masande Yalo[3], Jennifer Nambooze[4], Carolina H. Pohl[5], Gabré Kemp[5], Lekgoana K. Setsiba[5], Motlalepula G. Matsabisa[1]

[1]Department of Pharmacology, University of Free State, Bloemfontein - South Africa
[2]Cosmetics and Natural Products Research Centre (CosNat), Department of Pharmaceutical Technology, Naresuan University, Tha Pho, Phitsanulok - Thailand
[3]Department of Chemistry, Cape Peninsula University of Technology, Cape Town - South Africa
[4]Department of Chemistry, University of Free State, Bloemfontein - South Africa
[5]Department of Microbiology and Biochemistry, University of Free State, Bloemfontein - South Africa

ABSTRACT

Introduction: *Candida albicans* biofilm formation is a significant contributor to antifungal resistance, necessitating new treatment strategies. *Annona muricata* Lin., a traditional herbal remedy, has shown promise in combating microbial infections. The purpose of this study was to assess the antibiofilm activity of the methanol extract of *A. muricata* leaves alone or with the addition of fluconazole against *C. albicans*.

Methods: Phytochemicals from the methanol extract were analyzed by LC-MS, the XTT assay was used for metabolic activity, and morphological characteristics were examined using scanning electron microscopy (SEM). Molecular docking screening of identified compounds in *A. muricata* methanol leaves extract against a Sap3 receptor (PDB: 2H6T) was also performed.

Results: The LC-MS analysis detected 17 possible phytochemicals. The methanol extract showed a dose-dependent inhibition of biofilm formation, with maximum inhibition of ~60% observed at 240 µg/ml, and inhibition by fluconazole increased from 32% to 76% as the concentration increased from 15 to 240 µg/ml. The combination of *A. muricata* and fluconazole increased the inhibition significantly, from 74% to 78% at 15 µg/ml to 240 µg/mL, respectively. SEM of control and treated *C. albicans* biofilms showed an altered morphology and loss of cell integrity by the combination, corroborating the findings. Plant phytochemicals also possess high binding affinity (−9.7 to 8.0 kcal/mol, respectively) for the Sap3 enzyme and may therefore have therapeutic potential against *C. albicans*.

Conclusion: Consequently, the findings indicate that compounds in the *A. muricata* methanol extract may function in concert with fluconazole at sub-inhibitory concentrations to suppress *C. albicans* biofilm formation. This finding paves the way for the formulation and development of antifungal treatment regimens that may limit the development of fluconazole resistance employing this plant part.

Keywords: *A. muricata*, *Candida albicans*, Fluconazole, LC-MS, Synergism, XTT assay

Introduction

Seventy-five percent of human microbial infections are caused by the growth and persistence of biofilms, which are surface-attached microbial populations encased in a self-synthesized polymeric matrix (1). The ability of *Candida albicans* to form biofilms is a crucial component of its pathogenicity since it can increase tolerance to the host immune system and traditional antifungal medication (2). Most severe and recurring infections caused by *C. albicans* are linked to the development of biofilms on natural or synthetic surfaces (3). *C. albicans* biofilm has been known to cause persistent infections of organs and tissues invasively via seeding disseminated bloodstream infections, known as candidemia (4,5). Interestingly, secreted aspartyl proteinases (Saps) are among the hydrolytic enzymes that contribute significantly to the pathogenicity of the opportunistic pathogen *C. albicans* (6). It is believed that mucosal infections are associated with Sap 1-3, while systemic infections are associated with Sap 4-6 (7).

Herbal remedies have been utilized for millennia to cure a wide range of illnesses, both in Africa and elsewhere.

Received: June 17, 2024
Accepted: December 4, 2024
Published online: January 13, 2025

This article includes supplementary material

Corresponding author:
Abhay P. Mishra
email: abhaypharmachemhnbgu@gmail.com

This is mostly due to the perception that medicinal herbs are more accessible, more affordable, and more effective than Western medications (8). *Annona muricata* Lin. (Custard-apple, Annonaceae) is endemic to the West Indies and Central America, where it grows widely at elevations below 900 meters above sea level. It is also known by the names guanabana, paw-paw, soursop, and graviola. It grows in nations such as India, Angola, Puerto Rico, Brazil, Costa Rica, Colombia, and Venezuela that have tropical or subtropical climates (9). It has proven possible to isolate >200 bioactive chemicals from the *A. muricata*. Terpenoids, phenolics, and alkaloids are the most identified secondary metabolites of *A. muricata* (9-11). In Africa, India, and tropical America, *A. muricata* is frequently used as a folk remedy for a variety of human illnesses, including diabetes, rheumatism, cancer, and parasitic infections (12). The antibacterial, antifungal, anticancer, anticonvulsant, sedative, antiparasitic, and cardiodepressant properties of *A. muricata* leaves are just a few of its many potential uses (13,14). According to Rustanti and Fatmawati, *A. muricata* leaves ethanol extract showed antifungal activity, particularly against *C. albicans* (13). However, the literature presently has inadequate proof of the use of *A. muricata* leaf extract on biofilms of *C. albicans*.

Thus, this work aims to examine the antifungal activity and synergistic potential of the methanol extract of *A. muricata* leaf when combined with an antifungal agent, fluconazole, against *C. albicans* biofilm. Also, the existence of putative chemical components of *A. muricata* leaf extract, as well as the possibility of an interaction between identified compounds of *A. muricata* leaf and the Sap3 *C. albicans,* will be investigated to find new inhibitor candidates.

Experimental

Plant material collection

The *A. muricata* leaves were gathered in August 2020 at Mabira Forest in Uganda's Buikwe District, with Voucher specimen No. AMHa4567, the plant was authenticated and confirmed by a taxonomist at the Makerere University Herbarium, Department of Plant Science, Microbiology and Biotechnology, Makerere University, Uganda.

Extraction procedure

Briefly, properly washed, cleaned, and dried (21 days at room temperature), leaves were ground into fine powder by using an electrical grinder. Powdered leaves (1000 g) were extracted successively (2.5 L × 3) by macerating with n-hexane, dichloromethane, ethyl acetate, methanol, and water at room temperature for 72 hours to obtain four respective extracts. The extracts were filtered through cotton wool and then dried in a rotary evaporator set at 40°C. To remove any remaining moisture, the extracts were moved to sample bottles and put in a desiccator with anhydrous sodium sulfate. The dried extracts were then refrigerated at −20°C in t-stopped bottles for further analysis (15). According to the studies, polar solvents are better than non-polar solvents, most likely because they offer a higher phytocompound recovery yield (16,17). Therefore, the adoption of methanol extract for additional research was motivated by the increased extraction yield.

LC-MS parameters for secondary phytochemical analysis

An ABSCIEX 4000 QTRAP hybrid triple quadrupole ion trap mass spectrometer was used to analyze the samples, and its front end was a Shimadzu HPLC stack. The software Analyst 1.5 (AB SCIEX) was used for all data processing and collecting. A 20 µL sample was separated using a 10-minute gradient that started with 5% solvent A (H_2O containing 0.1% ammonium formate) and gradually progressed to 10% solvent B (MeOH with 0.1% ammonium formate). This separation was conducted on a C18 column (150 × 4.6 mm, Discovery, Supelco) at a flow rate of 0.5 mL/min. The solvent gradient was gradually increased to 30% B over the next 10 minutes, then to 50% B for an additional 10 minutes, and finally to 95% B over the subsequent 15 minutes. The total runtime for the experiment was 60 minutes, which allowed for column re-equilibration. Analytes that were eluted were electrosprayed into the TurboV ion source at 500°C to evaporate any excess solvent. The system used a nebulizer gas pressure of 30 psi, a heater gas pressure of 30 psi, and a curtain gas pressure of 20 psi. The ion spray voltage was adjusted to 5500V in positive ionization mode and −4500V in negative ionization mode. With fixed declustering and entrance potentials of 40 and 10V, respectively, the eluting analytes were mass measured on the mass spectrometer in Q1 scan mode, covering a range of 100 Da to 2000 Da for a 3-second cycle period.

Multiple optimizations and scans were done to reduce the background noise and come up with the best baseline stabilizations for accurate compound identifications.

The compounds were identified by comparing the outcomes of ESI-MS/MS observations articulated as tR and fragmentation configurations with those disclosed by investigations obtained from various database systems, such as the National Library of Medicine, Mass Bank of Europe, and related literature reviews. MS spectra, TIC, and possible identified compounds with their corresponding structures were retrieved from the library as well as the PubChem Compounds database.

Docking Studies

Using the Lamarckian genetic algorithm (LGA) as the scoring function, the PyRx virtual screening program was utilized to virtually screen ligands, including AutoDock and AutoDock Vina. Molecular docking analysis was used to determine the chemical compounds' binding affinity with the examined 2H6T protein's active site amino acids. The SDF format of Sap3 (PDB ID: 2H6T) protein 3D structure was downloaded from the protein data bank (PDB). The AutoDock tool was used to import the proteins with access codes 2H6T. After the water molecules attached to the structures were eliminated, hydrogen atoms were inserted. Similarly, LCMS-identified compound structures were also downloaded from the PubChem database. The ligands were docked using the active site dimensions, which were defined as a grid size

based on the XYZ axis. A maximum exhaustiveness of 10 was computed for every ligand. Prior to the docking process starting, AutoDock Vina applied charges to the structures of proteins and ligands (15,18). The 2D visualization of the ideal binding pose—which is the binding energy with the lowest value for each compound-protein combination—was studied using BIOVIA Discovery Studio software. Hence, there is a great chance that the ligands produced will be employed as medication candidates.

Antibiofilm activity

Strains used

For this investigation, *C. albicans* SC5314 was revived and maintained on Yeast Malt extract (YM) (10 g/L glucose, 3 g/L yeast extract, 3 g/L malt extract, 5 g/L peptone, and 16 g/L agar) agar plates and preserved at 4°C for all studies conducted.

XTT assay of biofilms

On YM agar plates, *C. albicans* cells were cultured and subsequently incubated for 24 hours at 30°C. Following incubation, 20 mL of yeast nitrogen base (YNB) glucose medium (10 g/L glucose, 6.7 g/L YNB) was filled with a loop full of cells, and the mixture was incubated for 24 hours at 30°C.

Using an Eppendorf centrifuge 5430R, cells were harvested and washed (3075 g × 3 for 5 minutes at 4°C) with phosphate-buffered saline (PBS) and resuspended in 10 mL of RPMI-1640 media (Sigma-Aldrich, UK) at a concentration of $1x10^{-6}$ cells/ml. Aliquots of 200 µL of the cell suspension, including *A. muricata* methanol extract (reconstituted in sterile water) (AM), fluconazole (FLU) and a combination of the extract and antifungal drug (AM + FLU) at final concentrations ranging from 15-240 µg/ml was dispensed into a 96-well microtiter plate (Corning Incorporated, Costar®, U.S.) and incubated for 48 hours at 37°C to allow biofilm formation. Standardized cells with RPMI-1640 media were used as the negative control. To get rid of non-adherent cells, wells were twice cleaned with 200 µL PBS after 48 hours. Kuhn et al.'s (19) method of assessing the mitochondrial metabolic activity of the biofilms was used for the reduction of 2,3-bis(2-methoxy-4-nitro-5-sulfophenyl)-5-[(phenylamino) carbonyl]-2H-tetrazolium hydroxide (XTT) (Sigma Aldrich, UK) in order to assess the viability of the yeast.

In the cellular supernatant, XTT was converted to colored, diffusible, water-soluble formazan, whose optical density was easily measured at 492 nm. Three biological duplicates of each three technical duplicates were used for this experiment. %Inhibition was calculated according to the following formula:

$$\left[\left(100-\frac{Absorbance\ of\ sample}{Absorbance\ of\ control}\right)\times 100\right]$$

After calculating the average and standard deviations, the student's t-test was performed to assess the significance of the data sets, with $P < 0.05$ being deemed significant. IC_{50} values were determined by performing non-linear fitting analysis using GraphPad Prism 8.0.2 software.

Scanning electron microscopy (SEM)

Biofilm was prepared as described above in a flat bottom 6-well plate (Greiner Bio-One, Germany) in 2 mL of RPMI-1640 medium containing either FLU (15 µg/mL), AM (15 µg/mL) or a combination of FLU (7.5 µg/mL) and AM (7.5 µg/mL) on sterile polymer discs (Isopore 0.2 µm hydrophilic polycarbonate membrane disc, Merck, Germany). The polymer discs were removed aseptically after incubation and left overnight in a primary fixative solution of 3% (v/v) glutardialdehyde (Merck, Germany) in phosphate buffer (pH 7.0). The biofilms underwent two PBS washes before being fixed for two hours at room temperature using 1% (v/v) osmium tetroxide (Merck, Germany) as a secondary fixative. This was followed by a second wash phase. The biofilms were air dried in a desiccator after being dehydrated in an ethanol series (50% for 20 minutes, 70% for 20 minutes, 95% for 20 minutes, and 100% for one hour – twice). Then, they were subsequently coated with gold using SEM coating equipment (EM ACE600, Leica, Austria) and exposed to critical point drying (Samdri®-795 Critical Point Dryer, Tousimis, United States of America) for 30 minutes. Biofilms were analyzed using a JSM-7800F field emission SEM (ZEISS, Germany).

Results and Discussion

LCMS profile of *A. muricata* methanol extract

A total of 17 phytochemicals were detected by LC/MS and 14 among them were identified (Table **1**). These included alkaloids (asimilobine **2**, swainsonine **3**, xylopine **7**, (+)-4'-O-methylcoclaurine **10**), flavonoids (isovitexin **4**, vitexin **5**, rutin **8**, quercetin-3-O-D-glucuronide **9**, kaempferol 3-O-rutinoside **11**, eriocitrin **15**, apigenin 6,8-di-C-glucoside **17**) and acetogenins (annonisin **13**, annomuricin A **14**, montanacin B/C **16**) **(Fig. 1)** from AM **(Fig. 1)**. A potential identification of the chemicals was predicated on contrasting the fragmentation patterns and retention times (tR) obtained from ESI-MS/MS experiments with those documented in research gathered from various databases.

The first-order mass spectrum of compound **3** showed an intense protonated molecular ion $[M+H]^+$ at *m/z* 174.3 and also showed a single loss of one hydroxyl group as water $[M+H-H_2O]^+$ at *m/z* at 156.2, which was identified as swainsonine (20-22). A similar trend was observed for compound **2**, where a protonated molecular ion $[M+H]^+$ was observed at *m/z* 268.6. The fragments at *m/z* 250.6 and 236.5 were assigned to the loss of the hydroxyl group as water $[M+H-H_2O]^+$ and methoxy group $[M+H-OCH_3]^+$, respectively, and this led to the identification of compound **2** as asimilobine and this was consistent with the results of Lima et al. and Mohanty et al. (23,24). Compound **7** was identified as xylopine based on the typical fragment ions at *m/z* 279.4 ($[M + H-OH]^+$) and 249.7 ($[M-CH_2O_2]^+$) (22,25,26). For compound **10**, the main fragment ion appeared at *m/z* 300.4 $[M+H]^+$ and another main fragment at *m/z* 283.9 $[M-OH]^+$, which corresponded to the loss of the hydroxyl group. Moreover, other fragments at *m/z* 251.8, 178.3, and 121.1 were observed, which led to the identification of compound **10** as (+)-4'-O-Methylcoclaurine (27).

TABLE 1 - Compounds detected by HPLC-ESI-MS/MS (negative and positive mode) in the methanol extract of *A. muricata* leaf

Peak	Compound name	t_R (min)	*m/z*	Ionization mode	Molecular formula	References
1	Unidentified	3.585	161.0	$[M-H]^-$	–	–
2	Asimilobine	4.749	268.6	$[M+H]^+$	$C_8H_{15}NO_3$	(24)
3	Swainsonine	9.286	174.3	$[M+H]^+$	$C_{17}H_{17}NO_2$	(20-22)
4	Isovitexin	12.663	431.0	$[M-H]^-$	$C_{21}H_{20}O_{10}$	(32)
5	Vitexin	13.832	431.0	$[M-H]^-$	$C_{21}H_{20}O_{10}$	(32)
6	Unidentified	16.112	407.0	$[M-H]^-$	–	–
7	Xylopine	18.298	296.2	$[M+H]^+$	$C_{20}H_{21}NO_4$	(22,25,26)
8	Rutin	17.381	609.7	$[M-H]^-$	$C_{27}H_{30}O_{16}$	(30)
9	Quercetin-3-O-D-glucuronide	17.429	477.1	$[M+H]^-$	$C_{21}H_{20}O_{13}$	(33)
10	(+)-4'-O-Methylcoclaurine	16.889	300.4	$[M-H]^+$	$C_{18}H_{21}NO_3$	(27)
11	Kaempferol 3-O-rutinoside	19.900	595.3	$[M+H]^+$	$C_{27}H_{30}O_{15}$	(28,29)
12	Unidentified	22.840	517.4	$[M+H]^-$	–	–
13	Annonisin	30.812	611.3	$[M+H]^+$	$C_{35}H_{62}O_8$	(36)
14	Annomuricin A	31.356	613.3	$[M+H]^+$	$C_{35}H_{64}O_8$	(38,39)
15	Eriocitrin	33.166	595.7	$[M+H]^-$	$C_{27}H_{32}O_{15}$	(31,34)
16	Montanacin B	38.016	611.2	$[M+H]^+$	$C_{35}H_{62}O_8$	(37)
17	Apigenin 6,8-di-C-glucoside	38.177	593.4	$[M+H]^-$	$C_{27}H_{30}O_{15}$	(31)

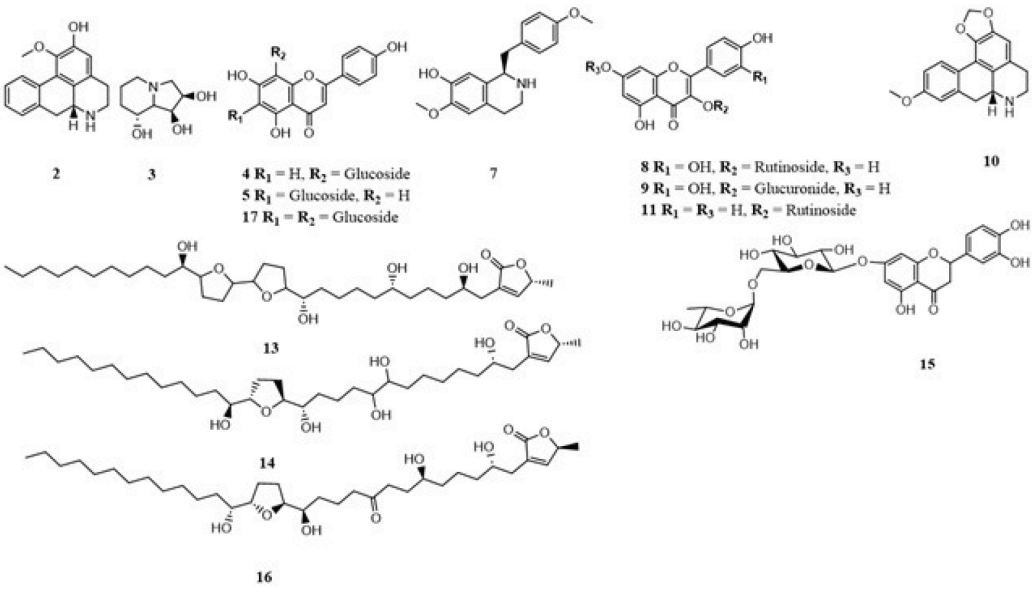

FIGURE 1 - Chemical structures of compounds identified from AM by LC-MS

The mass spectrum fragmentation of compound **11** appeared at *m/z* 595.3 $[M+H]^+$. The product ion spectrum of the compound **11** ion (*m/z* 595.3) showed fragment ion at m/z 577.4 $[M+H-H_2O]^+$ due to loss of water molecule. The fragments at m/z 449.4 and 287.4 indicated the loss of rhamnose and glucose sugar units, and therefore, compound **11** was identified as kaempferol 3-O-rutinoside (28,29). Similarly, a deprotonated molecular ion $[M-H]^-$ was observed at *m/z* 609.7 for compound **8**. The spectra showed the presence of the main fragments at m/z 463.2 $[M-H-146]^-$ and 301.1 $[M - H-146-162]^-$, indicating the loss of two sugar units consisting of rhamnose and a pyranose, and this led to the identification of compound **8** as rutin (30). Compound **17** showed a pseudo molecular ion peak at *m/z* 593.4 $[M-H]^-$.

MS showed fragment ions at *m/z* 431.1 [M−H-162] and 269.0 [M−H-162], corresponding to the presence of the hexose nature of *C*-glycoside flavone. Moreover, from the observed base peak fragment at *m/z* 269.0, it could be concluded that compound **17** was apigenin 6,8-di-C-glucoside (31). Similarly, compounds **4** and **5** were assigned as isovitexin and vitexin, respectively (32).

Compound **9** gave a pseudo-molecular ion at *m/z* 477.1 $[M-H]^-$. The MS/MS spectrum featured characteristic ion of *m/z* 301.1 $[M-H-178]^-$, derived from the loss of glucuronide, and this led to the identification of compound **9** as quercetin 3-O-glucuronide (33). For compound **15**, the LC-MS chromatogram yielded an intense peak at *m/z* 595.7 $[M-H]^-$. Moreover, another main fragments at *m/z* 449.2 $[M-H-146]^-$ and 287.0 $[M-H-162]^-$ were observed, which implies the loss of deoxyhexose and hexose as rhamnose and a pyranose, and therefore, compound 1**5** was identified as eriocitrin (31,34).

For compounds **13** and **16**, the LC-MS/MS chromatogram showed a molecular ion peak at *m/z* 611.2 $[M+H]^+$, which corresponds to the molecular formula $C_{35}H_{62}O_8$. Due to consecutive losses of water (18 Da), the mass fragments at m/z 575.4 $[M+H-H_2O]^+$, 557.4 $[M+H-2H_2O]^+$, 539.5 $[M+H-3H_2O]^+$, and 521.7 $[M+H-4H_2O]^+$ show the existence of four hydroxyl groups. This was in agreement with Gu et al. (35), who reported that fragment ions, indicative of the multihydroxylated structures of the acetogenins, were generated from consecutive losses of H_2O (three to five molecules). This, therefore, led to the identification of compounds **13** and **16** as annonisin and montanacin B, respectively (36,37). Compound **14** gave a molecular ion peak at *m/z* 613.35 $[M+H]^+$, which corresponds to the molecular formula $C_{35}H_{64}O_8$ (38). Similarly to compound **13** and **16**, compound **14** also had the same fragments at 577.4 $[M+H-H_2O]^+$, 559.2 $[M+H-2H_2O]^+$, 541.5 $[M+H-3H_2O]^+$, 523.6 $[M+H-4H^2O]^+$ and 505.6 $[M+H-5H_2O]^+$ due to successive losses of water (18 Da) which indicates the presence of five hydroxyl groups. These results were in agreement with the literature (38,39), and compound **14** was identified as annomuricin A.

Molecular docking

In order to produce docking scores that show the bioaffinity of the docked molecules, the molecular docking algorithm simulates ligand interactions in the target proteins' or receptors' active regions (40). *C. albicans* is reported to have Sap 1-10 genes. The Sap proteins are one of the classic pathogenic factors whose expression is controlled by numerous parameters such as pH levels, temperature, location of infection, and physicochemical ambient conditions. Since Sap3 is implicated in mucosal infections, the development of inhibitors targeting Sap3 is a promising strategy for addressing infections caused by *C. albicans* (7).

The molecular docking calculations presented in **Table 2** indicate that the enzyme Sap3 (2H6T) exhibited the utmost binding affinities with eriocitrin (-9.7 kcal/mol). The 2D visualization (**Fig. 2A)** displayed that eriocitrin established strong hydrogen bonds with GLY 34, ASP 86, SER 36, and ASN 192 at the protein active site. However, it also used a distinct pi bond

TABLE 2 - Phytochemicals of *A. muricata* leaf and their binding energies with Sap3 (2H6T) enzyme

S. No.	Compound Name	Macromolecule	Binding energy (kcal/mol)	Closest residues of docked ligands at the active site of macromolecule
A.	Eriocitrin	2H6T	–9.7	GLY 34, ASP 86, SER 36, ASN 192, ASP 218
B.	Apigenin 6,8-di-C-glucoside	2H6T	–8.9	GLY 220, THR 222, TYR 225, ASP 86, GLY 85, TYR 225
C.	Xylopine	2H6T	–8.5	GLY 220, GLY 85, TYR 225, ASP 218, ILE 305
D.	Isovitexin	2H6T	–8.5	ASP 86, THR 222, VAL 12, ASP 218, ILE 305
E.	Rutin	2H6T	–8.4	ASP 218, GLY 85, GLY 34, THR 221, ILE 82
F.	Vitexin	2H6T	–8.1	ASN 35, ILE 82, GLU 83, GLY 34,
G.	Asimilobine	2H6T	–8.1	ASP 32, 86, 218, THR 221, 222, ILE 123, 305, TYR 84, 225, GLY 34, 85, 220, SER 35
H.	Kaempferol 3-O-rutinoside	2H6T	–8.0	TYR 84, SER 35, GLU 83, GLY 34, 85, ILE 82, TYR 303
I.	(+)-4'-O-Methylcoclaurine	2H6T	–7.8	ILE 123, 305, TYR 84, 303, GLY 34, 85, 220, ASP 32, 86, 218, VAL 30, THR 221, SER 13
J.	Quercetin-3-O-D-glucuronide	2H6T	–7.3	ILE 123, TYR 221, GLY 85, 220, ASP 218
K.	Annonisin	2H6T	–7.2	ILE 82, 123, SER 13, 35, VAL 12, 30, ASP 32, 218, THR 221, GLY 34, 85, 220, TYR 84, 303, GLU 83
L.	Annomuricin A	2H6T	–6.8	ILE 123, 305, SER 13, VAL 12, 30, ASP 32, 86, 218, THR 221, 222, GLY 34, 85, 220, TYR 84, 225, 303, GLU 83
M.	Montanacin B	2H6T	–6.7	ILE 123, 305, SER 13, VAL 12, 30, ASP 32, 86, 218, THR 221, 222, GLY 34, 85, 220, TYR 84, 225, 303
N.	Montanacin C	2H6T	–6.4	ILE 82, 123, 305, VAL 12, 30, ASP 32, 86, 218, GLY 34, 85, 220, TYR 84, 303, GLU 83
O.	Swainsonine	2H6T	–5.6	GLY 34, SER 35

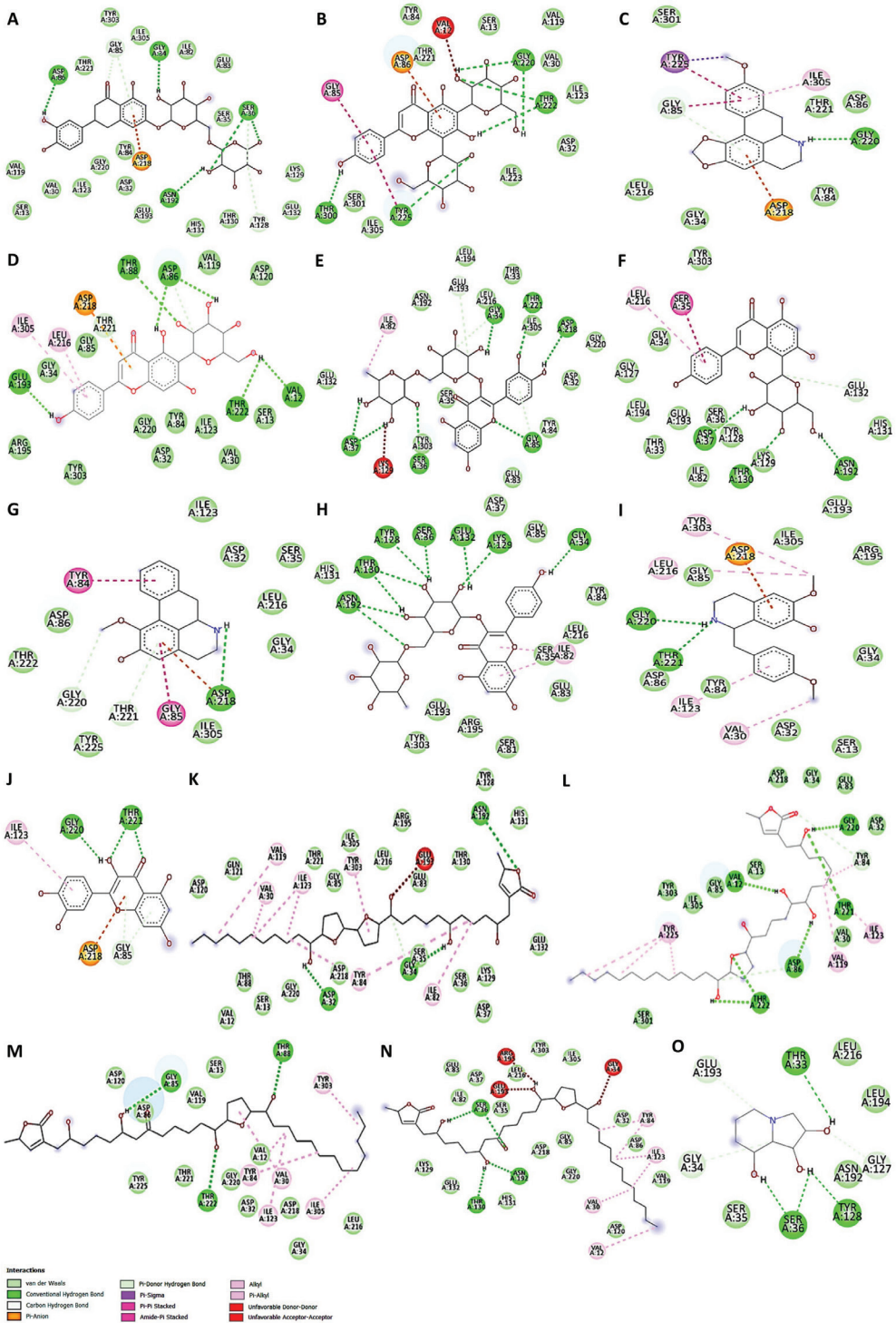

FIGURE 2 - 2D views of Sap3 active site amino acid residues interactions with *A. muricata* identified phytochemicals

to engage with ASP 218 at the catalytic pocket of the enzyme. In addition, the 2H6T macromolecule interaction with apigenin 6,8-di-C-glucoside showed the second-highest binding energy (−8.9 kcal/mol) through strong hydrogen bonds with GLY 220, THR 222, THR 300, and TYR 225 along with ASP 86 (π bond), GLY 85 (π-π stacked), as well as a noncovalent (amide-π stacking) interaction with TYR 225 **(Fig. 2B)**. The strength of binding between receptors and ligands is determined by the number of hydrogen bonds produced. Also, binding energy influences the efficiency of ligand binding to enzymes (7).

Another molecule, xylopine, also formed bonds with GLY 220 (H-bond), GLY 85 (π stacking), and TYR 225 (π-σ) with a binding energy of −8.5 kcal/mol **(Fig. 2C)**. Whereas

isovitexin-2H6T showed same binding energy as xylopine, by interacting with GLU 193, THR 88, ASP 86, THR 222 and VAL 12 amino acids through hydrogen bonds and with LEU 216 by π-alkyl interactions **(Fig. 2D)**. Intriguingly, the 2D viewpoint in **Fig. 2C-D** confirmed that the ASP 218 and ILE 305 amino acids are the brush border enzymes involved in π-anion and π-alkyl bond formation with both compounds, respectively. A noteworthy interaction has also been seen between rutin-2H6T molecular docking (binding energy of –8.4 kcal/mol). In such interactions, conventional hydrogen bonding consisted of ASP 37, ASP 218, SER 36, GLY 85, GLY 34, and THR 221, while alkyl bond formation occurred with ILE 82 amino acid **(Fig. 2E)**. Vitexin interacted with 2H6T at active sites via ASN 192, SER 36, 35, 81, ILE 82, GLU 83, 132, 193, LEU 194, 216, GLY 34, HIS 131, THR 130, ASP 37, and LYS 129 amino acids with binding energy of −8.1 kcal/mol **(Fig. 2F)** whereas asimilobine interacted with same binding energy thru ASP 32, 86, 218, THR 221, 222, ILE 123, 305, TYR 84, 225, GLY 34, 85, 220, SER 35, LEU 216 amino acids interaction **(Fig. 2G)**. Kaempferol 3-O-rutinoside interacted with 2H6T protein active sites through ASN192, THR 130, TYR 84, 128, SER 35, 36, 81, GLU 83, 132, 193 LYS 129, GLY 34, 85, ASP 37, HIS 131, LEU 216, ILE 82, ARG 195, and TYR 303 amino acids with binding energy of –8.0 kcal/mol **(Fig. 2H)**. Other possible identified compounds such as (+)-4'-O-methylcoclaurine, quercetin-3-O-D-glucuronide, annonisin, annomuricin A, montanacin B, and montanacin C showed binding energy < –8.0 kcal/mol **(Table 2)** by interacting with several amino acids as shown in **Fig. 2I-N**.

In addition, with a binding value of –5.6 kcal/mol, swainsonine likewise showed strong attraction for the 2H6T catalytic site by interacting with GLU 193, THR 33, LEU 216, 194, GLY 34, 127, ASN 192, TYR 128, SER 35, 36 amino acid residues **(Fig. 2O)**. All the ligands are docked inside the active site. As previously documented, the phytochemicals found in *A. muricata* exhibit potential antifungal activity against *C. albicans* (12,38,41,42). Thus, it is possible to infer that the inhibition of the Sap3 enzyme by the extract of *A. muricata* leaves (**Fig. 3)** is caused by the phytochemicals in the plant influencing the activity of the enzymes.

Effects of AM and AM+FLU on *C. albicans* biofilm formation

To determine if the predicted interaction may indeed cause an effect on biofilm formation of *C. albicans*, an *in vitro* antibiofilm assay was performed. The methanolic extract of *A. muricata* leaves showed a dose-dependent effect over *C. albicans* biofilm formation, as shown in **Fig. 3**.

The maximum level of inhibition observed was ~60% at 240 mg/mL. The biofilm inhibitory activities of a clinical antifungal drug used for the treatment of invasive fungal infections, fluconazole, were also evaluated in this study as positive control and showed a similar dose-dependent response, with ~70% inhibition observed at 120 mg/mL. Interestingly, at lower concentrations, the combined effect of the extract and fluconazole achieved synergistically increased levels of inhibition. At 15 mg/mL of the combination, biofilm formation was inhibited in excess of 70%. Our findings support Campos et al.'s 2023 investigation, which found that an ethanolic extract from *A. muricata* leaves has antifungal properties against a multidrug-resistant strain of *C. albicans* (38,42).

This synergism is also supported by the IC_{50} values **(Suppl. Table 1)**. As expected, FLU (IC_{50} = 18.33 µg/mL) had a lower IC_{50} value than the AM (IC_{50} = 128.70 µg/mL). Importantly, the IC_{50} value of the combination (IC_{50} = 0.83 µg/mL) is two orders of magnitude lower than fluconazole, demonstrating a pronounced synergistic activity. A low IC_{50} value indicates that the drug is effective at lower concentrations, resulting in reduced systemic toxicity when administered to patients (43). Identically, it has been seen that combined treatment is a proposed approach to overcome

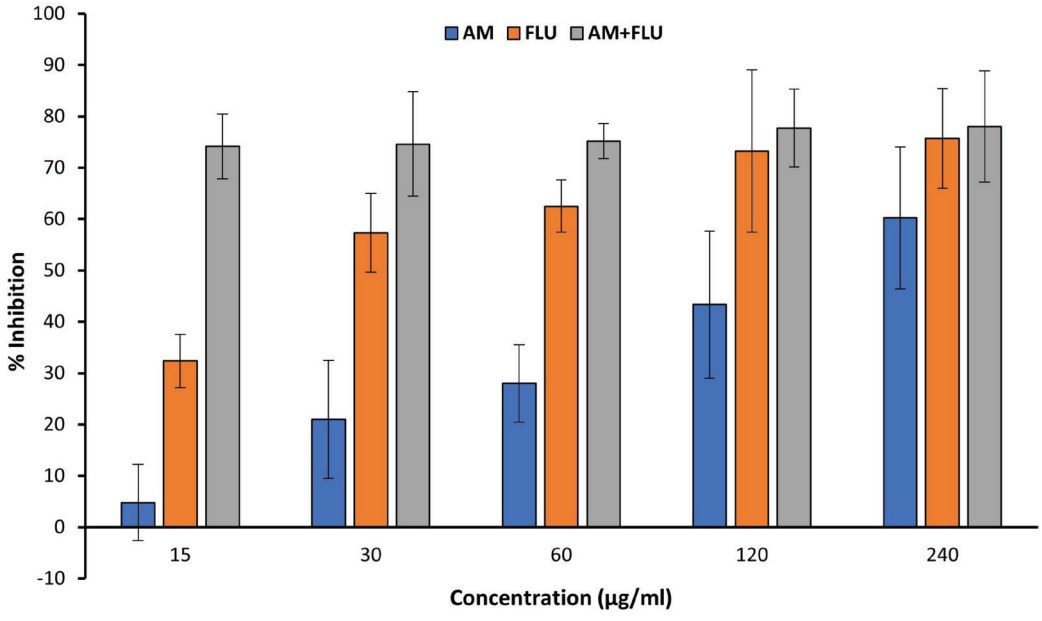

FIGURE 3 - Percent inhibition of *C. albicans* biofilms formation by *A. muricata* ethanol extract (AM), fluconazole (FLU), and the combination (AM + FLU, 1:1). All experiments were performed in biological and technical triplicates. The quantitative data are presented as mean ± standard deviation (SD).

the issues associated with single-agent therapy; numerous studies have shown that combination therapies are superior to single-agent therapy (44,45). Accordingly, flavonoids (such as quercetin, catechin, epigallocatechin gallate, etc.) are a promising synergistic agent when combined with fluconazole and are an effective antifungal agent against *C. albicans* biofilms (45-47). Therefore, the phytocomponents of *A. muricata* leaves may play a role in their promising antifungal properties and possibly produce a synergistic effect with fluconazole.

Effect of AM and AM + FLU on the cell surface of *C. albicans*

Scanning electron micrographs of the control and treated (AM and AM+FLU) biofilms showed that untreated cells formed normal biofilms consisting of hyphae with smooth surfaces **(Fig. 4A)**. As expected, the biofilms grown in the presence of FLU were less dense and hyphal formation was inhibited **(Fig. 4B)**. Biofilms exposed to AM alone, were inhibited compared to the controls, but still displayed hyphal formation **(Fig. 4C)**. In **Fig. 4D**, details of the biofilm exposed to the combination of fluconazole and extract can be seen. These biofilms were very sparse, and hyphal formation was inhibited. The release of cellular material can be seen. Studies have reported that *A. muricata* leaf extract causes modifications to the surface cells in biofilm cells by targeting the cell envelope of *C. albicans*. This effect may result from several identified compounds in the plant extract (38,42). We identified many of the same compounds reported previously (38), and there is a possibility that these compounds are responsible for generating a synergistic effect by interacting with fluconazole when AM + FLU is given as a combined treatment.

Conclusion

LC-MS analysis of methanol extract demonstrated that *A. muricata* contains several chemical constituents, 14 of which were identified. As indicated by molecular docking, some of these may interact with the secreted protease Sap3, which is an important hydrolytic enzyme of *C. albicans*. Our findings regarding the antibiofilm activity of AM leaf extract corroborate recent studies conducted by Campos and co-workers (38,42), who demonstrated that the ethanolic extract of *A. muricata* leaf is a promising anticandidal agent and can reduce fungal infection (*in vitro* and *in vivo*). In addition, we established that the combination of *A. muricata* methanol extract and fluconazole shows synergistic increased inhibition of biofilm formation, which may be advantageous in combating fluconazole resistance in *C. albicans* by lowering the effective dose required to inhibit biofilm formation. These results suggest that more research is necessary to fully understand the underlying mechanisms of action of AM + FLU and explore its potential as an anticandidal agent *in vivo*.

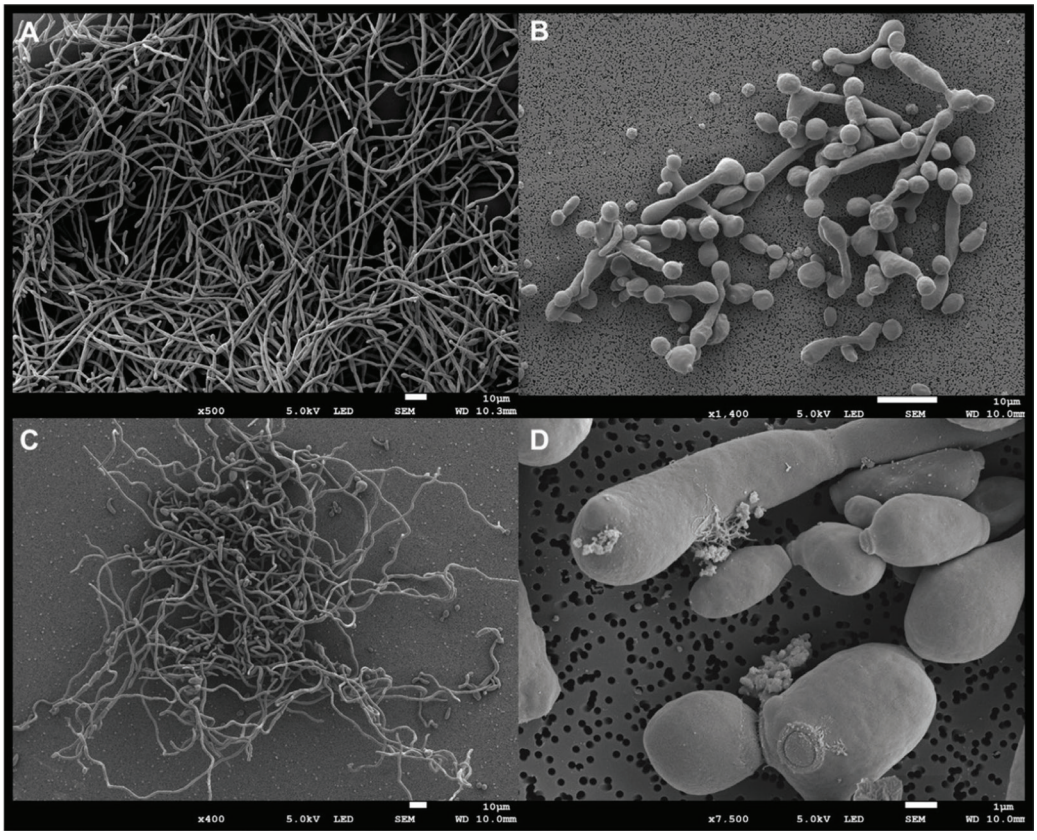

FIGURE 4 - Morphology of *C. albicans* biofilms grown on sterile polymer discs for 48 hours at 37°C. A. Control biofilms, B. Biofilms grown in the presence of 15 µg/mL FLU, C. Biofilms grown in the presence of 15 µg/mL AM, D. Detail of biofilm cells grown in the presence of both FLU (7.5 µg/mL) + AM (7.5 µg/mL).

Disclosures

Conflict of interest: The authors declare no conflict of interest.

Financial support: This research received no specific grant from any funding agency in the public, commercial, or not-for-profit sectors.

Data availability statement: The research data associated with this article are included within the article and in the supplementary material of this article.

Author's contribution: Conceptualization: APM, CHP; Data Curation: APM, MY, JN; Formal Analysis: LKS, GK, APM, CHP, MY; Investigation: APM, LKS, MY, GK; Methodology: APM, LKS, MY, GK; Project Administration: APM, MGM, CHP; Supervision: CHP, MGM; Writing Original Draft: APM; Writing – Review & Editing: APM, GK, CHP.

References

1. Miquel S, Lagrafeuille R, Souweine B, et al; Anti-biofilm activity as a health issue. Front Microbiol. 2016;7:592. CrossRef PubMed
2. Wang S, Wang P, Liu J, et al; Antibiofilm activity of essential fatty acids against Candida albicans from Vulvovaginal candidiasis and bloodstream infections. Infect Drug Resist. 2022;15:4181-4193. CrossRef PubMed
3. Pereira R, Dos Santos Fontenelle RO, de Brito EHS, et al; Biofilm of Candida albicans: formation, regulation and resistance. J Appl Microbiol. 2021;131(1):11-22. CrossRef PubMed
4. Fox E, Nobile C. The Role of Candida albicans Biofilms in Human Disease. In: Dietrich L, Friedmann T, eds. Candida Albicans: Symptoms, Causes and Treatment Options. Nova Science Publishers; 2013:1-24. Online (Accessed June 2024)
5. Gulati M, Nobile CJ. Candida albicans biofilms: development, regulation, and molecular mechanisms. Microbes Infect. 2016;18(5):310-321. CrossRef PubMed
6. Kim JS, Lee KT, Bahn YS. Secreted aspartyl protease 3 regulated by the Ras/cAMP/PKA pathway promotes the virulence of Candida auris. Front Cell Infect Microbiol. 2023;13:1257897. CrossRef PubMed
7. Gholam GM, Firdausy IA, Artika IM, et al; Molecular docking: bioactive compounds of Mimosa pudica as an inhibitor of Candida albicans Sap 3. Current Biochemistry. 2023;10(1):24-37. CrossRef
8. Ng'uni TL, dos Santos Abrantes PM, McArthur C, Klaasen JA, Fielding BC. Evaluation of synergistic anticandidal activity of Galenia africana extract and fluconazole against Candida albicans and Candida glabrata. J Herb Med. 2022;32:100503. CrossRef
9. Delgado Y, Cassé C, Ferrer-Acosta Y, et al. Biomedical effects of the phytonutrients turmeric, garlic, cinnamon, graviola, and oregano: A comprehensive review. Appl Sci (Basel). 2021;11(18):8477. CrossRef
10. Agu KC, Okolie PN. Proximate composition, phytochemical analysis, and in vitro antioxidant potentials of extracts of Annona muricata (Soursop). Food Sci Nutr. 2017;5(5):1029-1036. CrossRef PubMed
11. Coria-Téllez AV, Montalvo-Gónzalez E, Yahia EM, et al; Annona muricata: A comprehensive review on its traditional medicinal uses, phytochemicals, pharmacological activities, mechanisms of action and toxicity. Arab J Chem. 2018;11(5):662-691. CrossRef
12. Arthi S, Ramani P, Rajeshkumar S. Green synthesis of Annona muricata mediated selenium nanoparticles and its antifungal activity against Candida albicans. J Popul Ther Clin Pharmacol. 2023;30(16). CrossRef
13. Rustanti E, Fatmawati Z. The active compound of soursop leaf extract (Annona muricata, L.) as anti-vaginal discharge (Fluor albus). IOP Conf Ser Earth Environ Sci. 2020;456(1):012071. CrossRef
14. Egbo CC, Igboaka DC, Uzor PF. Antimicrobial assay and GC-MS profile of the extract of the endophytic fungus from Annona muricata (Annonaceae) leaf. Trop J Nat Prod Res. 2024;8(3):6731-6735.
15. Mishra AP, Nigam M, Nambooze J, et al; GC-MS analysis, antioxidant, and antidiabetic properties of methanol extract of Annona muricata L. leaves – An in vitro and in silico study. Curr Org Chem. 2023;27(17):1531-1541. CrossRef
16. Chigayo K, Mojapelo PEL, Mnyakeni-Moleele S, et al; Phytochemical and antioxidant properties of different solvent extracts of Kirkia wilmsii tubers. Asian Pac J Trop Biomed. 2016;6(12):1037-1043. CrossRef
17. Ahmed AS, McGaw LJ, Elgorashi EE, et al; Polarity of extracts and fractions of four Combretum (Combretaceae) species used to treat infections and gastrointestinal disorders in southern African traditional medicine has a major effect on different relevant in vitro activities. J Ethnopharmacol. 2014;154(2):339-350. CrossRef PubMed
18. Adi PJ, Yellapu NK, Matcha B. Modeling, molecular docking, probing catalytic binding mode of acetyl-CoA malate synthase G in Brucella melitensis 16M. Biochem Biophys Rep. 2016;8:192-199. CrossRef PubMed
19. Kuhn DM, Balkis M, Chandra J, et al; Uses and limitations of the XTT assay in studies of Candida growth and metabolism. J Clin Microbiol. 2003;41(1):506-508. CrossRef PubMed
20. Gardner DR, Molyneux RJ, Ralphs MH. Analysis of swainsonine: extraction methods, detection, and measurement in populations of locoweeds (Oxytropis spp.). J Agric Food Chem. 2001;49(10):4573-4580. CrossRef PubMed
21. Egan MJ, Kite GC, Porter EA, et al; Electrospray and APCI analysis of polyhydroxyalkaloids using positive and negative collision induced dissociation experiments in a quadrupole ion trap. Presented at SAC 99, Dublin, Ireland, July 25–30, 1999. Analyst. 2000;125(8):1409-1414. CrossRef
22. Fofana S, Keita A, Balde S, et al; Alkaloids from leaves of Annona muricata. Chem Nat Compd. 2012;48(4):714. CrossRef
23. Lima BRd, Silva F, Soares ER, et al; Integrative approach based on leaf spray mass spectrometry, HPLC-DAD-MS/MS, and NMR for comprehensive characterization of isoquinoline-derived alkaloids in leaves of Onychopetalum amazonicum RE Fr. J Braz Chem Soc. 2020;31:79-89. CrossRef
24. Mohanty S, Hollinshead J, Jones L, et al; Annona muricata (Graviola): Toxic or therapeutic. Natural Product Communications. 2008;3(1):1934578X0800300107. CrossRef
25. Ferraz CR, Silva DB, Prado LCDS, et al; Antidiarrhoeic effect and dereplication of the aqueous extract of Annona crassiflora (Annonaceae). Nat Prod Res. 2019;33(4):563-567. CrossRef PubMed
26. Nugraha AS, Haritakun R, Lambert JM, et al; Alkaloids from the root of Indonesian Annona muricata L. Nat Prod Res. 2021;35(3):481-489. CrossRef PubMed
27. Matsushige A, Kotake Y, Matsunami K, et al; Annonamine, a new aporphine alkaloid from the leaves of Annona muricata. Chem Pharm Bull (Tokyo). 2012;60(2):257-259. CrossRef PubMed
28. Cárdenas C, Torres-Vargas JA, Cárdenas-Valdivia A, et al; Non-targeted metabolomics characterization of Annona muricata leaf extracts with anti-angiogenic activity. Biomed Pharmacother. 2021;144:112263. CrossRef PubMed
29. Nawwar M, Ayoub N, Hussein S, et al; A flavonol triglycoside and investigation of the antioxidant and cell stimulating activities of Annona muricata Linn. Arch Pharm Res. 2012;35(5):761-767. CrossRef PubMed

30. Moghadamtousi SZ, Fadaeinasab M, Nikzad S, et al; Annona muricata (Annonaceae): a review of its traditional uses, isolated acetogenins and biological activities. Int J Mol Sci. 2015;16(7):15625-15658. CrossRef PubMed
31. Du J, Zhong B, Subbiah V, et al; LC-ESI-QTOF-MS/MS profiling and antioxidant activity of phenolics from Custard Apple fruit and by-products. Separations. 2021;8(5):62. CrossRef
32. George VC, Kumar DR, Rajkumar V, et al; Quantitative assessment of the relative antineoplastic potential of the n-butanolic leaf extract of Annona muricata Linn. in normal and immortalized human cell lines. Asian Pac J Cancer Prev. 2012;13(2):699-704. CrossRef PubMed
33. Cioffi, E., Comune, L., Piccolella, S., Buono, M., & Pacifico, S. (2023). Quercetin 3-O-Glucuronide from Aglianico Vine Leaves: A Selective Sustainable Recovery and Accumulation Monitoring. Foods, 12(14), 2646. CrossRef PubMed
34. Li L, Feng X, Chen Y, et al; A comprehensive study of eriocitrin metabolism in vivo and in vitro based on an efficient UHPLC-Q-TOF-MS/MS strategy. RSC Adv. 2019;9(43):24963-24980. CrossRef PubMed
35. Gu ZM, Zhou D, Wu J, et al; Screening for Annonaceous acetogenins in bioactive plant extracts by liquid chromatography/mass spectrometry. J Nat Prod. 1997;60(3):242-248. CrossRef PubMed
36. Al Kazman BSM, Harnett JE, Hanrahan JR. Identification of Annonaceous acetogenins and alkaloids from the leaves, pulp, and seeds of Annona atemoya. Int J Mol Sci. 2023;24(3):2294. CrossRef PubMed
37. Hidalgo JR, Gilabert M, Cabedo N, et al; Montanacin-L and montanacin-K two previously non-described acetogenins from Annona montana twigs and leaves. Phytochem Lett. 2020;38:78-83. CrossRef
38. Campos LM, Lemos ASO, Diniz IOM, et al; Antifungal Annona muricata L. (soursop) extract targets the cell envelope of multi-drug resistant Candida albicans. J Ethnopharmacol. 2023;301:115856. CrossRef PubMed
39. Duret P, Hocquemiller R, Cavé A. Annonisin, a bis-tetrahydrofuran acetogenin from Annona atemoya seeds. Phytochemistry. 1997;45(7):1423-1426. CrossRef
40. Apeh VO, Adegboyega AE, Chukwuma IF, et al; An in silico study of bioactive compounds of Annona muricata in the design of ani-prostate cancer agent: MM/GBSA, pharmacophore modeling and ADMET parameters. Inform Med Unlocked. 2023;43:101377. CrossRef
41. Abdul-Hammed M, Olaide IA, Adegoke HM, et al; Antifungal activities of phytochemicals from Annona muricate (Sour Sop): molecular docking and chemoinformatics approach. Majalah Obat Tradisional. 2022;27(3):218. CrossRef
42. Campos LM, Silva TP, de Oliveira Lemos AS, et al; Antibiofilm potential of Annona muricata L. ethanolic extract against multi-drug resistant Candida albicans. J Ethnopharmacol. 2023;315:116682. CrossRef PubMed
43. Berrouet C, Dorilas N, Rejniak KA, et al; Comparison of drug inhibitory effects (IC50) in monolayer and spheroid cultures. Bull Math Biol. 2020;82(6):68. CrossRef PubMed
44. Duarte D, Vale N. Evaluation of synergism in drug combinations and reference models for future orientations in oncology. Curr Res Pharmacol Drug Discov. 2022;3:100110. CrossRef PubMed
45. Gao M, Wang H, Zhu L. Quercetin assists fluconazole to inhibit biofilm formations of fluconazole-resistant Candida albicans in in vitro and in vivo antifungal managements of vulvovaginal candidiasis. Cell Physiol Biochem. 2016;40(3-4):727-742. CrossRef PubMed
46. da Silva CR, de Andrade Neto JB, de Sousa Campos R, et al; Synergistic effect of the flavonoid catechin, quercetin, or epigallocatechin gallate with fluconazole induces apoptosis in Candida tropicalis resistant to fluconazole. Antimicrob Agents Chemother. 2014;58(3):1468-1478. CrossRef PubMed
47. Liu W, Li LP, Zhang JD, et al; Synergistic antifungal effect of glabridin and fluconazole. PLoS One. 2014;9(7):e103442. CrossRef PubMed

DTI
Drug Target Insights 2025; 19: 11-17
ISSN 1177-3928 | DOI: 10.33393/dti.2025.3271
ORIGINAL RESEARCH ARTICLE

Exploring the in vitro anti-diabetic potential and in silico studies of 2, 3 and 2, 6-dichloroIndolinone

Abdur Rauf[1], Waqas Alam[1], Momin Khan[2], Hany W. Darwish[3], Maria Daglia[4], Ahmed A. Elhenawy[5], Haroon Khan[1,6]

[1]Department of Pharmacy, Abdul Wali Khan University, Mardan - Pakistan
[2]Department of Chemistry, Abdul Wali Khan University, Mardan - Pakistan
[3]Department of Pharmaceutical Chemistry, College of Pharmacy, King Saud University, Riyadh - Kingdom of Saudi Arabia
[4]Department of Pharmacy, University of Naples Federico II- Italy
[5]Department of Chemistry, Faculty of Science, Al-Azhar University, Cairo - Egypt
[6]Department of Pharmacy, Korea University, Sejong - South Korea

ABSTRACT

Introduction: Adequate hyperglycemic control is still a huge challenge with the clinically used therapeutics. New, more effective anti-diabetic agents are on the top list of drug discovery projects.
Methods: This article deals with the in vitro anti-diabetic potential of 2, 3 dichloroIndolinone (C1) and 2, 6-dichloroIndolinone (C2) on α-glucosidase and α-amylase followed by in silico analysis.
Results: Both compounds, C-1 and C-2, caused significant inhibition of α-glucosidase at various test concentrations with IC_{50} of 35.266 µM and 38. 379 µM, respectively. Similarly, compounds C-1 and C-2 elicited significant anti-α-amylase action with IC_{50} values of 42.449 µM and 46.708 µM, respectively. The molecular docking investigation regarding the α-glucosidase and α-amylase binding site was implemented to attain better comprehension with respect to the pattern in which binding mechanics occur between the C1 and C2 molecules and the active sites, which illustrated a higher binding efficacy in appraisal with reference inhibitor and acarbose. The interactions between the active compounds C1 and C2 with the active site residues were mainly polar bonds, hydrogen bonding, π–π, and π–H interactions, which contributed to a strong alignment with the enzyme backbone. Similarly, effective binding is frequently indicated by a strong and stable hydrogen-bonding pattern, which is suggested by the minimal fluctuation in MM-PBSA values.
Conclusion: In short, this study will contribute to providing these compounds with an improved anti-diabetic profile and decreased toxicity.
Keywords: 2, 3 and 2, 6-dichloroIndolinone, α-glucosidase/α-amylase inhibition, Molecular docking, Molecular simulation

Introduction

Diabetes mellitus (DM) is a prolonged metabolic state that can result from reduced insulin synthesis or decreased insulin's ability to facilitate the absorption of glucose. Hyperglycemia or extremely high blood glucose, and glucose intolerance are characteristics of DM (1). The World Health Organization (WHO) describes DM as a life-long metabolic disorder marked by increased blood glucose levels that eventually cause harm to the kidneys, eyes, nerves, cardiovascular system, and vascular system. Over ninety percent of the cases of DM are caused by type II DM (T2DM), which is described by tissue inadequate insulin or insulin resistance synthesis by the pancreatic β cells and an improper compensatory insulin secretory response (2). Diabetes is the tenth most common cause of death, accounting for over a million deaths annually. By 2030, the number of people with type 2 diabetes worldwide is expected to reach 7079 per 100,000, indicating a persistent increase in cases worldwide. Concerning evidence indicates that prevalence is on the rise in lower-income nations. There is a need for immediate clinical preventative and public health actions. (3). Type 2 diabetes, which develops in adult age, is defined by inadequate insulin production, either alone or in combination with insulin resistance (4). There are some key similarities between heart disease [cardiovascular disease (CVD)] and DM. One significant and unique risk factor for CVD is diabetes. The most frequent and expensive blood vessel consequence of diabetes is heart disease [coronary heart disease (CHD)] (5). There are presently no effective medications to treat this health condition, and the available therapies are successful for some

Received: August 23, 2024
Accepted: February 4, 2025
Published online: March 10, 2025

Corresponding author:
Haroon Khan
email: haroonkhan@awkum.edu.pk

people but not all. Innovative anti-diabetic drugs are therefore greatly needed. Diabetes management requires an extensive review of current pharmacotherapies and phytotherapies, as well as nutraceutical-based therapies for effective management of diabetes, along with their merits and limitations (6).

The first known oxindole derivative was discovered in the form of alkaloids from the bark of the tropical climber species known as cat claw's plant (*Uncaria tomentosa*), which is native to the dense rainforests of the Amazon region and other tropical regions of central and southern South America (7). Oxindoles are naturally occurring aromatic chemical compounds found in a variety of plant materials as well as in animal tissues and body fluids. A six-membered benzene ring and a five-membered ring containing nitrogen combine to form an oxindole (8). Several researchers have discovered, produced, generated, and analyzed oxindole derivatives for a range of biological effects and observed significant effects (9-12). Medicinal chemists are motivated to create new oxindole derivatives because of the oxindole nucleus's historical and current medicinal value. Oxindole-derived compounds are potent inhibitors of the α-glucosidase enzyme, which is a target enzyme in the treatment of DM (13). The breakdown and intestinal absorption of carbohydrates occur by important enzymes α-amylase and α-glucosidase, respectively. The therapy of non-insulin-dependent DM (NIDDM) can benefit greatly from the inhibition of these enzymes, which inhibits the rise in blood glucose levels following the consumption of carbohydrates (14). Similarly, 2, 3 and 2, 6-dichloroIndolinone have already shown potential drug-like properties coupled with antioxidant potential (15). In the present article, we are presenting the in vitro α-glucosidase and α-amylase activities of oxindoles, 2, 3 dichloroIndolinone (C1) and 2, 6-dichloroIndolinone (C2) (Figure 1) followed by molecular docking and molecular dynamic simulation.

Materials and Methods

Chemicals

Chemicals used were α-glucosidase, α-amylase, acarbose, glucopyranoside, phosphate buffer, and piperidine, Na_2CO_3, starch and dinitro salicylic acid -solution, hydrochloric acid and distilled water.

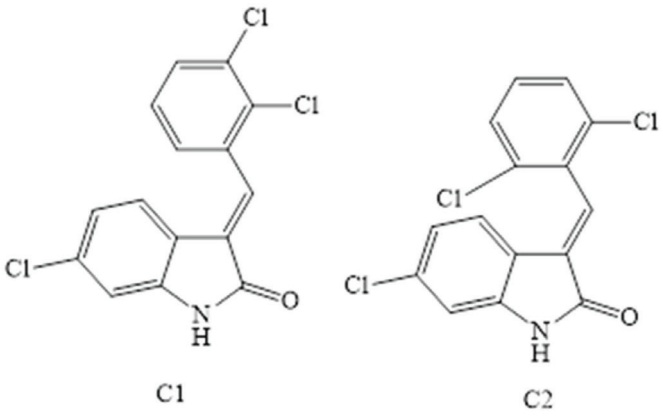

FIGURE 1 - Structures of test compounds.

α-Glucosidase Activity

In this test, Glucopyranoside is incorporated into the solvent (phosphate buffer). Several doses of the synthesized compounds, including 62.5 µg/mL, 125 µg/mL, 250 µg/mL, 500 µg/mL, and 1000 µg/mL, were used to create the sample solutions. Added 0.5 µg/mL of glucosidase in distilled water to the mixture described above. Subsequently, the resultant mixture was incubated at 37°C for 20 minutes (16). Hydrochloric acid was used to stop the reaction mixture after the incubation period. Using a spectrophotometer, the color intensity was determined at a wavelength of 540 nm. The percentage inhibition was computed using the following equation:

Inhibition (%) = (Control Abs − Test Abs/Control Abs) × 100

α-Amylase Activity

In this assay, previously published techniques were applied (16). α-amylase, phosphate buffer, and the sample solution were prepared by combining different amounts of the produced compounds (62.5 µg/mL, 125 µg/mL, 250 µg/mL, 500 µg/mL, and 1000 µg/mL). After mixing this solution with the starch solution, the mixture was left to incubate for around 20 minutes at 37°C. Following incubation, the reactant mixture was just maintained at 100°C in a water bath. At 656 nm, the color intensity was determined using a microplate reader. The following formula was used to get the inhibition percentage.

Inhibition (%) = (Control Abs - Test Abs/Control Abs) x 100

Molecular Docking

The synergistic effect of characteristics of active compounds C1 and C2 on α-glucosidase and α-amylase inhibitory actions was investigated using molecular docking studies (17). The protein data bank provided the α-glucosidase and α-amylase PDB IDs, which are 5NN5 and 4GQR, respectively.

Molecular Dynamic Simulation

We calculated the parameters, including binding free energy, van der Waals energy, electrostatic energy, kinetic energy, and potential energy changes using molecular dynamics simulations. Furthermore, we investigated the interactions that these compounds had with the proteins, glucosidase, and amylase throughout a time span of 0 to 250 ns. The binding free energy change values for the two compounds interacting with the proteins were also computed (18). The docking analysis was performed to explicate the potency of these desirable molecules in vitro against the epidermal growth factor receptor (EGFR) kinase through their potential interaction mechanisms with their crystal frameworks (PDB: 1b2y (19), PDB: 3A4A) (20)). The docking investigation was implemented through Glide's module®. The preliminary inhibitors (Acarbose) were relocked into the α-amylase crystal framework to verify the docking methodology. Furthermore, the efficacious performance of the targeted molecules was authenticated *via* the low values of RMSD (1.02 respectively), which were acquired through the

root mean square deviation between the native and relocked poses of the co-crystallized inhibitor.

Statistical Analysis

The data is illustrated as mean ± SEM of three distinct measurements. Analyisis of variance (ANOVA) at *p < 0.05 and the Bonferroni test showed static significance using GraphPad version 8.

Results

Effects of Compounds on α-glucosidase Inhibition

Figure 2 shows the α-glucosidase inhibition of selected compounds (C1-C2) when studied at various concentrations. In the assay, C1 produced marked inhibition that was increased with increasing drug concentrations, and the maximum effect (88%) was noted at 1000 µM. The IC_{50} value of C1 was estimated as 35.266 µM. Similarly, C2 displayed significant α-glucosidase inhibition when tested at various concentrations. The maximum inhibitory effect was 85% at a dose of 1000 µM in specified conditions. The potency was expressed as an IC_{50} value of 38.379 µM. In comparison, acarbose had IC_{50} values of 34.216 µM.

Effect of Compounds on α-amylase Inhibition

The α-amylase inhibitory potential of test compounds (C1-C2) when challenged at various concentrations are displayed in Figure 3. Compound 1 caused significant inhibition of α-amylase, and the overall effects were concentration dependant. The maximum inhibition of 90% was observed at

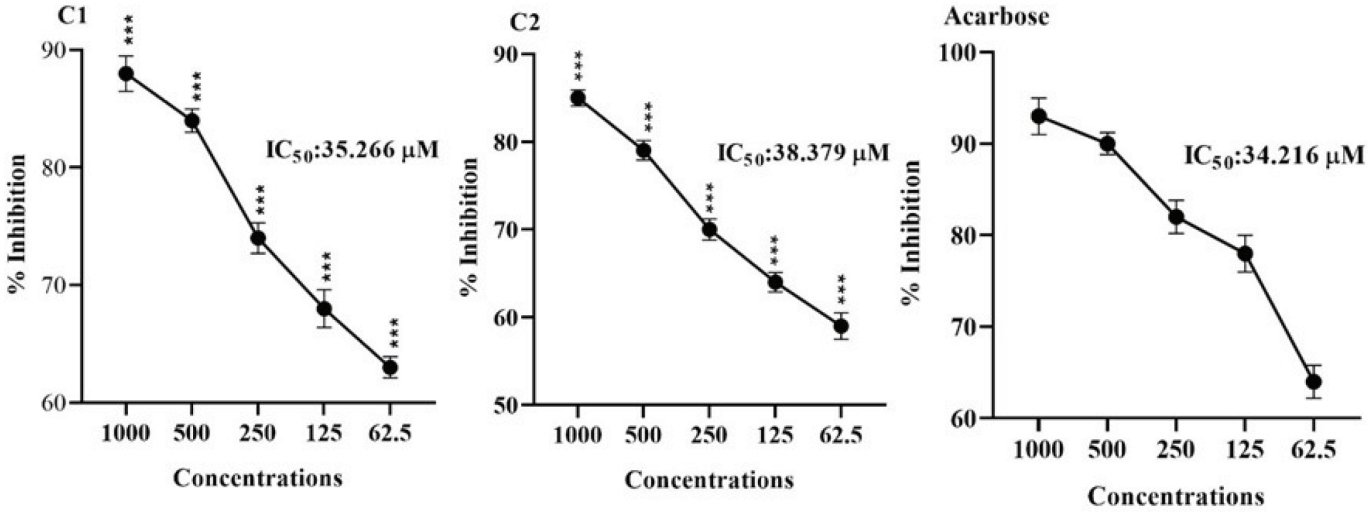

FIGURE 2 - Showing α-glucosidase inhibiting effects of Compounds (C1 and C2). The mean ± SEM of three distinct measurements was provided as the result. ANOVA at *p < 0.05 and the Bonferroni test showed static significance. At the same tested strengths, there are slight variations in ***p < 0.001 results when compared to the positive control (Acarbose).

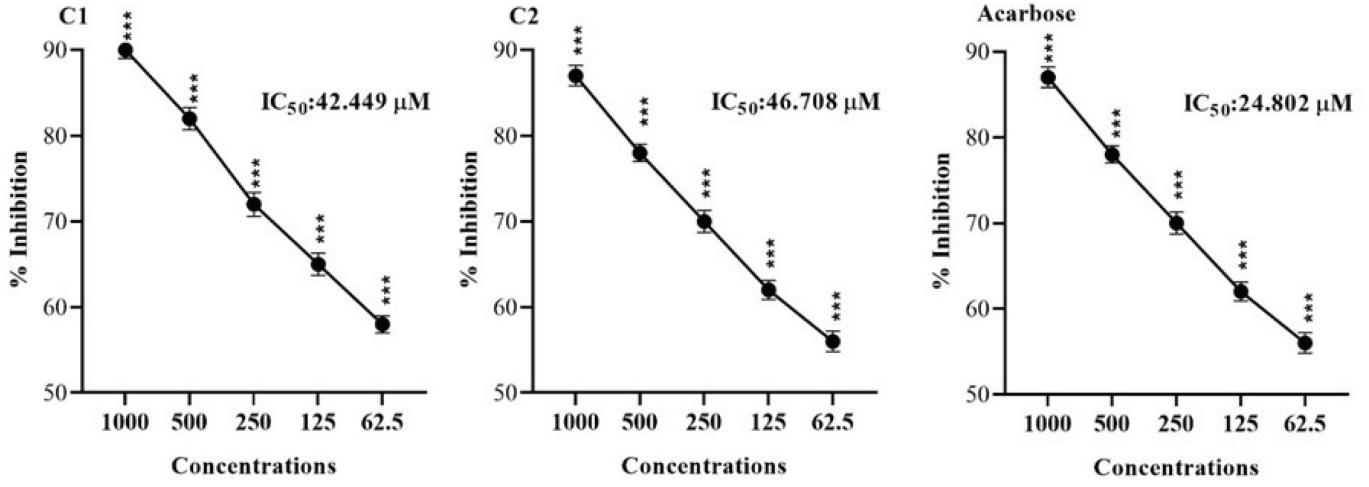

FIGURE 3 - Showing α-Amylase inhibiting effects of Compounds (C1 and C2). The Mean ± SEM of three distinct measurements was provided as the result. ANOVA at *p < 0.05 and the Bonferroni test showed static significance. At the same tested strengths, there are slight variations in ***p < 0.001 results when compared to the positive control (Acarbose).

1000 µM, and the IC_{50} was 42.449 µM. Similarly, compound 2 caused potential α-amylase inhibition at various doses from 62.50-1000 µM. The maximum inhibition, 87%, was demonstrated at 1000 µM. The overall effect of IC_{50} was 46.708 µM. The standard drug (Acarbose) had an IC_{50} value of 24.802 µM.

Molecular Docking Analysis

The binding free energies for ΔE are listed in (Table 1). The initial inhibitors have been adequately installed into their binding sites in order to attain their crystal configurations.

TABLE 1 - The binding affinity for compounds C1 and C2 with docking score (kcal/mol) against α-amylase

No.	*ΔG*	RMSD	H. B	EInt.	Eele	LE
α-glucosides						
C1	−5.898	0.893	−10.228	−6.188	−13.702	−6.604
C2	−6.312	1.285	−8.658	−4.223	−21.775	−4.912
Acarbose	−6.088	0.725	−15.129	−12.148	−31.340	−8.393
α-amylase						
C1	−5.449	0.955	24.364	−19.256	−8.526	2.10
C2	−5.497	1.257	19.021	−18.133	−8.679	2.253
Acarbose	−9.814	1.634	-34.746	−15.117	−55.322	2.885

Where *ΔG*: Free binding energy of the ligand; RMSD: *root-mean-square deviation;* H.B.: H-bonding energy between protein and ligand; EInt. Binding affinity of H-bond interaction with receptor; Eele: Electrostatic interaction over the receptor, Ki: inhibition constant.

For the docking analysis, we selected the most perforable docking conformations of C1 and C2 compounds that were detected inside the active site of α-glucosidase enzyme (PDB: 3A4A) with proper alignment. The active site includes the hydrophilic amino acids (ASP69, TYR72, GLU277, HIS351, ASP352, and ARG442), which interact with competitive inhibitor acarbose. We noticed that almost all investigated compounds interacted with significant residues in the binding pocket. We defined the inhibitory behavior in terms of binding energy BE that was evaluated with the receptor. Then, redocked compounds compared the results to the comparative reference inhibitor and obtained a root mean square deviation (RMSD), which is summarized in (Table 1). The C2 exhibited strong interactions with the enzyme, as indicated by their binding free energies of −6.312 Kcal/mol. Compared to the reference inhibitor, which had a binding free energy of −6.088 Kcal/mol and lower inhibitory activity, the C1 showed superior binding efficacies, −5.898 Kcal/mol. The docking analysis revealed that C2 had the highest binding affinity and formed a strong hydrogen bond with Gly353, Glu411, and ASP307, which are essential for enzyme activity. The second inhibitor, C1, had a similar binding mode to the reference inhibitor and established a strong hydrogen bond with GLn353, ARG213, and Gln182 (Figure 4).

The molecule docked prolifically into active sites in a mechanism similar to that of the original inhibitors. For amylase, compounds C1 and C2 demonstrated promising binding affinities (ΔE = −5.44 to −5.5 kcal/mol), which substantiated their promising potencies. The interactions between the

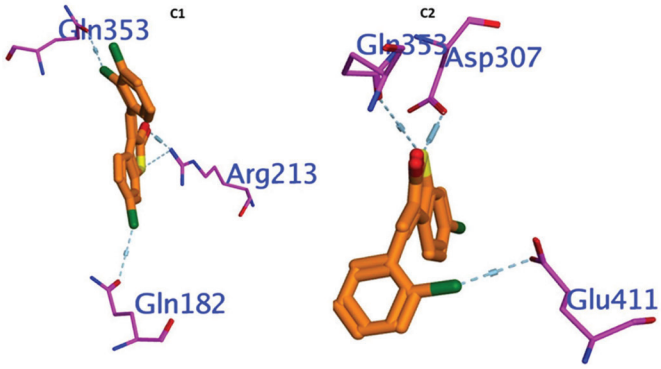

FIGURE 4 - Showing 3D Docking poses of C1, and C2 against α- glucosidase.

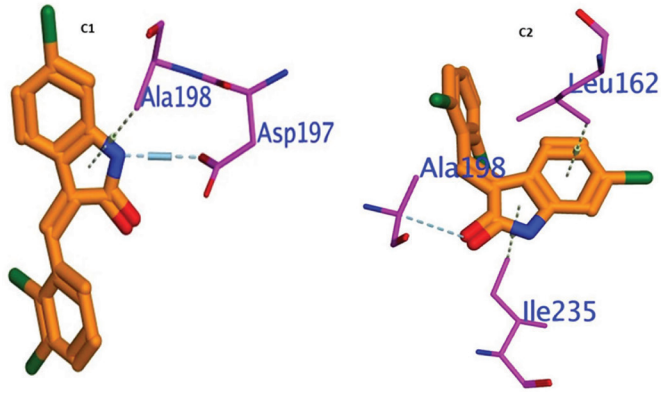

FIGURE 5 - Showing 3D Docking poses of C1, and C2 against α- amylase.

thirteen active compounds C1 and C2 with the active site residues were mainly polar bonds, hydrogen bonding, π–π, and π–H interactions, which contributed to a strong alignment with the enzyme backbone Figure 5. The active molecules C1 and C2 were attached deeply and comfortingly in the binding pocket by interacting with the hydrophilic Asp 198 hydrophobic binding pocket ALA197 and Ile 235. Compound C2 docked in the α-amylase binding pocket *via* hydrophobic interaction with Ala198. It is inferred that the formation of strong interactions with important residues can pinpoint α-amylase in the binding pocket. Lastly, according to the 3D-molecular docking, the C2 prefers a parallel orientation between the central indoline ring and the important hydrophilic Asp 197 into the binding pockets.

Molecular Dynamic Investigations of C1-C2

In order to comprehend enzymatic activity and create inhibitors, it is essential to investigate ligand-enzyme interactions, like the one that exists between the α-glucosidase protein and a ligand. Molecular Mechanics-Poisson-Boltzmann Surface Area (MM-PBSA) computations offer a thorough understanding of the molecular binding processes. The dynamic nature of molecular interactions is captured through a rigorous approach of accounting for the flexibility of α-glucosidase

protein complexes during contact tests at 2 ns intervals. The energy changes in Figure 6, which illustrate fluctuations in the binding free energy at 12-ns intervals, provide important information about the strength and stability of the binding throughout time. The significance of structural variations on binding affinity is highlighted by comparing the energy changes of the two dichloroindolinone molecules. Positive interactions were indicated by the binding parameter values that are negative, which is encouraging for the possible effectiveness of these compounds as inhibitors. Effective binding is frequently indicated by a strong and stable hydrogen-bonding pattern, which is suggested by the minimal fluctuation in MM-PBSA values.

It is unsuitable for illustrating the relationship between molecular docking computations and ligand-protein interactions at the ns level since the ligand molecules are rather flexible in the calculations. The ligand-amylase protein interaction is performed at 250 ns using MM-PSBA calculations. In MM-PSBA calculations, all compounds of amylase protein complexes have flexibility when checking the interaction every 2 ns, and the energy change is reported in Figure 7. The resulting graph in Figure 7 depicts the binding free energy changes and variations in all ten (ns) intervals. The energy

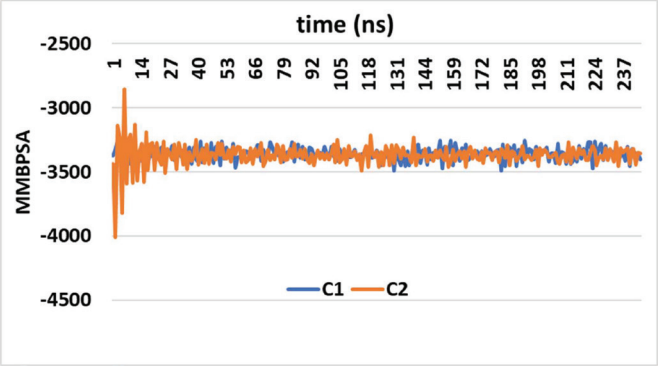

FIGURE 6 - The values of the test compounds C1 and C2 for the Gibbs free energy of ligand α-glucosidase protein.

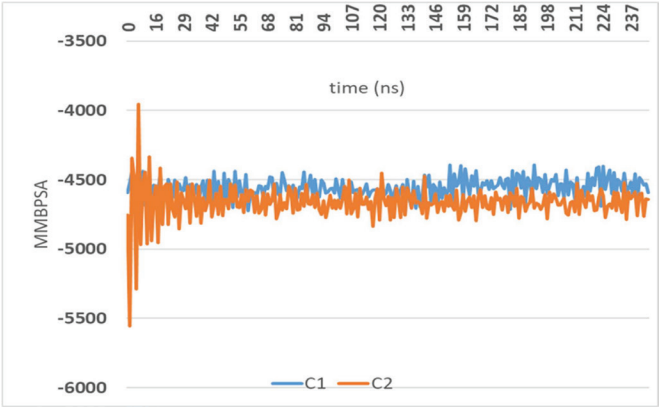

FIGURE 7 - The values of the test compounds C1 and C2 for the Gibbs free energy of ligand α-amylase protein.

changes of the most active two 2, 3 and 2, 6-dichloroIndolinone molecules were compared, and the calculations were performed to validate the determination of bonding free energies using the molecular MMPBSA approach. Negative values for the relevant parameters indicate improved binding. The small fluctuations for MM-PBSA for both complexed with amylase over the entire time scale indicated a robust contact between Ligand and amino acid backbone, indicating a firm H-bonding pattern.

Discussion

The study revealed significant in vitro α-glucosidase and α-amylase inhibition of oxindoles, 2, 3 dichloroIndolinone (C1) and 2, 6-dichloroIndolinone (C2), which were molecular docking and simulation studies.

The development of a new, more effective molecule with lower toxicity is always a primary target in research (21). Dichloroindolinone are oxindole derivatives that are utilized for a wide range of biological effects (10,22,23). Enzymes belonging to the glucosidases are present on the brush boundary surface of intestinal microglia. They cause starch 1,4-glycosidic bonds to break, releasing –D-glucose, which is absorbed. It consequently raises post-meal hyperglycemia. Therefore, it is essential to use these enzyme inhibitors in the management of type II diabetes. A class of enzymes known as α-glucosidases hydrolyzes the 1, 4-glycosidic bond in starch to produce α-D-glucose, which enters the bloodstream after absorption (24). As a result, it causes post-meal hyperglycemia. As a result, using these enzyme inhibitors is essential for managing T2DM. Proper absorption and digestion of monosaccharides may help avoid diabetes, obesity, hyperlipoproteinemia, and hyperlipidemia (25). These inhibitors may be used to treat malignancies, viral infections, and several other diseases, as well as to regulate the immune system (13). The early metabolism abnormality that arises in NIDDM, postprandial hyperglycemia, has been identified as a potential therapy for glucosidase (26). Our finding on the test compounds showed significant inhibition of the enzyme by both compounds and, therefore, could be potential candidates as glucosidase inhibitors.

The hydrolase enzyme α-amylase catalyzes the hydrolysis of internal -1, 4-glycosidic bonds in starch to create products like glucose and maltose. Since it is a calcium metalloenzyme, a metal cofactor is necessary for it to function (27). The class of enzymes known as amylases is responsible for hydrolyzing starch to produce low-molecular-weight dextrins and sugars, and they are crucial for the digestion of carbohydrates. Maltose, maltotriose, and other - (1,6) and - (1,4) oligoglucans can be broken down into glucose by various α-glucosidases and are the primary components of the final hydrolysate. Controlling the activity of HPA, which is a human pancreatic enzyme that is essential for the digestion of starch, could effectively lower blood glucose levels after meals (28). When combined, α-glucosidase and α-amylase inhibition can significantly reduce the rise in blood glucose that occurs after meals and could be an essential strategy for controlling blood glucose levels in people with T2DM. The main treatment targets for type-2 DM are thus pancreatic α-amylase and gut glucoamylases. Amylase antagonists are already available on

the market for the treatment of diabetes. Amylase inhibitors can also be used to treat obesity (29). We observed strong inhibition of the α-amylase by the test compounds at various concentrations and therefore augmented the overall anti-diabetic potential of these compounds as strong candidates for further studies.

Molecular docking tests revealed that the best-ranked conformation of the test compounds fit into the site of activity well, and its oxindole moiety interacted with important locations in the binding pocket. The interaction between ligands and enzymes was studied in docking investigations to gain a greater understanding of the in vitro outcomes. The structure data for the selected enzymes was obtained by searching the Protein Data Bank. The PDB IDs for α- Amylase and α-Glucosidase were 4GQR and 5NN5, respectively (28, 30). The process and enzyme preparation were completed with the aid of the Molecular Operating Environment (MOE) software. The enzymes were first removed from non-standard structures and inadequate bounded ligands in order to prepare them for docking in PDB format. Binding energies were investigated, and docking method outcomes were evaluated. It was demonstrated that the optimal ligand-enzyme interaction model produced increased negative values; the more negative values, the greater the probability of binding at that particular site. Various situations were used in order to see the key interaction between the ligands and enzymes, amino acid residues, binding pocket, and bond lengths were presented in different colors. The lowest score poses, and RMSD revealed increased stability in the binding pocket. The data was utilized to rank the docked poses and to select the most capable docked conformation of each compound. The hetero ring for Erlotinib and benzimidazole centered on the α-amylase pocket and interacted with HIS 305, ASP 300, AlA198, ASP 197, THR 163, LEU162, TYR 151, GLN 63, TRP 59. In the MM-PBSA calculations, the ligand-glucosidase and amylase protein interaction is monitored every 2 ns. The negative values indicate improved binding (more favorable interactions). The small fluctuations observed for MM-PBSA over the entire time scale suggest a stable interaction. The robust contact between the ligand and the amino acid backbone indicates firm hydrogen bonding.

Conclusion

In a dose-dependent way, the 6-chlorooxindole-derived compounds C1 and C2 showed potential in vitro α-glucosidase and α-amylase inhibition. C1 and C2 demonstrated a high binding and inhibitory potential when docked with the enzyme α-Glucosidase (5NN5) and α-amylase (4GQR) enzyme. Strong alignment with the enzyme backbone was achieved by the active chemicals C1 and C2 interacting primarily with the active site residues through polar bonds, hydrogen bonding, π–π, and π–H interactions. The minimal fluctuation in MM-PBSA values suggests a consistent and strong hydrogen-bonding pattern, which is often a hallmark of effective binding. The present investigation reveals improved anti-diabetic features for the 6-chlorooxindole derivatives. These focused compounds could help develop more potent antihyperglycemic medications in the future, but need further detailed studies.

Acknowledgments

The authors extend their appreciation to the Researchers Supporting Project number (RSPD2025R812), King Saud University, Riyadh, Saudi Arabia, for funding.

Disclosures

Financial support: The authors extend their appreciation to the Researchers Supporting Project number (RSPD2025R812), King Saud University, Riyadh, Saudi Arabia, for funding.

Conflict of Interest: The authors of this article declare no conflict of interest.

Data Availability Statement: The data that support the findings of the present study are available from the corresponding authors upon reasonable request.

References

1. Sagbo IJ, van de Venter M, Koekemoer T, et al. In vitro anti-diabetic activity and mechanism of action of Brachylaena elliptica (Thunb.) DC. Evidence-Based Complementary and Alternative Medicine, 2018. CrossRef PubMed
2. Galicia-Garcia U, Benito-Vicente A, Jebari S, et al. Pathophysiology of type 2 diabetes mellitus. Int J Mol Sci. 2020;21(17):6275. CrossRef PubMed
3. Khan MAB, Hashim MJ, King JK, et al. Epidemiology of type 2 diabetes—global burden of disease and forecasted trends. J Epidemiol Glob Health. 2020;10(1):107-111. CrossRef PubMed
4. Pozzilli P, Di Mario U. Autoimmune diabetes not requiring insulin at diagnosis (latent autoimmune diabetes of the adult): definition, characterization, and potential prevention. Diabetes Care. 2001;24(8):1460-1467. CrossRef PubMed
5. Resnick HE, Howard BV. Diabetes and cardiovascular disease. Annu Rev Med. 2002;53(1):245-267. CrossRef PubMed
6. Khursheed R, Singh SK, Wadhwa S, et al. Treatment strategies against diabetes: success so far and challenges ahead. Eur J Pharmacol. 2019;862:172625. CrossRef PubMed
7. Khetmalis YM, Shivani M, Murugesan S, et al. Oxindole and its derivatives: a review on recent progress in biological activities. Biomed Pharmacother. 2021;141:111842. CrossRef PubMed
8. Gassman PG, Van Bergen T. General method for the synthesis of oxindoles. J Am Chem Soc. 1973;95(8):2718-2719. CrossRef
9. Mukhliss L, Taha M, Rahim F, et al. Synthesis and novel structural hybrid analogs of oxindole derivatives bearing piperidine ring, their antidiabetics II activity and molecular docking study. *J Mol Struct*. 2025;1332:141666. CrossRef
10. Pirzada AS, Khan H, Alam W, et al. Physicochemical properties, pharmacokinetic studies, DFT approach, and antioxidant activity of nitro and chloro indolinone derivatives. Front Chem. 2024;12:1360719. CrossRef PubMed
11. Ahmad I, Khan H, Serdaroğlu G. Physicochemical properties, drug likeness, ADMET, DFT studies, and in vitro antioxidant activity of oxindole derivatives. Comput Biol Chem. 2023;104:107861. CrossRef PubMed
12. Kadhim MM, Heravi MRP, Mohammadi-Aghdam S, et al. Investigation of anti-tumor (E)-3-X-oxindole via functionalization of C20 nano structure: A DFT approach. *Comput Theor Chem*. 2022;1214:113763. CrossRef
13. Khan M, Yousaf M, Wadood A, et al. Discovery of novel oxindole derivatives as potent α-glucosidase inhibitors. Bioorg Med Chem. 2014;22(13):3441-3448. CrossRef PubMed

14. Altowyan MS, Barakat A, Al-Majid AM, et al. Spiroindolone analogues as potential hypoglycemic with dual inhibitory activity on α-amylase and α-glucosidase. Molecules. 2019; 24(12):2342. CrossRef PubMed
15. Rauf A, Khan H, Khan M, et al. In Silico, Swiss ADME, and DFT studies of newly synthesized oxindole derivatives followed by antioxidant studies. J Chem. 2023;2023(1):5553913. CrossRef
16. Huneif MA, Alshehri DB, Alshaibari KS, et al. Design, synthesis and bioevaluation of new vanillin hybrid as multitarget inhibitor of α-glucosidase, α-amylase, PTP-1B and DPP4 for the treatment of type-II diabetes. Biomed Pharmacother. 2022;150:113038. CrossRef PubMed
17. Taha M, Ismail NH, Khan A, et al. Synthesis of novel derivatives of oxindole, their urease inhibition and molecular docking studies. Bioorg Med Chem Lett. 2015;25(16):3285-3289. CrossRef PubMed
18. Irfan A, Faisal S, Ahmad S, et al. Structure-based virtual screening of furan-1, 3, 4-oxadiazole tethered N-phenylacetamide derivatives as novel class of hTYR and hTYRP1 inhibitors. pharmaceuticals, 2023, 16, (3), 344. CrossRef
19. Nahoum V, Roux G, Anton V, et al. Crystal structures of human pancreatic α-amylase in complex with carbohydrate and proteinaceous inhibitors. Biochem J. 2000;346(Pt 1):201-208. CrossRef PubMed
20. Yamamoto K, Miyake H, Kusunoki M, et al. Crystal structures of isomaltase from Saccharomyces cerevisiae and in complex with its competitive inhibitor maltose. FEBS J. 2010;277(20): 4205-4214. CrossRef PubMed
21. Schenone M, Dančík V, Wagner BK, et al. Target identification and mechanism of action in chemical biology and drug discovery. Nat Chem Biol. 2013;9(4):232-240. CrossRef PubMed
22. Rindhe SS, Karale BK, Gupta RC, et al. Synthesis, antimicrobial and antioxidant activity of some oxindoles. *Indian J Pharm Sci*. 2011;73(3):292-296. PubMed
23. Qi Y, Gong H, Wang Z, et al. Discovery of novel oxindole derivatives as TRPA1 antagonists with potent analgesic activity for pain treatment. Bioorganic Chemistry 154, 108088.
24. Casirola DM, Ferraris RP. α-Glucosidase inhibitors prevent diet-induced increases in intestinal sugar transport in diabetic mice. Metabolism. 2006;55(6):832-841. CrossRef PubMed
25. Derosa G, Maffioli P. α-Glucosidase inhibitors and their use in clinical practice. Arch Med Sci. 2012;8(5):899-906. CrossRef PubMed
26. Thilagam E, Parimaladevi B, Kumarappan C, et al. α-Glucosidase and α-amylase inhibitory activity of Senna surattensis. J Acupunct Meridian Stud. 2013;6(1):24-30. CrossRef PubMed
27. de Souza PM, de Oliveira Magalhães P. Application of microbial α-amylase in industry - a review. Braz J Microbiol. 2010;41(4), 850-861. CrossRef PubMed
28. Qin X, Ren L, Yang X, et al. Structures of human pancreatic α-amylase in complex with acarviostatins: implications for drug design against type II diabetes. J Struct Biol. 2011;174(1): 196-202. CrossRef PubMed
29. Jayaraj S, Suresh S, Kadeppagari RK. Amylase inhibitors and their biomedical applications. Stärke. 2013;65(7-8):535-542. CrossRef
30. Azam SS, Uddin R, Wadood A. Structure and dynamics of alpha-glucosidase through molecular dynamics simulation studies. J Mol Liq. 2012;174:58-62. CrossRef

DTI
Drug Target Insights 2025; 19: 18-30
ISSN 1177-3928 | DOI: 10.33393/dti.2025.3368
ORIGINAL RESEARCH ARTICLE

Withania somnifera root extract (LongeFera™) confers beneficial effects on health and lifespan of the model worm *Caenorhabditis elegans*

Nidhi Thakkar[1#], Gemini Gajera[1#], Dilip Mehta[2], Sujit Nair[2], Vijay Kothari[1]

[1] Institute of Science, Nirma University, Ahmedabad - India
[2] Phytoveda Pvt. Ltd., Mumbai - India

[#]Contributed equally

ABSTRACT

Background*: Withania somnifera* is among the most widely prescribed medicinal plants in traditional Indian medicine. Hydroalcoholic extract of the roots of this plant was investigated for its effects on the overall health and lifespan of the model worm *Caenorhabditis elegans*.
Methods: The extract's effect on worm lifespan and fertility was observed microscopically. Worm motility was quantified through an automated worm tracker. The metabolic activity of the worms was captured using the Alamar Blue® assay. Differential gene expression in extract-treated worms was revealed through a whole transcriptome approach.
Results: Extract-exposed gnotobiotic worms, in the absence of any bacterial food, registered longer lifespan, higher fertility, better motility, and metabolic activity. Whole transcriptome analysis of the extract-treated worms revealed the differential expression of the genes associated with lifespan extension, eggshell assembly and integrity, progeny formation, yolk lipoproteins, collagen synthesis, cuticle molting, etc. This extract seems to exert its beneficial effect on *C. elegans* partly by triggering the remodeling of the developmentally programmed apical extracellular matrix (aECM). Differential expression of certain important genes (*cpg-2*, *cpg-3, sqt-1, dpy-4, dpy-13,* and *col-17*) was confirmed through PCR assay too. Some of the differently expressed genes (*gfat-2, unc-68, dpy-4, dpy-13, col-109, col-169,* and *rmd-1*) in worms experiencing pro-health effect of the extract were found through co-occurrence analysis to have their homologous counterpart in humans.
Conclusions: Our results validate the suitability of *W. somnifera* extract as a nutraceutical for healthy aging.

Keywords: *Caenorhabditis elegans*, Fertility, Healthy aging, Healthspan, Longevity, Network analysis, Nutraceutical, *Withania somnifera* root, Worm transcriptome

Introduction

For centuries, humans have longed for a long and healthy life. A variety of plant extracts and polyherbal formulations have been claimed to impart the same in different systems of traditional medicine. However, the widespread application of such plant products in modern times requires scientific validation of the claimed activities. One of the most popular plants in the Indian system of *Ayurved* is *Withania somnifera* (L.) Dunal, commonly known as *Ashwagandha*. This plant belongs to the Solanaceae family and has a long history of >3000 years of being prescribed in indigenous medicine (1). In *Ayurved*, *W. somnifera* has been referred to as 'Rasayan,' which means a holistic therapy for suppressing the aging process, developing positive physical and mental health, boosting the immune system, and maintaining youth. Ancient texts mention *W. somnifera* as 'Avarada,' the meaning of which is related to longevity or regeneration. The multitude of activities (2) claimed in this plant include immunomodulatory, anti-inflammatory, neuroprotection, anticancer, anti-stress, and pro-fertility (3). Its regular consumption is believed to rejuvenate the reproductive organs and promote fertility, retard senescence, and relieve nervous exhaustion, sexual debility, muscular weakness, and geriatric problems. *W. somnifera* is expected to inhibit aging and catalyze the anabolic processes of the body (4). Among all parts of this plant, its root has received maximum attention in medicinal texts and practice. This is because its roots have the highest concentration of desired bioactive principles (5). Further, with respect to safety, only the root part of *W. somnifera* is recommended for therapeutic and internal administration (6).

Received: November 4, 2024
Accepted: March 5, 2025
Published online: April 2, 2025

This article includes supplementary materials

Corresponding author:
Vijay Kothari
email: vijay.kothari@nirmauni.ac.in

Mainstreaming the use of any herbal preparation for therapeutic as well as nutraceutical applications is dependent on the demonstration of claimed biological activities in them through appropriate scientific assays (7). Owing to concerns of ethics and feasibility, assays with higher animals and human volunteers are often challenging. Lower animals like the nematode worm *Caenorhabditis elegans* offer a useful and relatively convenient and biologically relevant platform for assessment of biological activities in natural as well as synthetic preparations at the whole organism level. In recent years, wild-type and transgenic strains of *C. elegans* have been employed widely as model organisms for assays (8) relevant to neurology, lifespan, diabetes, wound healing (9), and microbial virulence (10). Aging is a complex and multifactorial phenomenon, and it is difficult to model it, and more so, the assessment of longevity or lifespan within a shorter time frame. Though *C. elegans* has a short lifespan (a few days), the fundamental biological mechanisms and systems in this worm are similar to the mammalian system (11). The mechanisms associated with the increase in longevity identified in this worm are shown to follow a pattern similar to those in humans (12,13). Though the lifespan-enhancing effect of *W. somnifera* root extract has been reported earlier, too (14), much remains to be elucidated with respect to the underlying molecular mechanisms. This study attempted to fill the said gap by investigating the effect of the hydroalcoholic extract of *W. somnifera* root on the lifespan and overall healthspan of *C. elegans* through *in vivo* assays as well as gene expression analysis at the whole transcriptome level.

Methods

Plant extract

The hydroalcoholic extract (LongeFera™) of *Withania somnifera* root was procured from Phytoveda Pvt. Ltd., Mumbai. The roots of *W. somnifera* were collected from Madhya Pradesh, India. It was authenticated by a taxonomist at the Botanical Survey of India, Jodhpur, and the voucher specimen was deposited there with reference ID: BSI/AZRC/I.12012/Tech/19-20/PI.Id/671. The root material was washed, dried, and then pulverized. The resulting powder was then extracted with ethanol: water (8:2 v/v) at 60°C. A powdered form of this extract was then used for assay purposes. The extract was analyzed as per United States Pharmacopeia (USP) (15) for various quality control parameters. The content of withanosides and withanolides was determined using HPLC. Major phytocompounds identified in the extract are depicted in the supplementary chromatogram (Figure S1). The total withanolides content in the extract was found to be 2.69 ± 0.02%.

The extract powder was divided into two batches. One was suspended in water, and another in DMSO (Merck) for bioassay purposes. While the extract was fully soluble in DMSO, its insoluble fraction from the aqueous suspension was removed by centrifugation (7500 g at 25°C) for 10 minutes. The soluble fraction (supernatant) was filtered through a syringe filter (0.45 µm; Axiva), and the filtrate was stored in a sterile 15 mL glass vial (Borosil) under refrigeration. The solubility of the extract in water was 81.84%.

Test organism

Wild type N2 Bristol strain of *C. elegans* procured from the Caenorhabditis Genetics Center (Minneapolis, USA) was used as a model organism in this study. Lyophilized *E. coli* OP50 procured from Biovirid (Netherlands) was used as food for *C. elegans* while maintaining the worm on NGM agar plates (Nematode Growing Medium). Worm synchronization was done as described in literature (16). Prior to the *in vivo* assays, worms were kept without food for two days to make them gnotobiotic.

Lifespan assay

Synchronized (L3-L4 stage) gnotobiotic worms were incubated at 22 ± 1°C with different concentrations (5-1000 µg/mL) of the plant extract in 24-well plates (HiMedia). Each well contained 1 mL total volume (995 µL M9 buffer + 5 µL extract). Control wells contained only M9 buffer with worms but no extract. Ten worms were added in each well, and these 24-well plates were monitored over a 12-day period (till all worms died in the control wells) under a microscope (4× objective) for live-dead counting. Appropriate vehicle control containing 0.5%v/v DMSO was also included in the experiment.

Motility assay

Synchronized worms were incubated at 22±1°C with or without extract (600 ppm) in 24-well plates, wherein each well contained approximately 100 worms in 1 mL of M9 buffer. While microscopic observation qualitatively confirmed more agile movement in worm population incubated with extract, quantification of the motility in control vs. experimental wells was achieved employing an automated worm tracker machine, WMicrotracker ARENA (Phylumtech, Argentina). Worm activity counts were recorded once every day till progenies appeared in the extract-containing wells (because the presence of progenies will contribute to higher activity counts).

Metabolic activity assay

Alamar Blue® assay (17,18) was used to quantify the viability or metabolic activity of the worms. Synchronized worms were incubated at 22 ± 1°C with or without extract (600 ppm) in 24-well plates, wherein each well contained approximately 100 worms in M9 buffer. One hundred µL of Alamar Blue® (Thermofisher) was added into each well, making the total volume 1 mL, before incubation started. To quantify the amount of dye reduced, after every 24 h, content from wells was transferred into a separate plastic vial (1.5 mL), followed by centrifugation (13,600 g at 25°C) for 10 min. Then, the supernatant was read at 570 nm (Agilent Cary 60 UV-vis). A total of three wells were set for the control as well as the experimental worm population, and content from one well from the control and experimental group each was used on a particular day. Appropriate abiotic controls (containing the dye and other media components but no worms) were also included in the assay.

Whole Transcriptome Analysis

To unravel the molecular mechanisms through which *W. somnifera* conferred beneficial effects on the worms with respect to lifespan and fertility, the gene expression pattern of extract-treated worms was compared with that of the control worm population at the whole transcriptome scale. While harvesting the worms for RNA isolation on the seventh day of the experiment (when ~50% of worms in the control population were dead), progenies were separated from the experimental population by resting the tubes containing worms incubated with extract in static condition for a few minutes, allowing settling down of adult worms. Progenies were removed by collecting the upper layer of liquid. This removed liquid was microscopically observed to confirm the presence of largely progeny worms in it, and not the adult ones added at the starting day of the experiment. Following this, worms were washed thrice with sterile M9 buffer before proceeding further. The overall workflow of this whole transcriptome analysis (WTA) aimed at capturing a holistic picture regarding modes of action of the test extract is given in Figure S2, along with full methodological details.

All the raw sequence data were submitted to the Sequence Read Archive. The relevant accession number for the control and experimental worm population is SRX20790765 (https://www.ncbi.nlm.nih.gov/sra/SRX20790765) and SRX20790719 (https://www.ncbi.nlm.nih.gov/sra/SRX20790719) respectively.

Polymerase Chain Reaction (RT-PCR)

Differential expression of the potential hubs found using network analysis of DEG revealed from WTA was further confirmed using PCR. Primer designing for the shortlisted genes was carried out using Primer3 Plus. These primer sequences (Table 1; Figure S3) were checked for their binding exclusivity to the target gene sequence within the whole *C. elegans* genome. Following RNA extraction, cDNA synthesis was carried out using the synthesis kit SuperScript™ VILO™ (Invitrogen Biosciences). PCR assay employed the gene-specific primers purchased from Sigma-Aldrich. FastStart Essential DNA Green Master mix (Roche, Germany) was used as the reaction mix. The real-time PCR assay was performed on a Quant Studio 5 real-time PCR machine (Thermo Fisher Scientific, USA). The temperature profile followed is given in Table S2.

TABLE 1 – Primer sequences for RT-PCR validation of the selected genes

Gene ID/ Name	Primers	Amplicon size (bp)
WBGene 00005016 (*sqt-1*)	FP: 5′-GTTCCAGGACTTGACGGTGT -3′ RP: 5′-TCCGATCTTTCCGATTTGAC -3′	234
WBGene 00001066 (*dpy-4*)	FP: 5′-ATCACCCTCCCAATGGTGTA -3′ RP: 5′-CGCATTGCTCGTTGTAGGTA -3′	172
WBGene 00000606 (*col-17*)	FP: 5′-AACTGAGAGCCGTGAGAAGC -3′ RP: 5′-TGATCATTTGGAGCATCTGG -3′	156
WBGene 00001074 (*dpy-13*)	FP: 5′-TGCTTAGCCATGGACATTGA -3′ RP: 5′-TGCAGGTAAGGGCTTCGTTA -3′	227
WBGene 00011063 (*cpg-3*)	FP: 5′-TCGGAATCCTCTCGAACATC -3′ RP: 5′-GCTCCAATGCATTTTCCACT -3′	172
WBGene 00015102 (*cpg-2*)	FP: 5′-CCATCCAAATGGAGTTTGCT -3′ RP: 5′-AGTGCAAGCAGTGAATGACG -3′	223
WBGene 00014018 (Endogenous control)	FP: 5′-AGCGGAAAGATTTCAGACGA-3′ RP: 5′-CGATAAATGTGCTCCGGAAT-3′	187

Statistics

All values reported are derived from three or more independent experiments, wherein each experiment contained three replicates (unless specified otherwise). Statistical significance was assessed using a t-test performed in Microsoft Excel® (Version 2016), and data with $p \leq 0.05$ were considered to be significant.

Results and Discussion

Worms incubated with the root extract exhibited extended lifespans and higher fertility rates than the control population

We incubated worms with the water-soluble fraction of the root extract, or that dissolved in DMSO, and observed the worms over a period of 12 days (till almost all worms in control wells died) for live-dead count, morphology, agility, and whether any progenies were formed. While the comparison between control and experimental wells was made on a daily basis, two time points can particularly be considered important, i.e., the days on which the control population exhibited ~50% and ~100% death. With respect to these two endpoints, while the DMSO-dissolved extract could impart a longevity benefit to the worms at all tested concentrations ≥100 µg/mL, the water-soluble fraction of the extract could do so at ≥250 µg/mL. Additionally, concentrations ≥ 500 µg/mL of both DMSO-solubilized and water-solubilized extract supported worm fertility from day 4 onward, as evident from the appearance of progenies in the extract-containing wells and their absence in control wells (Videos S1–S2). Till day 12, these progenies could be differentiated from the parent worms based on size. Thereafter, almost all the parent worms in control wells were dead, and the size of the surviving parent worms and their progenies in the experimental wells became similar to the extent that they could not be differentiated. The magnitude of survival benefit (i.e., the higher number of

surviving worms in extract-containing wells than in control wells) conferred on the worms by DMSO-solubilized extract (Figure 1A) was somewhat higher than that of water-solubilized extract (Figure 1B), except at 750 µg/mL. At the latter concentration, the water-solubilized fraction of the extract performed better ($p = 0.0004$) than the DMSO-solubilized extract, as per the final-day endpoint. We decided to perform further experiments with water-solubilized fraction only, as water-solubility of any therapeutic preparation is looked at favorably with respect to bioavailability (19).

While the results described in Figure1A-1B demonstrated the beneficial effect of test extract on worm lifespan as well as fertility, to investigate its effect on worm longevity separately from fertility, we repeated this assay using FUdR (5-fluoro-20-deoxyuridine; HiMedia)- pre-treated worms, wherein eggs were allowed to hatch on FUdR-containing plates pre-seeded with *E. coli* OP50, and then resulting L3-L4 stage worms were washed with M9 buffer before being transferred to a fresh NGM agar plate for further use. FUdR can sterilize the adult nematode worms without affecting their development (20). However, FUdR-pre-treated worms could not benefit from the pro-longevity effect of the water-soluble fraction of the *W. somnifera* root extract except at 750 µg/mL on day 12 (Figure 1C), and here, too, the effect was much lesser than when FUdR was not used (Figure 1B). These results raise caution regarding the use of FUdR in lifespan assays with *C. elegans*, as this may lead to false-negative conclusions. Though the practice of using FUdR-treated worms is popular (in order to avoid the laborious separation of offspring from adults during the reproductive period) among the worm researchers studying longevity and aging, our results show that FUdR can prevent the detection of pro-longevity activity in a bioactive extract, even when the said activity is there. This corroborates with the earlier suggestion by Aitlhadj and Stürzenbaum (21) that the effect of FUdR is not neutral and owing to its mechanism of actions (inhibition of DNA and RNA synthesis, death of mitotic cells, and the inhibition of protein synthesis), its inclusion in the assays may result in misinterpretation. Hence, it can be suggested that while investigating any natural product's biological effect in the *C. elegans* model, it is more useful to do a wholistic assay assessing multiple parameters like lifespan, health, metabolic activity, fertility, etc., rather than doing an assay exclusively focusing on longevity using additional chemicals like FUdR which may prove to be a confounding factor.

W. somnifera root extract positively affects worm motility and metabolic activity

Worms incubated in the presence of the test extract exhibited more active movement (Figure 2A), which can be considered another indicator of overall good health. This observation matches well with the high fertility of extract-exposed worms described in the preceding section since the egg-laying active state and the defecation motor program are both linked to changes in forward and reverse locomotion (22,23). Automated monitoring of *C. elegans'* movement is a useful and faster healthspan-based method to study aging (24). Besides positively impacting worm lifespan, fertility, and motility, the root extract also had a stimulatory effect on worm metabolic activity (Fig. 2B). Worms incubated in the presence of the extract were found to have higher reducing potential (captured in terms of their ability to reduce the dye Alamar blue), which can be taken as an indication of better health, as healthy living cells maintain a reducing state within their cytosol (25).

Overall, the root extract imparted its beneficial effect on multiple health parameters of the worm, i.e., lifespan, fertility, motility, and metabolic activity. Although many natural products have been reported to impart pro-longevity effects on different biological model organisms based on lifespan assays, which is a conventional method to monitor aging, it should be noted that a compound or formulation that extends lifespan may not necessarily maintain health (26). Lifespan extension makes sense only if it does not cost on the healthspan front (27). Increased egg laying in extract-exposed older adults reflects an increase in the number of eggs expelled per vulval opening, as well as longer active behavior states. Since the timing of expulsive behaviors (defecation and egg laying) is regulated by sensory mechanisms that detect changes in internal pressure and/or stretch to maintain homeostasis (28), we believe that the test extract had a multifactorial impact on worm physiology at different levels. Feedback of successful egg laying in the presence of the extract might have signaled the germ line to continue the production of oocytes for fertilization. A potential trade-off between reproductive capacity and somatic maintenance in *C. elegans* has already been mentioned in earlier published literature. Higher levels of progeny production are a biomarker for studying aging and correlate positively with a longer lifespan (29,30). Prolonged reproduction can have a beneficial impact on lifespan.

Since the most promising effect of the root extract on the worm's overall health (i.e., lifespan and fertility) was observed while using a water-soluble fraction of the extract, and the maximum beneficial effect was observed at 600-750 µg/mL, we decided to investigate the gene expression pattern of worms exposed to the test extract at 600 µg/mL at the whole transcriptome level. Since the biological effect of both these concentrations (600 and 750 µg/mL) was statistically similar ($p>0.05$), we went ahead with 600 µg/mL. While all experiments presented in Figure 1-2 were performed with gnotobiotic worms facing starvation, we also compared the effect of this root extract on worms fed with their regular lab food, *E. coli* OP50. Since the worm's response to the *W. somnifera* extract was not affected (data not shown) owing to the presence of the bacterial food, we performed the transcriptome study with gnotobiotic worms only to avoid any possible confounding role of bacteria.

W. somnifera root extract exerts its beneficial effect on the nematode worm by triggering differential expression of multiple genes

A whole transcriptome level comparison of the gene expression profile of the extract-treated worms with their extract-non-exposed counterparts revealed all the DEG in the experimental worm population. Keeping the criteria of

log FC ≥1.5 and FDR (false discovery rate) ≤0.05, the differentially expressed gene (DEG) count was 85. However, to have higher confidence in our data interpretation, we set more stringent dual criteria of log FC ≥ 2 and FDR ≤ 0.01 to shortlist the genes for further analysis. A total of 16 upregulated and 29 downregulated DEGs passing the said dual criteria are listed in Table 2. These 45 DEG comprise 0.83% of the total *C. elegans* genome (~5423 genes). Function-wise categorization of these DEG is presented in Figure 3, and the corresponding heat map (Fig. S4) and volcano plot (Fig. S5) are provided in the supplementary file. A detailed discussion on important up/down-regulated genes and how their differential expression would have contributed to the observed results is provided in the supplementary file "Appendix A."

Since the transcriptome data has identified multiple genes associated with worm exoskeleton components and muscle structure as differently expressed in extract-fed worms, it is clear that the root extract used in the present study has caused restructuring of the exoskeleton in such a way that age-associated development of stiffness in worm skeleton is delayed, and the worm can age in a healthier fashion. We had conducted transcriptome profiling from the worms after seven days of extract exposure, but the classic signs of old age and fertility loss usually observed in worms at this stage of the life cycle did not yet arise in the presence of the extract. Hence, *W. somnifera* root extract can be concluded to be capable of delaying aging and senescence. Under routine conditions, at day seven of adulthood, sarcopenia is apparent in histologically examined worms, which leads to behavioral change in terms of reduced motor activity. Reduced motility stems from stiffening and thickening of the cuticle, which itself results from unregulated collagen biosynthesis (31), and the root extract used in this study seems to have affected collagen synthesis in such a way that stiffening/ thickening of the cuticle was delayed in the extract-fed worms, and thereby maintaining them in an active motility state for a longer period.

Identifying the most important DEG through network analysis

To identify the proteins with high network centrality, i.e., hub proteins from among the DEG, we generated a protein-protein interaction (PPI) network of upregulated (Fig. 4A) and downregulated (Fig. 5A) genes separately. We arranged members of the PPI network of upregulated genes in decreasing order of node degree (Table S3), and those with a score of ≥5 were subjected to ranking by different cytoHubba methods. Then, we looked for genes that appeared among the top 5 ranked candidates by ≥6 cytoHubba methods, and five such shortlisted genes (Table 3) were further checked for interactions among themselves, followed by cluster analysis (Fig. 4B). The PPI network generated through STRING showed these five important genes to be distributed among three different local network clusters. Since *cpg-3* appeared to be part of two different clusters, and both the *cpg* genes had multiple edges connecting them together (node degree score was 3 for both of them), we selected these two genes (*cpg-2* and *cpg-3*) for further RT-PCR validation. PCR assay did confirm the upregulation of these two proteins in extract-exposed worms (Fig. 6A).

We arranged members of the PPI network for the downregulated genes (Fig. 5A) in decreasing order of node degree (Table S4), and those with a score of ≥5 were subjected to ranking by different cytoHubba methods. Then, we looked for genes that appeared among the top-6 ranked candidates by ≥6 cytoHubba methods, and six such shortlisted genes (Tabl 4) were further checked for interactions among themselves, followed by cluster analysis (Fig. 5B). Four (*sqt-1, dpy-4, dpy-13,* and *col-17*) of these six genes belonged to a single cluster (each with a node degree score of 4) and were chosen for further RT-PCR validation. PCR assay did confirm the downregulation of these proteins in extract-exposed worms (Fig. 6B).

Identifying the most important DEG based on their homology with the human genome

To have an empirical idea about the relevance of the results of this study performed in *C. elegans*, with respect to *W. somnifera's* possible beneficial effect in humans, we conducted a co-occurrence analysis between all the 45 DEG in extract-treated *C. elegans* and the human genome. This analysis resulted in the identification of 16 genes whose counterparts are present in humans (Fig. 7). The presence of multiple genes in the human genome with homology to those expressed differently in extract-exposed worms indicates a good probability of similar effect on humans as observed in *C. elegans* in this study. Among the DEG, *gfat-2* seemed to have the highest similarity with its homolog in humans. The *C. elegans gfat-2* (glutamine-fructose 6-phosphate aminotransferase-2) is 88.3% similar to *gfat-1* (glutamine-fructose 6-phosphate aminotransferase-1) in amino acid sequence, and the latter is considered as a longevity gene (32). gfat-1 is the key enzyme of the hexosamine pathway and has been mentioned as a regulator of protein quality control and longevity. Increased functionality of *gfat-1* induces endoplasmic reticulum-associated protein degradation and autophagy and correlatively extends lifespan and ameliorates a wide spectrum of proteinopathies. It can be said that *W. somnifera* root extract promotes health and extends the lifespan of *C. elegans* through endogenous modulation of protein quality control. The upregulation of *gfat-1* in our long-lived worms corroborates with the previously published observation that hexosamine pathway metabolites enhance protein quality control and extend life (33). In mammals, too, *gfat* is the rate-limiting enzyme of the hexosamine pathway. Discussion on important genes listed in Figure-7 other than *gfat-2* has been done in preceding sections.

Conclusion

The present study has demonstrated the efficacy of *W. somnifera* root extract in extending the lifespan of the model worm *C. elegans* while simultaneously supporting healthy aging and allowing progeny formation in the absence of any bacterial food. The study found the hydroalcoholic root extract of *W. somnifera* (LongeFera™) to offer multiple beneficial health effects to the model organism. Worm lifespan and healthspan (motility, metabolic activity, and fertility) were both positively influenced by the test extract. The whole transcriptome analysis of the extract-exposed worms revealed the multiple mechanisms through which the extract would have exerted its pro-health effect (Fig. 8).

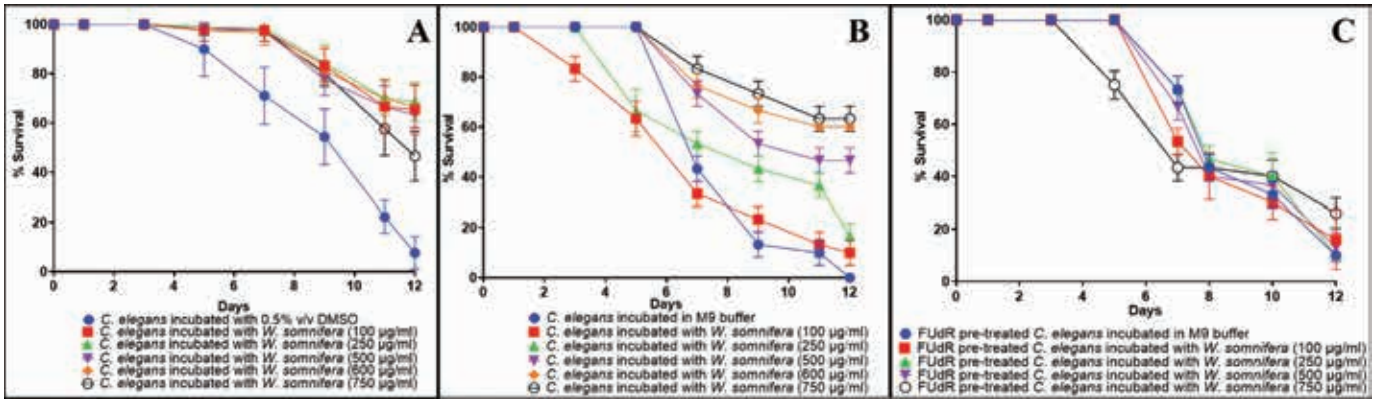

FIGURE 1 - *Withania somnifera* imparts longevity extension on *C. elegans*. All worms in control wells (i.e., worms not fed with extract) were dead by the 12th day. Concentrations ≥500 µg/mL of both DMSO-solubilized and water-solubilized extract supported worm fertility from day 4 onward. Bigger body size, higher motility, and progeny formation in the presence of the extract in experimental wells can be visualized in supplementary videos S1–S4. DMSO (0.5%v/v) or FUdR (15 mM/mL of NGM agar) did not affect worm lifespan. Only selected concentrations are displayed in this figure to avoid graph overcrowding. (A) Worms fed with DMSO-solubilized *W. somnifera* extract at 100, 250, 500, 600, 750 µg/mL scored 65.55%*** ± 10.13, 68.88%*** ± 7.81, 63.33%*** ± 5, 66.66%*** ± 8.66 and 46.66%*** ± 10 better survival on the 12th day compared to control. (B) Worms fed with water-solubilized *W. somnifera* at 100, 250, 500, 600, 750 µg/mL scored 10%*** ± 5, 16.66%*** ± 5, 46.66%*** ± 5, 60%*** ± 0 and 63.33%*** ± 5 better survival on the 12th day compared to control. (C) FUdR pre-treated worms fed with water-solubilized *W. somnifera* extract did not display any extended lifespan except at 750 µg/mL (26.66%*** ± 5.16 better survival on the 12th day compared to control. *** p ≤ 0.001

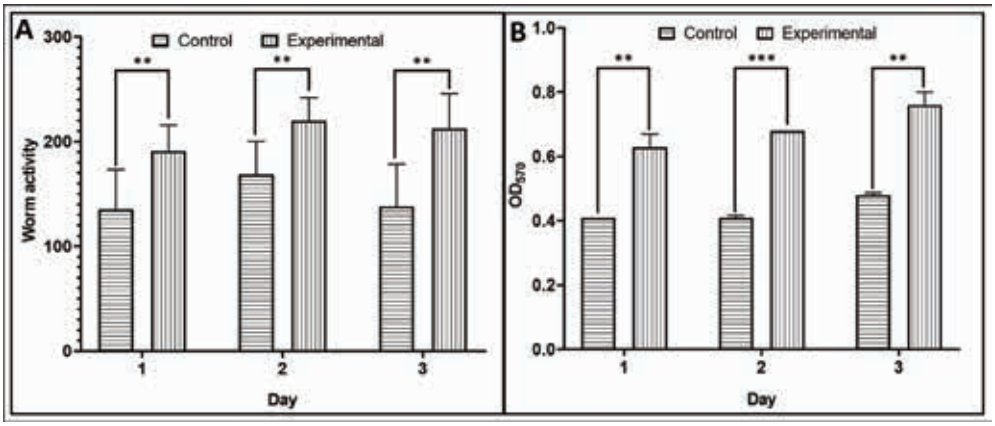

FIGURE 2 - *W. somnifera* root extract has a positive effect on worm motility (A) and metabolic activity. (B) Worm activity plotted on the y-axis in Figure (A) is the quantification of their movement as measured by an automated worm tracker. Higher motility in extract-treated worms plotted here is in line with the visual observation under the microscope. OD_{570} in Figure (B) corresponds to the amount of dye reduced by the metabolic activity of the worm population. **p ≤ 0.01, ***p ≤ 0.001; Extract concentration used was 600 µg/mL.

TABLE 2 – List of DEG satisfying the dual criteria of log fold-change ≥2 and FDR≤0.01

Sr. No	Gene ID	Gene	Product/function	Up-/Down-regulation	Log fold change
1	WBGene00006929	*vit-5*	Vitellogenin-5	↑	10.78
2	WBGene00012592	Y38E10A.14	Uncharacterized protein	↓	9.02
3	WBGene00011501	*rmd-1*	Regulator of microtubule dynamics protein 1	↑	8.06
4	WBGene00013391	Y62H9A.3	Uncharacterized protein	↑	7.92
5	WBGene00019146	H02F09.3	Uncharacterized protein	↓	7.75
6	WBGene00017501	*pud-3*	PUD domain-containing protein	↑	5.97
7	WBGene00012261	*lpr-3*	Lipocalin-Related protein	↓	5.74
8	WBGene00021005	*ule-1*	Chitin-binding type-2 domain-containing protein	↑	5.63
9	WBGene00012186	*mlt-11*	Uncharacterized protein	↓	5.52

Sr. No	Gene ID	Gene	Product/function	Up-/Down-regulation	Log fold change
10	WBGene00006926	*vit-2*	Vitellogenin-2	↑	5.36
11	WBGene00009429	*irg-5*	CUB like domain-containing protein	↓	5.35
12	WBGene00000683	*col-109*	Cuticle collagen N-terminal domain-containing protein	↓	5.04
13	WBGene00019148	H03E18.1	Uncharacterized protein	↓	5.04
14	WBGene00017498	*pud-4*	PUD domain-containing protein	↑	4.97
15	WBGene00000742	*col-169*	Cuticle collagen N-terminal domain-containing protein	↓	4.9
16	WBGene00022033	Y65B4BL.1	Uncharacterized protein	↓	4.9
17	WBGene00006930	*vit-6*	Vitellogenin-6	↑	4.49
18	WBGene00000618	*col-41*	Cuticle collagen N-terminal domain-containing protein	↓	4.43
19	WBGene00018268	F41C3.2	Uncharacterized protein	↓	4.4
20	WBGene00016636	*perm-2*	Permeable eggshell	↑	4.35
21	WBGene00001074	*dpy-13*	Cuticle collagen dpy-13	↓	4.27
22	WBGene00009035	*gfat-2*	Glutamine-fructose-6-phosphate transaminase (isomerizing)	↑	4.19
23	WBGene00017892	F28B4.3	Uncharacterized protein	↓	4.16
24	WBGene00000606	*col-17*	Collagen	↓	4.04
25	WBGene00012468	Y17G7B.17	Uncharacterized protein	↓	3.98
26	WBGene00022816	*fbn-1*	Fibrillin homolog	↓	3.81
27	WBGene00022103	*cdh-12*	Cadherin family	↓	3.81
28	WBGene00001066	*dpy-4*	Cuticle collagen N-terminal domain-containing protein	↓	3.78
29	WBGene00015102	*cpg-2*	Chondroitin proteoglycan-2	↑	3.76
30	WBGene00010790	*sodh-1*	Alcohol dehydrogenase 1	↑	3.76
31	WBGene00006787	*unc-52*	Basement membrane proteoglycan; Ig-like domain-containing protein	↓	3.7
32	WBGene00005018	*sqt-3*	Cuticle collagen 1	↓	3.58
33	WBGene00011063	*cpg-3*	Chondroitin proteoglycan 3	↑	3.54
34	WBGene00007709	*clec-87*	C-type lectin domain-containing protein 87	↑	3.52
35	WBGene00011321	*fil-1*	Fasting Induced Lipase	↑	3.48
36	WBGene00007723	C25F9.2	DNA-directed DNA polymerase	↓	3.37
37	WBGene00005016	*sqt-1*	Cuticle collagen sqt-1	↓	3.37
38	WBGene00010070	*nep-17*	Neprilysin metallopeptidase family	↓	3.28
39	WBGene00006436	*ttn-1*	Titin homolog	↓	3.09
40	WBGene00006801	*unc-68*	Uncharacterized protein	↓	3.08
41	WBGene00002915	*let-805*	Uncharacterized protein	↓	3.07
42	WBGene00004130	*ketn-1*	Uncharacterized protein	↓	3.05
43	WBGene00000998	*dig-1*	Mesocentin	↓	3
44	WBGene00006876	*vab-10*	GAR domain-containing protein	↓	2.89
45	WBGene00220238	ZK185.9	Uncharacterized protein	↑	2.74

Genes in this table are arranged in decreasing order of fold-change value.

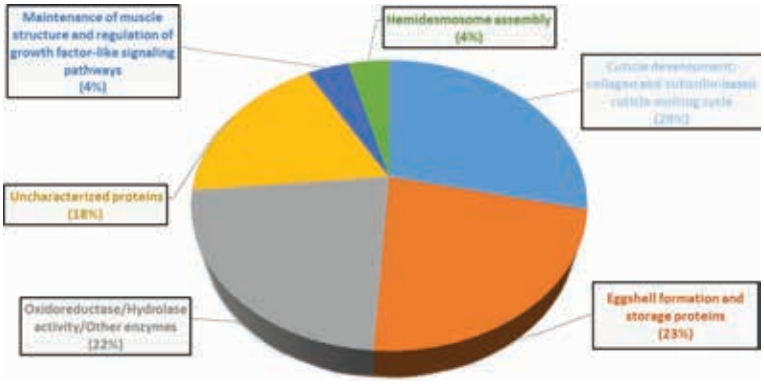

FIGURE 3 - Function-wise categorization of the differentially expressed genes in *W. somnifera*-exposed *C. elegans*. Genes contributing to more than one function are considered in any one category only. Values in parentheses are % of the total DEG.

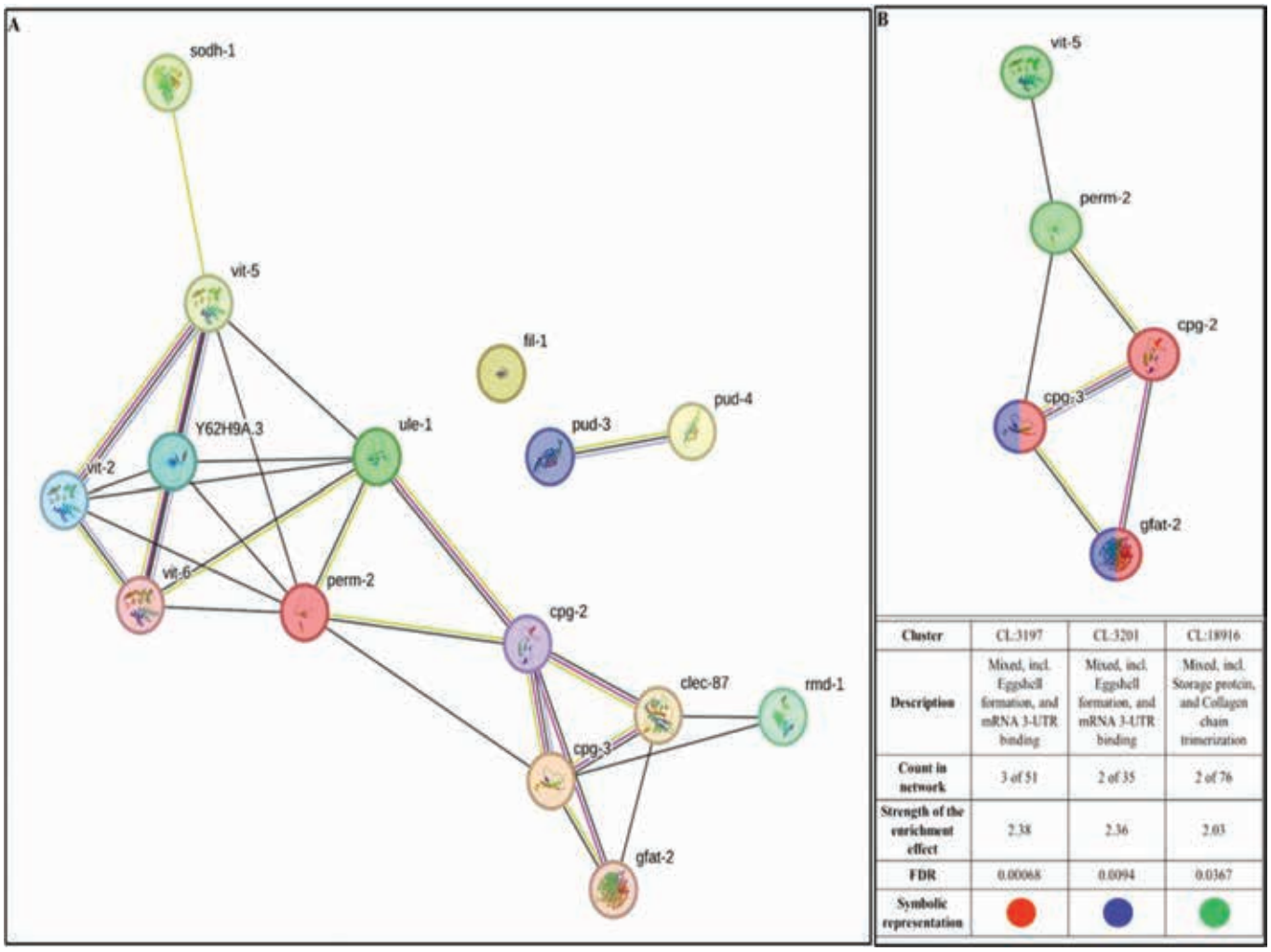

Cluster	CL:3197	CL:3201	CL:18916
Description	Mixed, incl. Eggshell formation, and mRNA 3-UTR binding	Mixed, incl. Eggshell formation, and mRNA 3-UTR binding	Mixed, incl. Storage protein, and Collagen chain trimerization
Count in network	3 of 51	2 of 35	2 of 76
Strength of the enrichment effect	2.38	2.36	2.03
FDR	0.00068	0.0094	0.0367
Symbolic representation			

FIGURE 4 - (A) Protein-Protein Interaction (PPI) network of upregulated genes following the dual criteria of fold change ≥ log 2 and FDR ≤ 0.01 in *W. somnifera*-exposed *C. elegans*. PPI enrichment p-value 1.0e-16. This network contains 15 nodes connected through 28 edges, with an average node degree of 3.73. Since the number of edges (28) in this PPI network is 28-fold higher than expected (01), this network can be believed to possess significantly more interactions among the member proteins than what can be anticipated for a random set of proteins of the same sample size and degree distribution. (https://string-db.org/cgi/network?taskId=badc9unayQGh&sessionId=bmZFhfliKMsM). **(B)** PPI network of top-ranked genes shortlisted using cytoHubba among upregulated genes in *W. somnifera*-exposed *C. elegans*. PPI enrichment p-value 3.24e-10. With an average node degree score of 2.4, this network possesses more edges (06) than expected (0) for any similar random set of proteins. The value of node degree score for *cpg*-2, *cpg*-3, and *perm*-2 is 3, and that for *gfat*-2 and *vit*-5, 2 and 1, respectively. (https://string-db.org/cgi/network?taskId=bbPybwRHQ9La&sessionId=bmZFhfliKMsM)

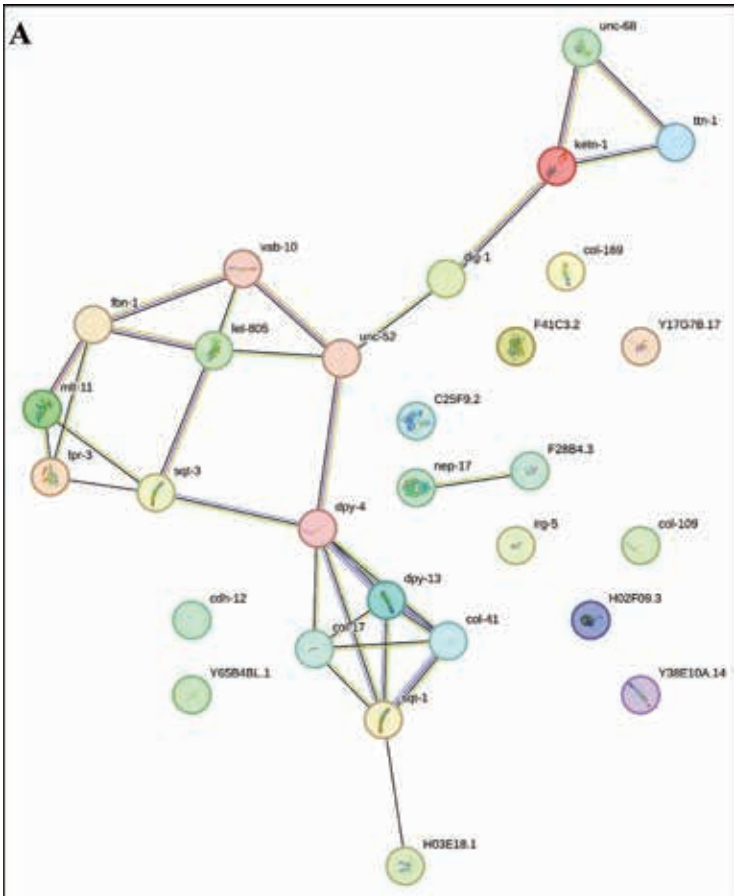

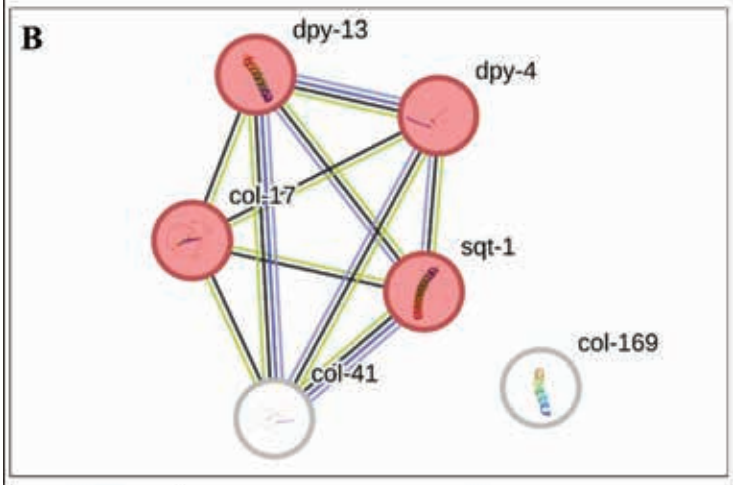

Cluster	CL:22815
Description	Cuticle development involved in collagen and cuticulin-based cuticle molting cycle, and collagen
Count in network	4 of 10
Strength of the enrichment effect	3.13
False discovery rate	8.17E-09
Symbolic representation	

FIGURE 5 - (A) Protein-Protein Interaction (PPI) network of downregulated genes following the dual criteria of fold change ≥ log 2 and FDR ≤ 0.01 in *W. somnifera*-exposed *C. elegans*. PPI enrichment p-value 1.0e-16. This network contains 29 nodes connected through 30 edges, with an average node degree of 2.07. Since the number of edges (30) in this PPI network is 30-fold higher than expected (01), this network can be believed to possess significantly more interactions among the member proteins than what can be anticipated for a random set of proteins of the same sample size and degree distribution. (https://string-db.org/cgi/network?taskId=bRhNGHhVNwKu&sessionId=bmZFhfliKMsM). **(B)** PPI network of top-ranked genes short-listed using cytoHubba among downregulated genes in *W. somnifera*-exposed *C. elegans*. PPI enrichment p-value 1.0e-16. With an average node degree score of 3.88, this network also possessed more edges (10) than expected (0) for any similar random set of proteins. The node degree score of all the genes shown in this network was 4, except *col-169* (node degree: zero) (https://string-db.org/cgi/network?taskId=bSBgDIecdxCg&sessionId=bmZFhfliKMsM).

TABLE 3 - CytoHubba ranking of the top five upregulated high node degree genes

No.	Gene ID	Gene symbol	No. of methods ranking this protein among the top five	Names of 12 ranking methods of CytoHubba and rank score provided by them											
				Degree	MNC	DMNC	MCC	Bottleneck	Eccentricity	Closeness	Radially	Betweenness	Stress	CC	E
1	WBGene00006929	*vit-5*	12	8	8	0.758	2880	1	0.5	8.5	2.222	0.571	4	0.928	3.993
2	WBGene00016636	*perm-2*	10	9	9	-	2904	2	1	9	2.333	3.401	14	–	4.101
3	WBGene00011063	*cpg-3*	9	9	9	-	2904	-	1	9	2.333	3.401	14	–	4.1
4	WBGene00015102	*cpg-2*	9	8	8	-	-	1	0.5	8.5	2.222	2.452	10	–	3.982
5	WBGene00009035	F22B3.4	8	8	8	-	-	1	0.5	8.5	2.222	2.452	10	–	–

'-' indicates that the given method did not rank that particular gene among the top five.

Table 4 – CytoHubba ranking of the top six downregulated high node degree genes

No.	Gene ID	Gene symbol	No. of methods ranking these proteins among the top six	Names of 12 ranking methods of CytoHubba and rank score provided by them											
				Degree	MNC	DMNC	MCC	Bottleneck	Eccentricity	Closeness	Radially	Betweenness	Stress	CC	E
1	WBGene 00005016	*sqt-1*	12	5	5	0.648	120	1	0.5	5	0.7	0	0	1	3.273
2	WBGen e00001066	*dpy-4*	12	5	5	0.648	120	1	0.5	5	0.7	0	0	1	3.309
3	WBGene 00000606	*col-17*	12	5	5	0.648	120	1	0.5	5	0.7	0	0	1	3.303
4	WBGene 00000742	*col-169*	9	5	5	0.648	120	-	0.5	5	0.7	-	-	1	3.243
5	WBGene 00001074	*dpy-13*	8	5	5	0.648	120	-	0.5	5	0.7	-	-	-	3.251
6	WBGene 00000618	*col-41*	8	5	5	0.648	120	-	0.5	5	0.7	-	-	-	3.285

'-' indicates that the given method did not rank that particular gene among the top six.

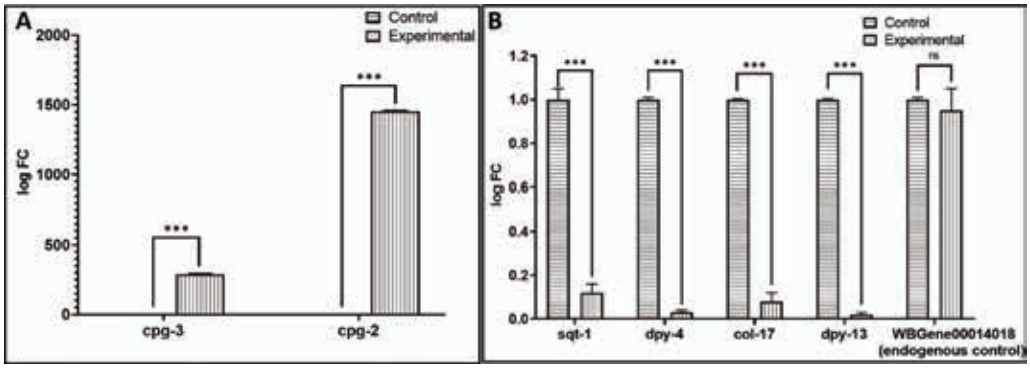

FIGURE 6 - Confirmation of differential expression of selected **(A)** upregulated and **(B)** downregulated genes in *W. somnifera*-exposed *C. elegans* through RT-PCR.
*** $p \leq 0.001$, ns: not significant; The gene employed as endogenous control codes for an RNA-binding protein

Organism	Potential hubs up/down regulated in *W. somnifera* -exposed *C. elegans*															
	gfat-2	Unc-68	dpy-4	col-169	col-109	rmd-1	sqt-3	dpy-13	F41C3.2	Y17G7B.17	nep-17	vab-10	sodh-1	col-41	unc-52	sqt-1
Homo sapiens	■	■	■	■	■	■	■	■	■	■	■	■	■	■	■	■

FIGURE 7 - Co-occurrence analysis of differentially expressed genes in extract-treated *C. elegans* with the human genome. The darker the shade of the square, the higher the homology between the genes being compared. Genes from left to right are arranged in descending order of homology. Functions of the genes shown here in humans are listed in Table S5.

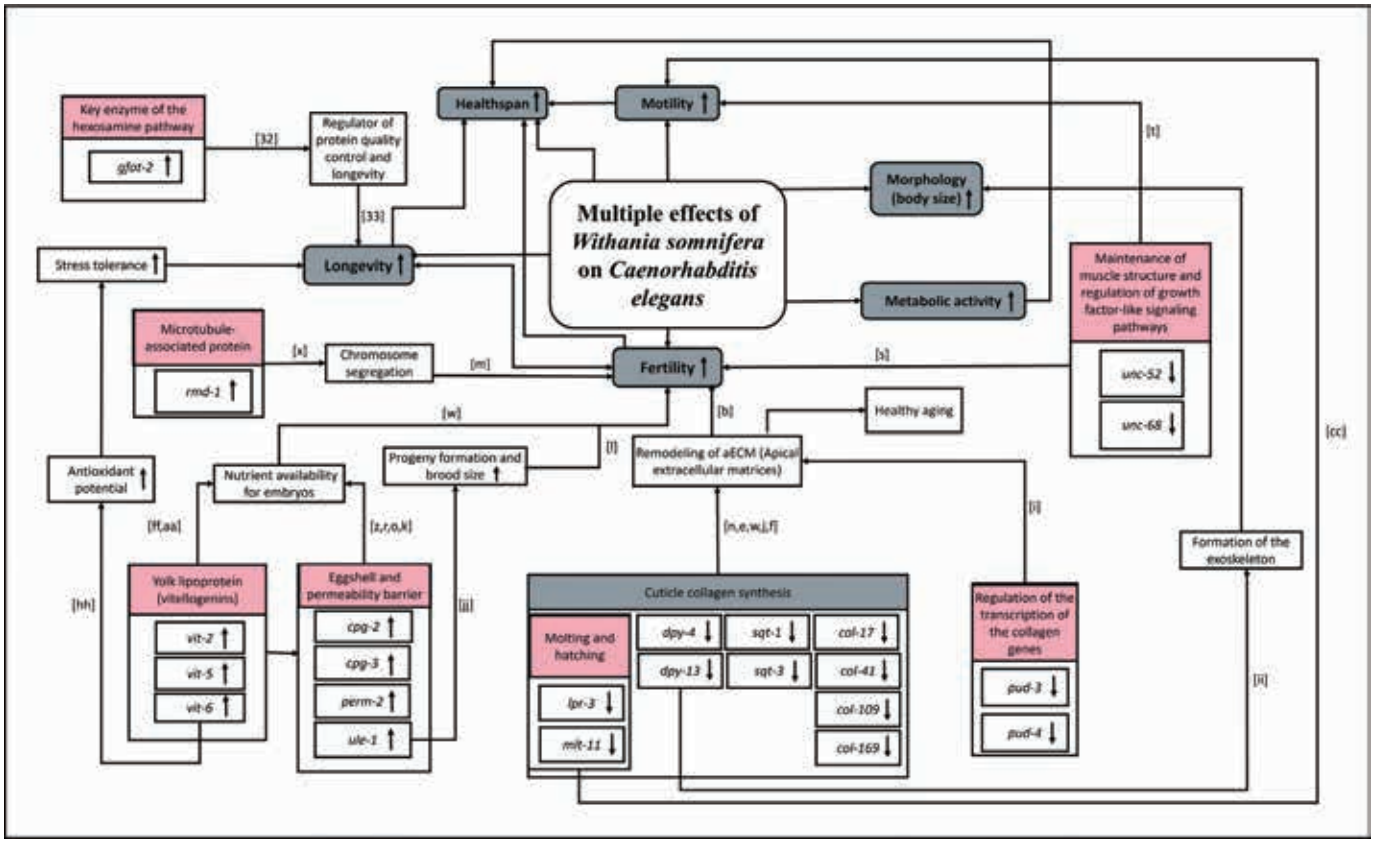

FIGURE 8 - A schematic summary of multiple effects of *W. somnifera* on *C. elegans* The small alphabet in square brackets in this figure corresponds to the references cited in the supplementary file "Appendix A."

Among the major modes of action underlying the observed biological effect of this extract was upregulation of the yolk lipoprotein vitellogenins, remodeling of the apical extracellular matrix, modulation of eggshell permeability, alteration of collagen synthesis, cuticle development, and molting cycle. Many of the differentially expressed genes in the extract-fed worms have a homologous counterpart in humans. Considering various parameters like fold-change value, network centrality, cytoHubba ranking, contribution towards more than one function, and homology with the human genome, the most important among all DEG are *gfat-2, sqt-1, dpy-13, dpy-4, cpg-3, vit-5,* and *col-169.* The results of this study validate the pro-health efficacy of *W. somnifera* claimed in traditional medicine systems like *Ayurved* and strengthen the candidature of this plant as a potential nutraceutical for healthy aging. Our results also raise caution against the use of anti-fertility agents like FUdR in worm assays, as that not only may prove a confounding factor in the interpretation of results but also precludes simultaneous assessment of lifespan, fertility, and other healthspan parameters in a single assay. To the best of our awareness, this is the first report describing molecular mechanisms associated with the beneficial effects of *W. somnifera* root extract on the model worm *C. elegans*.

Acknowledgements

We thank NERF (Nirma Education and Research Foundation), Ahmedabad, for infrastructural support. This article was initially available as a preprint on BioRxiv on August 2, 2024. CrossRef

Disclosures

Data availability statement: While all other data is provided within the manuscript or supplementary information files, the sequence data pertaining to worm transcriptome have been deposited in the NCBI-SRA database, which can be accessed at: (https://www.ncbi.nlm.nih.gov/sra/SRX20790765) and (https://www.ncbi.nlm.nih.gov/sra/SRX20790719).

Conflict of interest: DM and SN are affiliated with Phytoveda Pvt. Ltd., which markets *Withania somnifera* extract. However, this in no way has influenced the design of the study or the interpretation of results. NT receives a stipend from NERF; GG acknowledges the scholarship from the Government of Gujarat via their SHODH scheme. The rest of the authors declare no competing interests.

Financial support: This work was funded by Phytoveda Pvt. Ltd.

Author Contributions: Conceptualization: DM and VK; Methodology: GG, NT, and SN; Formal analysis, investigation, data curation: NT, GG, and VK; Resources: DM and VK; Writing—original draft preparation: NT, GG, and VK; Writing—review and editing: NT, GG, SN, DM and VK; Supervision and project administration: VK; Funding acquisition: DM and VK. All authors have read and agreed to the published version of the manuscript.

References

1. Bharti VK, Malik JK, Gupta RC. Ashwagandha: multiple health benefits. In: Nutraceuticals 2016 (pp. 717-733). Academic Press. CrossRef
2. Kumar S, Mathew SO, Aharwal RP, et al. A pleiotropic anticancer agent from the Indian medicinal plant Withania somnifera (L.) Dunal. Pharmaceuticals (Basel). 2023;16(2):160. CrossRef PubMed
3. Sengupta P, Agarwal A, Pogrebetskaya M, et al. Role of Withania somnifera (Ashwagandha) in the management of male infertility. Reprod Biomed Online. 2018;36(3):311-326. CrossRef PubMed
4. Baliga MS, Meera S, Shivashankara AR, et al. The health benefits of Indian traditional ayurvedic Rasayana (Anti-Aging) drugs: a review. Foods and Dietary Supplements in the Prevention and Treatment of Disease in Older Adults. 2015:151-61. CrossRef
5. Basudkar V, Gujrati G, Ajgaonkar S, et al. Emerging vistas for the nutraceutical withania somnifera in inflammaging. Pharmaceuticals (Basel). 2024;17(5):597. CrossRef PubMed
6. Vaidya VG, Naik NN, Ganu G, et al. Clinical pharmacokinetic evaluation of Withania somnifera (L.) Dunal root extract in healthy human volunteers: a non-randomized, single dose study utilizing UHPLC-MS/MS analysis. J Ethnopharmacol. 2024;322:117603. CrossRef PubMed
7. Verpoorte DR. New times for traditional medicine research. J Ethnopharmacol. 2017;197(197):1. CrossRef PubMed
8. Goyache I, Yavorov-Dayliev D, Milagro FI, et al. Caenorhabditis elegans as a screening model for probiotics with properties against metabolic syndrome. Int J Mol Sci. 2024;25(2):1321. CrossRef PubMed
9. Xu S, Hsiao TI, Chisholm AD. The wounded worm: using C. elegans to understand the molecular basis of skin wound healing. In: Worm 2012 (Vol. 1, No. 2, pp. 134-138). Taylor & Francis. CrossRef
10. Sifri CD, Begun J, Ausubel FM. The worm has turned – microbial virulence modeled in Caenorhabditis elegans. Trends Microbiol. 2005;13(3):119-127. CrossRef PubMed
11. Arya U, Das CK, Subramaniam JR. Caenorhabditis elegans for preclinical drug discovery. Curr Sci. 2010;1669-1680. Online
12. Kojima T, Kamei H, Aizu T, et al. Association analysis between longevity in the Japanese population and polymorphic variants of genes involved in insulin and insulin-like growth factor 1 signaling pathways. Exp Gerontol. 2004;39(11-12):1595-1598. CrossRef PubMed
13. Suh Y, Atzmon G, Cho MO, et al. Functionally significant insulin-like growth factor I receptor mutations in centenarians. Proc Natl Acad Sci USA. 2008;105(9):3438-3442. CrossRef PubMed
14. Kumar R, Gupta K, Saharia K, et al. Withania somnifera root extract extends lifespan of Caenorhabditis elegans. Ann Neurosci. 2013;20(1):13-16. CrossRef PubMed
15. United States Pharmacopeial Convention. Ashwagandha root; powdered ashwagandha root; and powdered ashwagandha root extract, U.S. Pharmacopeia, N. Formulary (Eds.), Dietary supplements compendium. Rockville, MD, 2019.
16. Corsi AK, Wightman B, Chalfie M. A transparent window into biology: a primer on Caenorhabditis elegans. Genetics. 2015;200(2):387-407. CrossRef PubMed
17. Hamid R, Rotshteyn Y, Rabadi L, et al. Comparison of alamar blue and MTT assays for high through-put screening. Toxicol In Vitro. 2004;18(5):703-710. CrossRef PubMed
18. Tritten L, Braissant O, Keiser J. Comparison of novel and existing tools for studying drug sensitivity against the hookworm Ancylostoma ceylanicum in vitro. Parasitology. 2012;139(3):348-357. CrossRef PubMed
19. Bhalani DV, Nutan B, Kumar A, et al. Bioavailability enhancement techniques for poorly aqueous soluble drugs and therapeutics. Biomedicines. 2022;10(9):2055. CrossRef PubMed

20. Mitchell DH, Stiles JW, Santelli J, et al. Synchronous growth and aging of Caenorhabditis elegans in the presence of fluorodeoxyuridine. J Gerontol. 1979;34(1):28-36. CrossRef PubMed
21. Aitlhadj L, Stürzenbaum SR. The use of FUdR can cause prolonged longevity in mutant nematodes. Mech Ageing Dev. 2010;131(5):364-365. CrossRef PubMed
22. Hardaker LA, Singer E, Kerr R, et al. Serotonin modulates locomotory behavior and coordinates egg-laying and movement in Caenorhabditis elegans. J Neurobiol. 2001;49(4):303-313. CrossRef PubMed
23. Nagy S, Huang YC, Alkema MJ, et al. Caenorhabditis elegans exhibit a coupling between the defecation motor program and directed locomotion. Sci Rep. 2015;5(1):17174. CrossRef PubMed
24. Zavagno G, Raimundo A, Kirby A, et al. Rapid measurement of ageing by automated monitoring of movement of C. elegans populations. Geroscience. 2024;46(2):2281-2293. CrossRef PubMed
25. Longhin EM, El Yamani N, Rundén-Pran E, et al. The alamar blue assay in the context of safety testing of nanomaterials. Front Toxicol. 2022;4:981701. CrossRef PubMed
26. Banse SA, Lucanic M, Sedore CA, et al. Automated lifespan determination across Caenorhabditis strains and species reveals assay-specific effects of chemical interventions. Geroscience. 2019;41:945-960. CrossRef
27. Bansal A, Zhu LJ, Yen K, et al. Uncoupling lifespan and healthspan in Caenorhabditis elegans longevity mutants. Proc Natl Acad Sci USA. 2015;112(3):E277-E286. CrossRef PubMed
28. Ravi B, Garcia J, Collins K. The HSN egg-laying command neurons regulate the defecation motor program in Caenorhabditis elegans: integration. MicroPubl Biol. 2019;2019. PubMed
29. Klass MR. Aging in the nematode Caenorhabditis elegans: major biological and environmental factors influencing life span. Mech Ageing Dev. 1977;6(6):413-429. CrossRef PubMed
30. Pickett CL, Dietrich N, Chen J, et al. Mated progeny production is a biomarker of aging in Caenorhabditis elegans. G3 (Bethesda). 2013;3(12):2219-2232. CrossRef PubMed
31. Herndon LA, Schmeissner PJ, Dudaronek JM, et al. Stochastic and genetic factors influence tissue-specific decline in ageing C. elegans. Nature. 2002;419(6909):808-814. CrossRef PubMed
32. Ruegenberg S, Horn M, Pichlo C, et al. Loss of GFAT-1 feedback regulation activates the hexosamine pathway that modulates protein homeostasis. Nat Commun. 2020;11(1):687. CrossRef PubMed
33. Denzel MS, Storm NJ, Gutschmidt A, et al. Hexosamine pathway metabolites enhance protein quality control and prolong life. Cell. 2014;156(6):1167-1178. CrossRef PubMed

DTI
Drug Target Insights 2025; 19: 31-40
ISSN 1177-3928 | DOI: 10.33393/dti.2025.3304
ORIGINAL RESEARCH ARTICLE

Establishment and evaluation of a naked-eye diagnostic assay for tuberculosis utilizing reverse isothermal amplification-assisted CRISPR-Cas in resource-limited settings

Ankush Kaushik[1], **Jitendra Singh**[2], **Zeeshan Fatima**[1], **Saif Hameed**[1]

[1]Amity Institute of Biotechnology, Amity University Haryana, Gurugram (Manesar), Haryana - India
[2]Department of Translational Medicine, All India Institute of Medical Sciences, Bhopal - India

ABSTRACT

Introduction: The current scenario of tuberculosis (TB) caused by *Mycobacterium tuberculosis* (MTB) has presented an almost insurmountable challenge to hospitals with high patient numbers. Delayed diagnosis of TB is a major hurdle in preventing the employment of efficient therapeutics, leading to the development of drug resistance. Hence, an easily accessible diagnostic method, particularly for resource for resource-limited settings, is pertinent for the rapid identification of MTB-infected patients. In pursuit of developing such an assay, the present study offers a CLAP-TB (CRISPR-Cas coupled RT-LAMP Amplification Protocol for Tuberculosis) assay, which will allow us to diagnose TB rapidly and visually.

Methods and results: Herein, the visual MTB detection consists of a method utilizing 232 different samples (sputum, urine, serum) from 82 patients for reverse transcription loop-mediated isothermal amplification (RT-LAMP). Additionally, the assay also utilizes the integration of a CRISPR-Cas12-based system using different guide RNAs of *IS6110* and an internal control *POP7* (human RNase P) genes along with visual detection via lateral flow readout-based dipsticks with the unaided eye (~134 min). Overall, the limit of detection for CLAP-TB assay was up to 1 ag of RNA, while the clinical sensitivity and specificity were 98.27% and 100%, respectively, on the pilot scale.

Conclusion: Together, our CLAP-TB assay offers proof of concept for a rapid, sensitive, and specific method with the minimum technical expertise required for TB diagnosis in developing and resource-limited settings.

Keywords: CRISPR-Cas12, Lateral flow readout, *Mycobacterium tuberculosis*, RT-LAMP, Tuberculosis

Introduction

Mycobacterium tuberculosis (MTB), which is the causative agent for tuberculosis (TB), affects around one-third of the world population and continues to wreak havoc across the globe, leading to unimaginable loss of human lives (1,2). The healthcare infrastructure of several countries, particularly Asian countries, is overburdened. This evocative scenario of TB is leading to deaths because of a lack of quick diagnosis and effective treatment. Some drugs viz. Rifampicin and Isoniazid are available in the regimen, but it takes around 4-6 months for the proper treatment; thus, the emergence of drug resistance becomes another obstacle against efficient therapeutics (3,4). Although the lung is the most common site of infection, mycobacteria can infect extrapulmonary sites, leading to extrapulmonary tuberculosis (EPTB) accounting for almost one-fourth of TB cases.

Additionally, diagnosis of EPTB is more challenging as specimens of EPTB (such as cerebrospinal and pleural fluids) are not readily available by non-invasive methods used to obtain sputum and are less sensitive (5,6). Among current diagnostic assays, culture-based diagnostic methods are slow, time-consuming, and less sensitive, while PCR-based methods are relatively faster but costly (7-9). Therefore, the development of simple yet sensitive diagnostic methods is needed for the diagnosis of efficient epidemiological management of TB patients.

Loop-mediated isothermal amplification (LAMP) is a nucleic acid-based detection method that is efficiently used for human pathogens (viruses, bacteria, and malaria), including TB, but suffers the drawback of false positive and specificity issues. Additionally, LAMP-based methods fail to detect viable MTB cells even though numerous LAMP-based methods are available in clinical diagnostics labs (10). CRISPR (Clustered Regularly Interspaced Short Palindromic Repeats)/Cas system is a genome editing tool that is utilized in molecular diagnostic systems. CRISPR, with precision and

Received: September 17, 2024
Accepted: April 14, 2025
Published online: May 9, 2025

This article includes supplementary materials

Corresponding authors:
Saif Hameed; Zeeshan Fatima
email: saifhameed@yahoo.co.in; drzeeshanfatima@gmail.com

specificity at a single nucleotide level, can identify the target nucleic acid with the help of a guided nucleotide sequence (gRNA) (11,12). Cas enzyme leads to indiscriminate cleavage activity, and this property is utilized to develop nucleic acid endonuclease-targeted CRISPR trans reporter (DETECTR) system for targeting nucleic acid detection.

In the current study, we have developed a CLAP-TB (CRISPR-Cas coupled RT-LAMP Amplification Protocol for Tuberculosis) assay, which will allow rapid (~134 min) and visual diagnosis of TB. The CLAP-TB assay involves a method for the detection of MTB from various clinical samples such as sputum, urine, and serum that can visually be detected with an unaided eye. CLAP-TB is based on the integration of RT-LAMP with the CRISPR-Cas technique (to take care of false positive and specificity issues) that allows the faster detection of *Mycobacterium* cells from patient samples with high accuracy within one hundred and thirty-four minutes. Taken together, we have developed a simple, rapid, sensitive, and specific assay to visually diagnose MTB from sputum as well as other body fluids. This would facilitate the onsite usage for enhanced testing throughout the country, particularly in places with limited resources, such as those present in tier II and tier III locations. Given the challenges associated with TB detection, such as the lack of successful therapeutics and delayed diagnosis, this assay would greatly facilitate visual TB detection based on lateral flow strips and help save valuable human lives.

Materials and methods

Clinical sample collection and decontamination

The patient samples and Healthy control samples were collected at All India Institute of Medical Sciences (AIIMS), Bhopal. The samples were collected in two categories and processed accordingly. (i) Specimens like sputum and urine were collected under sterile conditions to avoid contamination. (ii) In other patient groups, blood samples were collected for serum required for the method development, evaluation, and validation. A total of 232 clinical samples were collected based on their Ziehl-Neelsen (ZN) staining, Acid-fast bacilli (AFB) culture, and GeneXpert reports, where 161 were true positive patient samples (PS), and 71 were true negatives considered as negative controls (NS), which also included 20 healthy controls (serum and urine).

The clinical specimens received from the patients were first decontaminated by the NALC-NaOH method (modified Petroff's method) (13), and the smear was prepared for the ZN staining from the direct and decontaminated specimens. In brief, about 5-6 mL contaminated specimen was mixed with an equal volume of 0.5% NALC – 4% NaOH mixture in a 50 mL Oakridge capped round bottom processing tube; the mixture was vortexed and incubated at 37°C for 10 minutes. After incubation, the mixture was neutralized with phosphate buffer (pH 6.8) up to 50 mL total volume, followed by centrifugation at 8000× g for 10 minutes. The pellet was resuspended in 2 ml phosphate buffer (pH 6.8). From the decontaminated sample, 0.2 mL of suspension was used to isolate RNA. The samples were properly labeled and placed in a cryo box and further kept in a leak-proof box containing dry ice for subsequent transfer to the Biosafety laboratory of Amity University Haryana.

RNA isolation

RNA was isolated from MTB using the RNeasy Mini Kit (Qiagen, Germany) (14) in accordance with the manufacturer's instructions and treated with DNase I. Separately, purified genomic DNA was also used as a negative control for validation of the proposed assay to ensure any non-specific amplification. The isolated RNA was visualized for size and integrity by agarose gel electrophoresis. The concentration of purified RNA was measured spectrophotometrically using NanoDrop™ (ThermoFisher) and diluted in nuclease-free water to working concentrations.

Primers, lateral flow reporters, and guide RNAs

Two different primers set for RT-LAMP were used in this study, one for the *IS6110* gene transcript and one for the *POP7* gene transcript (Table 1). The primers for all the genes were designed using the NEB primer designing tool. These regions were further modified to meet the requirements for RT-LAMP. Similarly, compatible gRNAs were designed to target the *IS6110* and *POP7* genes. The lateral flow reporter (/56-FAM/TTATTATT/3Bio/, IDT) used in this study was previously reported (14,15).

RT-LAMP Reaction

The corresponding LAMP primer group consists of the six specific primers with their stock concentrations as: an upstream outer primer F3 (2 µM), a downstream outer primer B3 (2 µM), an upstream inner primer FIP (16 µM), a downstream inner primer BIP (16 µM), an upstream ring primer LF (8 µM) and a downstream ring primer LB (8 µM). The 10× primer mix of 50 µL was prepared by using the above-mentioned primers and then used for the RT-LAMP reaction. The RT-LAMP reaction was performed by using the New England BioLabs Protocol (Online). A total volume of 12.5 µL was used to set the RT-LAMP reaction. The reaction was prepared by using 6.25 µL of 2× Warmstart Colorimetric Master mixes as per the manufacturer guidelines comprising Bst Polymerase and reverse transcriptase enzyme in it, 1.25 µL of 10X Primer mix containing RT-LAMP primers and one µl of purified RNA with 2.5 µL of NFW. Reactions were performed separately for *ISS6110* and *POP7* genes at 65°C for 40 minutes in a water bath. In the NEB Warmstart master mix, one component is phenol red dye (indicator for pH change), which changes from pink to yellow as the pH changes. During the amplification, protons (H^+) ions are released as a byproduct of dNTPs hydrolysis. This lowers the pH and causes the color to change from pink to yellow.

CRISPR-Cas12 assay

Nucleoprotein complex

The nucleoprotein complex (Cas12a-gRNA complex) is formed as Lb Cas12a, a site-specific DNA endonuclease guided by a single 41-44 nucleotide guide RNA (gRNA). This targeting requires a gRNA complementary to the target site

TABLE 1 - List of primers and guide RNA sequences used in the study

Primers/gRNAs	Sequences and modifications	Length	Genes
F3	5'-CCGCGGTCAGCACGATT-3'	17 nt	IS6110
B3	5'-CGACGCGGTCTTTAAAATCG-3'	20 nt	IS6110
FIP	5'-TTACGCACCGTCTCCGCGCTTTTAGTGGGCAGCGATCAGT-3'	40 mer	IS6110
BIP	5'-CCGGGACCACGACCGAAGATCGCAATTCGGCGTTGTC-3'	37 mer	IS6110
LF	5'-CTGAGCTGAAGCGCTTGC-3'	19 nt	IS6110
BF	5'-CTGAGCTGAAGCGCTTGC-3'	18 nt	IS6110
gRNA	5'-UAAUUUCUACUAAGUGUAGAUAGUGGGCAGCGAUCAGUGAG-3'	41 mer	IS6110
F3	5'-TTGATGAGCTGGAGCCA-3'	17 nt	RNase POP 7
B3	5'-CACCCTCAATGCAGAGTC-3'	18 nt	RNase POP 7
FIP	5'-GTGTGACCCTGAAGACTCGGTTTTAGCCACTGACTCGGATC-3'	41 mer	RNase POP 7
BIP	5'-CCTCCGTGATATGGCTCTTCGTTTTTTTCTTACATGGCTCTGGTC-3'	45 mer	RNase POP 7
LF	5'-ATGTGGATGGCTGAGTTGTT-3'	20 nt	RNase POP 7
BF	5'-CATGCTGAGTACTGGACCTC-3'	20 nt	RNase POP 7
gRNA	5'-UAAUUUCUACUAAGUGUAGAUAAUUACUUGGGUGUGACCCU-3'	41 mer	RNase POP 7

as well as a 5' TTTN or TTN protospacer adjacent motif (PAM) on the DNA strand opposite the target sequence. The cleavage by LbCas12a occurs ~18 bases 3' of the PAM and leaves 5' overhanging ends. For the formation of nucleoprotein complex, a final volume of 25 µl was prepared by using 16 µl of LbCas12a enzyme. In 1X NEB buffer 2.1, 3µl gRNA of *IS6110* and *POP7* genes, 2.5 µl of 10X NEB buffer 2.1, and 3.5 µl of nuclease-free water (NFW) kept at 37°C for 30 minutes inside an incubator. The complex was used immediately or stored at 4°C for further use.

Trans-cleavage reaction

After the formation of the nucleoprotein complex (Cas12a-gRNA complex), 100µl of reaction was set up with 10µl of 10X NEB buffer 2.1, 2 µl of RT-LAMP product, 50nM of lateral flow reporter, 18 µl of nucleoprotein complex, and 65 µl of NFW. The reaction was incubated at 37°C for 60 minutes in an incubator.

Lateral flow readout

To check the trans cleavage reaction, we use the lateral strips from Milenia Hybrid (Cat no MGHD 1), which are coated with gold nanoparticles and anti-FAM antibodies. Around 15 µL of the trans-cleavage reaction mixture was applied on the sample application area of the lateral flow strip, and the sample application area of the strip was placed into 60 µL of buffer in an upright position. The result was visualized after approximately 3 min. A single band (control band) close to the sample application area indicated a negative result, whereas a single band (test band) close to the top of the strip or the appearance of both bands indicated a positive result. Reactions were performed separately for *IS6110* and *POP7* genes.

The lateral-flow readout chemistry is based on the cleavage of a FAM-biotin reporter by Cas12a enzyme (14,16). The reporter is labeled with FAM at one end and biotin at another end. The streptavidin, which specifically binds to biotin, is present on the C-line (control), and the anti-rabbit antibody (FAM antibody) is present on the T-line (Test). When there is no collateral cleavage, the dual-labeled reporter remains intact, and the biotin is bound by the streptavidin, while the FAM label is bound by the mobile anti-FAM antibodies conjugated to the gold nanoparticles. This results in a strong C-line and the absence of a T-line. When there is collateral cleavage, the biotin-free FAM-labelled probe bound by the anti-FAM antibody moves and develops on the T-line, giving a positive test band.

Statistical analysis

The statistical analysis for the CLAP-TB assay was calculated according to the following equations: TPR (True positive rate) = True Positive/(True Positive + False Negative). TNR (true negative rate) = True Negative/(False Positive + True Negative). FNR (False negative rate = False Negative/(True Positive + False Negative). FPR (False Positive Rate = False Positive/(False Positive + True Negative). The sensitivity and specificity of the CLAP-TB assay were calculated as described elsewhere (14,17).

Results

CLAP-TB assay for IS6110 gene

First, we sought to perform the RT-LAMP of MTB RNA for the gene *IS6110*. The amplification of MTB target *IS6110* gene RNA was visible from the naked eye by a color change from pink to yellow, contrary to the negative template control (NTC), which retained a pink color (Fig. 1a). This amplification was also validated by gel electrophoresis which showed a distinct banding pattern (Fig. 1b). Further, CRISPR-Cas reaction was deployed, and results were interpreted on lateral flow

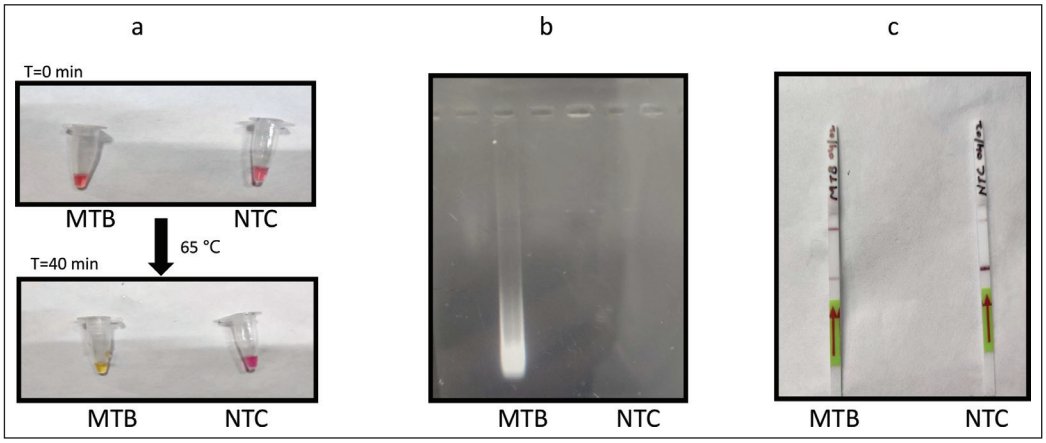

FIGURE 1 - CLAP-TB assay with MTB RNA (a) RT-LAMP reaction of *IS6110* gene for MTB RNA and NTC visualized by color change from pink to yellow after 40 min at 65°C. (b) The agarose gel image of the amplified product was obtained from the RT-LAMP reaction. (c) The lateral flow readout results of the *IS6110* gene for MTB and NTC after 3 min. NTC, non-template control.

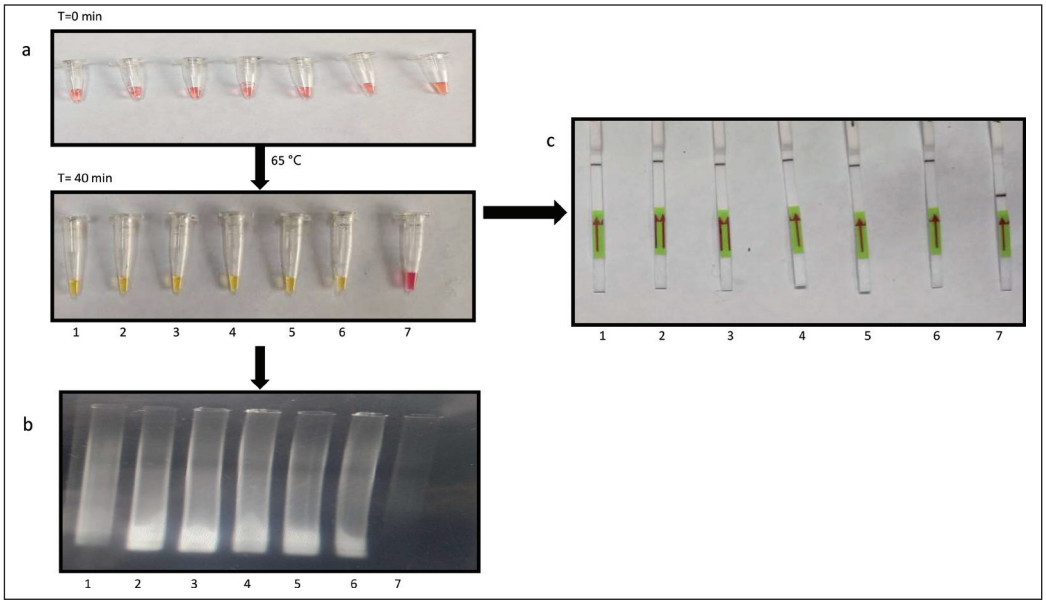

FIGURE 2 - Sensitivity of CLAP-TB assay (a) RT-LAMP reaction of *IS6110* gene for MTB RNA with various dilutions in lanes 1) 1000 fg, 2) 100 fg, 3) 10 fg, 4) 100 ag, 5) 10 ag, 6) 1 ag, and 7) NTC visualized by color change from pink to yellow after 40 min at 65°C. (b). The agarose gel image of the amplified product was obtained from the RT-LAMP reaction. (c) Lateral flow readout results for the sensitivity of CLAP-TB assay.

strips. We found that test band intensity was negligible in NTC, contrary to the MTB RNA depicting a clear test band (Fig. 1c).

Sensitivity of CLAP-TB assay

The limit of detection (LOD) for our CLAP-TB assay was determined using different dilutions of extracted RNA from pure cultures of MTB. LOD was considered the lowest dilution of RNA detected on the lateral flow strips by our CLAP-TB assay. We observed that on the lateral flow strip strips, the LOD for CLAP-TB was up to 1 ag of RNA (~1 copy) per reaction (Fig. 2). Next, we sought to compare the LOD of CLAP-TB with DNA as a template instead of RNA. We observed that LOD using DNA was only till 100 fg (Fig. 3a), contrary to 1 ag using RNA as a template (Fig. 3b).

Specificity of CLAP-TB assay

To evaluate the specificity of the CLAP-TB assay, we used four different strains viz. *Mycobacterium marinum*, *Mycobacterium smegmatis*, *Candida auris, Escherichia coli* other than MTB. The RT-LAMP reaction was performed at 65°C for 40 minutes using RNA as a template isolated from *M. marinum*, *M. smegmatis*, *C. auris,* and *E. coli.* The amplification of MTB target *IS6110* gene RNA was visible from the naked eye by a color change from pink to yellow contrary to the *M. marinum*, *M. smegmatis*, *C. auris, E. coli,* and negative template control (NTC), which retained pink color (Fig. 4a). This amplification was also validated by gel electrophoresis which showed a distinct banding pattern (Fig. 4b). Upon integration of CRISPR technology for the specific detection of MTB for the *IS6110* gene, we observed that in *M. marinum*, *M. smegmatis*, *C. auris, E. coli* and NTC, the test band intensity was negligible contrary to the MTB RNA *IS6110* gene depicting clear test band (Fig. 4c).

Validation of CLAP-TB assay with different clinical samples (Sputum, Urine, Serum)

After standardizing the CLAP-TB assay on MTB culture RNA, we sought to check the suitability of the developed assay from different clinical samples of TB patients. The collected sputum

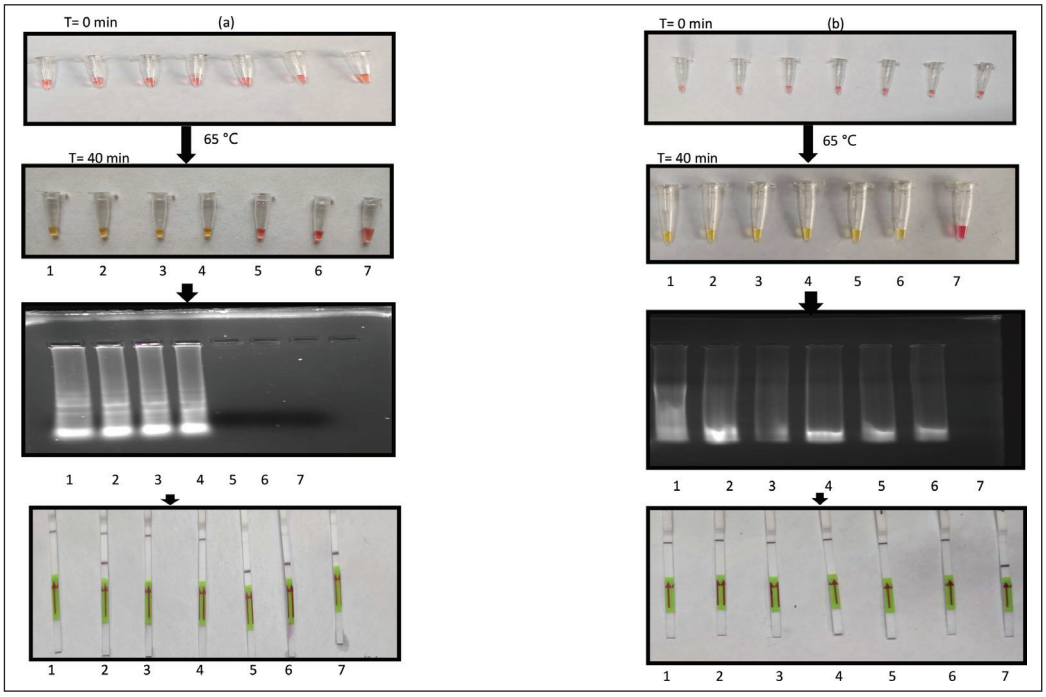

FIGURE 3 - Comparison of the sensitivity of CLAP-TB between DNA and RNA templates. LAMP and RT-LAMP reaction of *IS6110* gene for MTB with various dilutions of DNA (a) and RNA (b) in lanes 1) 1000 ng, 2) 1000 pg, 3) 1000 fg, 4) 100 fg, 5) 10 fg, 6) 1 ag, and 7) NTC visualized by color change from pink to yellow after 40 min at 65°C. The agarose gel image of the amplified product was obtained from LAMP (left panel) and RT-LAMP (right panel) reactions. Lateral flow readout results for sensitivity of CLAP-TB assay with DNA (left panel) and RNA (right panel).

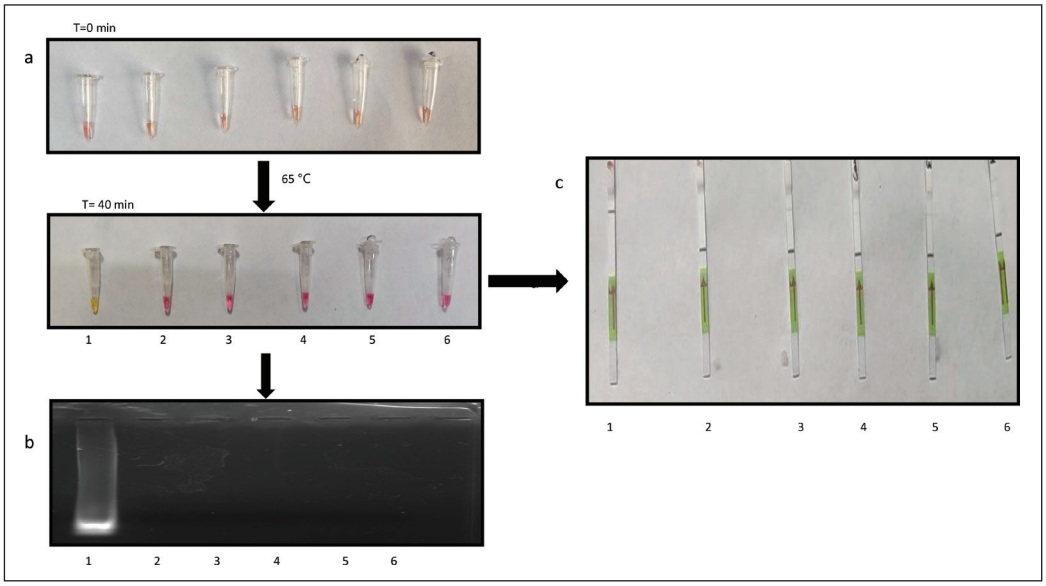

FIGURE 4 - Specificity of CLAP-TB assay (a) RT-LAMP reaction of *IS6110* gene from RNA of 1) MTB ($H_{37}R_v$), 2) *M. marinum,* 3) *M. smegmatis*, 4) *C. auris,* 5) *E. coli* and 6) NTC visualized by color change from pink to yellow after 40 min at 65°C. (b) The agarose gel image of the amplified product was obtained from the RT-LAMP reaction. (c) The lateral flow readout results of the *IS6110* gene for MTB, *M. marinum, M. smegmatis*, *C. auris, E. coli,* and NTC after 3 min.

(Fig. 5), urine (Fig. 6), and serum (Fig. 7) samples were utilized for the RT-LAMP reaction using *IS6110* gene primers. The color changes were observed in all positive clinical samples (PS), confirming positive amplification. There was no change in RNA isolated from patient samples (NS) that were negative for TB or NTC. Further, results were interpreted on lateral flow strips, and it was found that test band intensity was negligible in NTC, contrary to the MTB RNA isolated from sputum, urine, and serum samples, which depicted clear test bands.

POP7 gene (RNase P) used as an internal control for CLAP-TB assay

We utilized the *POP7* gene, which codes for RNase P and was used as an internal control for all positive and negative samples. *POP7* gene primers were used to set the RT-LAMP reaction on RNA isolated from PS, NS, and NTC. As expected, the color change was noticed for both PS and NS except the NTC, which was also confirmed by gel electrophoresis. Further, results were interpreted on lateral flow strips, and it was found that test band intensity was negligible in NTC, contrary to the MTB RNA isolated from positive and negative samples, which depicted clear test bands (Fig. 8).

Statistical validation of CLAP-TB assay

Lastly, we performed the statistical validation of the CLAP-TB assay as described in the methods. Out of the 232 different categories of clinical samples, 161 were true positive samples, and 71 were true negative samples, along with

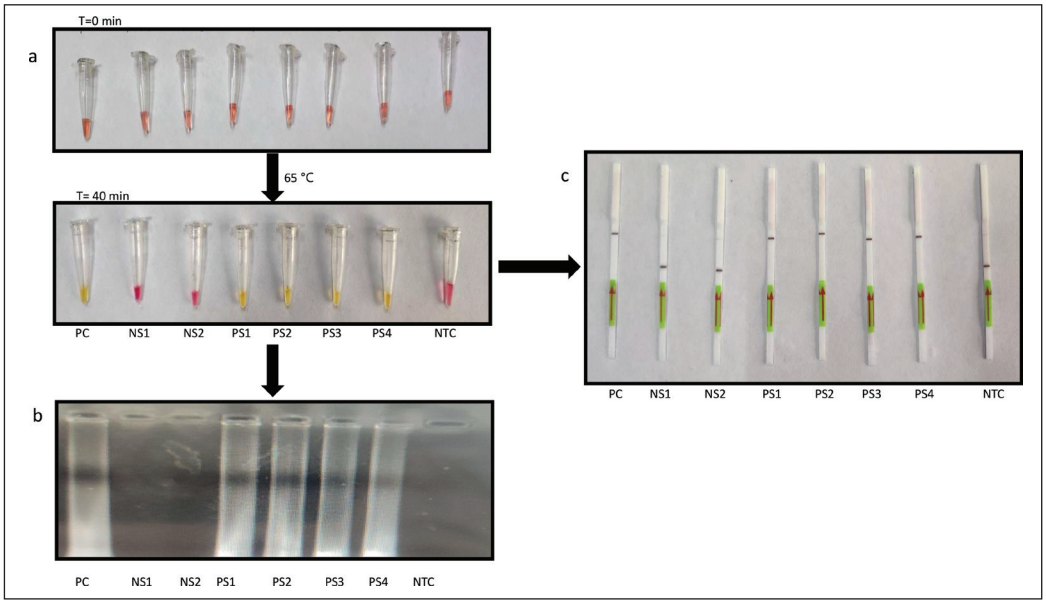

FIGURE 5 - CLAP-TB assay with clinical sputum samples (a) Representative RT-LAMP reaction of *IS6110* gene from MTB culture RNA as a positive control (PC), two negative samples (NS1 and NS2), four positive samples (PS1-4) and NTC visualized by color change from pink to yellow after 40 min at 65°C. (b) The agarose gel image of the amplified product was obtained from the RT-LAMP reaction. (c) The lateral flow readout results of the *IS6110* gene from MTB culture RNA as a positive control (PC), two negative samples (NS1 and NS2), four positive samples (PS1-4), and NTC.

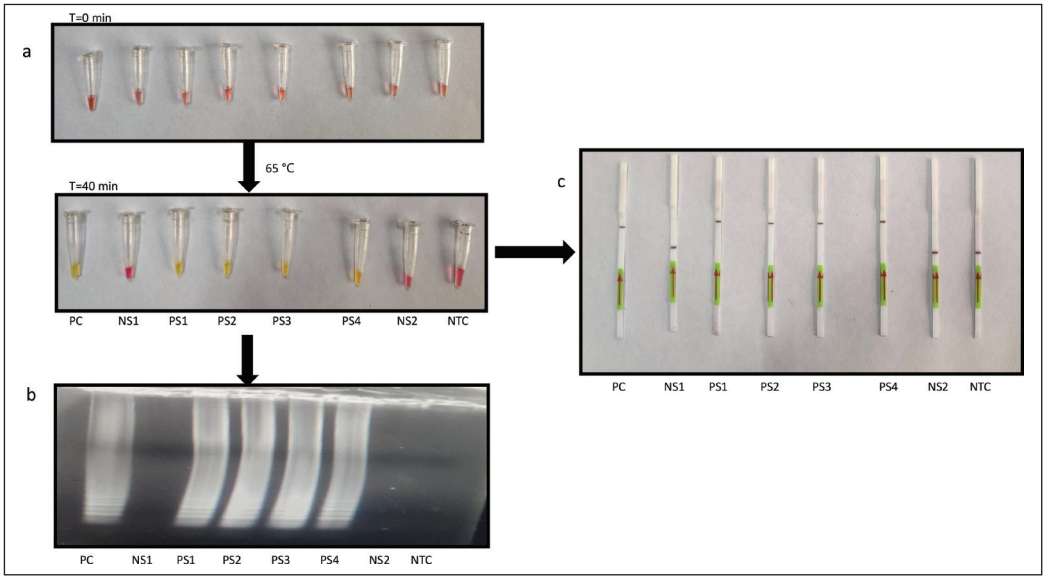

FIGURE 6 - CLAP-TB assay with clinical urine samples (a) Representative RT-LAMP reaction of *IS6110* gene from MTB culture RNA as a positive control (PC), two negative samples (NS1 and NS2), four positive samples (PS1-4) and NTC visualized by color change from pink to yellow after 40 min at 65°C. (b) The agarose gel image of the amplified product was obtained from the RT-LAMP reaction. (c) The lateral flow readout results of the *IS6110* gene from MTB culture RNA as a positive control (PC), two negative samples (NS1 and NS2), four positive samples (PS1-4), and NTC.

20 healthy control samples based on the ZN staining, AFB culture, and GeneXpert reports obtained from AIIMS, Bhopal. We confirmed that 157 PS (true positives) tested positive with our CLAP-TB assay, while four samples showed false negatives by CLAP-TB assay, and all the 71 NS (true negatives) tested negative (Fig. 9; Table S1). Further, the TPR, FPR, FNR, and TNR were calculated and found to be 97.51%, 0%, 2.49%, and 100%, respectively. Moreover, for the detection of these 232 clinical samples, the overall clinical sensitivity of the assay was 98.27%.

Discussion

Rapid and user-friendly detection methods for TB diagnosis are still a concern. The current diagnostic methods mainly involve AFB smear microscopy by ZN staining, culture-based methods, and molecular detection (18,19). ZN staining is not only less sensitive but fails to detect MTB from non-tuberculous mycobacteria (NTM). Similarly, culture methods, although they are more sensitive than ZN staining, require long incubation times (2-8 weeks) apart from being non-specific. Advancements in molecular diagnostics are impeded due to high costs and the requirement for infrastructure, which limits their use in less developed nations. Thus, to achieve the TB elimination goal, rapid, sensitive, and user-friendly diagnostics methods are urgently needed and could be deployed, particularly in resource-limiting regions.

In recent times, isothermal amplification techniques such as loop-mediated isothermal amplification (LAMP), recombinase polymerase amplification (RPA), and recombinase-aided amplification (RAA) have emerged as a better alternative to

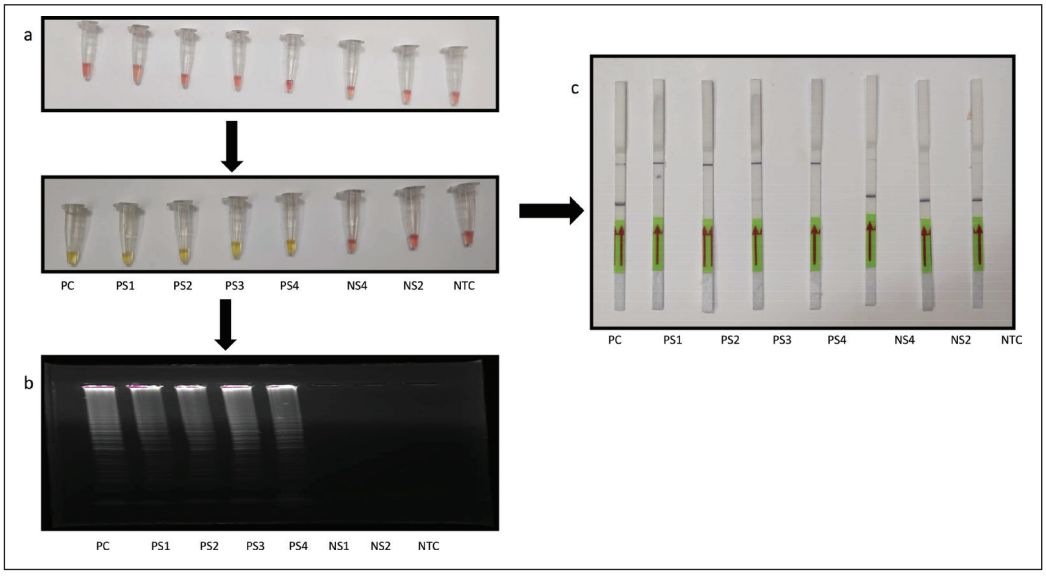

FIGURE 7 - CLAP-TB assay with clinical serum samples (a) Representative RT-LAMP reaction of *IS6110* gene from MTB culture RNA as the positive control (PC), three negative samples (NS1-3), two positive samples (PS1 and PS2) and NTC visualized by color change from pink to yellow after 40 min at 65°C. (b) The agarose gel image of the amplified product was obtained from the RT-LAMP reaction. (c) The lateral flow readout results of the *IS6110* gene from MTB culture RNA as the positive control (PC), two negative samples (NS1-3), two positive samples (PS1 and PS2), and NTC.

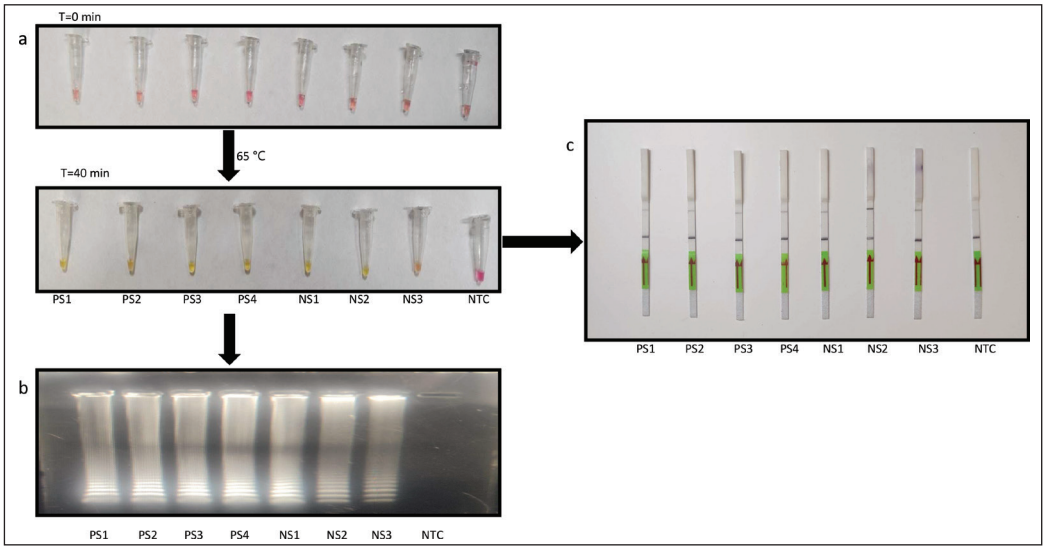

FIGURE 8 - CLAP-TB assay for internal control *POP7* gene (a) Representative RT-LAMP reaction of *IS6110* gene from four positive samples (PS1-4), three negative samples (NS1-3), and NTC visualized by color change from pink to yellow after 40 min at 65°C. (b) The agarose gel image of the amplified product was obtained from the RT-LAMP reaction. (c) The lateral flow readout results of the POP7 gene for four positive samples (PS1-4), three negative samples (NS1-3), and NTC.

Clinical samples (PS)	TPR=TP/(TP+FN)= 157/157+4=97.51%	FNR=FN/(TP+FN) = 4/157+4 =2.49%
Negative samples (NS)	FPR=FP/(FP+TN)= 0/0+71 =0%	TNR=TN/(TN+FP) = 71/71+0 = 100%

FIGURE 9 - Statistical analysis of the performance of the CLAP-TB assay. Statistical analysis of the *IS6110* gene was performed on 232 clinical samples, comprising 161 positive (PS) and 71 negative (NS) samples. True positive rate (TPR) and false negative rate (FNR) are depicted for PS in the upper box, while false positive rate (FPR) and true negative rate (TNR) are depicted for NS in the lower box.

PCR due to their simplicity and sensitivity (20,21). Likewise, recent research has demonstrated the considerable diagnostic potential of CRISPR technology in TB detection. However, in general, CRISPR-based diagnostic methods rely on two steps involving nucleic acid amplification followed by CRISPR-guided sequence detection that confers the specificity attributes (17,19,22-25). LAMP, coupled with CRISPR, has emerged as a promising tool for developing highly sensitive, specific, and user-friendly diagnostic methods (26,27). However, the drawback of the LAMP technique is that it fails to detect viable MTB cells. Hence, the present study offers to overcome this limitation of prior technology and instead developed an RT-LAMP integrated CRISPR-based method for TB diagnosis, which is not only rapid and user-friendly but sensitive and specific, allowing rapid (~134 min) visual TB diagnosis.

Around 25 copies of the *IS6110* gene are present in the MTB H37Rv genome, and due to this abundance, priorities in the detection of MTB (28). Moreover, it is reported to be absent in NTM, thus presenting a specific target (29). Therefore, we selected the *IS6110* gene segment as the target for our CRISPR-Cas coupled RT-LAMP amplification protocol for TB detection (nominated as CLAP-TB assay). Firstly, the CLAP-TB assay was standardized on MTB RNA. Visual detection by color change was confirmed from an RT-LAMP system designed to provide fast and clear visual detection of amplification based on the production of protons and subsequent drop in pH that occurs from the extensive DNA polymerase activity in an RT-LAMP reaction, producing a change in solution color from pink to yellow. The reaction was performed on RNA, followed by gel electrophoresis validation (Figs 1a and b). Then CRISPR-Cas was integrated, and positive results were interpreted by the banding pattern on the lateral flow dipsticks (Fig. 1c). In the present study, we used the Cas 12a enzyme. Additionally, there are different types of Cas9 and Cas 13 enzymes, but the Cas 9 enzyme does not have collateral cleavage activity and is mostly used in gene editing studies. On the other hand, although Cas 13 has collateral cleavage activity but against single-stranded RNA, unlike DNA, Cas 12 hence suffers from RNA stability issues. Moreover, Cas 12 is widely used in different types of bacteria and virus infection (23,30).

Next, we explored the LOD of CLAP-TB assay and found to be 1 ag of RNA per reaction, which agreed with our laterflow readout result (Fig. 2). Previous reports have shown that RT-LAMP is 10 to 100 times more sensitive than conventional PCR assays and other isothermal amplification techniques, e.g., CPA, PSR, or HAD (9). Additionally, the amplification efficiency of RT-LAMP is high with a short reaction time (40 min). A considerable number of LAMP-based studies have been reported on TB diagnosis (31). However, we also compared the sensitivity of CLAP-TB assay using DNA as a template and intriguingly found that using RNA was more sensitive than DNA (Fig. 3). Furthermore, we observed that CLAP-TB assay could also distinguish between MTB and other strains used in the study including two ZN positive bacteria, one Gram-negative bacteria and one human pathogenic fungus where we could detect specific detection of MTB RNA only as apparent from RT-LAMP amplicon color change (Fig. 4a), gel electrophoresis (Fig. 4b) and lateral flow strips band pattern (Fig. 4c).

Based on these results, further, we sought to use the clinical samples (PS/NS) to validate the CLAP-TB assay. For this, we utilized three different types of clinical samples, namely sputum, urine, and serum, where all the samples were isolated from the same patient (Figs 5-7; Table S1). The CRISPR-Cas further confirmed that the true positive clinical samples were tested positive while true negative samples were tested negative by our assay (Figs 5-7). There are reports which suggest that TB can be diagnosed with samples other than sputum, such as urine (32) and serum (33). CLAP-TB can diagnose TB from three different sample types, i.e., sputum, urine, and serum; hence, it opens new avenues for sample collection for the sake of easiness. For instance, urine collection doesn't require any invasive method. Similarly, collecting blood is much easier than sputum collection. Furthermore, CLAP-TB assay detecting MTB from urine may help in the diagnosis of EPTB, which is not easy to detect. Additionally, the isolation of RNA from serum will also aid in overcoming the decontamination step required in the case of sputum and urine.

For further confirmation, a cellular housekeeping gene (internal control) for humans, the *POP7* gene, which encodes for human ribonuclease P and is readily used to detect the presence of cellular materials in patient samples (14,15,34) was utilized. Our CLAP assay confirmed that the color change was observed in both PS and NS contrary to NTC (Figs 8a and b). Similarly, the lateral flow readouts also depicted distinguishable banding patterns as compared to NTC (Fig. 8c). Lastly, the CLAP-TB assay overall showed good correlation with the laboratory results and depicted 98.27% clinical sensitivity and specificity, respectively (Fig. 9; Table S1). The CLAP-TB assay has been worked out with a water bath in the present study; hence, this process does not require an incubator or any heavy equipment. However, to ensure the applicability for the remote areas, the assay has also been standardized in the water kettle or thermos flask (supplementary file; Fig S1 and S2).

Conclusion

Although the proposed CLAP-TB assay may suffer from the drawback of testing only a limited number of clinical samples for this study, nevertheless, the study has demonstrated considerable proof-of-concept that warrants investigation on many clinical samples. Considering the WHO guidelines, where rapid, accurate, and affordable diagnostic assays for TB that do not require sophisticated infrastructure are being investigated in the future, the CLAP-TB assay could be a promising tool serving the purpose in this direction. Moreover, the proposed assay has provided an alternative method to not only detect pulmonary TB but extrapulmonary TB, which is difficult to diagnose.

Acknowledgments

We are grateful to Sarman Singh, Mandira Varma-Basil, Pramod Mehta, and Arunaloke Chakrabarty for providing *M. smegmatis* mc^2155, MTB $H_{37}R_v$, *M. marinum,* and *C. auris* as generous gifts, respectively. We are thankful to Devashish

Rath and Mandeep Singh for their technical help in guiding RNA design. We also thank the Central Instrumentation Research Facility (CIRF), Amity University Haryana, for gel documentation experiments.

Disclosures

Conflict of Interests: The authors declare no conflict of interest

Financial support: Financial assistance to SH from the Indian Council of Medical Research (ICMR), New Delhi (5/8/5/9/ITRC/Diag/2022/ECD-1) and (EM/Dev/SG/180/3028/2023) is deeply acknowledged.

Ethics approval: The study was approved by the institutional ethical committee at Amity University Haryana (IEC-AIB/AUH/2024/01) and AIIMS, Bhopal (IHEC-LOP/2023/EL099). All patients were recruited in accordance with the study's inclusion criteria, and written consent was obtained from each patient prior to the collection of samples.

Author contributions: AK: Data curation, formal analysis, investigation, methodology, validation, visualization, roles/writing, and original draft. JS: Resources, Supervision, Validation, Writing, review and editing. ZF: Conceptualization, project administration, resources, Supervision, validation, Writing, review, and editing. SH: Conceptualization, formal analysis, investigation, methodology, project administration, resources, software, supervision, validation, visualization, roles/writing, original draft, writing, review, and editing.

References

1. World Health Organization. Global tuberculosis report 2024. Online (Accessed September 2024)
2. Thakku SG, Lirette J, Murugesan K, et al. Genome-wide tiled detection of circulating Mycobacterium tuberculosis cell-free DNA using Cas13. Nat Commun. 2023;14(1):1803. CrossRef PubMed
3. Sandhu GK. Tuberculosis: current situation, challenges and overview of its control programs in India. J Glob Infect Dis. 2011;3(2):143-150. CrossRef PubMed
4. Thakur G, Thakur S, Thakur H. Status and challenges for tuberculosis control in India – Stakeholders' perspective. Indian J Tuberc. 2021;68(3):334-339. CrossRef PubMed
5. Lee JY. Diagnosis and treatment of extrapulmonary tuberculosis. Tuberc Respir Dis (Seoul). 2015;78(2):47-55. CrossRef PubMed
6. Purohit M, Mustafa T. Laboratory Diagnosis of extra-pulmonary tuberculosis (EPTB) in resource-constrained setting: state of the art, Challenges and the Need. J Clin Diagn Res. 2015;9(4):EE01-EE06. CrossRef PubMed
7. Wang Y, Wang Y, Ma AJ, et al. Rapid and sensitive isothermal detection of nucleic-acid sequence by multiple cross displacement amplification. Sci Rep. 2015;5(1):11902. CrossRef PubMed
8. Kohli M, Schiller I, Dendukuri N, et al. Xpert® MTB/RIF assay for extrapulmonary tuberculosis and rifampicin resistance. Cochrane Database Syst Rev. 2018;27;8(8):CD012768. CrossRef
9. Obande GA, Banga Singh KK. Current and future perspectives on isothermal nucleic acid amplification technologies for diagnosing infections. Infect Drug Resist. 2020;13:455-483. CrossRef PubMed
10. Wu D, Kang J, Li B, et al. Evaluation of the RT-LAMP and LAMP methods for detection of Mycobacterium tuberculosis. J Clin Lab Anal. 2018;32(4):e22326. CrossRef PubMed
11. Koonin EV, Makarova KS, Zhang F. Diversity, classification and evolution of CRISPR-Cas systems. Curr Opin Microbiol. 2017;37:67-78. CrossRef PubMed
12. Aman R, Mahas A, Mahfouz M. Nucleic acid detection using CRISPR/Cas biosensing technologies. ACS Synth Biol. 2020;9(6):1226-1233. CrossRef PubMed
13. Sharma A, Agarwal A. Evaluation of the performance of a novel sputum processing ReaSLR methodology for culture of sputum samples in solid and liquid media in comparison with modified Petroff's method. Indian J Tuberc. 2021;68(2):255-260. CrossRef PubMed
14. Bhatt A, Fatima Z, Ruwali M, et al. CLEVER assay: a visual and rapid RNA extraction-free detection of SARS-CoV-2 based on CRISPR-Cas integrated RT-LAMP technology. J Appl Microbiol. 2022;133(2):410-421. CrossRef PubMed
15. Broughton JP, Deng X, Yu G, et al. CRISPR-Cas12-based detection of SARS-CoV-2. Nat Biotechnol. 2020;38(7):870-874. CrossRef PubMed
16. Tsou JH, Leng Q, Jiang F. A CRISPR test for detection of circulating nucleic acids. Transl Oncol. 2019;12(12):1566-1573. CrossRef PubMed
17. Ren W, Zhou Y, Li H, et al. Development and clinical evaluation of a CRISPR/Cas13a-based diagnostic test to detect Mycobacterium tuberculosis in clinical specimens. Front Microbiol. 2023;14:1117085. CrossRef PubMed
18. Cao Y, Wu J, Pang B, et al. CRISPR/Cas12a-mediated gold nanoparticle aggregation for colorimetric detection of SARS-CoV-2. Chem Commun (Camb). 2021;57(56):6871-6874. CrossRef PubMed
19. Garcia-Venzor A, Rueda-Zarazua B, Marquez-Garcia E, et al. SARS-CoV-2 direct detection without RNA isolation with loop-mediated isothermal amplification (LAMP) and CRISPR-Cas12. Front Med (Lausanne). 2021;8:627679. CrossRef PubMed
20. Ai JW, Zhou X, Xu T, et al. CRISPR-based rapid and ultra-sensitive diagnostic test for Mycobacterium tuberculosis. Emerg Microbes Infect. 2019;8(1):1361-1369. CrossRef PubMed
21. Lu R, Wu X, Wan Z, et al. Development of a novel reverse transcription loop-mediated isothermal amplification method for rapid detection of SARS-CoV-2. Virol Sin. 2020;35(3):344-347. CrossRef PubMed
22. Yan L, Zhou J, Zheng Y, et al. Isothermal amplified detection of DNA and RNA. Mol Biosyst. 2014;10(5):970-1003. CrossRef PubMed
23. Wang Y, Li J, Li S, et al. LAMP-CRISPR-Cas12-based diagnostic platform for detection of Mycobacterium tuberculosis complex using real-time fluorescence or lateral flow test. Mikrochim Acta. 2021;188(10):347. CrossRef PubMed
24. Huang T, Zhang R, Li J. CRISPR-Cas-based techniques for pathogen detection: Retrospect, recent advances, and future perspectives. J Adv Res. 2023;50:69-82. CrossRef PubMed
25. Sam IK, Chen YY, Ma J, et al. TB-QUICK: CRISPR-Cas12b-assisted rapid and sensitive detection of Mycobacterium tuberculosis. J Infect. 2021;83(1):54-60. CrossRef PubMed
26. Yang X, Huang J, Chen Y, et al. Development of CRISPR/Cas12b-based multiple cross displacement amplification technique for the detection of Mycobacterium tuberculosis complex in clinical settings. Microbiol Spectr. 2023;11(2):e0347522; Epub ahead of print. CrossRef PubMed
27. Mao X, Xu M, Luo S, et al. Advancements in the synergy of isothermal amplification and CRISPR-cas technologies for pathogen detection. Front Bioeng Biotechnol. 2023;11:1273988. CrossRef PubMed
28. Yigci D, Atçeken N, Yetisen AK, Tasoglu S. Loop-mediated isothermal amplification-integrated CRISPR methods for infectious disease diagnosis at point of care. ACS Omega. 2023;8(46):43357-43373. CrossRef PubMed

29. Khan MA, Mirza SH, Abbasi SA, et al. Peripheral blood-based polymerase chain reaction in diagnosis of pulmonary tuberculosis. J Ayub Med Coll Abbottabad. 2006;18(2):25-28. PubMed
30. Thabet S, Souissi N. Transposition mechanism, molecular characterization and evolution of IS6110, the specific evolutionary marker of Mycobacterium tuberculosis complex. Mol Biol Rep. 2017;44(1):25-34. CrossRef PubMed
31. Gao H, Shang Z, Chan SY, et al. Recent advances in the use of the CRISPR-Cas system for the detection of infectious pathogens. J Zhejiang Univ Sci B. 2022;23(11):881-898. CrossRef PubMed
32. Bumbrah GS, Jain S, Fatima Z, et al. Efficacy of LAMP assay for Mycobacterial spp. detection to prevent treatment delays and onset of drug resistance: a systematic review and meta-analysis. Drug Target Insights. 2023;17:78-89. CrossRef PubMed
33. Thakku SG, Lirette J, Murugesan K, et al. Genome-wide tiled detection of circulating Mycobacterium tuberculosis cell-free DNA using Cas13. Nat Commun. 2023;14(1):1803. CrossRef PubMed
34. Patel K, Nagel M, Wesolowski M, et al. Evaluation of a urine-based rapid molecular diagnostic test with potential to be used at point-of-care for pulmonary tuberculosis: Cape Town cohort. J Mol Diagn. 2018;20(2):215-224. CrossRef PubMed

DTI
Drug Target Insights 2025; 19: 41-48
ISSN 1177-3928 | DOI: 10.33393/dti.2025.3499
ORIGINAL RESEARCH ARTICLE

Anti-Inflammatory and Regenerative Properties of Herbal Extracts: Wound Management in Equine Models

Gustavo W. Fehrenbach[1,2], Katie Sheils[3], Mariana J. Silva[1,2], Jessica Walshe[3], Lena Madden[3], Ian Major[1,2], Niall Burke[4], Tim Yeomans[4], Emanuele Rezoagli[5,6], Emma J. Murphy[1,2]

[1]Bioengineering Organ-on-Chip Research Group, Centre for Applied Bioscience Research, Technological University of the Shannon – Midwest Campus, Limerick - Ireland
[2]PRISM Institute, Technological University of the Shannon – Midlands Campus, Westmeath - Ireland
[3]Centre for Applied Bioscience Research, Technological University of the Shannon – Midwest Campus, Limerick - Ireland
[4]Centre for Applied Bioscience Research, Munster Technological University, Kerry - Ireland.
[5]School of Medicine and Surgery, University of Milano-Bicocca, Fondazione IRCCS San Gerardo dei Tintori, Monza - Italy
[6]Department of Emergency and Intensive Care, Fondazione IRCCS San Gerardo dei Tintori, Monza - Italy

ABSTRACT

Introduction: Wound management presents significant challenges, requiring effective treatments. Herbal extracts have been traditionally used to support healing due to their anti-inflammatory, antimicrobial, and cell-regenerative properties.

Methods: This study aimed to evaluate the therapeutic efficacy of Pau D'Arco (*Tabebuia*), Yarrow (*Achillea millefolium*), Gotu Kola (*Centella asiatica*), Figwort (*Scrophularia nodosa*), and Broadleaf (*Plantago major*) extracts, both individually and combined, on wound healing *in vitro* and *in vivo* in equine models. *In vitro* tests using human macrophages and keratinocyte cell lines to assess cellular responses such as cytokine secretion and phagocytic activity under simulated inflammatory conditions. Additionally, pilot case studies on equines with open wounds provided practical insights into the extracts' healing capabilities.

Results: MTT assay was used to assess cytotoxicity. The extracts did not significantly affect the viability of HaCaT or THP-1 cells. The herbal extracts reduced IL-8 levels and increased phagocytic activity in macrophages, indicating an ability to modulate inflammatory responses. *In vivo*, the extracts were well tolerated and associated with supported healing in equines. These effects were suggested to be attributed to the synergistic actions of the herbal components.

Conclusion: These findings suggest that the herbal extracts may be useful for supporting wound healing. Their natural anti-inflammatory and healing properties could provide an additional option alongside traditional wound management approaches.

Keywords: Anti-inflammatory agents, Herbal extracts, Natural compounds, Synergistic effects, Tissue regeneration, Wound healing

Introduction

Wound healing stands as a critical challenge in both human and veterinary medicine, underscoring the pressing demand for novel agents with potent wound-healing capabilities (1). As the largest organ of the body, the skin provides a barrier against infections, minimizes water loss, and it is also among the most frequently injured organs. In response to damage, the skin undergoes repair mechanisms aimed at restoring its integrity and functions. Skin wounds are classified as acute or chronic, based on their development and outcomes (2). Chronic wounds, in particular, present substantial challenges to healthcare, contributing to patient suffering and increased mortality rates (3,4).

During wound healing, the immune system activates processes to restore tissue structure, progressing through four overlapping phases: hemostasis, inflammation, proliferation, and remodeling. Hemostasis rapidly interrupts bleeding (5), followed by an immune-driven inflammatory response where platelets start the coagulation cascade and attract neutrophils and macrophages by releasing growth factors (2,6).

Macrophages play an important role in wound healing, initially adopting a pro-inflammatory (M1) phenotype characterized by antigen presentation, phagocytosis of debris, and the secretion of cytokines and growth factors. As healing advances, they transition to an anti-inflammatory (M2) phenotype, highlighting their role in the later remodeling phase. Disruptions in macrophage function can lead to improper healing, resulting in chronic wounds or excessive scarring.

Received: February 17, 2025
Accepted: May 7, 2025
Published online: May 30, 2025

Corresponding authors:
Emma J. Murphy
email: emma.murphy@tus.ie

Understanding macrophages' precise contributions and phenotypic variations in wound repair is essential for developing targeted therapies for wound healing disorders (7).

Subsequently, in the proliferative phase, tissue is rebuilt through granulation, new blood vessel formation, and skin surface repair (3,4). Finally, in the remodeling phase, scar tissue forms and immune cells are cleared from the epidermis through apoptosis or reintegration into the dermis, completing the healing process (3,8).

Wound management in veterinary practice requires an understanding of the healing process and the range of products available to support it. The field is growing quickly, with new products often based on research from human medicine, where conditions such as pressure sores and diabetic ulcers are widely studied (9).

Historically, various botanicals have been used to support the healing process due to their anti-inflammatory, antimicrobial, and cell-regenerative properties. Notably, plants such as Pau d'Arco (*Tabebuia*), yarrow (*Achillea millefolium*), gotu kola (*Centella asiatica*), figwort (*Scrophularia nodosa*), and broadleaf (*Plantago major*) have been documented for their efficacy in traditional healing practices across different cultures. These plants contain active compounds that have been demonstrated to affect cellular activities critical to wound repair, such as inflammation modulation and new tissue formation (10-12).

Pau d'arco, also known as red lapacho or taheebo bark, is derived from the inner bark of the *Tabebuia impetiginosa* and *Tabebuia avellanedae* (TA) trees. These trees belong to the Bignoniaceae family and are native to Central and South America. The inner bark of these trees has been used for medicinal purposes for thousands of years, with indications that may pre-date the Incas. It has been known to be used against diseases like cancer, syphilis, malaria, fevers, trypanosomiasis, fungal infections, bacterial infections, and stomach disorders. Pau d'arco is highly valued for its immune-strengthening properties (11,13,14).

Achillea millefolium, commonly known as yarrow, is an herbaceous plant originally from Greece and a member of the Asteraceae family. It is one of the oldest botanicals known to be used in traditional medicine across various cultures and traditionally used to treat a range of conditions, including spasmodic gastrointestinal and hepatobiliary disorders, gynecological issues, inflammation, and wounds. Additionally, yarrow is known for its effectiveness in treating respiratory ailments such as pneumonia, the common cold, and coughs (10,15,16).

Centella asiatica, known as gotu kola, referred to as *Centella asiatica* (L.) Urb., is an herb used in traditional Chinese and Southeast Asian medicine to address various ailments. Extensive research, including animal and cellular studies, has been conducted on gotu kola and its bioactive compounds. The plant is known for containing several pentacyclic triterpenoids, such as asiaticoside, brahmoside, and madecassic acid, in addition to other components like centellose, centelloside, and madecassoside (12). The extract of *C. asiatica* and its triterpenoid components have been found to have therapeutic benefits and provide relief for conditions such as acne, baldness, vitiligo, atopic dermatitis, and wounds, promoting tissue regeneration (17–20).

Scrophularia nodosa, commonly known as figwort, is a native medicinal plant found in moist and cultivated waste areas. It contains various compounds, including saponins, cardioactive glycosides, flavonoids, resin, sugars, and organic acids. Traditionally, figwort is used for its anti-inflammatory effects and to treat skin disorders. Additionally, it possesses diuretic and cardiac stimulant properties (21).

Plantago major, a perennial herb from the Plantaginaceae family and genus Plantago, is commonly referred to as common broadleaf. It's known to be used especially in Europe, America, and Asia. In addition, Plantago major grows wildly and has been used since ancient times in most parts of Iran. This herb contains several active compounds such as flavonoids, polysaccharides, terpenoids, lipids, iridoid glycosides, and caffeic acid derivates, and is used in traditional medicine for its anti-inflammatory properties and for the treatment of ulcers, diabetes, diarrhea, inflammation, and viral infections (22,23).

For this purpose, this study aims to evaluate the therapeutic potential of extracts from these plants in promoting wound healing. The efficacy of five herbal extracts was investigated - Pau d'Arco (*Tabebuia*), yarrow (*Achillea millefolium*), gotu kola (*Centella asiatica*), figwort (*Scrophularia nodosa*), and broadleaf (*Plantago major*) - both individually and in combination, in models of wound irritation *in vitro* and their potential effects *in vivo* on wound closure on equine wound sites.

Methods

Sample sourcing and preparation

The five herb samples (0.1 g each) were mixed with 1 mL of a 60:40 acetonitrile: methanol (ACN:MeOH) solution and vortexed for 1 minute. Batch samples (0.1 g each) were mixed with 0.2 mL of the same ACN:MeOH solvent mixture and vortexed for 1 minute. Subsequently, all samples were sonicated for 10 minutes and incubated overnight at 37°C to facilitate the extraction of bioactive compounds. After incubation, the samples were dried by evaporation. Subsequently, the samples were weighed and then reconstituted in dimethyl sulfoxide (DMSO) to ensure the solubility of each compound. Since DMSO is toxic at high concentrations, it needed to be diluted 100-fold, resulting in a final concentration of 30 µg/mL on the cells from the initial 3000 µg/mL extract. The combination mixture was formulated through a patented technique that incorporates petroleum jelly, enabling the efficient release of bioactive compounds into the petroleum for *in vivo* applications.

Tissue cell conditions

HaCaT cells, a keratinocyte cell line at passage 90, and THP-1 monocyte cells at passage 14 were originally obtained from the American Type Culture Collection (ATCC). HaCaT cells were cultured in DMEM supplemented with 10% fetal calf serum, 1% penicillin G (100 U/mL), and streptomycin (100 µg/mL) solution, maintained at 37°C in a 5% CO_2 environment. THP-1 cells were cultured in RPMI, supplemented

similarly, and maintained under the same conditions. To induce differentiation into macrophages, THP-1 monocyte cells were treated with phorbol 12-myristate 13-acetate (PMA) at a concentration of 25 nM for 48 hours.

Cell irritation and treatment

Injury assays were performed using LPS at 100 ng/mL. For the injury assays, THP-1 PMA-differentiated macrophage cells were seeded at a density of 4×10^5 cells per well in 96-well plates. After 24 hours, they were subjected to LPS in RPMI supplemented with 1% penicillin/streptomycin. Similarly, HaCaT cells were seeded at a density of 4×10^5 cells per well in 96-well plates. After 24 hours, these cells were exposed to LPS (100 ng/mL) in RPMI supplemented with 1% penicillin/streptomycin. Following 3 hours of exposure, the cells were washed three times with PBS and subsequently treated with 30 µg/mL of extracts in their respective cell culture media for an additional 24 hours before analysis (24).

Cytotoxicity assessment

Cytotoxicity was assessed by MTT assay following a 24 hour treatment with various drug concentrations. The culture medium was removed, and cells were exposed to 10% MTT in RPMI for 4 hours at 37°C in a humidified incubator with 5% CO_2. After the incubation, both the MTT solution and culture medium were aspirated, and the formazan product was dissolved by adding 100 µL of DMSO per well. The dissolved product was quantitatively assessed at 540 nm. The results were expressed as percentage viability relative to the vehicle control (25).

ELISA analysis of secreted soluble mediators (IL-8 and IL-10)

A Ready-SET-Go human ELISA kit (Thermo Fisher) was used to measure the levels of interleukin-8 (IL-8) and interleukin-10 (IL-10) in the medium after injury and treatment. All ELISA assays were performed according to the manufacturer's instructions, and the results were expressed in pg/mL. Dexamethasone (30 µg/mL) (Thermo Fisher) was used as a control in the inflammation assay following LPS induction due to its well-established role as a potent anti-inflammatory agent. As a corticosteroid, it has been widely used to treat various inflammatory conditions and immune-mediated diseases. Its inclusion as a positive control allowed for a comparison of the inflammatory effects of the test compounds against a reliable standard drug (26-28).

Phagocytic assessment of THP-1 (monocytes) cells

Macrophage phagocytic activity was evaluated using the Vybrant Phagocytosis Assay Kit (Thermo Fisher) following the manufacturer's instructions. After the cells were cultured as described previously, they were exposed to LPS (100 ng/mL) for 4 hours. Subsequently, the culture medium was replaced, and the cells were treated with various batch products or herbs for 12 hours. Following this treatment, the culture medium was removed, and fluorescein-labelled Escherichia coli bioparticles were introduced. After a 120-minute incubation, the supernatant was extracted, and 100 µL of trypan blue was added to each well for 1 minute to halt extracellular fluorescence. Excess trypan blue dye was removed by aspiration, and the plate was analyzed using a microplate reader with excitation at 480 nm and emission at 520 nm. The results were expressed as the percentage of phagocytosis relative to the untreated cells.

In vivo application

Pilot studies on the treatment of equine injuries were conducted by veterinary practitioners on horses that presented to the clinic with open wounds and were adapted to each individual case as required, since the cases involved different wound severities and conditions. The case studies are described in detail in the results section. The wound healing progression was visually monitored, and photographs were taken to document the process.

Statistical analysis

Data are presented as mean ± SEM (n = 4). Statistical analysis was performed using one-way ANOVA followed by Dunnett's multiple comparisons test. Differences were considered significant at $p < 0.05$.

Results

Cytotoxicity assessment

The MTT assay was used to determine whether the extracts, either alone or in combination, influenced cell viability and subsequently affected cellular responses. Individually, the extracts had no significant impact on cell viability on either cell type as seen in Figure 1, panel A (HaCaT) and THP-1 (Fig. 1, panel B). They were tested alone and combined in petroleum, where the bars represent the mean ± standard error of the mean of the different tested compounds.

ELISA analysis of secreted soluble mediators (IL-8 and IL-10)

To evaluate the effects of the extracts on keratinocytes, HaCaT cells were treated with each extract alone and in combination, followed by quantification via ELISA of cytokine secretion quantification. Under uninjured conditions (Fig. 2, panel A), the herbal combination increased IL-8 expression compared to PBS, figwort, and broadleaf alone. Following LPS-induced injury (Fig. 2, panel B), IL-8 levels were significantly reduced, suggesting an anti-inflammatory response from both the individual and combined herbal extracts. The levels of IL-10, an anti-inflammatory mediator, were significantly higher when the cells were treated with yarrow and figwort (Fig. 2, panel C).

Similarly, to assess the impact on macrophages, THP-1 cells were treated with the extracts, and cytokine secretion levels were evaluated using ELISA. To simulate injury or inflammation like a wound environment, macrophages were stimulated with LPS. All herbs, whether used alone or combined, significantly reduced the levels of IL-8 (Fig. 2, panel D), demonstrating an anti-inflammatory response comparable to the control, dexamethasone.

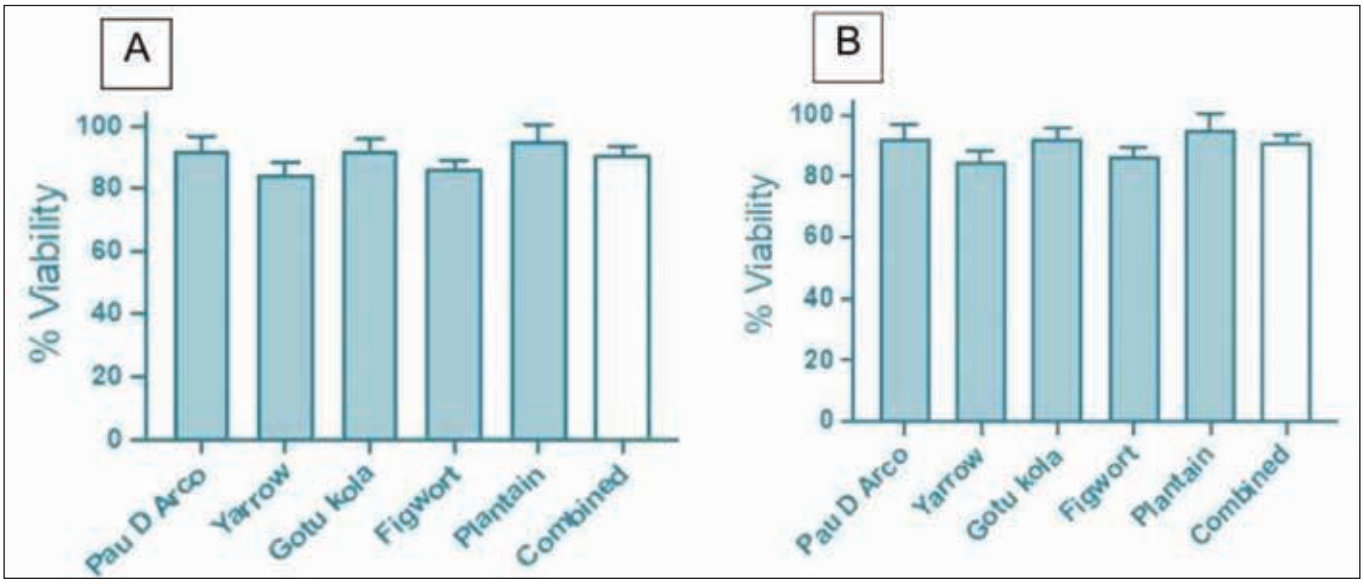

FIGURE 1 - Effect of individual and combined herbal extracts on the viability of HaCaT keratinocytes (A) and PMA-differentiated THP-1 macrophages (B) after 24 hours of treatment. THP-1 monocyte cells were differentiated using 25 nM phorbol 12-myristate 13-acetate (PMA) for 48 hours prior to treatment. No significant effect on cell viability was observed. Results are expressed as percentage viability relative to the untreated control set at 100%, shown as mean ± standard error of the mean (SEM).

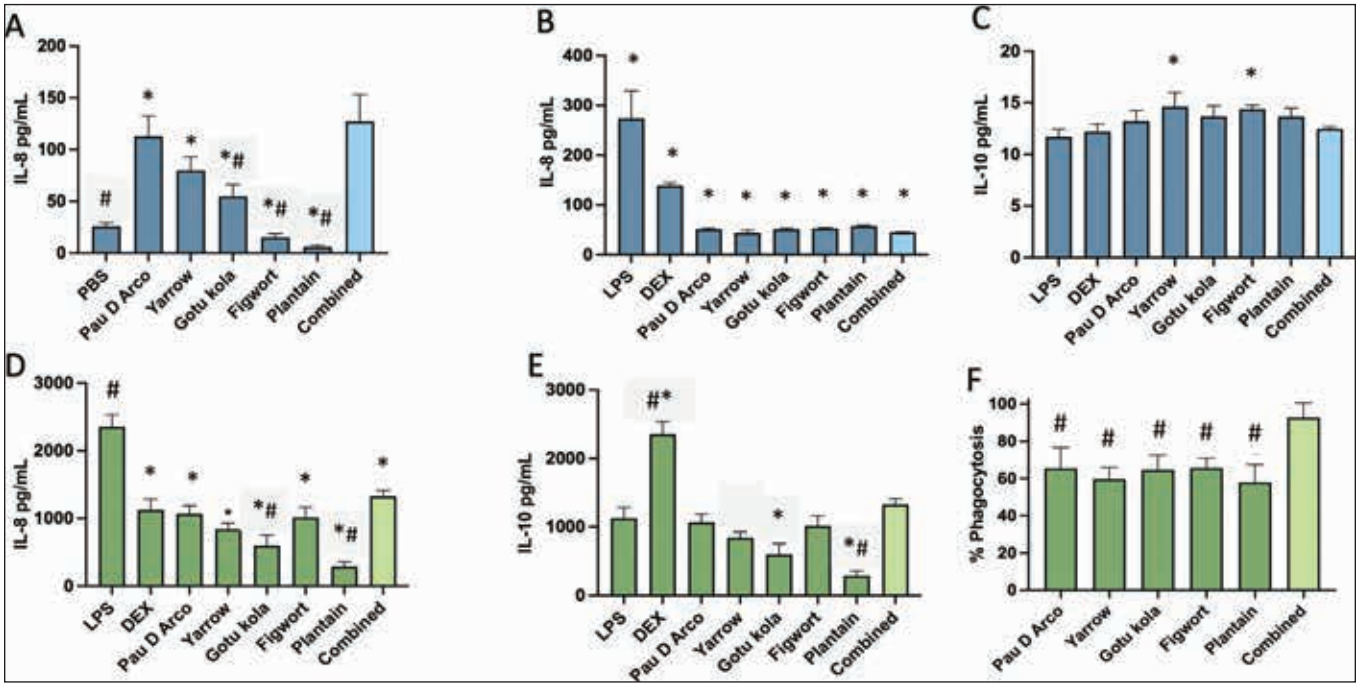

FIGURE 2 - Effect of herbal extracts alone and in combination, on cytokine secretion and phagocytic activity in HaCaT keratinocytes and PMA (25 nM, 48 h) differentiated THP-1 macrophages. (A) IL-8 levels in uninjured HaCaT cells; (B) IL-8 levels in HaCaT cells injured with 100 ng/mL LPS; (C) IL-10 levels in LPS-injured HaCaT cells; (D) IL-8 levels in THP-1 macrophages injured with 100 ng/mL LPS; (E) IL-10 levels in LPS-injured THP-1 macrophages; (F) Phagocytic activity in LPS-injured THP-1 macrophages. Phagocytic activity is expressed as a percentage relative to PBS-treated controls. Cells were treated with 30 µg/mL extracts for 24 hours. Dexamethasone (DEX, 30 µg/mL) was used as an anti-inflammatory control. Pau D'Arco, Yarrow, Gotu Kola, Figwort, and Broadleaf and their combination in petroleum were tested. Results are expressed as mean ± standard error of the mean (SEM). # = $p < 0.05$ versus Combined;* = $p < 0.05$ versus PBS/ LPS.

Phagocytic assessment of THP-1 (monocytes) cells

To explore how different extracts, both alone and in combination, affect the phagocytic activity of macrophages, THP-1 cells were treated with each extract, and their phagocytic activity was assessed using the Vybrant Phagocytosis Assay Kit (Fig. 2, panel F). To simulate injury or inflammation like that at a wound site, the macrophages were stimulated with LPS. The results showed that the combined herbal extracts significantly enhanced phagocytic activity compared to the individual extracts.

In vivo case studies

Case study 1: equine fetlock wound

A horse was presented with a deep, penetrating wound on its fetlock, the joint located between the cannon and long pastern bones, which serves as the horse's ankle. This area is important for lower limb movement and is highly sensitive. Due to its extensive motion and less vascular skin, wounds in this region can be slow to heal and often require extensive care. The treatment involved daily cleaning and application of a combination of five herbs infused in petroleum jelly for twenty days (Fig. 3).

Case study 2: equine wound in left hock

A horse presented with a large wire cut on the front of its left hock, a wound that was unsuitable for stitching due to the location and nature of the injury (Fig. 4). The hock joint, essential for the performance and mobility of horses, includes multiple small bones, such as the calcaneus, which contribute to its complex, angular structure. Due to the horse's high usage and critical role in the horse's hind legs, healing this area presents unique challenges. These include the joint's high mobility, limited available skin for repair, and poor blood supply, which complicate suture retention and overall wound closure. Over a five-month period, the horse underwent treatment that included bandaging, sequential surgical debridement, various topical applications, and several laser therapy sessions. Although the wound initially healed well, it developed a persistent granulomatous area that did

FIGURE 3 - Visual progression of the equine fetlock wound treatment using the combination of the five herbs in petroleum applied topically for 20 days. Panel A: Initial presentation of the wound on day 1. Panel B: Condition of the wound on day 4. Panel C: By day 9, the wound exhibited significant granulation. Panel D: On day 20, the wound showed good healing, with almost complete restoration of skin integrity.

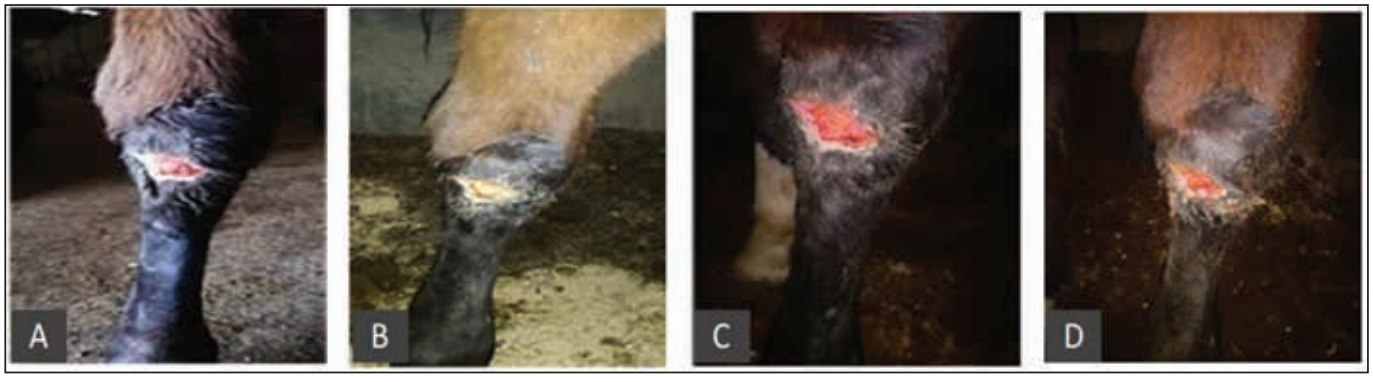

FIGURE 4 - Visual progression of the treatment of equine left hock wound using the combination of the five herbs in petroleum applied topically for 40 days. Panel A: Initial presentation of the wound on day 1 of topical application. Panel B: Condition of the wound on day 6. Panel C: By day 20. Panel D: On day 40, the wound significantly decreased in size.

not resolve. Consequently, the blend of five herbs infused in petroleum jelly was topically applied. Prior to application, the area around the wound was clipped, cleaned, and moistened with gauze for 40 days.

Case study 3: equine wire lesion

A horse presented with a cut on the front of the hock on its hind leg, caused by wire (Fig. 5). The treatment involved liberally applying ointment (5 herbs in jelly) twice daily—once in the morning and again in the evening after cleaning and drying the wound with clean gauze. This regimen was followed for 18 days.

Case study 4: equine forearm cut

A horse presented with a two-week-old cut Figure. 6 on the forearm (front leg, above the knee). The wound was purulent and appeared infected, and the surrounding leg was notably swollen. A treatment regimen was initiated using a blend of five herbs infused in petroleum jelly. The treatment protocol included preparing the wound area twice daily: the surrounding fur was clipped, the wound was cleaned, and the skin was moistened with gauze. Following preparation, the herbal ointment was applied liberally each morning and evening for 22 days. The herbal treatment produced a positive outcome. The wound's size reduced significantly, the tissue healed properly, and the infection was resolved, demonstrating the efficacy of the herbal infusion in treating complex equine wounds.

Discussion

Severe tissue damage and wound infection are major contributors to delayed healing and poor wound closure. This study evaluated the therapeutic potential of Pau d'Arco, yarrow, gotu kola, figwort, and broadleaf in wound healing, using both *in vitro* and *in vivo* equine models. The results demonstrated that these herbal extracts modulate inflammatory responses, enhance macrophage activity, and accelerate tissue repair, supporting their potential as complementary treatments for wound management.

In vitro, macrophage and keratinocyte assays confirmed that the herbal extracts were non-cytotoxic while significantly influencing cytokine production. IL-8 levels decreased following LPS-induced inflammation in both cell models, indicating anti-inflammatory effects, while yarrow and figwort increased IL-10 expression, further supporting their immunomodulatory role. Phagocytic activity assays revealed enhanced macrophage function, particularly when extracts were combined, suggesting a synergistic effect in immune modulation.

In vivo, equine wound models exhibited positive healing outcomes, including reduced infection rates, accelerated granulation, and enhanced tissue regeneration. However, these findings should be interpreted with caution, as there

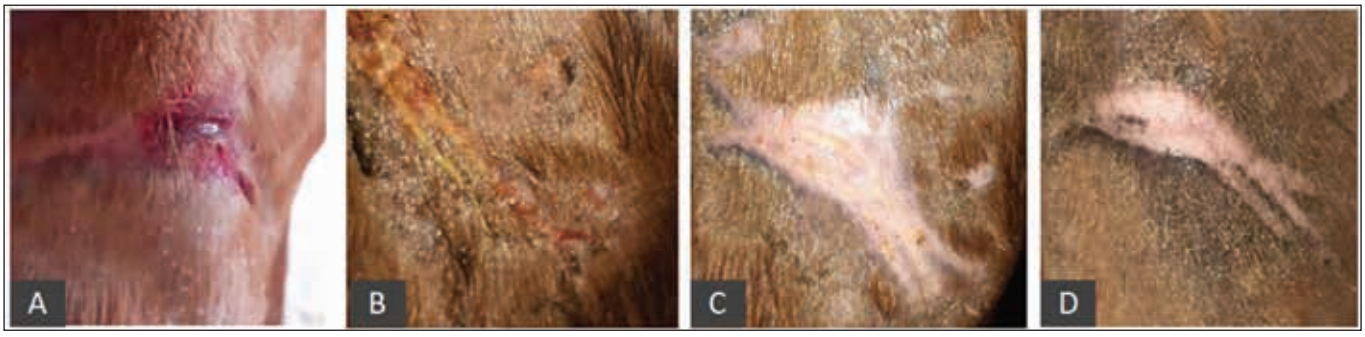

FIGURE 5 - Visual progression of the treatment of a wound caused by a wire using the combination of the five herbs in petroleum applied topically for 18 days. Panel A: Initial presentation of the wound on day 1 of topical application. Panel B: Condition of the wound on day 3. Panel C: By day 6. Panel D: On day 18, demonstrating the healed wound.

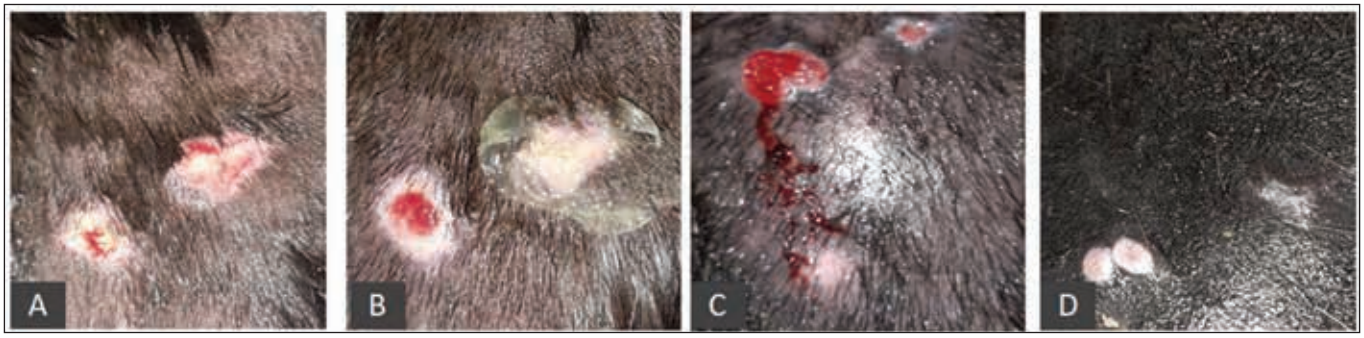

FIGURE 6 - Visual progression of the treatment of equine forearm cut using the combination of the five herbs in petroleum applied topically for 22 days. Panel A: Initial presentation of the wound on day 1 of topical application. Panel B: Condition of the wound on day 4. Panel C: By day 11. Panel D: On day 22, demonstrating the healed wound, no infection that has decreased in size.

was no comparison to an untreated control group. While the observed improvements, combined with the *in vitro* findings, point toward a therapeutic benefit, spontaneous recovery cannot be ruled out. These results mainly demonstrate the tolerability of topical application of extracts in equine models, rather than confirming their efficacy. Further studies need to be made to assess the therapeutic potential of these formulations in a controlled manner.

The wound-healing properties observed align with previous findings on individual components. Pau d'Arco and its active compounds, such as lapachol and β-lapachone, have been reported to suppress PGE2 and COX-2, key mediators of inflammation (14,29). Yarrow, widely recognized for its wound-healing effects, has been shown to regulate inflammatory cytokines and promote fibroblast proliferation (30,31). Gotu kola and its triterpenoids have been linked to enhanced keratinocyte migration and improved skin repair (32), while figwort and broadleaf contribute to anti-inflammatory and antimicrobial responses (33,34).

These findings demonstrate the potential of multi-herbal formulations in wound management by modulating inflammation, promoting immune function, and accelerating tissue repair. Future research should focus on identifying the specific bioactive compounds responsible for these effects, elucidating their molecular mechanisms, and conducting expanded clinical trials to further validate their efficacy in veterinary medicine.

Conclusions

This study highlights the therapeutic potential of Pau d'Arco, yarrow, gotu kola, figwort, and plantain in wound healing by modulating inflammatory responses and promoting tissue regeneration. The extracts effectively reduced pro-inflammatory markers such as IL-8 and, in some cases, enhanced IL-10 expression, demonstrating their immunomodulatory properties *in vitro*. Additionally, preliminary studies in equine wound models suggested favorable healing outcomes; however, these findings are not sufficient to establish causality and necessitate subsequent investigation.

This research supports the integration of herbal formulations as complementary therapies in veterinary wound management. Future research should focus on conducting expanded clinical trials to further validate their efficacy. Additionally, a deeper understanding of their pharmacological properties could facilitate the development of natural, evidence-based treatments for both veterinary and human medicine.

Disclosures

Conflict of interest: The authors declare no conflicts of interest.

Financial support: This research was funded by Enterprise Ireland Innovation Voucher Scheme. The funders had no role in the design of the study, in the collection, analysis, or interpretation of data, or in the writing of the manuscript. The funders supported the decision to publish the results.

Author's contributions: G.W.F: Conceptualization, Data curation, Formal analysis, Investigation, Methodology, Resources, Supervision, Validation, Writing – Original draft. E.M: Conceptualization, Data curation, Formal analysis, Investigation, Methodology, Visualization, Project administration, Resources, Supervision, Validation, Writing – Original draft, Writing – Review and editing. K.S: Data curation, Formal analysis, Investigation, Validation. J.W: Data curation, Formal analysis, Investigation, Validation. N.B: Formal analysis, Investigation, and Validation. T.Y: Methodology, Project administration, Supervision. L.M: Methodology, Supervision. E.R: Data curation, Formal analysis, Validation, Writing - Review and editing. I.M: Writing – Review and editing. M.J.S: Writing – Review and editing.

References

1. Metwally AA, Abdel-Hady AAA, Haridy MAM, et al. Wound healing properties of green (using Lawsonia inermis leaf extract) and chemically synthesized ZnO nanoparticles in albino rats. *Environ Sci Pollut Res Int*. 2022;29(16):23975-23987. CrossRef PubMed
2. Larouche J, Sheoran S, Maruyama K, et al. Immune regulation of skin wound healing: mechanisms and novel therapeutic targets. *Adv Wound Care (New Rochelle)*. 2018;7(7):209-231. CrossRef PubMed
3. Ellis S, Lin EJ, Tartar D. Immunology of wound healing. *Curr Dermatol Rep*. 2018;7(4):350-358. CrossRef PubMed
4. Rodrigues M, Kosaric N, Bonham CA, et al. Wound healing: a cellular perspective. *Physiol Rev*. 2019;99(1):665-706. CrossRef PubMed
5. Julier Z, Park AJ, Briquez PS, Martino MM. Promoting tissue regeneration by modulating the immune system. *Acta Biomater*. 2017;53:13-28. CrossRef PubMed
6. Diegelmann RF, Evans MC. Wound healing: an overview of acute, fibrotic and delayed healing. *Front Biosci*. 2004;9(1-3):283-289. CrossRef PubMed
7. Mahdavian Delavary B, van der Veer WM, van Egmond M, et al. Macrophages in skin injury and repair. *Immunobiology*. 2011;216(7):753-762. CrossRef PubMed
8. Tottoli EM, Dorati R, Genta I, et al. Skin wound healing process and new emerging technologies for skin wound care and regeneration. *Pharmaceutics*. 2020;12(8):1-30. CrossRef PubMed
9. Aisa J, Parlier M. Local wound management: a review of modern techniques and products. *Vet Dermatol*. 2022;33(5):463-478. CrossRef PubMed
10. Ali SI, Gopalakrishnan B, Venkatesalu V. Pharmacognosy, phytochemistry and pharmacological properties of Achillea millefolium L.: a review. *Phytother Res*. 2017;31(8):1140-1161. CrossRef PubMed
11. Lira AAM, Sester EA, Carvalho ALM, et al. Development of lapachol topical formulation: anti-inflammatory study of a selected formulation. *AAPS PharmSciTech*. 2008;9(1):163-168. CrossRef PubMed
12. Sun B, Wu L, Wu Y, et al. Therapeutic potential of Centella asiatica and its triterpenes: a review. *Front Pharmacol*. 2020;11:568032. CrossRef PubMed
13. Gómez Castellanos JR, Prieto JM, Heinrich M. Red Lapacho (Tabebuia impetiginosa)—a global ethnopharmacological commodity? *J Ethnopharmacol*. 2009;121(1):1-13. CrossRef PubMed
14. McClure C, Bollen M, Buttolph L, et al. Safety and tolerability of Pau d' Arco (*Tabebuia avellanedae)* for primary dysmenorrhea: a single-arm, open-label trial on adults ages 18-45. *Adv Integr Med*. 2022;9(3):159-166. CrossRef PubMed
15. Farasati Far B, Behzad G, Khalili H. *Achillea millefolium*: mechanism of action, pharmacokinetic, clinical drug-drug interactions and tolerability. *Heliyon*. 2023;9(12):e22841. CrossRef PubMed

16. Tilwani K, Patel A, Parikh H, et al. Investigation on anti-Corona viral potential of Yarrow tea. *J Biomol Struct Dyn*. 2023;41(11):5217-5229. PubMed
17. Choi YM, An S, Lee J, et al. Titrated extract of Centella asiatica increases hair inductive property through inhibition of STAT signaling pathway in three-dimensional spheroid cultured human dermal papilla cells. *Biosci Biotechnol Biochem*. 2017;81(12):2323-2329. CrossRef PubMed
18. Ju Ho P, Jun Sung J, Ki Cheon K, et al. Anti-inflammatory effect of Centella asiatica phytosome in a mouse model of phthalic anhydride-induced atopic dermatitis. *Phytomedicine*. 2018;43:110-119. CrossRef PubMed
19. Ling Y, Gong Q, Xiong X, et al. Protective effect of madecassoside on H_2O_2-induced oxidative stress and autophagy activation in human melanocytes. *Oncotarget*. 2017;8(31):51066-51075. Accessed February 6, 2025. CrossRef PubMed
20. Sawatdee S, Choochuay K, Chanthorn W, et al. Evaluation of the topical spray containing Centella asiatica extract and its efficacy on excision wounds in rats. *Acta Pharm*. 2016;66(2):233-244. CrossRef PubMed
21. Ahmad M, Muhammad N, Jahan N, et al. Spasmolytic effects of Scrophularia nodosa extract on isolated rabbit intestine. Pak J Pharm Sci 2012. Online
22. Adom MB, Taher M, Mutalabisin MF, et al. Chemical constituents and medical benefits of Plantago major. *Biomed Pharmacother*. 2017;96:348-360.CrossRef PubMed
23. Najafian Y, Hamedi SS, Farshchi MK, et al. Plantago major in traditional Persian medicine and modern phytotherapy: a narrative review. *Electron Physician*. 2018;10(2):6390-6399. CrossRef PubMed
24. Murphy EJ, Rezoagli E, Pogue R, et al. Immunomodulatory activity of β-glucan polysaccharides isolated from different species of mushroom - a potential treatment for inflammatory lung conditions. *Sci Total Environ*. 2022;809:152177. CrossRef PubMed
25. Murphy EJ, Masterson C, Rezoagli E, et al. β-Glucan extracts from the same edible shiitake mushroom Lentinus edodes produce differential in-vitro immunomodulatory and pulmonary cytoprotective effects — implications for coronavirus disease (COVID-19) immunotherapies. *Sci Total Environ*. 2020;732:732. CrossRef
26. Jitprasertwong P, Khamphio M, Petsrichuang P, et al. Anti-inflammatory activity of soluble chito-oligosaccharides (CHOS) on VitD3-induced human THP-1 monocytes. *PLoS One*. 2021;16(2):e0246381. CrossRef PubMed
27. Pereira RB, Rahali FZ, Nehme R, et al. Anti-inflammatory activity of essential oils from Tunisian aromatic and medicinal plants and their major constituents in THP-1 macrophages. *Food Res Int*. 2023;167:112678. CrossRef PubMed
28. Xeroudaki M, Rafat M, Moustardas P, et al. A double-crosslinked nanocellulose-reinforced dexamethasone-loaded collagen hydrogel for corneal application and sustained anti-inflammatory activity. *Acta Biomater*. 2023;172:234-248. CrossRef PubMed
29. Lee JH, Cheong J, Park YM, et al. Down-regulation of cyclooxygenase-2 and telomerase activity by β-lapachone in human prostate carcinoma cells. *Pharmacol Res*. 2005;51(6):553-560. CrossRef PubMed
30. Tadić V, Arsić I, Zvezdanović J, et al. The estimation of the traditionally used yarrow (Achillea millefolium L. Asteraceae) oil extracts with anti-inflammatory potential in topical application. *J Ethnopharmacol*. 2017;199:138-148. CrossRef PubMed
31. Mohamed ME, Elsayed SA, Madkor HR, et al. Yarrow oil ameliorates ulcerative colitis in mice model via regulating the NF-κB and PPAR-γ pathways. *Intest Res*. 2021;19(2):194-205. CrossRef PubMed
32. Singkhorn S, Tantisira MH, Tanasawet S, et al. Induction of keratinocyte migration by ECa 233 is mediated through FAK/Akt, ERK, and p38 MAPK signaling. *Phytother Res*. 2018;32(7):1397-1403. CrossRef PubMed
33. Zubair M, Ekholm A, Nybom H, et al. Effects of Plantago major L. leaf extracts on oral epithelial cells in a scratch assay. *J Ethnopharmacol*. 2012;141(3):825-830. CrossRef PubMed
34. Hussan F, Mansor AS, Hassan SN, et al. Anti-inflammatory property of Plantago major leaf extract reduces the inflammatory reaction in experimental acetaminophen-induced liver injury. *Evid Based Complement Alternat Med*. 2015;2015:347861. CrossRef PubMed

DTI
Drug Target Insights 2025; 19: 49-58
ISSN 1177-3928 | DOI: 10.33393/dti.2025.3574
ORIGINAL RESEARCH ARTICLE
Open Access

Integrative *in silico* and Petra/Osiris/Molinspiration (POM) analysis of baicalein: identification of therapeutically relevant pharmacophores against keloid pathology

Abhay P. Mishra[1], Anothai Tangsumranjit[2], Manisha Nigam[3], Harish Chandra[4], Faisal A. Almalki[5], Taibi B. Hadda[6], Neti Waranuch[1,2]

[1]Cosmetics and Natural Products Research Center (CosNat), Faculty of Pharmaceutical Sciences, Naresuan University, Phitsanulok - Thailand
[2]Department of Pharmaceutical Technology, Faculty of Pharmaceutical Sciences and Center of Excellence for Innovation in Chemistry, Naresuan University, Phitsanulok - Thailand
[3]Department of Biochemistry, H. N. B. Garhwal University, Srinagar Garhwal, Uttarakhand - India
[4]Department of Botany and Microbiology, Gurukula Kangri (Deemed to be University), Haridwar, Uttarakhand - India
[5]Department of Pharmaceutical Sciences, Faculty of Pharmacy, Umm Al-Qura University, Makkah - Saudi Arabia
[6]Euromed University of Fes (UEMF), Meknes Road, Fez - Morocco

ABSTRACT

Introduction: Keloid scars are a kind of skin disorder in which the scar grows beyond the boundaries of the original wound. Baicalein, a flavonoid, may treat keloids by targeting fibrosis, inflammation, and possible viral factors.
Methods: In silico studies were conducted to evaluate the potential anti-keloid effects of baicalein by predicting its interactions with three key proteins of the transforming growth factor-β (TGF-β) family (PDB IDs: 1VJY, 3TZM, and 7DV6). POM analysis was also used to understand the conditions that could enhance baicalein's efficacy.
Results: The results indicated that baicalein binds effectively to TGF-β family proteins via hydrogen bonds, showing strong affinities (1VJY: -9.9 kcal/mol, 3TZM and 7DV6: -9.3 kcal/mol), indicating its potential as a TGF-β receptor ligand. Osiris analysis gave a drug score of 75% for baicalein, while Molinspiration indicated good bioavailability with a cLogP of 2.84. Atomic charge distribution and pharmacophore site mapping through POM analysis indicate that baicalein exhibits an antiviral pharmacophoric moiety akin to known antiviral agents. This indicates that baicalein may act as a pro-drug, undergoing metabolic transformation to form a bis-bidentate ligand. Such ligands are crucial for forming bimetallic complexes that can function as efficient biocatalysts against various biological targets.
Conclusion: In-silico analysis suggests that baicalein may influence TGF-β receptors and exhibit anti-keloid activity. Additionally, POM analysis recommends that baicalein may serve as a lead compound with the potential to modulate TGF-β signalling and exhibit antiviral properties, indicating it as a dual-action agent against keloids and viral infections.

Keywords: *O. indicum*, baicalein, keloid, transforming growth factor-β, anti-inflammatory, anti-viral activity

Introduction

A keloid is an abnormal scar that forms in the dermis following skin injury. This condition, known as Keloid Disease (KD), is a benign but locally aggressive fibroproliferative disorder characterized by scar tissue that extends beyond the original wound boundaries into the surrounding healthy skin (1). KD typically manifests between the ages of 10 and 30 and is less common in older individuals. It is more prevalent among people with darker skin tones, particularly those with a family history of keloid formation (2). Keloid scarring does not follow the typical pattern of evolution, stabilization, and involution observed in hypertrophic scars. It may develop soon after an injury or appear years later, sometimes arising from a previously stable and mature scar (2).

Transforming growth factor-β (TGF-β) family of cytokines significantly promotes fibrosis by stimulating the production and remodelling of extracellular matrix (ECM) in fibroblasts and connective tissues. Additionally, TGF-β is crucial for enforcing immune tolerance and suppressing inflammation, as it restricts the functioning of the immune systems (adaptive and innate) (3). According to a study, TGF-β1 and TGF-β2 cause skin scarring; however, TGF-β3 appears to have the opposite effect (4). On the other hand, elevated TGF-β1 and TGF-β2 expression may negatively impact the healing process by promoting the development of scars (5). According to

Received: May 15, 2025
Accepted: June 23, 2025
Published online: July 16, 2025

This article includes supplementary material.

Corresponding author:
Neti Waranuch
email: netiw@nu.ac.th

another study, proper modulation of TGF-β and TGF-β receptor expression is crucial for optimal wound healing (5).

It is commonly recognised that tissue repair involves TGF-β1, TGF-β receptor type I (TGF-βRI), and TGF-β receptor type II (TGF-βRII) (6,7). Chin et al. reported that keloid fibroblasts exhibit altered responses to TGF-β due to differences in receptor expression. Specifically, the study found that keloid fibroblasts express higher levels of TGF-βRI and TGF-βRII compared to normal human fibroblasts (8). In addition, Bock et al. investigated the expression levels of TGF-β1, TGF-β2, and TGF-β3, along with the mRNAs of TGF-βRI and TGF-βRII receptors. Their findings revealed that hypertrophic scars exhibited significantly lower TGF-βRI mRNA expression, whereas keloid scars showed reduced TGF-βRII mRNA expression. Consequently, the TGF-βRI/TGF-βRII ratio was elevated in keloid scars compared to hypertrophic scars (9).

In contrast, when TGF-βRI/TGF-βRII receptor expression levels were compared between keloid and normal human dermal fibroblasts, the findings indicated that keloid tissues were found to exhibit significantly elevated levels of these receptors (8,10). Several treatment approaches have been put forth to lessen the severity of keloid scarring. Various signalling pathways, such as mitogen-activated protein kinase (MAPK), sphingosine-1-phosphate (S1P), nuclear factor kappa B (NF-κB), insulin-like growth factor-I (IGF-I), TGF-β1, wingless-related integration site (Wnt), janus kinase (JAK)/signal transducer and activator of transcription (STAT), and integrin pathways have been investigated as potential mechanisms involved in keloid formation. However, despite extensive research, the underlying molecular mechanisms of this skin disorder remain poorly understood and inconclusive (11,12).

It has been suggested that natural compounds with diverse bioactive properties such as asiaticoside, quercetin, madecassoside, oxymatrine, and curcuminoids extracted from plants including *Salvia miltiorrhiza* Bunge, *Astragalus membranaceus* Bunge, and *Aneilema keisak* Hassk, may have therapeutic potential in the treatment of keloid disorder (11).

Oroxylum indicum (L.) Kurz (Bignoniaceae), also called the Indian trumpet flower, is widely found across various Asian countries, including Thailand, Vietnam, Malaysia, Indonesia, the Philippines, Japan, China, Taiwan, and India (13). The plant is renowned for its therapeutic properties (14). For millennia, it has been utilized in Asian ethnomedical systems as a traditional medicine to prevent and treat a wide range of illnesses, including jaundice, rheumatoid arthritis, peptic ulcers, cancers, respiratory conditions, diabetes, diarrhea, and dysentery, among others (15). Flavonoids, alkaloids, tannins, glycosides, saponins, phenols, and quinones are only a few of the many secondary metabolites that contribute to the biological activity of the *O. indicum* plant. Chrysin, baicalein, oroxylin-A, baicalein-7-O-diglucoside, and baicalein-7-O-glucoside are all derived from this group. Among all the flavonoids found in *O. indicum*, baicalein is the most common and the most significantly active component (13). Baicalein strongly inhibits endoproteases and proprotein convertases, contributing to its broad spectrum of biological effects, including anti-inflammatory, anticancer, antihyperglycemic, neurogenic, anti-adipogenic, cardioprotective, antibacterial, and wound healing activities (13-16). It also inhibits collagen synthesis and cell proliferation (16) and exhibits anti-inflammatory properties (17). Moreover, it is believed that using baicalein can alleviate keloid scarring.

Therefore, the current study is aimed at performing *in silico* studies to predict baicalein as an anti-keloid scar molecule by targeting TGF-βRI and II receptors.

Methodology

Structure preparation

Protein Data Bank (PDB) IDs 1VJY (TGF-βRI), 3TZM (TGF-βRI), and 7DV6 (TGF-βRII) were used to download the crystalline structures and sequences of TGF-βRI and II receptors through the Research Collaboratory for Structural Bioinformatics (RCSB) protein repository (Online). Using BIOVIA Discover Studio 2021, hetero-atoms and water, as well as inhibitors, were carefully eliminated from the target receptor. The three-dimensional (3D) molecular structures of the ligands, baicalein and conventional medications (1,5-Naphthyridine;4-(5-benzo(1,3)dioxol-5-yl-4-pyridin-2-yl-1H-imidazol-2-yl)benzamide and 5-[(3S)-5,5-dimethyloxolan-3-yl]-6-methoxy-3-(2-methoxypyridin-4-yl)pyrazolo[1,5-a] pyrimidine), in the structured data format (SDF) (Fig. SI A-D) were obtained using PubChem databank (Table SI). BIOVIA Discover Studio 2021 was used to convert the ligands' SDF to PDB file format. Open Babel 2.4.1 software, which was in line with PyRx, was used to convert all PDB file types into PDBQT file formats to generate atomic coordinates. The Open Babel was also utilized to minimize the energy of ligands following the insertion of H-atoms.

Ramachandran plot and hydropathy analysis

Ramachandran plot and hydropathy analysis were carried out to assess the structural and physicochemical properties of the proteins (18-20). In brief, the Procheck server (Online) was used to verify the stereochemical character of the proteins obtained via the Protein Data Bank (PDB). The relevance and positioning of secondary structural elements, such as α-helices and β-sheets, were tested for relevance using Ramachandran plot analysis, which examines the φ (phi) and Ψ (psi) dihedral angles to determine the conformational stability of the polypeptide backbone. Protein modeling and structural evaluations were guided by these angular measurements. The statistical distribution of amino acids within the secondary structures was also analyzed. Additionally, the amphiphilic nature of the receptor molecule was confirmed using a hydropathy plot generated by BIOVIA Discovery Studio Software 2021.

Molecular docking

PyRx, written in Python, is a virtual molecular screening tool that docks ligands to macromolecules to locate the compounds of interest with the necessary biological significance. The application of this in silico technique in computer-aided drug design is well established (21).

The ligand and macromolecule (target proteins 1VJY, 3TZM, and 7DV6) were uploaded to the PyRx tool to closely monitor and assess any potential interaction between the ligand

(a chemical compound) and target protein. The output included a list of models arranged in accordance with the anticipated binding energies in kilocalorie per mole (kcal/mol), whereas the input included a ligand, docking box, flexible receptor, and rigid receptor (21). All targeted TGF-β receptors and docking simulations were started with active sites as the CASTp server suggested (22). Discovery Studio was used to view several interactions posed to assess theresidual interaction of ligands with the target enzyme.The Discovery Studio Visualizer was used to extract and align the docking model containing the lowest possible energy related to the receptor.

Absorption, distribution, metabolism, excretion properties (ADME) and drug-likeness prediction

Swiss ADME (http://www.swissadme.ch/), a free online tool, examines ligands' drug-likeness prediction and ADME properties (23). Drug-likeness was evaluated based on Lipinski's rule of five, which states that a compound is more likely to be orally active if it meets the following criteria: no more than five hydrogen bond donors, no more than ten hydrogen bond acceptors, a molecular weight below 500 Da, a calculated LogP value (lipophilicity) ≤ 5, and a polar surface area (PSA) ≤ 140 Å². Compounds that violate two or more of these criteria are generally considered to have poor absorption and bioavailability (24).

Target prediction

Finding potential crossover reactions or physiological adverse effects from the intercommunication of tiny biomolecules requires pharmacological research (25). Canonical SMILES of baicalein were entered into the Swiss Target Prediction website (Online) for target prediction research, and the results were examined.

Toxicity prediction

Animal and human models are essential for predicting the toxicological profile of a molecule, which is essential for determining its acceptability before administration. The Protox II server (Online) was used to assess the molecule's toxicity. To predict toxicity, the canonical SMILES of baicalein that were obtained from PubChem were utilised as input (26).

POM analysis

The identification of the pharmacophore sites of drugs is performed with great precision, based on the geometric and electronic properties of the functionalised groups. The organigram of POM theory is shown in Fig. S1. This model was developed using a combination of three computational tools: 1) Petra: Calculation of atomic charges (27), 2) Osiris: for the prediction of potential side effects, bioavailability, and Drug-score (Online), 3) Molinspiration: for the evaluation of Lipinski's five rules and 3D structure optimisation (Online).

Results and discussion

Baicalein chemistry

Baicalein ($C_{15}H_{10}O_5$) belongs to the flavone subclass of flavonoids (Fig. S2 A). It is naturally found in the leaves of *Thymus vulgaris* L. and *O. indicum* as well as in the roots of *Scutellaria baicalensis* Georgi (28,29). Baicalein is a potent anti-inflammatory that primarily works by binding to several chemokines, such as IL-8, monocyte chemotactic protein-2, and macrophage inflammatory protein-1β, thereby inhibiting their biological activity. Furthermore, baicalein has been shown to modulate the immune response by promoting the polarization of macrophages from the pro-inflammatory M1 phenotype to the anti-inflammatory M2 phenotype (30). These properties highlight baicalein's potential in mitigating inflammatory processes (31,32). Given that, inflammation plays a crucial role in keloid pathogenesis, baicalein's anti-inflammatory activity may contribute to its therapeutic potential in managing keloid disease.

Interestingly, baicalein's therapeutic use was constrained due to its low bioavailability and solubility. Therefore, it is essential to modify baicalein using biological and chemical approaches to generate analogues with improved solubility and absorption. Baicalein contains three hydroxyl groups (5-OH, 6-OH, and 7-OH) on ring A (Fig. S2A), with the C-6 and C-8 positions serving as active sites for nucleophilic substitution reactions. The 5-OH group is a key structural feature linked to the cytotoxic activity of baicalein and its derivatives. Furthermore, nitrogenous and water-soluble amino acids can be used as substituents in structural modifications to enhance solubility (33). Researchers have successfully replicated the biosynthetic conversion of chrysin to baicalein in laboratory testing by employing a multistep synthetic strategy (34-36). After conducting a groundbreaking study, Chen et al. developed a novel and efficient method for synthesizing baicalein from 3,4,5-trimethoxyphenol. This approach offers a promising and more effective strategy for the large-scale production of baicalein (14,34). In addition, Huang et al. synthesized baicalein, oroxylin A, and wogonin very effectively by employing inexpensive reagents and working in mild conditions (37).

Our results emphasized the significance of baicalein as the key active compound, highlighting its strong binding affinity to the active sites of TGF-βRI and TGF-βRI. Additionally, baicalein exhibited notable anti-inflammatory properties, thereby revealing potential mechanisms for its therapeutic application in keloid disease. It also served as an essential tool for assessing the structural stability of the molecule and validating the amphiphilic nature of the receptor, respectively (18).

Ramachandran plot and hydropathy analysis

The Ramachandran plot illustrates the stable conformations of amino acid residues by identifying favourable and unfavourable regions, particularly highlighting low-energy configurations for the torsion angles φ and Ψ. Each point on the plot represents the φ and Ψ angles of an amino acid residue in a three-dimensional protein structure (Fig. S3). Upon analysing the sequences of 1VJY, 3TZM, and 7DV6, it was found that 268, 265, and 275 non-glycine and non-proline residues were present, respectively, out of a total of 299, 295, and 304 residues in the corresponding proteins.

The stereochemical characteristics are displayed in Table S-II for all likely values of φ and Ψ for the dihedral angle. This includes hydrophilic and hydrophobic regions in the amino acid chain, starting at the N-terminal and progressing

towards the C-terminal, further supporting protein architectures (Fig. S4).

Molecular docking assessment for targeting TGF-β receptors

Binding energies measured with PyRx software powered by Autodock Vina were **-9.9** (1VJY-Baicalein), -**9.3** (3TZM-Baicalein) and -**9.3** kcal/mol (7DV6-Baicalein) with favourable root mean square deviation (RMSD) values compared with reference standards, 1,5-Naphthyridine (-10.3 kcal/mol), 4-(5-benzo(1,3) dioxol-5-yl-4-pyridin-2-yl-1H-imidazol-2-yl)benzamide (-10.8 kcal/mol) and 5-[(3S)-5,5-dimethyloxolan-3-yl]-6-methoxy-3-(2-methoxypyridin-4-yl)pyrazolo[1,5-a]pyrimidine (-9.3 kcal/mol), respectively (Table 1). The ASP 351 and GLU 245 residues are targeted by the baicalein interaction with 1VJY through hydrogen bonding at the protein's active site. Additionally, they used several pi bonds to engage with LYS 232, VAL 219, ILE 211, ALA 350, 230, and LEU 260 at the enzyme's catalytic pocket. Van der Waals interactions were observed with more amino acids, including LEU 278, 352, 340, TYR 249, PHE 262, LEU 278, VAL 231, 279, SER 280, and GLY 286 (Fig. 1A).

Interestingly, it is noteworthy that the target macromolecule 3TZM active binding pocket contains the amino acid GLU 245 via a traditional hydrogen bond with baicalein. Furthermore, GLY 286, LEU 352, VAL 231, 279, PHE 262, and TYR 249 interacted through van der Waals at the protein catalytic site, while VAL 219, LEU 260, and ALA 350 interacted through various pi-bonds (Fig. 2A). The binding site of 7DV6-baicalein, another receptor interaction, was made up of hydrogen-bonded HIS 328 and VAL 250 residues. Through various pi-bonds, baicalein targets VAL 258, LEU 305, 386, LYS 277, ALA 275, and CYS 396. Via van der Waals, it targets ALA 326, 329, ASN 332, GLY 251, THR 325, LEU 323, PHE 294, 327, and ASP 397. The sole amino acid interacting with the ligand through a carbon-hydrogen bond is GLY 331 (Fig. 3A).

TABLE 1 - Baicalein's protein-ligand binding energy values with TGF-βRI and RII receptors

S.N.	Target molecule	Binding Energy (kcal/mol)			
		Baicalein	**1,5-Naphthyridine**	**4-(5-benzo(1,3)dioxol-5-yl-4-pyridin-2-yl-1H-imidazol-2-yl) benzamide**	**5-[(3S)-5,5-dimethyloxolan-3-yl]-6-methoxy-3-(2-methoxypyridin-4-yl) pyrazolo[1,5-a]pyrimidine**
1.	1VJY (TGF-βRI)	−9.9	−10.3	---	---
2.	3TZM (TGF-βRI)	−9.3	---	−10.8	---
3.	7DV6 (TGF-βRII)	−9.3	---	---	−9.3

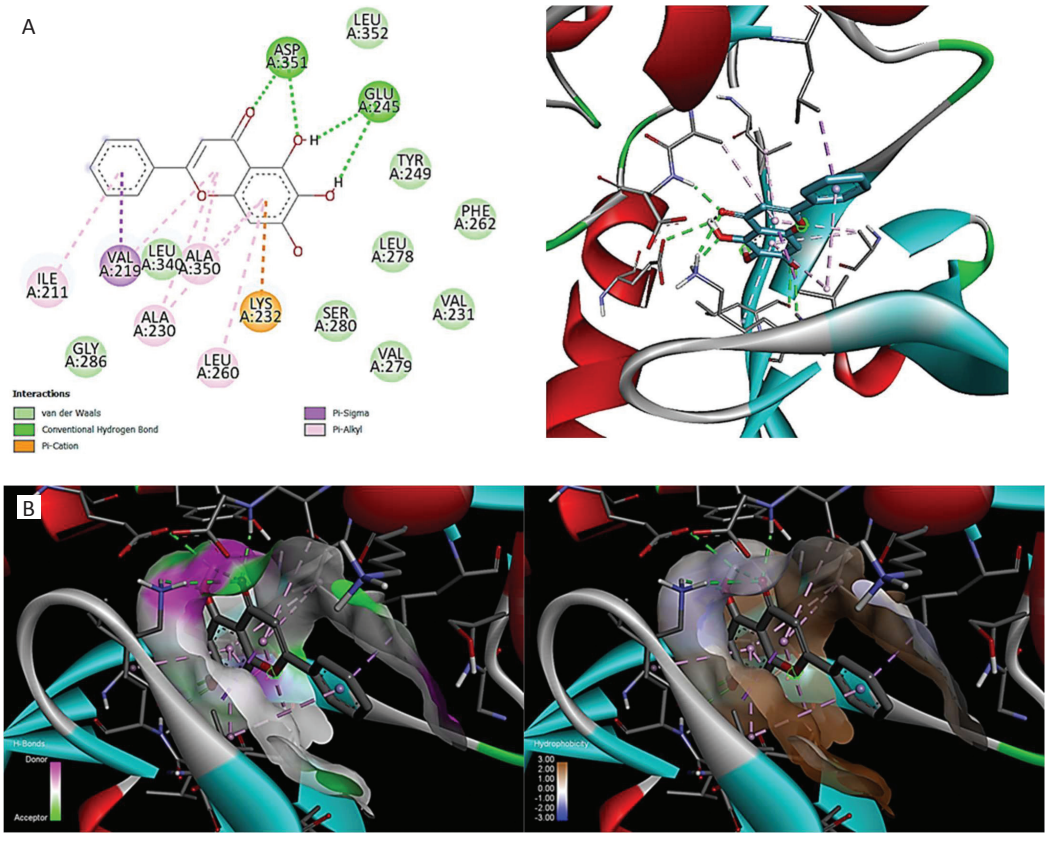

FIGURE 1 - A. 2D (left) and 3D (right) view of protein ligand interaction (1VJY-Baicalein). B. Hydrogen (Left) and Hydrophobicity (Right) surface view of receptor-ligand interaction (1VJY-Baicalein).

The strength of the interaction between a ligand and its target protein is predicted by the hydrogen interactions between the two, which is why our study closely examined the donor and recipient regions of the hydrogen bonds between the two, as well as the distance between the interacting atoms (Figs 1B-3B).

Swiss ADME and drug-likeness prediction

Table S-III displays the baicalein's drug-likeness and ADME data. The scores showed that baicalein met the requirements of Lipinski's rule of five, indicating that it's a reliable medication that works well when taken orally. In summary, this molecule is said to have good permeability, oral bioavailability, low toxicity, and favorable absorption characteristics. The bioavailability radar map summarized the drug-likeness of baicalein (Fig. S5). The pink area represents the molecule's (baicalein) effective range for each attribute.

The gastrointestinal absorbency and brain penetrative effectiveness of baicalein are predicted by the boiled-egg plot between the water partition coefficient (WLOGP) and topological polar surface area (TPSA), as illustrated in Fig. S6. Baicalein is quickly absorbed into the gastrointestinal tract and cannot cross the blood-brain barrier (BBB) by interacting with the innermost yellow nucleus/yolk, as the plot (Fig. S6) demonstrates. The red dot indicates that baicalein is a non-substrate of permeability glycoprotein.

Swiss target prediction

A pie chart was created to illustrate the leading 15 plausible targets (Fig. S7). These predicted targets include 26.7% enzymes, 20% lyases and kinases, 13.3% cytochrome P450 enzymes, and 6.7% each for oxidoreductases, primary active transporters, and erasers.

The prediction algorithms estimate potential target interactions for the molecule, with likelihood scores ranging from 1.0000 to 0.3299. These values suggest a high probability of the molecule binding to its intended targets. The target prediction results displayed on the server page contributed to several significant findings (Table S-IV).

ProTox 3.0 toxicity prediction

The organ toxicity (hepatotoxicity), Tox21 Stress response pathways, Tox21 Nuclear receptor signalling pathways, and toxicity endpoints (immunotoxicity, carcinogenicity, mutagenicity, and cytotoxicity) served as the foundation for the toxicity prediction. Table S-V provides a summary of the toxicity prediction results. According to class 5 projected toxicity, baicalein's LD50 was 3919 mg/kg, with an average similarity of 81.74% and a prediction accuracy of 70.97% (Fig. S8).

One of the main causes of keloid scar development has been identified as aberrant regulation of the apoptotic pathway. Keloid fibroblasts' inability to halt proliferation

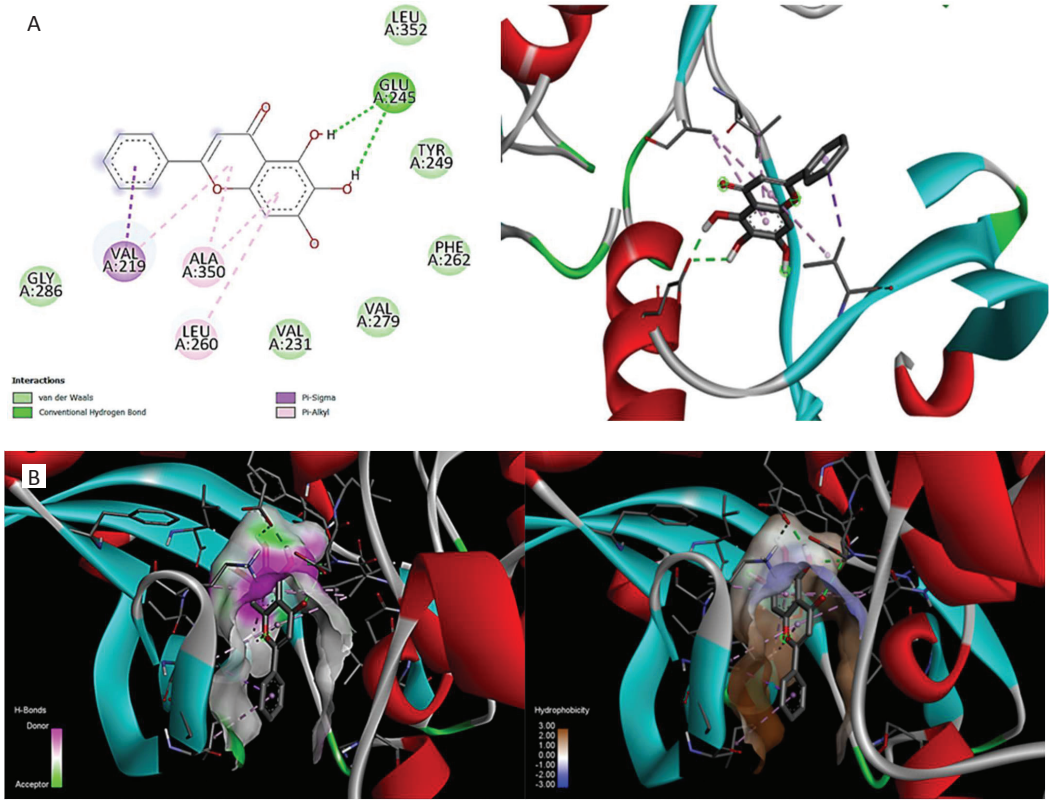

FIGURE 2 - A. 2D (left) and 3D (right) view of 3tzm-Baicalein interaction. B. Hydrogen (Left) and Hydrophobicity (Right) surface view of receptor-ligand interaction (3tzm-Baicalein).

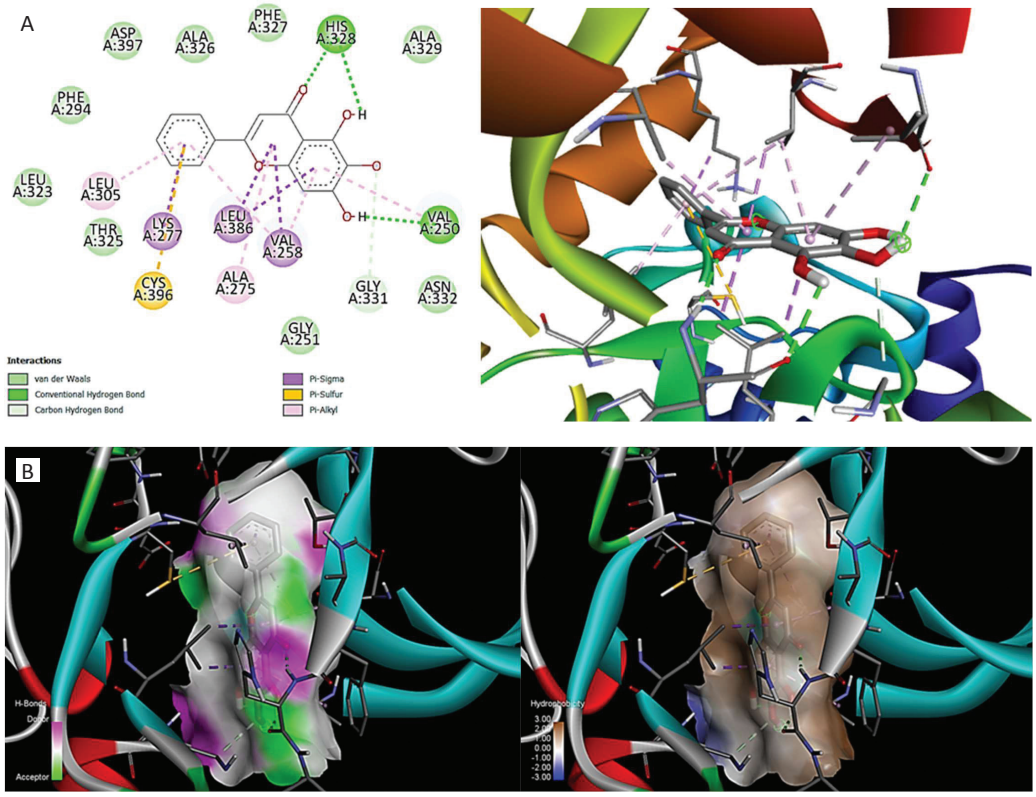

FIGURE 3 - A. 2D (left) and 3D (right) view of 7dv6-Baicalein interaction. B. Hydrogen (Left) and Hydrophobicity (Right) surface view of receptor-ligand interaction (7dv6-Baicalein).

and collagen formation due to their resistance to apoptotic behaviour causes an imbalance in the deposition and breakdown of collagen. Although the basic molecular mechanism of keloid development is still unknown, it is widely accepted that the TGF-β1 pathway plays a significant role in keloid pathogenesis (2,11,38).

Interestingly, maintaining the integrity of an organism depends heavily on the TGF-β regulatory mechanism. TGF-β signaling controls metazoan embryo development, tissue homeostasis, and damage repair through its coordinating impacts on the proliferation of cells, phenotypic variability, migration, metabolic flexibility, and immune monitoring of various cell types in communal environments (39). The pathogenesis of fibrosis and scars is caused by defects in TGF-β signalling, which disrupt immune tolerance, increase inflammation, and result in abnormal collagen synthesis and deposition, a higher proportion of collagen I/III, and the formation of abnormally cross-linked collagen fiber bundles. These defects are especially prevalent in epithelial cells, tissue fibroblasts, and immune cells (3,39,40). It is now thought that flavonoids are primarily responsible for lowering scar formation by inhibiting the production of collagen and fibroblast proliferation. The suppression of TGF-β1 and -β2 and SMAD proteins may be the mechanism underlying these inhibitory actions (41).

According to multiple pharmacological studies, baicalein is closely linked to a number of the plant's biological actions, including anti-inflammatory, antibacterial, antiviral, anti-cardiovascular, and anti-neurodegenerative illnesses (13,42-45). Interestingly, baicalein shows promise as a treatment for skin fibrogenesis. It inhibits the TGF-β/Smad2/3 signalling pathway in fibroblasts *in vitro* and *in vivo* by down-regulating the amounts of phosphorylated Smad2/3 in a dose-dependent manner. Baicalein effectively decreases the activation and multiplication of hypertrophic scar-derived fibroblast cells. It restrains the α-SMA expression throughout the proliferative stage of scarring in a mouse model triggered by mechanical strain. This results in decreased collagen accumulation and attenuated scar development by impairing the contractile and migratory capabilities of fibroblasts produced from hypertrophic scars (40). Zhang et al. (40) suggested that without affecting the expression of Smad6/7, TGF-β1, or TGF-β receptor I/II, baicalein selectively binds to the ATP-binding pocket of activin receptor-like kinase 5 (ALK5), a TGF-β receptor I. Furthermore, it is well known that the TGF-β1 pathway is a major contributor to keloid scarring (1).

Any chemical entity's intricate journey to its destination usually involves successfully navigating several obstacles and surviving a challenging biological process. Several factors and processes determine a chemical entity's bioavailability, which can significantly affect its pharmacokinetic characteristics. Historically, there was a high attrition rate in the development of new medications; ADME issues were linked to over 40% of all therapy failures. Comprehensive studies of ADME techniques are routinely carried out at the early stage of drug development to lower the attrition rate, and the combined evaluation of the biological properties and efficacy of active compounds has been standardized. Researchers are using computational methods to predict a drug's future by

identifying the early dangers of toxicity. Before doing *in vitro* tests, *in silico*-based ADMET profiling techniques are commonly employed to give a general understanding (18).

Using molecular docking, baicalein was employed as a substance (ligand) to assess the compound's possibilities as an anti-keloid molecule (Table 1). This was done by utilising the compound's capacity to attach and downregulate the TGF-βs/Activin pathway. The 3D-interaction map of the best-ranking posture in our investigation demonstrated that baicalein docked nicely inside the catalytic area of all three receptors and formed favourable interactions.

POM analysis

In collaboration with National Cancer Institute (NCI) and Tuberculosis Antimicrobial Acquisition and Coordinating Facility (TAACF) of the USA, Prof. Taibi Ben Hadda (Principal inventor) group has developed a bioinformatic platform (POM theory). This POM theory is able to make pharmacological investigations and drug design easier than in the past. Its crucial role is the determination of different types of pharmacophore sites with high accuracy, on the basis of their atomic charges and 3D geometry (Fig. S1) (46,47).

For this reason, we were interested, for the first time, in looking at the role of baicalein in scar management, via a bioinformatics POM approach.

Osiris calculations of compounds

The outcomes of the pharmacokinetic profile and bioactivity score assessment of the three flavonoids (apigenin, fisetin acid, cosmosin) and baicalein are shown in Table S-VI. We chose three flavonoids (apigenin, fisetin acid, and cosmosin) for one evident reason: the flavonoids are subject to opening the central ring in acidic media. This rearrangement of flavonoids always offers two pockets, ready to chelate with two metal atoms. This structure of bimetallic complexes plays a crucial role in producing bioactive species. Hence, their structural similarities with baicalein suggest a comparable potential for pharmacological relevance.

The results show that the drug score was promising (baicalein: 75%, apigenin: 47%, cosmosiin: 44%, and fisetin acid: 40%) (Table S-VI). The toxicity risks and molecular characteristics of all flavonoids were estimated. In contrast to baicalein, all examined structures were found to be non-cancerogenic and safe.

Molinspiration calculations of compounds

The Molinspiration calculation of molecular properties of flavonoids is presented in Table S-VI. These bioavailability scores could be categorized as good (if the score cLog P < 3), moderately active (if the score was 4-5), or inactive (if the score was more than 6). Verification of every bioactivity metric revealed that most flavonoid derivatives exhibited biological activity against every enzyme (Table S-VI).

Atomic charge calculation of compounds

Based on the findings of the atomic charge calculations displayed in Fig. S9, it is evident that the most potent molecules possess an antiviral pharmacophore site (O $^{\delta-}$, O' $^{\delta-}$, O'' $^{\delta-}$). As a result, most hits were associated with antiviral drugs. Consequently, it was determined to be a pharmacophore site for the chemical baicalein, having antiviral qualities.

Identification of antiviral pharmacophore sites

Baicalein exhibits moderate to good antiviral activity ratings and can be characterized as subjects of opening/closing central rings based on the results of the theoretical and experimental POM calculations (Fig. 4).

The POM Theory is used to get more insight into the mode and mechanism of action of this (baicalein) natural product. It can be seen from Fig. 5 that baicalein is involved in the regeneration of metabolites that can coordinate with the biotargets (M = Cu, Ni, Zn, Pt, Pd, Mn, Mg, Ru, etc.) and modulate pathological processes. As a result, the regenerated metabolites may directly inhibit viral replication and the virus life cycle, and baicalein's ability to target and block TNF-β receptors would prevent abnormal scar formation. However, it's important to note that currently, there is no definitive evidence that a specific virus directly causes keloids. This is why an experimental study on anti-keloid and antiviral effect of baicalein is important because it could potentially reveal a viral factor contributing to the development of keloids, which could lead to new preventative and treatment strategies for this disfiguring skin condition (48,49).

Molecular docking is a computational technique used to predict the interaction between a small molecule (ligand) and a target macromolecule (typically a protein). In the context of baicalein, docking studies have gained attention due to its diverse pharmacological activities, including anticancer, antiviral, anti-inflammatory, and neuroprotective effects. Researchers can prioritize targets and analogues for experimental validation by using docking scores, which offer a relative assessment of the binding affinity between baicalein and certain protein targets. Docking studies reveal the preferred orientation of baicalein within the active site of the target, providing insights into key molecular interactions (e.g., hydrogen bonding, π-π stacking). These insights are crucial for structure-based drug design and rational modification of baicalein derivatives to enhance efficacy (50-52).

While molecular docking provides valuable preliminary insights into the potential interactions between baicalein and target proteins, it is imperative to recognize its limitations. Despite its utility, molecular docking has several inherent limitations that must be considered when interpreting the docking score of baicalein. Docking scores should be interpreted with caution and validated through experimental studies to ensure accurate predictions of biological activity.

Conclusion

The study demonstrates the potential of baicalein as an effective anti-keloid scar agent by targeted interaction with the TGF-βRI and TGF-βRII receptors, essential for tissue healing and scar formation. Strong binding affinities were observed between baicalein and these target proteins via in silico docking experiments, suggesting its capability to modulate critical signalling pathways implicated in keloid pathogenesis.

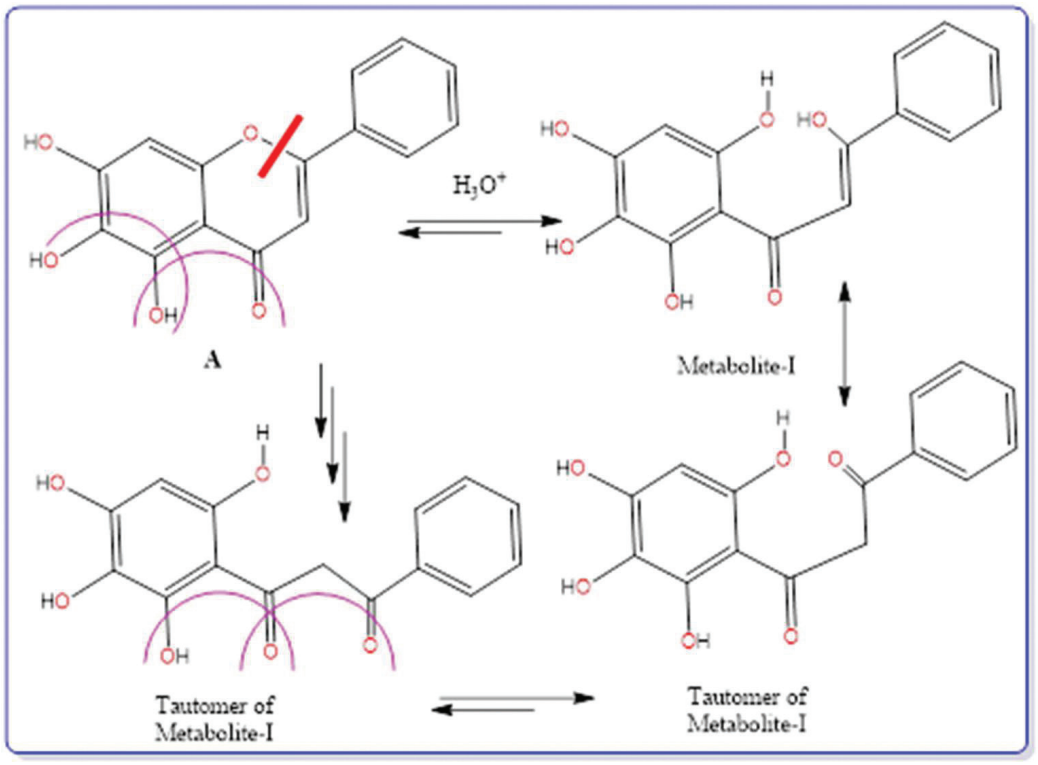

FIGURE 4 - Proposed mechanism of opening/closing the central ring leading to regeneration of the antiviral pharmacophore sites for compound baicalein.

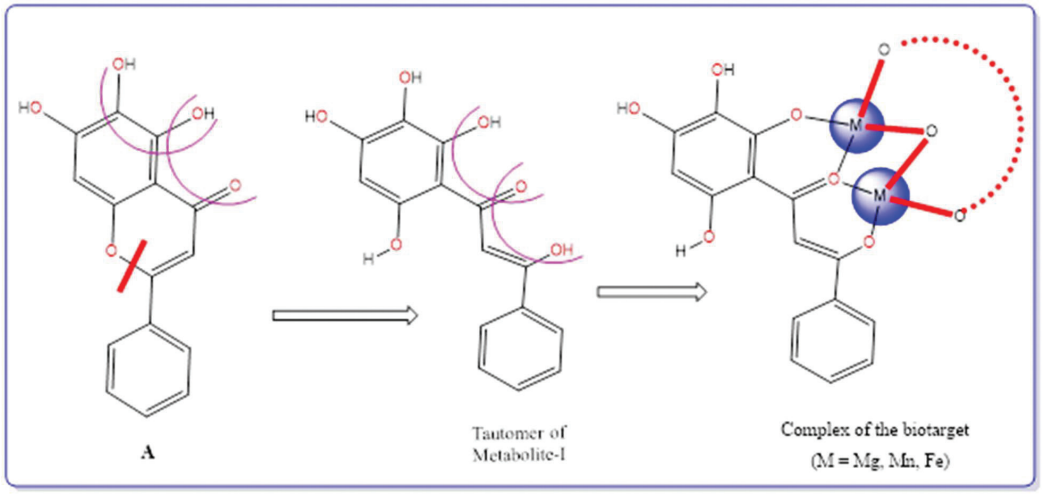

FIGURE 5 - Plausible mechanism of action of baicalein in the scar management and fibrotic disorders, showing its action as an anti-HIV drug.

Baicalein's potential as a therapeutic agent is further reinforced by its favourable ADME profile and drug-like properties. However, further *in vitro* and *in vivo* studies are necessary to elucidate its precise mechanisms of action and validate its safety and efficacy for clinical application. This study lays a promising foundation for the development of baicalein-based therapies for keloid scars and other fibrotic disorders. Moreover, the study highlights the significance of natural compounds in addressing the limitations of traditional keloid treatments, which are often associated with severe side effects and inconsistent results.

Notably, the current understanding of keloid formation remains incomplete, involving a complex interplay of genetics and the immune response. The role of viral triggers is a particularly intriguing and underexplored area, warranting further investigation to establish any causal relationship between viral infections and keloid development.

Given this context, it becomes both urgent and necessary to explore the possible link between antiviral and anti-keloid activities. This could be achieved by investigating the coordination behaviour of baicalein with various transition metals (e.g., Cu, Ni, Zn, Pt, Pd, Mn, Mg, Ru) and evaluating their catalytic bioactivity and enzyme inhibition potential. Further research is needed to clarify its mechanisms and explore its role in antiviral-based keloid prevention, particularly if a viral link is confirmed.

Furthermore, while molecular docking scores serve as valuable tools in the early stages of drug discovery, providing insights into potential targets and interaction mechanisms, their predictive value is limited by both computational and biological constraints. Therefore, docking outcomes should be interpreted with caution and always corroborated with experimental validation.

Acknowledgments

Our special thanks to the bioinformatic platform (principal inventor is Taibi Ben Hadda) for performing POM analysis.

Disclosures

Conflict of interest: The authors declare no conflict of interest.

Financial support: This work was partially supported by the Global and Frontier Research University Fund, Naresuan University; Grant number R2566C053.

Authors contribution: Conceptualization, A.P.M. and M.N.; methodology, A.P.M., T.B.H. and H.C.; formal analysis, A.P.M., H.C., F.A.A. and T.B.H.; investigation, A.P.M., and T.B.H.; resources, F.A.A., A.P.M. and T.B.H.; writing—original draft preparation, A.P.M.; writing—review and editing, T.B.H., H.C., M.N., N.W. and A.P.M.; supervision, H.C. and M.N.; project administration, A.P.M., and N.W.; funding acquisition, N.W. and A.T. All authors have read and agreed to the published version of the manuscript.

References

1. Shih B, Bayat A. Genetics of keloid scarring. Arch Dermatol Res. 2010;302(5):319-339. CrossRef PubMed
2. Bran GM, Goessler UR, Hormann K, Riedel F, Sadick H. Keloids: current concepts of pathogenesis (Review). Int J Mol Med. 2009;24(3):283-293. CrossRef PubMed
3. Massagué J, Sheppard D. TGF-β signaling in health and disease. Cell. 2023;186(19):4007-4037. CrossRef PubMed
4. Shah M, Foreman DM, Ferguson MWJ. Neutralisation of TGF-β 1 and TGF-β 2 or exogenous addition of TGF-β 3 to cutaneous rat wounds reduces scarring. J Cell Sci. 1995;108(Pt 3):985-1002. CrossRef PubMed
5. Frank S, Madlener M, Werner S. Transforming growth factors β1, β2, and β3 and their receptors are differentially regulated during normal and impaired wound healing. J Biol Chem. 1996;271(17):10188-10193. CrossRef PubMed
6. Huang Y, Wang Y, Wang X, et al. The effects of the transforming growth factor-β1 (TGF-β1) signaling pathway on cell proliferation and cell migration are mediated by ubiquitin specific protease 4 (USP4) in hypertrophic scar tissue and primary fibroblast cultures. Med Sci Monit. 2020;26:e920736. CrossRef PubMed
7. Kamal R, Awasthi A, Pundir M, et al. Healing the diabetic wound: unlocking the secrets of genes and pathways. Eur J Pharmacol. 2024;975:176645. CrossRef PubMed
8. Chin GS, Liu W, Peled Z, et al. Differential expression of transforming growth factor-β receptors I and II and activation of Smad 3 in keloid fibroblasts. Plast Reconstr Surg. 2001; 108(2):423-429. CrossRef PubMed
9. Bock O, Yu H, Zitron S, et al. Studies of transforming growth factors beta 1-3 and their receptors I and II in fibroblast of keloids and hypertrophic scars. Acta Derm Venereol. 2005;85(3):216-220. CrossRef PubMed
10. Jagadeesan J, Bayat A. Transforming growth factor beta (TGFbeta) and keloid disease. Int J Surg. 2007;5(4):278-285. CrossRef PubMed
11. Unahabhokha T, Sucontphunt A, Nimmannit U, et al. Molecular signalings in keloid disease and current therapeutic approaches from natural based compounds. Pharm Biol. 2015;53(3):457-463. CrossRef PubMed
12. Boo YC. Insights into how plant-derived extracts and compounds can help in the prevention and treatment of keloid disease: established and emerging therapeutic targets. Int J Mol Sci. 2024;25(2):1235. CrossRef PubMed
13. Nik Salleh NNH, Othman FA, Kamarudin NA, et al. The biological activities and therapeutic potentials of baicalein extracted from Oroxylum indicum: A systematic review. Molecules. 2020;25(23):1-23. CrossRef PubMed
14. Munjal K, Goel Y, Gauttam VK, et al. Molecular targets and therapeutic potential of baicalein: a review. Drug Target Insights. 2024;18(1):30-46. CrossRef PubMed
15. Dinda B, SilSarma I, Dinda M, et al. Oroxylum indicum (L.) Kurz, an important Asian traditional medicine: from traditional uses to scientific data for its commercial exploitation. J Ethnopharmacol. 2015;161:255-278. CrossRef PubMed
16. Yang L, Li X, Zhang S, et al. Baicalein inhibits proliferation and collagen synthesis of mice fibroblast cell line NIH/3T3 by regulation of miR-9/insulin-like growth factor-1 axis. Artif Cells Nanomed Biotechnol. 2019;47(1):3202-3211. CrossRef PubMed
17. Lee W, Ku SK, Bae JS. Anti-inflammatory effects of Baicalin, Baicalein, and Wogonin in vitro and in vivo. Inflammation. 2015;38(1):110-125. CrossRef PubMed
18. Gupta KK, Sharma KK, Chandra H, et al. The integrative bioinformatics approaches to predict the xanthohumol as anti-breast cancer molecule: targeting cancer cells signaling PI3K and AKT kinase pathway. Front Oncol. 2022;12(December):950835. CrossRef PubMed
19. Bawazeer S, Rauf A, Shahidullah A, et al. Structural insights behind protein tyrosine phosphatase 1B inhibitory activity of diospyrin. Indian J Pharm Sci. 2019;81(3):565-568. CrossRef
20. Alhumaydhi FA, Rauf A, Rashid U, et al. In vivo and in silico studies of flavonoids isolated from Pistacia integerrima as potential antidiarrheal agents. ACS Omega. 2021;6(24):15617-15624. CrossRef PubMed
21. Dallakyan S, Olson AJ. Small-molecule library screening by docking with PyRx BT - chemical biology: methods and protocols. In: York SN, ed. Hempel JE, Williams CH. 2015:243-250, CrossRef
22. Tian W, Chen C, Lei X, et al. CASTp 3.0: computed atlas of surface topography of proteins. Nucleic Acids Res. 2018;46(W1):W363-W367. CrossRef PubMed
23. Daina A, Michielin O, Zoete V. SwissADME: a free web tool to evaluate pharmacokinetics, drug-likeness and medicinal chemistry friendliness of small molecules. Sci Rep. 2017;7(1):42717. CrossRef PubMed
24. Lipinski CA. Lead- and drug-like compounds: the rule-of-five revolution. Drug Discov Today Technol. 2004;1(4):337-341. CrossRef PubMed
25. Enmozhi SK, Raja K, Sebastine I, et al. Andrographolide as a potential inhibitor of SARS-CoV-2 main protease: an in silico approach. J Biomol Struct Dyn. 2021;39(9):3092-3098. CrossRef PubMed
26. Banerjee P, Eckert AO, Schrey AK, et al. ProTox-II: a webserver for the prediction of toxicity of chemicals. Nucleic Acids Res. 2018;46(W1):W257-W263. CrossRef PubMed
27. Löw P, Saller H. (1988). PETRA: Software Package for the Calculation of Electronic and Thermochemical Properties of Organic Molecules. In: Jochum C, Hicks MG, Sunkel J. (eds)

Physical Property Prediction in Organic Chemistry. Springer, Berlin, Heidelberg. CrossRef
28. Jelić D, Lower-Nedza AD, Brantner AH, et al. Baicalin and baicalein inhibit Src tyrosine kinase and production of IL-6. J Chem. 2016;2016:2-7. CrossRef
29. de Oliveira MR, Nabavi SF, Habtemariam S, Erdogan Orhan I, Daglia M, Nabavi SM. The effects of baicalein and baicalin on mitochondrial function and dynamics: A review. Pharmacol Res. 2015;100:296-308. CrossRef PubMed
30. Zhu W, Jin Z, Yu J, et al. Baicalin ameliorates experimental inflammatory bowel disease through polarization of macrophages to an M2 phenotype. Int Immunopharmacol. 2016;35:119-126. CrossRef PubMed
31. Zhang J, Teng C, Li C, et al. Deliver anti-inflammatory drug baicalein to macrophages by using a crystallization strategy. Front Chem. 2020;8(September):787. CrossRef PubMed
32. Zhang X, Tian H, Wu C, et al. Effect of baicalin on inflammatory mediator levels and microcirculation disturbance in rats with severe acute pancreatitis. Pancreas. 2009;38(7):732-738. CrossRef PubMed
33. Lei, L, Liu WY, Feng F, et al. Synthesis and in vitro cytotoxicity evaluation of baicalein amino acid derivatives. Chin J Nat Med. 2013;11(3):284-288. CrossRef PubMed
34. Chen DZ, Yang J, Yang B, et al. Total synthesis of baicalein. J Asian Nat Prod Res. 2010;12(2):124-128. CrossRef PubMed
35. Williams IS, Chib S, Nuthakki VK, et al. Biotransformation of chrysin to baicalein: selective C6-hydroxylation of 5,7-dihydroxyflavone using whole yeast cells stably expressing human CYP1A1 enzyme. J Agric Food Chem. 2017;65(34):7440-7446. CrossRef PubMed
36. Zhao Q, Cui MY, Levsh O, et al. Two CYP82D enzymes function as flavone hydroxylases in the biosynthesis of root-specific 4′-deoxyflavones in Scutellaria baicalensis. Mol Plant. 2018;11(1):135-148. CrossRef PubMed
37. Huang WH, Chien PY, Yang CH, et al. Novel synthesis of flavonoids of Scutellaria baicalensis Georgi. Chem Pharm Bull (Tokyo). 2003;51(3):339-340. CrossRef PubMed
38. Pakyari M, Farrokhi A, Maharlooei MK, et al. Critical role of transforming growth factor beta in different phases of wound healing. Adv Wound Care (New Rochelle). 2013;2(5):215-224. CrossRef PubMed
39. Nong X, Rajbanshi G, Chen L, et al. Effect of artesunate and relation with TGF-β1 and SMAD3 signaling on experimental hypertrophic scar model in rabbit ear. Arch Dermatol Res. 2019;311(10):761-772. CrossRef PubMed
40. Zhang T, Wang XF, Wang ZC, et al. Current potential therapeutic strategies targeting the TGF-β/Smad signaling pathway to attenuate keloid and hypertrophic scar formation. Biomed Pharmacother. 2020;129:110287. CrossRef PubMed
41. Gauglitz GG. Management of keloids and hypertrophic scars: current and emerging options. Clin Cosmet Investig Dermatol. 2013;6:103-114. CrossRef PubMed
42. Wei F, Nian Q, Zhao M, et al. Natural products and mitochondrial allies in colorectal cancer therapy. Biomed Pharmacother. 2023;167:115473. CrossRef PubMed
43. Zhang T, Deng W, Deng Y, et al. Mechanisms of ferroptosis regulating oxidative stress and energy metabolism in myocardial ischemia-reperfusion injury and a novel perspective of natural plant active ingredients for its treatment. Biomed Pharmacother. 2023;165:114706. CrossRef PubMed
44. Roy MK, Nakahara K, Na TV, et al. Baicalein, a flavonoid extracted from a methanolic extract of Oroxylum indicum inhibits proliferation of a cancer cell line in vitro via induction of apoptosis. Pharmazie. 2007;62(2):149-153. CrossRef PubMed
45. Wang J, Wu Z, Peng J, et al. Multiple roles of baicalin and baicalein in the regulation of colorectal cancer. Front Pharmacol. 2024;15(February):1264418. CrossRef PubMed
46. Abdellattif MH, Elkamhawy A, Hagar M, et al. Novel saccharin analogs as promising antibacterial and anticancer agents: synthesis, DFT, POM analysis, molecular docking, molecular dynamic simulations, and cell-based assay. Front Pharmacol. 2022;13:958379. CrossRef PubMed
47. Gour PB, Ahmed S, Gajendhiran R, et al. Design, synthesis, and biological evaluation of benzo[d]oxazole-2-thio and oxazolo[4,5-b]pyridine-2-thio derivatives: molecular docking, POM analysis, in silico pharmacokinetics, and pharmacophore insights for antitumor, GPCR, and kinase targets. J Mol Struct. 2025;1333:141705. CrossRef
48. Lee CC, Tsai CH, Chen CH, et al. An updated review of the immunological mechanisms of keloid scars. Front Immunol. 2023;14:1117630. CrossRef PubMed
49. Alonso PE, Rioja LF, Pera C. Keloids: a viral hypothesis. Med Hypotheses. 2008;70(1):156-166. CrossRef PubMed
50. Xiang H, Lei H, Liu Z, et al. Network pharmacology and molecular docking analysis on molecular targets: mechanisms of baicalin and baicalein against hyperuricemic nephropathy. Toxicol Appl Pharmacol. 2021;424:115594. CrossRef PubMed
51. Wang W, Zhang Y, Yang Y, et al. Network pharmacology and molecular docking to explore the mechanism of Kangxian decoction for epilepsy. Evid Based Complement Alternat Med. 2022;2022:3333878. CrossRef PubMed
52. Farias SAS, Rocha KML, Nascimento ÉCM, et al. Docking and electronic structure of rutin, myricetin, and baicalein targeting 3CLpro. Int J Mol Sci. 2023;24(20):15113. CrossRef PubMed

DTI
Drug Target Insights 2025; 19: 59-70
ISSN 1177-3928 | DOI: 10.33393/dti.2025.3562
ORIGINAL RESEARCH ARTICLE

The Bushenhuoxue formula improves prothrombotic state in recurrent spontaneous abortion: network pharmacology and experimental validation

Xuan Yang[1], Shulan Su[2], Lijing Liu[3], Pan Liu[4], Maoqing Lu[5], Yinuo Wei[5], Yaqiong Gao[1]

[1]Department of Gynecology, Shanghai University of Traditional Chinese Medicine affiliated Shuguang Hospital Anhui Hospital, Anhui, Hefei - China
[2]Jiangsu Provincial Key Laboratory of Prescription High Technology Research, Nanjing University of Traditional Chinese Medicine, National and Local Joint Engineering Research Center for the Industrialization of Traditional Chinese Medicine Resources and Innovative Prescriptions, Jiangsu Province Traditional Chinese Medicine Resource Industrialization Process Collaborative Innovation Center, Nanjing, Jiangsu - China
[3]Department of Gynecology, Wuxi Traditional Chinese Medicine Hospital, Wuxi, Jiangsu - China
[4]Department of Emergency Medicine, Shanghai University of Traditional Chinese Medicine affiliated Shuguang Hospital Anhui Hospital, Anhui, Hefei - China
[5]Clinical Medicine of Traditional Chinese and Western Medicine, Anhui University of Traditional Chinese Medicine, College of Integrated Traditional Chinese and Western Medicine, Anhui, Hefei - China

ABSTRACT

Introduction: Bushenhuoxue formula is a traditional Chinese medicine formula with relatively safe clinical effects, but its mechanism in recurrent spontaneous abortion (RSA) is still unclear. Our present study used Network pharmacology an experimental validation to discuss how Bushenhuoxue formula improves prethrombotic state in RSA.
Materials and methods: The active ingredients of Bushenhuoxue formula (Drug) were acquired from our previous study. The putative targets of ZYP relevant to AS were obtained from TCMSP, Swiss Target Prediction, STITCH, DisGeNET, and Gene Cards databases. Protein-protein interactions (PPI) network, Gene Ontology (GO), and Kyoto Encyclopedia of Genes and Genomes (KEGG) analysis were conducted using the Cytoscape software. Furthermore, *in vivo* experiments were carried out for target validation in BALB/c mice, collecting placental tissue from different groups, the cell apoptosis by TUNEL assay; the pathology by HE staining; relative mRNA expression by qRT-PCR assay; relative protein expression by IHC and WB assay.
Results: Animal experiments, compared with the NC group, the AT-III, PROG, HCG, APC and t-PA concentrations were significantly depressed (P<0.05, respectively), Apoptosis cell numbers were significantly up-regulated with PI3K/AKT/HIF-1α VEGF significantly depressing (P<0.001, respectively). With Bushenhuoxue formula supplement, AT-III, PROG, HCG, APC and t-PA concentrations were significantly improved in RSA model mice; and improved pathological changes and apoptosis cell number in placenta tissues (P<0.05, respectively). However, with LY294002 supplement, the drug treatment effects were disappeared.
Conclusion: Bushenhuoxue formula improves prethrombotic state in RSA *via* stimulating PI3K/AKT/HIF-1α/VEGF pathway *in vivo.*

Keywords: Bushenhuoxue Formula, RAS, PI3K, AKT, Network Pharmacology

Introduction

Recurrent spontaneous abortion (RSA) refers to the occurrence of two or more consecutive natural miscarriages before the 20th week of pregnancy in women of reproductive age with no changes in sexual partners (1). Despite extensive research, our knowledge of the etiology of RSA remains limited, involving factors such as immune factors, endocrine factors, genetic disorders, congenital uterine developmental abnormalities, infections and coagulation function anomalies, with immune irregularities emerging as a prominent contributor (2). The disruption of the immune equilibrium due to abnormal inflammatory responses at the maternal-fetal interface is significant in fetal loss. Notably, macrophages, the principal immunoactive cells in the uterine milieu, play a crucial role in regulating the uterine immune microenvironment and mediating inflammatory responses (3). Macrophages can polarize into M1 and M2 phenotypes based on microenvironmental cues, and skewed polarization at any stage may lead to spontaneous abortion (4,5).

In recent years, the rising incidence of RSA has markedly impacted the well-being of women of reproductive age. The specific pathogenesis of RSA is not yet clear. Positive

Received: April 16, 2025
Accepted: July 14, 2025
Published online: August 19, 2025

This article includes supplementary material.

Corresponding author:
Shulan Su
email: sushulan1975@126.com

antiphospholipid antibodies are currently known immune factors related to RSA, which can affect the body's coagulation state, thrombosis, cause fetal hypoxia and death, leading to RSA (6). The treatment of Western medicine for antiphospholipid antibody positive RSA mainly focuses on anti-thrombosis, immunosuppression, and other aspects. In clinical practice, drugs such as aspirin and progesterone are often used for treatment, but their effectiveness in treating antiphospholipid antibody positive RSA is limited, and there are still problems such as low success rates of delivery (7). At present, there is no clear evidence to indicate which treatment plan is optimal for the treatment of anti-phospholipid antibody positive RSA. It is urgent to explore an efficient treatment plan for anti-phospholipid antibody positive RSA.

A previous study indicated that Bushenhuoxue formula, might enhance the condition of miscarriage-prone mice by regulating uterine and placental vasculature (8). Furthermore, the Bushenhuoxue formula has demonstrated potential in improving RSA to some extent (9). Nevertheless, the impact and underlying mechanisms of the Bushenhuoxue formula on the prothrombotic state of RSA require further elucidation. To address this gap in knowledge, the present study used network pharmacology theory and molecular docking technology to uncover the effective chemical constituents of the Bushenhuoxue formula and clarify its mechanisms involved in improving RSA. Additionally, the present study established a positive anticardiolipin antibody (ACA) mouse model of RSA, delving into the therapeutic effects and associated mechanisms of the Bushenhuoxue formula on the prothrombotic state in ACA-positive RSA mice.

Materials and methods

Network pharmacology approach

Overlapping targets between the Bushenhuoxue formula and RSA. The eight constituents of the Bushenhuoxue formula were input into the TCM Systems Pharmacology Database and Analysis Platform (TCMSP, Online). The set criteria were as follows: Oral bioavailability (OB), ≥30%; drug-likeness (DL), ≥0.18 and defaults for others to retrieve information for each constituent. Canonical SMILES data from the PubChem database (Online) were used to predict corresponding targets of every constituent in the SwissTargetPrediction database (Online) with parameters 'Homo sapiens' and probability, ≥0 to filter duplicate targets. The GeneCards database (Online) with a relevance score, ≥5 was used to identify disease-associated targets using the keyword 'RSA'. The intersection of Bushenhuoxue formula constituent targets and RSA-related targets were identified to obtain potential targets of the Bushenhuoxue formula for RSA treatment.

Construction of the 'constituent-disease target' network. The chemical constituents of the Bushenhuoxue formula and the shared targets obtained in the previous step were imported into Cytoscape (version 3.9.0) (Online). The 'constituent-disease target' network was then established. The CytoNCA tool within the Cytoscape software was used to compute degree, betweenness centrality and closeness centrality for every constituent. Chemical constituents with strong interactions with disease-related targets were identified based on centrality measurements.

Construction of the protein-protein interaction (PPI) network. The previously obtained intersected targets were input into the STRING database (Online). The settings 'multiple proteins', species 'Homo sapiens' were configured. The relevant data were then extracted and imported into Cytoscape. The CytoNCA tool was used to calculate degree, betweenness centrality and closeness centrality for every target and identify significant targets within the PPI network.

Gene ontology (GO) enrichment analysis and Kyoto Encyclopedia of Genes and Genomes (KEGG) pathway analysis of shared targets. GO and KEGG enrichment analyses were conducted using the database for annotation, visualization and integrated discovery (DAVID; Online). The GO enrichment analysis encompassed three categories: i) Biological processes (BPs); ii) molecular functions (MFs); and iii) cellular components (CCs). The results of the analyses were visualized using a bioinformatics platform (Online).

Laboratory animals. 36 BALB/c pregnant mice aged 8 weeks, with an average weight of 25±2 g, were obtained from the Animal Core Facility of Nanjing Medical University with a male-to-female ratio of 2:1.

Bushenhuoxue formula and reagents. Bushenhuoxue formula is comprised of Tu Si Zi (*Cuscutae semen*), Sang Ji Sheng (*Taxilli herba*), Xu Duan (*Dipsaci radix*), Dang Shen (*Codonopsis radix*), Bai Zhu (*Atractylodis macrocephalae* rhizoma), Dang Gui (*Angelicae sinensis radix*), Dan Shen (*Salviae miltiorrhizae radix*) and Chuan Xiong (Chuanxiong rhizoma) as granules prepared by Sichuan New Green Pharmaceutical Technology Development Co., Ltd., and was purchased from the West Branch of the First Affiliated Hospital of Anhui University of Chinese Medicine. Human β2-GP I (p2-glycoprotein-I) was obtained from Prospec-Tany TechnoGene, Ltd. PI3K, phosphorylated (p)-PI3K), AKT, p-AKT, CD31, CD34, HIF-1α, VEGF and GAPDH were purchased from Abcam. The anticardiolipin antibody (IgG) kit was sourced from Shanghai Lianshuo Biological Technology Co. Ltd (Online). LY294002 was acquired from Sigma-Aldrich and Merck KGaA.

Modeling (10). Human β2-GP-1 was dissolved in sterile PBS to achieve a concentration of 100 µg/0.25 mL. On day 1, an injection of a solution containing human β2-GP-1 and Complete Freund's Adjuvant (CFA) was administered in a 1:1 ratio (50 µL). On day 8, incomplete Freund's Adjuvant (IFA) instead of CFA was used for booster immunization (50 µL human β2-GP-1 solution mixed with IFA in a 1:1 ratio). On day 18, female and male mice were co-housed in a 2:1 ratio, and the observation of vaginal plugs was counted as day 0 of pregnancy. On day 15 of pregnancy, the pregnant mice were euthanized, their eyeballs were collected for blood sampling, and the embryo resorption rate was calculated. The placental tissue was fixed with 4% paraformaldehyde and then paraffin sections were prepared for standard pathology, TUNEL and immunohistochemical testing, while fresh placental tissue was stored at -80ºC for reverse transcription-quantitative PCR (RT-qPCR) and western blotting. Blood samples were allowed to stand at room temperature for 10 min before centrifugation at 3,000 x g for 10 min at 4°C; the supernatant was collected and stored at -20°C. Aseptic dissection was immediately performed to examine, weigh and photograph the uteri and ovaries. Finally, the tissues were isolated and rapidly placed in liquid nitrogen for storage at -80°C.

The negative control (NC) group consisted of mice undergoing normal mating and giving birth. The model, model + Bushenhuoxue formula, and model + Bushenhuoxue formula + LY294002 groups were established using the aforementioned RSA modeling procedure. In the model + Bushenhuoxue formula group, each pregnant mouse was orally administered Bushenhuoxue formula at a dose of 0.5 g (11). In the model + Bushenhuoxue formula + LY294002 group, pregnant mice were administered the same dose of Bushenhuoxue formula orally and concurrently injected with 8.0 mg/kg LY294002 (12).

The present study was approved by the Ethics Committee of Anhui Province Integrated Traditional Chinese and Western Medicine Hospital (approval no. 2022102351).

Hematoxylin and eosin (H&E) staining of placental tissues. On day 12 of pregnancy, fasting for 12 h was followed by intraperitoneal injection of 2% pentobarbital sodium (40 mg/kg) the following day by anesthesia. After anesthesia, euthanasia was performed on pregnant mice using the cervical dislocation method, and placental tissues were collected and processed through fixation, dehydration, embedding, sectioning, deparaffinization, H&E staining and rinsing for 1-20 min. Subsequent differentiation involved treating sections with 1% hydrochloric acid alcohol for 5-10 sec, followed by rinsing. Bluing was accomplished using ammonia water for 5-10 sec and staining with 0.5% eosin solution for 3-5 min. After rinsing, the sections underwent dehydration, clearing, mounting and imaging using a light microscope.

Immunofluorescence (IF) staining for CD31, CD34, HIF-1α and VEGF expression in placental tissues. Placental tissues from every group of pregnant mice were embedded in paraffin, and subsequent deparaffinization was carried out through ethanol-water cycles, alternating boiling and cooling in 5-min intervals, repeated twice. Sections were subsequently washed three times with PBS for 5 min, blocked at room temperature for 30 min, exposed to primary antibodies (CD31, 1:500, ab28364, Abcam; CD34,1:500, ab8158, Abcam; HIF-1*α*, 1:500, ab16066, Abcam; VEGF, 1:500, ab115805, Abcam) overnight at 4°C, washed three times with PBS for 5 min, incubated with Alexa Fluor 594-conjugated goat anti-rabbit secondary antibody (ImmunoWay Biotechnology Company) at 37°C for 30 min, subjected to DAPI staining for 10 min at room temperature, washed again three times with PBS for 5 min, and finally mounted. Images of placental tissues were captured using an Olympus fluorescence microscope (Olympus) and analyzed using ImageJ 1.51k software (National Institutes of Health).

Calculation of embryo loss rate. The total embryo count, viable embryo count and miscarried embryo count were recorded to calculate the embryo loss rate. The embryo loss rate (ELR) was determined using the equation: ELR (%) = (number of miscarried embryos)/(number of miscarried embryos + number of viable embryos) x 100%.

Enzyme-linked immunosorbent assay (ELISA). Frozen serum samples were thawed, and ELISA assays were conducted as per the provided kit instructions (AT-III ELISA kit, ml025687, Mlbio; PROG ELISA kit, ml057583, Mlbio; HCG ELISA kit, ml024543, Mlbio; E2 ELISA kit, ml002009, Mlbio; t-PA ELISA kit, ml037187, Mlbio; APC ELISA kit, APC ELISA kit, ml002190, Mlbio). Standard samples and serum were added to designated wells. After successive steps involving incubation, washing, antibody addition and subsequent incubation, color development occurred. Optical density was measured at 450 nm using a microplate reader. Serum concentrations of PROG (progesterone), HCG (human chorionic gonadotropin), E2 (estradiol), AT-III (antithrombin III), t-PA (tissue plasminogen activator) and APC (activated protein C) are derived from the standard curve.

Western blotting. Proteins were extracted from placental tissues using the BCA method to enable quantification. A 10% SDS-PAGE gel was prepared, followed by electrophoresis and subsequent wet transfer to a membrane. The membrane was blocked with 5% skim milk for 2 h, after which it was incubated with primary antibodies, including PI3K (1:1,000, catno. ab283852; Abcam), AKT (1:1,000, catno. ab8805, Abcam), *p*-PI3K (1:1,000, catno. ab 278545, Abcam), *p*-AKT (1:1,000 catno. ab38449, Abcam), HIF-1*α* (1:1,000, catno. ab308637, Abcam), VEGF (1:1,000, catno.ab 315238, Abcam), and GAPDH (1:1,000, catno. ab313650, Abcam) overnight at 4ºC. The next day, the membrane underwent washing with 1X TBS-0.1% Tween-20 (cat. no. 9997; Cell Signaling Technology, Inc.), followed by incubation with secondary antibodies (1:2,000) for 1 h with gentle agitation. This was succeeded by an additional 2-h incubation at room temperature. After thorough washing, visualization was achieved through exposure to enhanced chemiluminescence reagents. Band intensities were analyzed using ImageJ, with GAPDH used as the internal control.

RT-qPCR. Frozen placental tissue samples (20 mg) were pulverized using liquid nitrogen. Total RNA was extracted using the TRIzol reagent. Following RNA quantification (1 μg), cDNA synthesis was conducted using a RT kit. qPCR took place using the amplification kit and the following thermocycling conditions: 95°C pre-denaturation for 30 sec, denaturation at 95°C for 5 sec and annealing at 60°C for 30 sec, totaling 40 cycles. The relative expression level of the target gene was computed using the $2^{-\Delta\Delta Ct}$ method (13) with GAPDH serving as the reference gene. Primer sequences were provided by Beijing Lainuo BioTech Co., Ltd (Table 1).

TABLE 1 - Primer sequence

Gene Name	F:(5'-3')	R:(5'-3')
PI3K	ACGACTACAAGAAGGAGCGAG	CAGCCAATATCTTCAGGCCG
AKT	GGACAACCGCCATCCAGACT	GCCAGGGACACCTCCATCTC
HIF-1α	GGATGAGTTCTGAACGTCGAAAAG	ACATTGTGGGGAAGTGGCAA
VEGF	ATGAACTTTCTGCTGTCTTGG	TCACCG CCTCGGCTTGTCACA
U6	CTCGCTTCGGCAGCACA	AACGCTTCACGAATTTGCGT
GAPDH	GGTGAAGGTCGGTGTGAACG	GCTCCTGGAAGATGGTGATGG

TUNEL staining. Paraffin-embedded placental tissues were sectioned to 5-µm-thick slices on glass slides after fixation in 4% paraformaldehyde. TUNEL fluorescence detection was carried out according to the manufacturer's instructions. After PBS buffer washing, cell nuclei were re-stained with DAPI. Slides were incubated at room temperature for 2 min before mounting. The sections were observed and imaged using a fluorescence microscope and TUNEL$^+$ cells were counted.

Statistical analysis. SPSS (version 23.0; IBM Corp.) was used for statistical analysis. Normally distributed measurement data were presented as mean ± standard deviation. Group comparisons were conducted through analysis of variance, and homogeneity of variance was determined using the LSD test for equal variances or the Games-Howell test for unequal variances. P<0.05 was considered to indicate a statistically significant difference.

Results

Network pharmacology. The GSE26787 dataset encompassed gene data from five RSA placental tissues and five placental tissues from normal deliveries. Subsequent analysis unveiled a total of 2,169 differentially expressed genes. Among these, 1,061 genes were underexpressed in RSA placental tissues, while 1,108 genes were overexpressed. A volcano plot was generated accordingly (Fig. 1A), and the top 20 genes with the most significant differential expression in both categories were selected for further investigation. To visually represent these findings, a heatmap was plotted (Fig. 1B). Through the GeneCards database analysis, it was identified that 2,169 targets were linked to RSA, while 195 targets were connected to the efficacious components of the Bushenhuoxue formula. Among these, 20 targets were identified as shared between Bushenhuoxue formula constituents and the disease (Fig.2). Relative data including active ingredient, targeting gene loci and disease targeting gene loci were collected. A 'Drug constituent-shared target' network was built using Cytoscape (Fig. 3). The CytoNCA tool was used to compute the degree, betweenness centrality, and closeness centrality of the targets, thereby pinpointing the most pivotal components (Fig. 3). The interactions among the 20 shared targets were elucidated by STRING database analysis (https://www.string-db.org/; version 11.5), and the outcomes were depicted *via* Cytoscape, resulting in the creation of a PPI network (Fig. 4). As revealed by the PPI network analysis, the PI3K target exhibited the greatest potential for therapeutic intervention. DAVID was used to conduct GO functional enrichment analysis, and the significance threshold was set at P<0.05. The top 20 entries with the highest gene counts are shown in Fig. 5. For BP, the most prominent term was 'regulation of response to wounding'. In terms of CC, a significant association was observed with 'plasma membrane raft', while MF was primarily linked to 'steroid binding'. KEGG pathway enrichment analysis was conducted using DAVID with a significance threshold of P<0.05. A total of 22 enriched pathways were identified and ranked by gene count (Fig. 6). The five most enriched pathways were 'cellular senescence', 'chemical carcinogenesis - receptor activation', 'p53 signaling pathway', 'HIF-1 signaling pathway'and 'linoleic acid metabolism'.

Intergroup comparison of embryo loss rates. Compared with the NC group, the model group exhibited a significantly increased embryo loss rate (P<0.05). By contrast, the model + Bushenhuoxue formula group demonstrated a significant reduction in embryo loss rate compared with the model group (P<0.05). However, when simultaneous LY294002 intervention was introduced, the model + Bushenhuoxue formula + LY294002 group displayed a significant increase in embryo loss rate compared with the model + Bushenhuoxue formula group (P<0.05; Table 2).

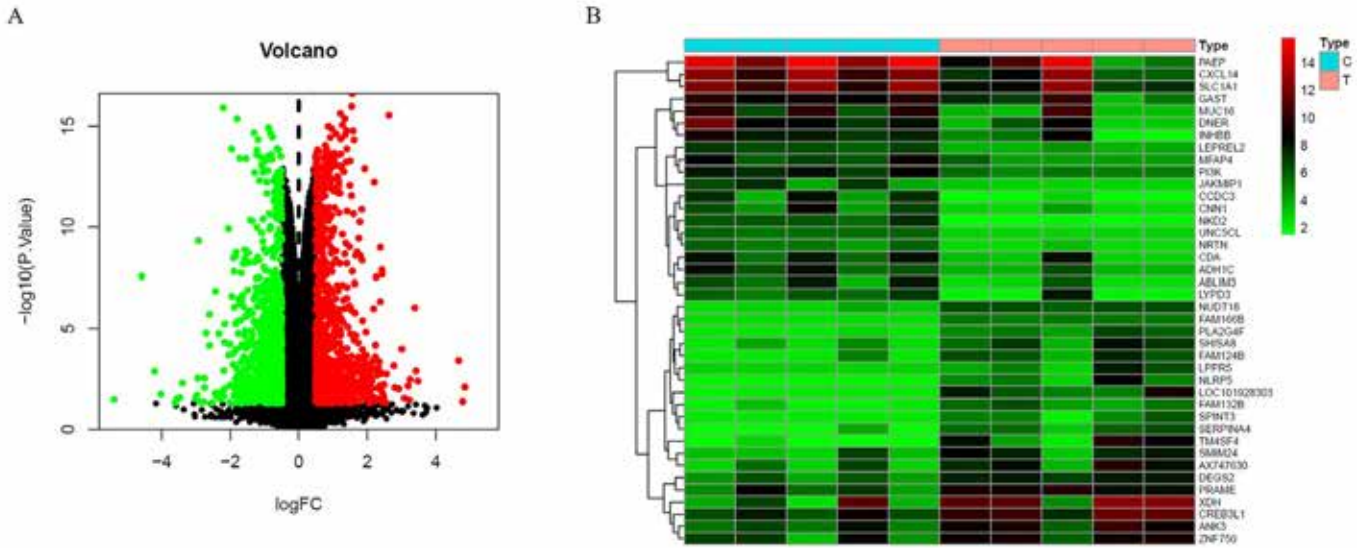

FIGURE 1 - Differential gene expression analysis in RSA. (A) volcano plot and (B) heart map.

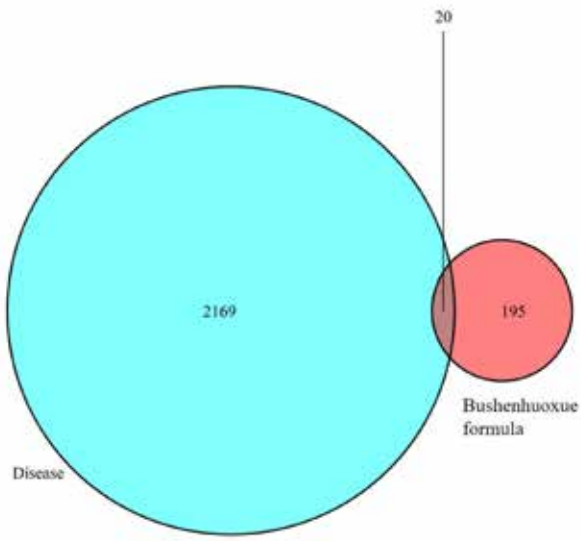

FIGURE 2 - Intersection of Bushenhuoxue formula constituent targets and RSA-related targets. RSA, recurrent spontaneous abortion.

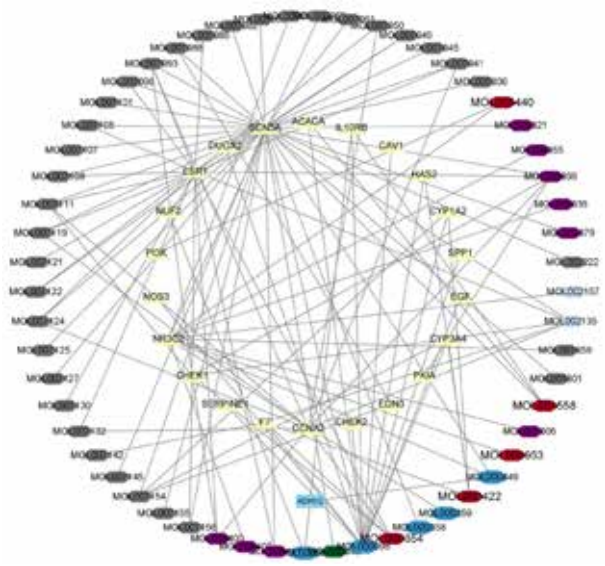

FIGURE 3 - Analysis of Bushenhuoxue formula constituent-target network.

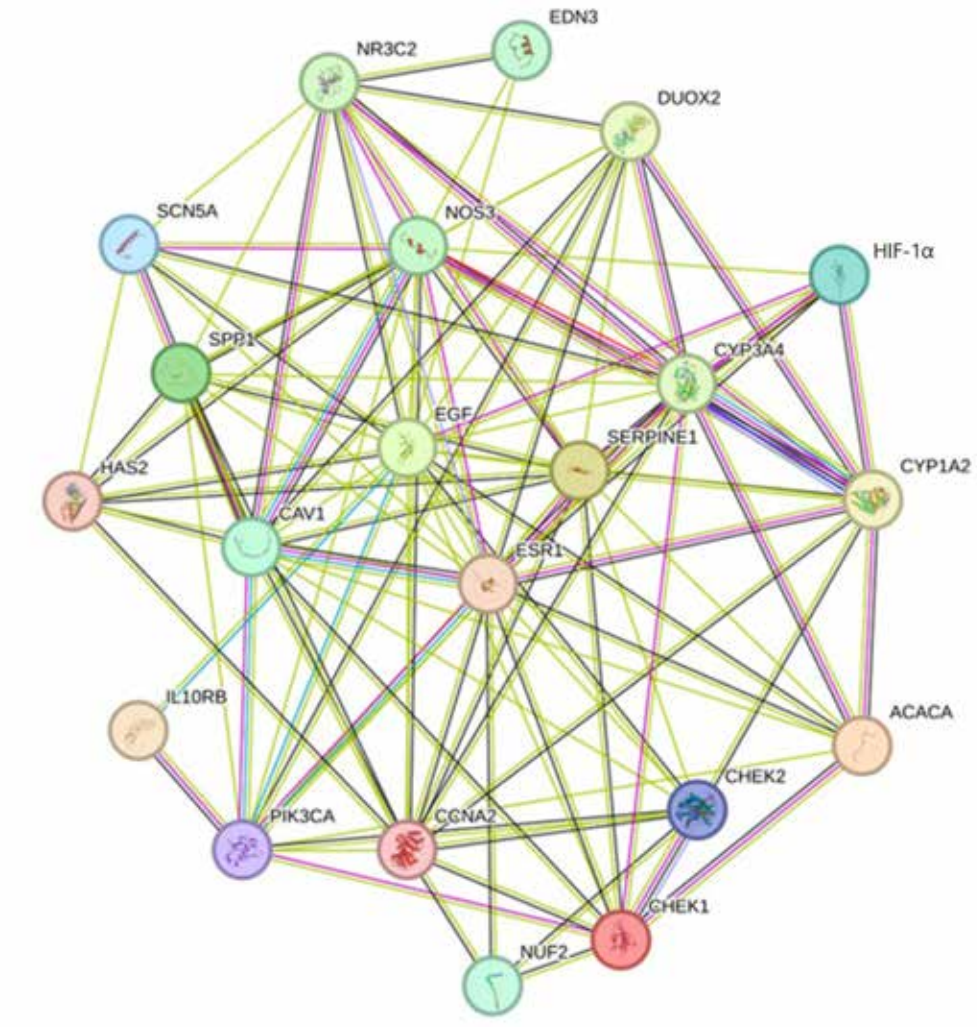

FIGURE 4 - Protein-protein interaction network analysis of shared target interactions.

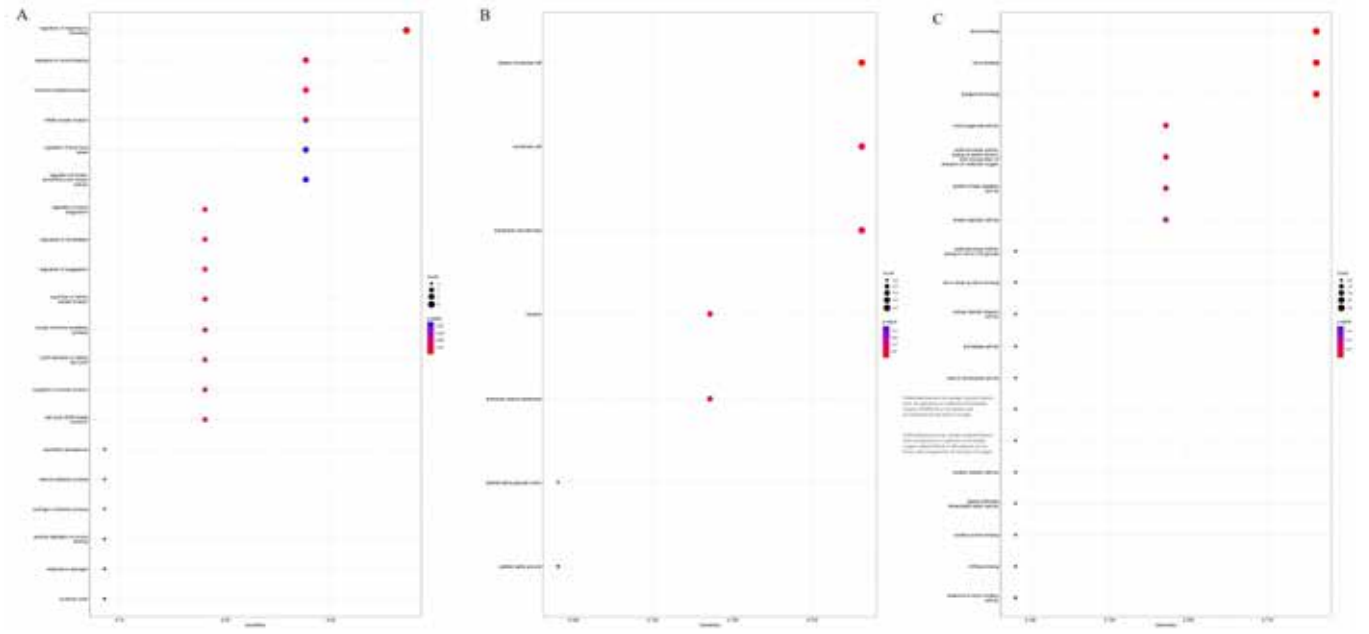

FIGURE 5 - Enrichment analysis of shared targets in Gene Ontology terms. (A) BP, (B) CC and (C) MF. BP, biological process; MF, molecular function; CC, cellular component. (Also available as supplementary figure A).

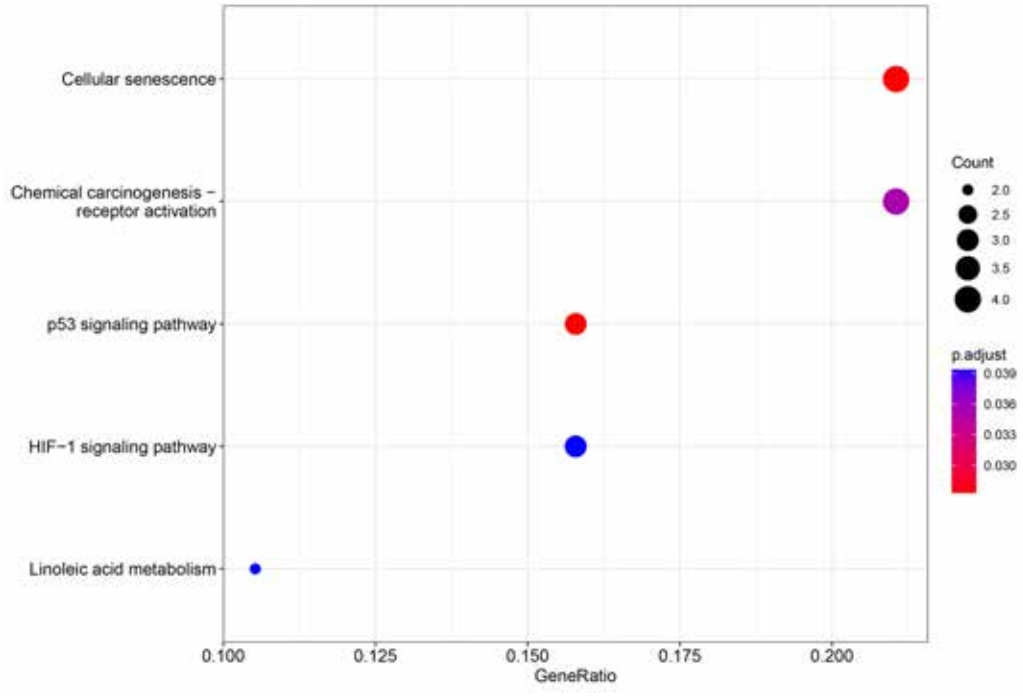

FIGURE 6 - Kyoto Encyclopedia of Genes and Genomes enrichment analysis of shared targets.

TABLE 2 - Comparison of embryo loss rate in each group (Mean±SD, n = 9)

Group	Total number of embryos	Number of aborted embryos	ELR(%)
NC	54	5	5.76±4.84
Model	86	23	25.95±8.54*
Model+Drug	81	12	10.57±6.19#
Model+Drug+LY294002	85	22	24.95±7.16@

*:P<0.05, compared with NC; #: P<0.05, compared with Model; @: P<0.05, compared with Model+Drug

Intergroup comparison of serum hormone levels and coagulation factor levels. In comparison with the NC group, the model group exhibited a significant decrease in the serum levels of AT-III, t-PA, P, APC and HCG (all P<0.05; Fig. 7). Conversely, the model + Bushenhuoxue formula group demonstrated significantly elevated levels of serum AT-III, t-PA, P, APC and HCG compared with the model group (all P<0.05; Fig. 7). Notably, with the administration of LY294002, the model + Bushenhuoxue formula + LY294002 group exhibited a significant rise in the serum levels of AT-III, t-PA, P, APC and HCG compared with the model + Bushenhuoxue formula group (all P<0.05; Fig. 7).

Comparison of pathological morphological changes in placental regions. The H&E staining results (Fig. 8A) revealed distinct variations in placental tissue morphology among different groups. In the NC group, the decidua, and the syncytiotrophoblast and labyrinth layers exhibited normative structures. Compared with the NC group, the model group demonstrated partial shedding of the decidua, along with syncytiotrophoblast necrosis characterized by diminished numbers, focal necrosis in the labyrinth layer and notable infiltration of inflammatory cells. By contrast, the model + Bushenhuoxue formula group presented well-defined structures across all placental layers, featuring only focal necrosis in the labyrinth layer and minimal inflammatory cell infiltration. Notably, other structures displayed no significant pathological changes. However, concurrent administration of LY294002 nullified the therapeutic effects of the Bushenhuoxue formula.

Comparison of changes in apoptosis of placental tissues. Evaluation of TUNEL staining outcomes disclosed that compared with the NC group, the model group exhibited a significant increase in TUNEL$^+$ apoptotic cells (P<0.05; Fig. 8B). Introducing Bushenhuoxue formula intervention, the model + Bushenhuoxue formula group showcased a significant reduction in the number of TUNEL$^+$ apoptotic cells compared with the model group (P<0.05; Fig. 8B). Nonetheless, the simultaneous application of LY294002 yielded a marked increase in the tally of TUNEL$^+$ apoptotic cells in the model + Bushenhuoxue formula + LY294002 group compared with the model + Bushenhuoxue formula group (P<0.05; Fig. 8B).

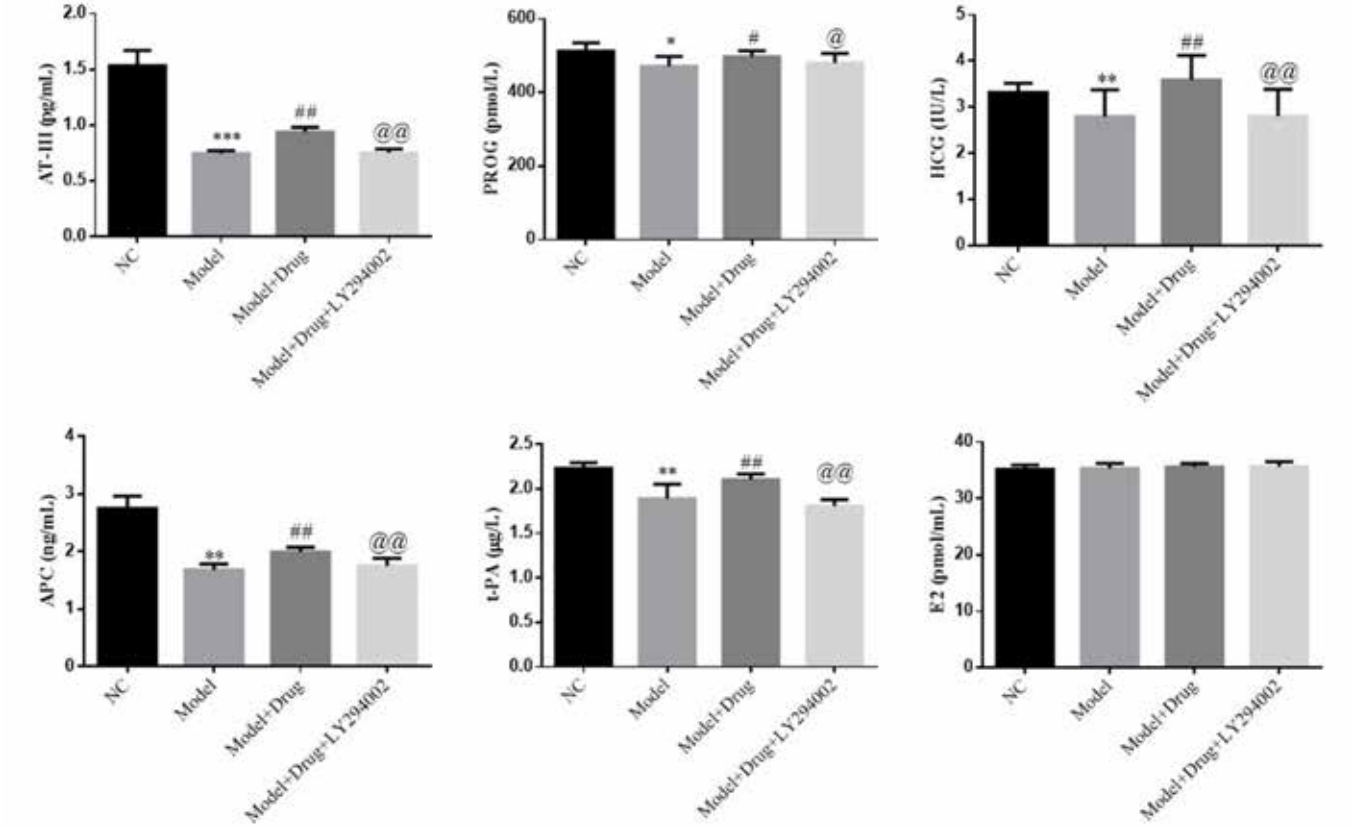

FIGURE 7 - Intergroup comparison of serum hormone levels and coagulation factor levels.
*P<0.05, **P<0.01, ***P<0.001, compared with the NC group; #P<0.05, ##P<0.01, compared with the model group; @P<0.05, @@P< 0.01, compared with the model + Bushenhuoxue formula group. NC, negative control

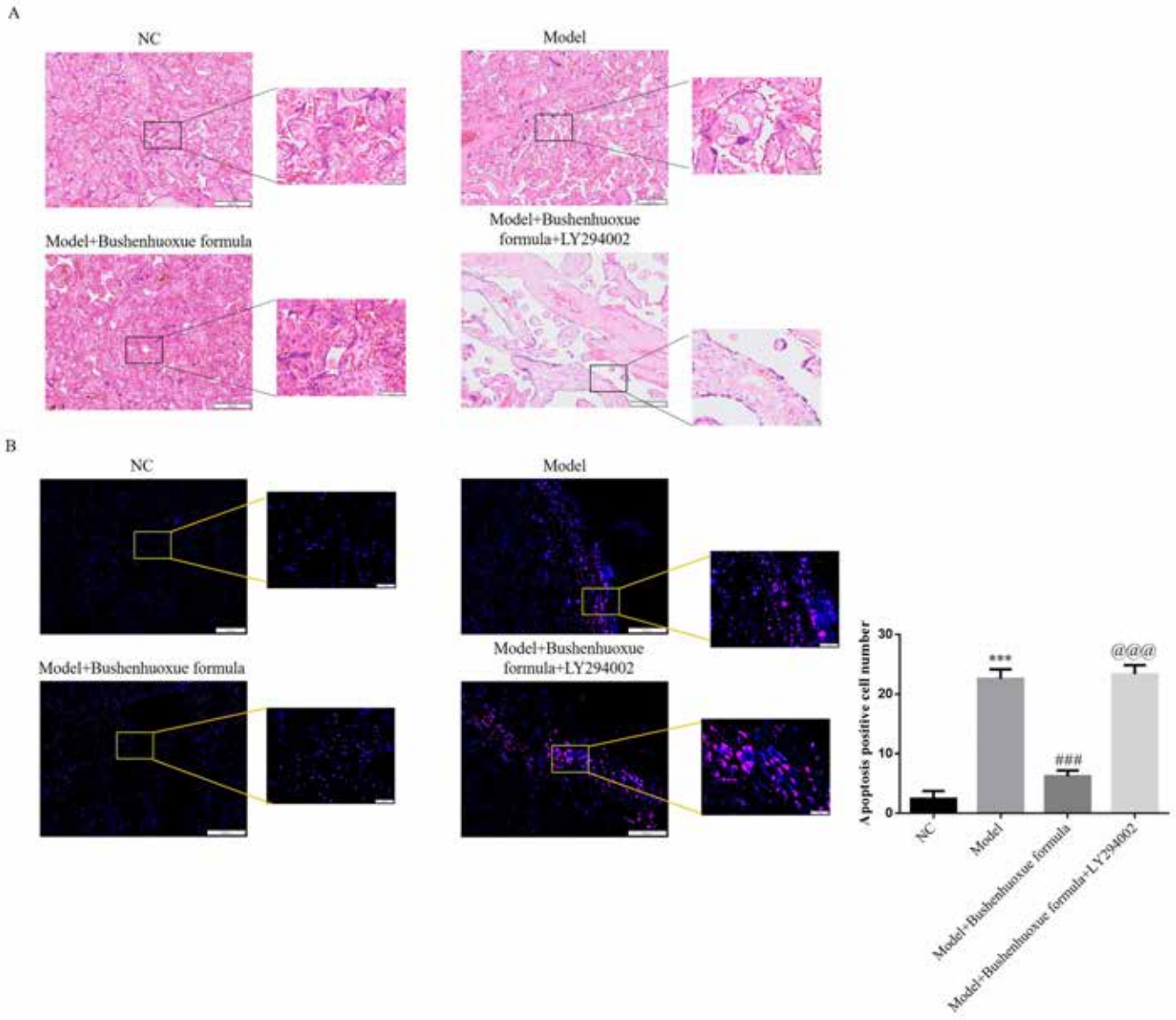

FIGURE 8 - Pathological changes in each group.
A. Comparison of pathological morphological changes in placental regions using H&E staining (magnification, x100; scar bar, 200μm; magnification, x400; scar bar, 200μm); B. Comparison of changes in apoptosis of placental tissues using TUNEL assay (magnification, x100; scar bar, 200μm; magnification, x400; scar bar, 200μm). ***P<0.001, compared with the NC group; ###P<0.001, compared with the model group; @@@P<0.001, compared with the model + Bushenhuoxue formula group. NC, negative control

Comparison of CD31 and CD34 protein expression in placental tissues. IHC analysis showed that compared with the NC group, the model group exhibited significantly reduced levels of CD31 and CD34 protein expression (P<0.05; Figs. 9A and 9B). On the other hand, subsequent Bushenhuoxue formula intervention in the model + Bushenhuoxue formula group elicited significantly heightened levels of CD31 and CD34 protein expression contrary to the model group (P<0.05; Figs. 9A and 9B). The concurrent administration of LY294002 led to a significant reduction in CD31 and CD34 protein expression levels within the model + Bushenhuoxue formula + LY294002 group compared with the model + Bushenhuoxue formula group (P<0.05; Figs. 9A and 9B).

Comparison of relevant gene expression in placental tissues. RT-qPCR revealed that compared with the NC group, the model group exhibited a significant reduction in the gene expression levels of PI3K, AKT, HIF-1*α* and VEGF (all P<0.001; Fig. 9C). Subsequent intervention with Bushenhuoxue formula in the model + Bushenhuoxue formula group prompted a significant increase in the gene expression levels of PI3K, AKT, HIF-1*α* and VEGF when compared with the model group (all P<0.001; Fig. 9C). Nevertheless, simultaneous administration of LY294002 resulted in a significant decrease in the gene expression levels of PI3K, AKT, HIF-1*α* and VEGF within the model + Bushenhuoxue formula + LY294002 group compared with the model + Bushenhuoxue formula group (all P<0.001; Fig. 9C).

Comparison of relevant protein expression in placental tissues. Western blotting showed that compared with the NC group, the model group exhibited a significant decrease in the protein expression levels of *p*-PI3K/PI3K, p-AKT/AKT, HIF-1*α* and VEGF (all P<0.001; Fig. 9D). Introducing the Bushenhuoxue formula in the model + Bushenhuoxue formula group led to a significant escalation in the protein expression levels of *p*-PI3K/PI3K, *p*-AKT/AKT, HIF-1*α* and VEGF compared with the model group (all P<0.001; Fig. 9D). Nonetheless, simultaneous administration of LY294002 yielded a significant decrease in the protein expression levels of p-PI3K/PI3K, p-AKT/AKT, HIF-1*α* and VEGF within the model + Bushenhuoxue formula + LY294002 group contrary to the model + Bushenhuoxue formula group (all P<0.001; Fig. 9D).

Comparison of HIF-1α and VEGF protein expression in placental tissues. The IHC analysis showed that compared with the NC group, the model group demonstrated a significant reduction in HIF-1*α* and VEGF protein expression (P<0.001; Fig. 9E and 9F). By contrast, the administration of the Bushenhuoxue formula in the model + Bushenhuoxue formula group led to significant elevations in HIF-1*α* and VEGF protein expression compared with the model group (P<0.001; Fig. 9E and 9F). However, the concurrent administration of LY294002 resulted in a significant reduction in HIF-1*α* and VEGF protein expression levels in the model + Bushenhuoxue formula + LY294002 group compared with the model + Bushenhuoxue formula group (P<0.001; Fig. 9E and 9F).

Discussion

RSA is a prevalent reproductive disorder affecting women of childbearing age, with the etiology of 50-60% of the cases remaining ambiguous. In light of its intricate pathogenesis and the significant challenges in treatment, RSA has emerged as a notable research domain in recent years (14, 15). From the implantation of a fertilized egg to childbirth, a delicate equilibrium between heightened coagulability and augmented vulnerability to bleeding is meticulously upheld. Disturbance to this equilibrium can wield profound impacts on crucial processes, including fertilized egg implantation, establishment of pathological placenta and even miscarriage (16). The intimate nexus between ACA and RSA has gathered increasing attention. Earlier investigations predominantly ascribed the pathogenesis of ACA provoking vascular thrombosis and tissue infarction at the placental locale, resulting in harm to placental vascular epithelial cells. However, subsequent studies have shown that thrombosis alone may not be the sole causative factor (17, 18). Anti-phospholipid antibodies can engage directly with trophoblast phospholipids, triggering apoptosis, fostering coagulation cascades and inciting unbridled immune responses. These antibodies also hinder the differentiation and maturation of trophoblasts, engendering compromised syncytiotrophoblast fusion. This compromise in turn impairs HCG synthesis, curtails trophoblast invasiveness and derails uterine spiral artery remodeling, thus resulting in trophoblast impairment, apoptosis and thwarted embryo implantation (19). Our previous study showed that the Bushenhuoxue formula had effects to improve recurrent miscarriage (20). However, there were some tractions from Bushenhuoxue formula; the mechanism has been unclear, and based on the results it was decided to investigate the mechanism using network pharmacology and *in vivo* study for validation. In the present study, it was shown that the Bushenhuoxue formula had treatment effects through regulation of the PI3K/AKT pathway based on network pharmacology analysis; the data were validated through animal experiments.

The PI3K/AKT signaling pathway is a marked cellular mechanism governing the intricate orchestration of cell proliferation, apoptosis and the cell cycle (16). Activation of the PI3K/AKT pathway can enhance cell proliferation and suppress apoptosis. PI3K, positioned as a cardinal upstream molecule within the PI3K/AKT/HIF-1*α* pathway, spurs p110*α* enzyme activity through its subunit PIK3CA, thereby inciting cell growth that operates autonomously from external growth factors (21). AKT, serving as a crucial downstream effector of PI3K, and its activated variant, p-AKT, can phosphorylate an array of components closely interlinked with apoptosis, thus fostering cellular survival (22). As an ensuing cascade of the PI3K/AKT pathway (23, 24), the HIF-1*α*/VEGF signaling pathway holds promise in angiogenesis and the amelioration of hemostatic conditions (25, 26). In the current study, the methodology of network pharmacology was harnessed to dissect the plausible mechanisms underlying the influence of Bushenhuoxue formula on the prothrombotic state associated with RSA. The results cogently suggested that the formula may enact its effects through the activation of the PI3K/AKT signaling pathway. To substantiate this proposition, animal experiments were conducted, the findings of which affirmed that the formula efficaciously triggers the PI3K/AKT signaling pathway, thereby subsequently engaging the downstream HIF-1*α*/VEGF pathway. This sequence of activations ushers in elevated levels of serum AT-III, t-PA, P, APC and HCG, thereby furnishing robust protection against RSA. Furthermore, the formula was shown to mitigate trophoblast apoptosis, and escalate vascular density, as indicated by the increased CD34 and CD31 protein expression (27, 28). However, it is noteworthy that the therapeutic efficacy of the Bushenhuoxue formula rendered void in the presence of LY294002, a PI3K inhibitor .

Conclusion

The combined findings stemming from network pharmacology analysis and animal experimentation coalesce to portray that the Bushenhuoxue formula has the propensity to activate the PI3K/AKT signaling pathway. This activation curtails trophoblast apoptosis induced by RSA, while the orchestration of the downstream HIF-1*α*/VEGF pathway engenders a mitigation of the prothrombotic state and fosters vasculogenesis, thereby achieving robust fortification against RSA. There were some limitations in the present study; we just discussed the Bushenhuoxue formula's treatment effects *in vivo* study, the clearly mechanism has been unclear. In future research, this limitation will be addressed by carrying out *in vitro* experiments.

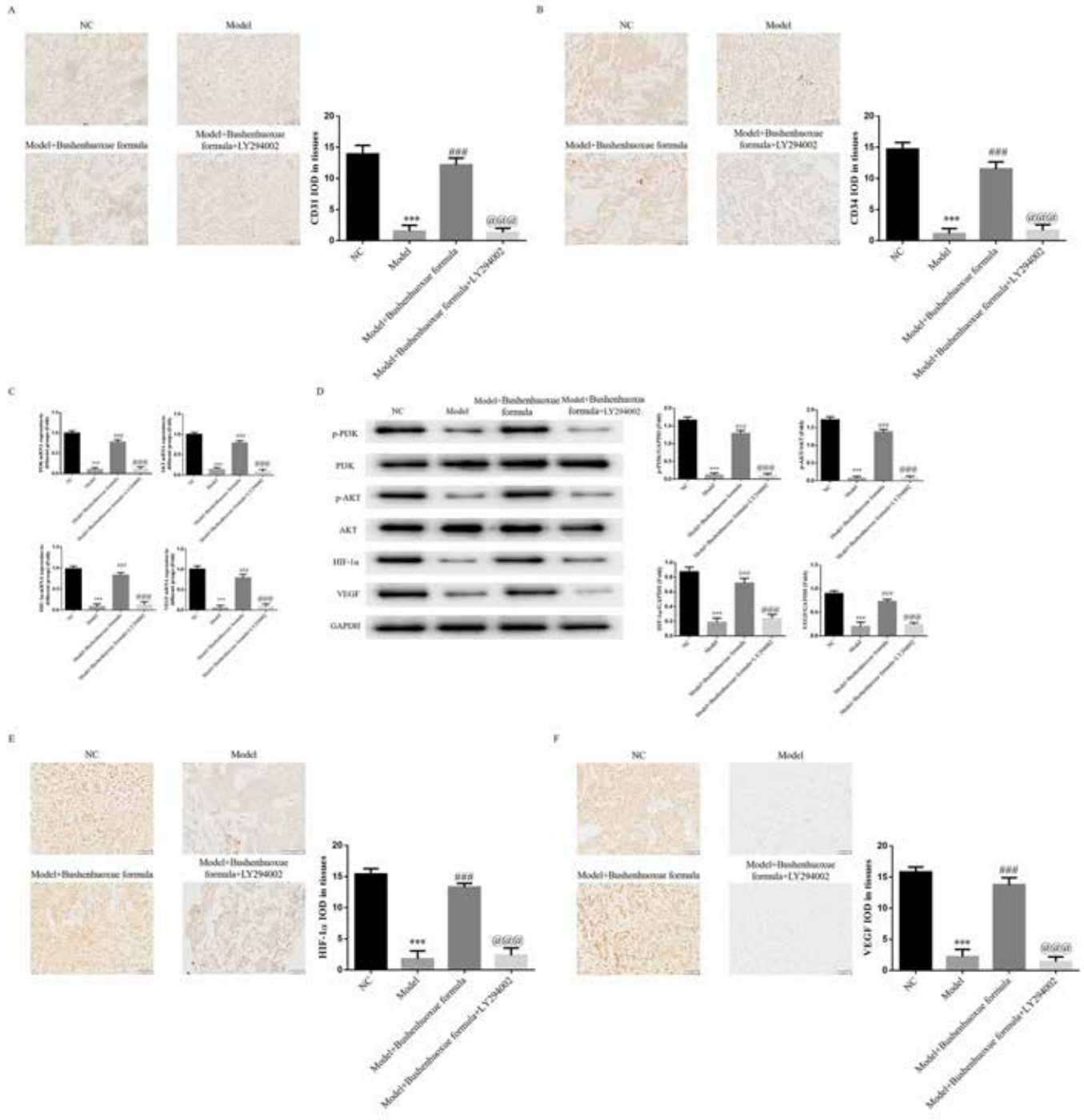

FIGURE 9 - Relative mRNA and Protein expression.
A. CD31 protein expression in placental tissues using immunohistochemistry (magnification, x100; scar bar, 100μm). ***P<0.001, compared with the NC group; ###P<0.001, compared with the model group; @@@P<0.001, compared with model + Bushenhuoxue formula group. NC, negative control; B. CD34 protein expression in placental tissues using immunohistochemistry (magnification, x100; scar bar, 100μm). ***P<0.001, compared with the NC group; ###P<0.001, compared with the model group; @@@P<0.001, compared with model + Bushenhuoxue formula group. NC, negative control; C. Comparison of relevant gene expression in placental tissues (magnification, x100). ***P<0.001, compared with the NC group; ###P<0.001, compared with the model group; @@@P<0.001, compared with model + Bushenhuoxue formula group. NC, negative control; D. Relative proteins expression in placenta tissues using western blotting. ***P<0.001, compared with the NC group; ###P<0.001, compared with the model group; @@@P<0.001, compared with model + Bushenhuoxue formula group. NC, negative control; E. HIF-1α protein expression in placental tissues using immunohistochemistry (magnification, x100; scar bar, 100μm). ***P<0.001, compared with the NC group; ###P<0.001, compared with the model group; @@@P<0.001, compared with model + Bushenhuoxue formula group. NC, negative control; F. VEGF protein expression in placental tissues using immunohistochemistry (magnification, x100; scar bar, 100μm). ***P<0.001, compared with the NC group; ###P<0.001, compared with the model group; @@@P<0.001, compared with model + Bushenhuoxue formula group. NC, negative control.

Disclosures

Conflict of interest: The authors declare that they have no competing interests.

Financial support: The present study was funded by the Anhui Province Higher Education Science Research Project (gran no. 2022AH050443) and the Anhui Red Cross Society Traditional Chinese medicine inheritance innovation development research project (grant no. 2022ZYYD08).

Authors' contributions: XY and SLS designed the study, performed the experiments, analyzed and interpreted the data and wrote the manuscript. LJL, PL, MQL, YNW and YQG collected samples and clinical data, analyzed and interpreted the data, and wrote the manuscript. LJL and PL provided and analyzed the samples, and interpreted the results and clinical data of the patients. MQL, YNW and YQG confirm the authenticity of all the raw data. All authors have read and approved the final version of the manuscript.

Data availability statement: The datasets used and/or analyzed during the current study are available from the corresponding author on reasonable request.

Ethics approval and consent to participate: The present study was approved by the Ethics Committee of Shanghai University of Traditional Chinese Medicine affiliated Shuguang Hospital Anhui Hospital (approval no. 2022102351).

References

1. Wang F, Jia W, Fan M, et al. Single-cell Immune Landscape of Human Recurrent Miscarriage. Genomics Proteomics Bioinformatics. 2021;19(2):208-222. CrossRef PubMed
2. Tian Y, Fu Z, Lan H, et al. Chinese traditional herbs enhanced the clinical efficacy of low-molecular-weight heparin in the treatment of recurrent spontaneous abortion complicated with thrombophilia. Heliyon. 2023;9(2):e13120. CrossRef PubMed
3. Wang X, Zhao Y, Zhong X. Protective effects of baicalin on decidua cells of LPS-induced mice abortion. J Immunol Res. 2014;2014:859812. CrossRef PubMed
4. Lin P, Ji HH, Li YJ, Guo SD. Macrophage Plasticity and Atherosclerosis Therapy. Front Mol Biosci. 2021;8:679797. CrossRef PubMed
5. Svensson-Arvelund J, Ernerudh J, Buse E, et al. The placenta in toxicology. Part II: systemic and local immune adaptations in pregnancy. Toxicol Pathol. 2014;42(2):327-338. CrossRef PubMed
6. Li J, Feng D, He S, Wu Q, Su Z, Ye H. Meta-analysis: association of homocysteine with recurrent spontaneous abortion. Women Health. 2021;61(7):713-720. CrossRef PubMed
7. Liu Z, Sun S, Xu H, et al. Prognostic analysis of antibody typing and treatment for antiphospholipid syndrome-related recurrent spontaneous abortion. Int J Gynaecol Obstet. 2022;156(1):107-111. CrossRef PubMed
8. Song Y, Zhou F, Tan X, et al. Bushen Huoxue recipe attenuates early pregnancy loss via activating endometrial COX2-PGE2 angiogenic signaling in mice. BMC Complement Med Ther. 2021;21(1):36. CrossRef PubMed
9. Zhao J, Chen P, Xu G, et al. [Bushen Huoxue Fang improves recurrent miscarriage in mice by down-regulating the JAK2/STAT3 pathway]. Nan Fang Yi Ke Da Xue Xue Bao. 2023;43(2):265-270. PubMed
10. Katzav A, Menache zm A, Maggio N, Pollak L, Pick CG, Chapman J. IgG accumulates in inhibitory hippocampal neurons of experimental antiphospholipid syndrome. J Autoimmun. 2014;55:86-93. CrossRef PubMed
11. Luo S, Jing J, Zhang Y, Yu W, Gao W. Network pharmacology and the experimental findings of Bushenhuoxue formula for improving hippocampal neuron injury in vascular demented rats. J Integr Neurosci. 2021;20(4):847-859. CrossRef PubMed
12. Cai Q, Li Q, Zhong S, et al. Ultrasound-targeted microbubble destruction rapidly improves left ventricular function in rats with ischemic cardiac dysfunction. Int J Cardiol. 2024;404:131943. CrossRef PubMed
13. Livak KJ, Schmittgen TD. Analysis of relative gene expression data using real-time quantitative PCR and the 2(-Delta Delta C(T)) Method. Methods. 2001;25(4):402-408. PMID:CrossRef PubMed
14. Reddel HK, Bacharier LB, Bateman ED, et al. Global Initiative for Asthma Strategy 2021: executive summary and rationale for key changes. Eur Respir J. 2021;59(1):2102730. CrossRef PubMed
15. Grandone E, Tiscia GL, Mastroianno M, et al. Findings from a multicentre, observational study on reproductive outcomes in women with unexplained recurrent pregnancy loss: the OTTILIA registry. Hum Reprod. 2021;36(8):2083-2090. CrossRef PubMed
16. Liu X, Chen Y, Ye C, Xing D, Wu R, Li F, Chen L, Wang T. Hereditary thrombophilia and recurrent pregnancy loss: a systematic review and meta-analysis. Hum Reprod. 2021 20;36(5):1213-1229. CrossRef
17. Al Jameil N, Tyagi P, Al Shenefy A. Incidence of anticardiolipin antibodies and lupus anticoagulant factor among women experiencing unexplained recurrent abortion and intrauterine fetal death. *Int J Clin Exp Pathol*. 2015;8(3):3204-3209. PubMed
18. Bose P, Black S, Kadyrov M, et al. Adverse effects of lupus anticoagulant positive blood sera on placental viability can be prevented by heparin in vitro. *Am J Obstet Gynecol*. 2004;191(6):2125-2131. CrossRef PubMed
19. Sung N, Khan SA, Yiu ME, et al. Reproductive outcomes of women with recurrent pregnancy losses and repeated implantation failures are significantly improved with immunomodulatory treatment. *J Reprod Immunol*. 2021;148:103369. CrossRef PubMed
20. Yang X, Su S, Ren Q, et al. BushenHuoxue Recipe for the Treatment of Prethrombotic State of ACA-Positive Recurrent Miscarriage via the Regulation of the PI3K-AKT Signaling Pathway. *Evid Based Complement Alternat Med*. 2022;2022:2385534. CrossRef PubMed
21. García-Escudero R, Segrelles C, Dueñas M, et al. Overexpression of PIK3CA in head and neck squamous cell carcinoma is associated with poor outcome and activation of the YAP pathway. *Oral Oncol*. 2018;79:55-63. CrossRef PubMed
22. del Peso L, González-García M, Page C, Herrera R, Nuñez G. Interleukin-3-induced phosphorylation of BAD through the protein kinase Akt. *Science*. 1997;278(5338):687-689. CrossRef PubMed
23. Xie W, Zhou P, Qu M, et al. Corrigendum: Ginsenoside Re Attenuates High Glucose-Induced RF/6A Injury *via* Regulating PI3K/AKT Inhibited HIF-1a/VEGF Signaling Pathway. *Front Pharmacol*. 2020;11:1312. CrossRef PubMed
24. Tayler HM, MacLachlan R, Güzel Ö, Miners JS, Love S. Elevated late-life blood pressure may maintain brain oxygenation and slow amyloid-β accumulation at the expense of cerebral vascular damage. Brain Communications. 2023 ;5(2):fcad112. CrossRef PubMed
25. Li H, Zhao B, Liu Y, Deng W, Zhang Y. Angiogenesis in residual cancer and roles of HIF-1α, VEGF, and MMP-9 in the development of residual cancer after radiofrequency ablation and surgical resection in rabbits with liver cancer. *Folia Morphol (Warsz)*. 2020;79(1):71-78. PubMed

26. Wu YF, Jin KY, Wang DP, et al. VEGF loaded nanofiber membranes inhibit chronic cerebral hypoperfusion-induced cognitive dysfunction by promoting HIF-1a/VEGF mediated angiogenesis. *Nanomedicine*. 2023;48:102639. CrossRef PubMed
27. Pusztaszeri MP, Seelentag W, Bosman FT. Immunohistochemical expression of endothelial markers CD31, CD34, von Willebrand factor, and Fli-1 in normal human tissues. *J Histochem Cytochem*. 2006;54(4):385-395. CrossRef PubMed
28. Luczynska E, Niemiec J, Ambicka A, et al. Correlation between blood and lymphatic vessel density and results of contrast-enhanced spectral mammography. *Pol J Pathol*. 2015;66(3):310-322. CrossRef PubMed

DTI
Drug Target Insights 2025; 19: 71-90
ISSN 1177-3928 | DOI: 10.33393/dti.2025.3495
ORIGINAL RESEARCH ARTICLE

Integrated *in vitro*, microarray, and network pharmacology analysis reveals the multi-target anti-diabetic potential of *Vigna unguiculata*

Haseeba Sardar[1], Fatima Noor[2], Syed Muhammad Mukarram Shah[3], Ashraf Ullah Khan[4], Jamelah S Al-Otaibi[5], Fazal Hadi[1], Maria Daglia[6,7], Haroon Khan[1,8]

[1]Department of Pharmacy, Abdul Wali Khan University, Mardan - Pakistan
[2]Institute of Molecular Biology and Biotechnology, The University of Lahore, Lahore - Pakistan
[3]Department of Pharmacy, University of Swabi, Swabi - Pakistan
[4]Faculty of Pharmaceutical Sciences, Abasyn University, Peshawar - Pakistan
[5]Department of Chemistry, College of Science, Princess Nourah Bint Abdulrahman University, Riyadh - Saudi Arabia
[6]Department of Pharmacy, University of Naples Federico II, Naples - Italy
[7]International Research Center for Food Nutrition and Safety, Jiangsu University, Zhenjiang - China
[8]Department of Pharmacy, Korea University, Sejong - South Korea

ABSTRACT

Introduction: Diabetes mellitus (DM), particularly type 2 DM (T2DM), is a chronic metabolic disorder requiring novel therapeutic approaches as the available therapies are not meeting the current challenges. This study investigates the anti-diabetic potential of Vigna unguiculata using a network pharmacology approach, supported by *in vitro* and *in silico* analyses.

Methods: The plant was collected from Khyber Pakhtunkhwa, Pakistan, and subjected to hydroalcoholic extraction and fractionation. *In vitro* assays included α-amylase, α-glucosidase, and aldose reductase. Target prediction using STITCH and SwissTargetPrediction identified 88 common genes linked to T2DM. Protein-protein interaction (PPI) network analysis highlighted key genes like EGFR, PTGS2, and TLR4 as central nodes in diabetes-related pathways. Molecular docking was used to study the binding affinities of compounds.

Results: IC50 values were determined using IBM SPSS Statistics 21 software. The data underwent analysis using one-way ANOVA followed by Dunnett's multiple comparison test. Significance value was determined at *$p < 0.05$, **$p < 0.01$ and ***$p < 0.001$. In-vitro assays demonstrated significant α-amylase, α-glucosidase, and aldose reductase inhibitory activities. Phytochemical screening identified several bioactive compounds. Functional annotation and KEGG pathway analysis confirmed these genes' roles in crucial metabolic pathways. Virtual screening revealed strong binding affinities of compounds like Stigmasterol, Luteoline, and Quercetin with GSK3B, PTGS2, and TLR4. The Molecular Dynamics (MD) simulation, binding free energy calculations (MM-PBSA and MM-GBSA), confirmed the results of Virtual screening.

Conclusion: In short, these findings underscore *V. unguiculata* as a promising source for anti-diabetic agents, supporting further clinical trials for T2DM management.

Keywords: Diabetes, *In vitro,* Molecular docking, MD simulation, Network pharmacology, Protein-protein interaction (PPI) network, *Vigna unguiculata*

Introduction

Type 2 diabetes mellitus (T2DM) is a growing and important health issue worldwide, characterized by continuous high blood sugar levels caused by resistance to insulin and eventual malfunction of pancreatic beta-cells (1). The impact of this prevalent form of diabetes is significant worldwide, accounting for around 90% of cases. This impact is felt deeply in terms of both individual health and healthcare systems (2,3). T2DM's worldwide occurrence is on the rise due to factors like longer life expectancy, lack of physical activity, and shifts in eating habits, which makes it a significant issue in the epidemiology of non-communicable diseases (4). The mortality rates linked to T2DM are concerning, since it leads to cardiovascular diseases, kidney failure, lower limb amputation, and diabetic retinopathy, as well as other complications (5). The mortality rate linked to T2DM is measured in scientific research using hazard ratios or relative risks when compared to non-diabetic groups. For example, people with T2DM have

Received: February 12, 2025
Accepted: June 18, 2025
Published online: August 21, 2025

This article includes supplementary material.

Corresponding author:
Haroon Khan
email: haroonkhan@awkum.edu.pk; haroonkhan@korea.ac.kr

double the likelihood of dying at any age compared to those without the condition.

Treatment for T2DM mainly focuses on controlling blood sugar levels using lifestyle changes, oral anti-diabetic medications, and insulin treatment (6). The methods mentioned typically do not fully tackle the multifaceted characteristics of the illness. Many traditional treatments focus on only one element of the disease's intricate pathophysiology, potentially resulting in less than ideal results and failing to stop the advancement of the disease (7). With these restrictions in mind, there is an urgent requirement for a transition towards multi-target drug discovery. This method seeks to create medications that can concurrently impact numerous pathways associated with T2DM, providing a more comprehensive treatment option. These approaches are expected to enhance treatment effectiveness and patient outcomes by tackling the various mechanisms involved in the development and advancement of the disease. Therefore, T2DM continues to be a significant health challenge with substantial morbidity and mortality. The insufficiency of current single-target treatments emphasizes the need for innovative treatment approaches, especially those involving multi-target interventions, to more effectively handle and potentially reverse this intricate and widespread disease.

Conventional treatments primarily focus on managing blood glucose levels and mitigating symptoms, yet they often fail to address the underlying causes and multiple pathways involved in the disease's progression. Recent advancements in network pharmacology have underscored the importance of targeting multiple biological pathways simultaneously to achieve more effective therapeutic outcomes. Network pharmacology is a cutting-edge approach that integrates systems biology, multi-target drug actions, and bioinformatics to systematically explore the therapeutic potential of drugs, including those derived from medicinal plants (8,9). This approach is especially relevant in the context of T2DM, where the interplay between insulin signaling, inflammation, and oxidative stress contributes to the disease's complexity. In this study, we explore the potential of *V. unguiculata*, a plant with a rich history in traditional medicine, as a source of multi-target anti-diabetic agents. *V. unguiculata* (commonly known as cowpea or lobia) is a leguminous plant belonging to the *Fabaceae* family (10). Traditionally used in various medicinal practices, it has been suggested to possess anti-diabetic properties, potentially due to its bioactive compounds that may influence glucose metabolism and insulin sensitivity (11,12). However, the exact mechanism is currently unknown.

Following that, this study provides compelling evidence for the anti-diabetic potential of *V. unguiculata* through an integrated approach that combines traditional knowledge with modern scientific techniques. The study highlights the importance of a multi-target therapeutic strategy, particularly in managing complex diseases like T2DM, where multiple biological processes are dysregulated. The *V. unguiculata* has been traditionally employed for the ailment of various diseases, including DM. However, the mechanism by which *V. unguiculata* exhibits anti-diabetic activity has not been explored. Based on the previously reported activities, the bioactive extract of the *V. unguiculata* has been evaluated against DM using *in vitro* studies, network pharmacology, molecular docking, MD simulation, and binding free energies with the intention to explore the potential anti-diabetic mechanism. In this study, the key approach was adopted to explore the pathways, which plays crucial role in the pathogenesis of the DM, i.e., by inducing damage to the insulin producing cells and confer insulin resistance such as PTGS2, Glycogen Synthases Kinase 3 Beta (GSK3B) and Toll-like receptor-4 (TLR-4) signaling (13-15). The GSK3B has been focused recently on diabetes management due to its involvement in insulin resistance, insulin synthesis, and protection of the B-cells (Islet of Langerhans cells). Similarly, the role of TLR-4 has also been implicated in the pathogenesis of various diseases, including diabetes; enhanced TLR-4 activity paves the way for inflammation of various tissues, including the pancreas, and cross-talk with multiple signaling pathways such as MAPKs, NF-kB, and JAK/STAT signaling (16,17). Primarily, in this study, *V. unguiculata* plant bioactive compounds were employed against the multiple signaling pathways involved in Diabetes pathogenesis. By employing comprehensive computational approaches, it was assumed that bioactive compounds from the *V. unguiculata* interact with the multiple biological signaling pathways concerned with glucose metabolism, insulin resistance, and the inflammatory process, which will eventually improve diabetes symptoms by regulating the blood glucose level (13-15).

Currently, several classes of anti-diabetic drugs are in clinical practice for the management of DM. However, the existing drugs are associated with various unwanted side effects such as weight gain, lactic acidosis, urinary tract infections, and the cases of DM are increasing globally. Thus, there is a need for the exploration of new drugs, which are not only effective but also associated with fewer side effects. Natural products offer a cheap source for new drug development, and they can be used to discover drugs that fight various diseases, including DM (18,19). The use of *V. unguiculata* plant as an anti-diabetic has been reported traditionally; thus, based on the previous reported studies, it was anticipated that *V. unguiculata* would be effective against DM.

Methodology

Plant material collection, identification, and extraction

In August 2022, a fresh whole plant (14kg) of *V. unguiculata* was gathered from Village Rustam, district Mardan, Khyber Pakhtunkhwa, Pakistan. Dr. Mohib Shah from the Department of Botany, AWKUM, authenticated and identified the plant specimen by comparing it with existing specimens at the Department of Botany, AWKUM, and the flora of Pakistan. The Department of Botany, AWKUM, assigned Voucher No. AWKUM.Bot.100.31.3.9 to the plant specimen. After cleaning, fresh plant material was dried in the shade at room temperature. The entire dried plant was crushed, resulting in 838 gm of powdered plant. The powdered plant was macerated using a hydroalcoholic solvent (90 % methanol and 10% distilled water) following the procedure described by Mistriyani et al. (20). The procedure was repeated three times to achieve the highest extraction possible. The solvent was evaporated using a rotary evaporator

to concentrate the filtrate. The concentrated extract was then dried in an oven at approximately 40 °C. Ultimately, 186g of oily, viscous extract was acquired and stored in a refrigerator at 2-8 °C.

Fractionation

Distilled water at a warm temperature was added to the hydro-methanolic extract. The mixture was then separated using n-hexane in a separating funnel. The remaining methanol extract was then fractionated using ethyl acetate to yield n-hexane, ethyl acetate, and water fractions. This process was repeated multiple times to obtain the maximum fractions. The fractions were further concentrated using a vacuum rotary evaporator and then dried in an oven at approximately 40 °C.

In-vitro *anti-diabetic activity*

The *in vitro* anti-diabetic activities of both the crude hydro-methanolic extract and the subsequent fractions were examined.

α-amylase inhibitory activity

The already established technique was used to conduct the alpha amylase inhibitory assay (21). In a 96-well microplate, 5 µL of the enzyme solution and 15 µl of sample, diluted in phosphate buffer at various concentrations, were added. The reaction was initiated with the addition of 20 µl starch solution and then incubated for 10 minutes at 37 °C, followed by further incubation at 37 °C for 30 minutes. HCl (10 µl of 1M) and iodine reagent (75 µL) were added to each well to stop the reaction. Acarbose at a concentration of 64 µg/mL served as the positive control, and a blank was created using phosphate buffer (pH 6.9). The absorbance at 580 nm was measured, and the percentage inhibitory activity was calculated using the provided equation:

% Inhibition = Abs of Control – Abs of sample /Abs of control x 100

α-glucosidase inhibitory activity

The already established method for measuring alpha-glucosidase inhibitory activity was used (22). Test samples at different concentrations (20 µl), alpha-glucosidase (1 U/ml) (10 µl), and phosphate buffer (100 mM, pH = 6.8) (50 µl) were combined and allowed to preincubate for 15 minutes at 37°C in a 96-well microplate. Following the addition of P-nitrophenyl glucopyranoside (5 mM) as the substrate (20 µl), the mixture was incubated for 20 minutes at 37°C. The reaction was stopped by adding 50 µl of 0.1 M sodium carbonate (Na_2CO_3). The absorbance of the liberated p-nitrophenol was determined at 405 nm using a microplate reader. Acarbose was utilized as a standard in different concentrations. Each experiment was conducted in triplicate, with a parallel setup that did not contain any test sample. The % inhibitory activity was calculated using the provided equation:

% Inhibition = Absorbance of Control – Absorbance of sample /Absorbance of control x 100

Aldose reductase inhibitory assay

The evaluation of aldose reductase inhibitory activity was conducted using a previously established method (23) with some modifications. Upon euthanasia, the eyes of normal Swiss albino mice were promptly extracted, and the lenses were subsequently cleansed with normal saline. The weights of the lenses were then re-determined. Once transparent lenses were obtained, a 10 % homogeneous solution was prepared in 0.1 M phosphate buffer saline (pH 7.4). This solution was then subjected to centrifugation at 5000 × g for 10 minutes. The resulting supernatant was collected and stored on ice. The protein content of the lens homogenate was determined. A sample cuvette containing 0.7 mL of phosphate buffer, 0.1 mL of NADPH (25 × 10−5 M), 0.1 mL of lens supernatant, and 0.1 mL of DL-glyceraldehyde (5 × 10−4 M) was utilized to assess the aldose reductase inhibitory activity of the fractions, with a final volume of 1 mL. Absorbance measurements were taken in comparison to a reference cuvette devoid of DL-glyceraldehyde. The pH of the reaction mixture was adjusted to 6.2, and the enzymatic reaction was initiated upon mixing the substrate with the solution mixture. The absorbance was then monitored at 340 nm for three minutes at 30-second intervals. The extract was dissolved in phosphate buffer saline (PBS) to produce a stock solution containing all the fractions. Cuvettes treated with 0.1 mL of each fraction from various stock solutions, with final concentrations of 10, 25, 50, 100, 200, and 300 µg/mL, were used as reference and standard cuvettes to evaluate aldose reductase inhibitory activity. The process was initiated by adding 0.1 mL of DL-glyceraldehyde. The percentage inhibitions of the aldose reductase assay for the extract were calculated assuming that the lens of a normal mouse exhibited 100 % activity. IC_{50} values were calculated for each sample.

Phytocompounds Screening

Active compounds of *V. unguiculata* were identified from existing literature and several databases of biologically active phytochemicals, including Indian Medicinal Plants, Phytochemistry, and Therapeutics (IMPPAT) (24), KNApSAcK (25). The keyword' *Vigna unguiculata*' was used for database searches, while a comprehensive literature review was conducted using PubMed and Google Scholar. The bioavailability (F) and drug-likeness (DL) of all ingredients were assessed to determine their ADME (absorption, distribution, metabolism, and excretion) properties. Compounds were selected based on a DL value of at least 0.18 and an OB value of at least 30%. The OB and DL values for all active compounds were calculated using SwissADME and ADMETlab. Additionally, chemical information such as CID number, structure, and molecular weight was collected from PubChem and ChemSpider.

Retrieval of potential targets of selected compounds

Swiss Target Prediction (26) and the STITCH database (27) were used to predict the potential targets of selected compounds. These compounds were uploaded to the STITCH database with the options set to '*Homo sapiens*' and using screening criteria as combined scores 0.7 or higher. Further,

the SMILES notation of each compound was inputted into the Swiss Target Prediction web application to predict targets by employing the reverse pharmacophore mapping approach and predicted scores with a probability score of 0.7. In network pharmacology, this prediction is very commonly employed for the generation of possible compound-target interactions using available data. The validation of the predicted targets and subsequently comparing them with the known DM target is crucial. Hence, the reliability of the predicted targets was enhanced using publicly available curated databases, i.e., GeneCards and DisGeNET databases and the predicted targets of the STICTH database were compared.

Microarray data analysis

In order to validate the findings of the study, three microarray datasets, including GSE22435, GSE43950, and GSE92724, were obtained from the NCBI GEO database (Online) (28). GEO is a high-throughput gene expression data repository, including microarray and hybridization arrays. In this study, DEGs were analyzed using the Limma R package. Limma is widely known for its efficient tools for reading, normalizing, and analyzing gene expression data for DEGs, and hence, it is the first preferred choice for high-throughput and microarray data. Screening criteria to identify candidate genes were adjusted p-value less than 0.05 and absolute value of log (Fold Change) greater than 1.0 but less than −1.0. In the R program, we used the ggplot2 package to create a volcano plot to differentiate between statistically significant and nonsignificant genes.

Pathway and Functional Enrichment Analysis

The Database for Annotation, Visualization, and Integrated Discovery (DAVID) was employed to carry out functional annotation and enrichment analysis (29). Key targets were examined using DAVID to predict functions across three categories: biological process (BP), molecular function (MF), and cellular component (CC). A threshold of an adjusted p-value ≤ 0.05 was used, and the top 10 Gene Ontology (GO) enrichments and the top 10 KEGG pathways with the highest counts were selected for further exploration.

Network Construction

Network analysis was conducted to elucidate the mechanisms through which *V. unguiculata* affects T2DM. This analysis was facilitated by Cytoscape 3.8.0 (30), a software platform that provides tools for importing, visualizing, and analyzing biomolecular interaction networks. In the constructed network, the nodes are the target genes, and the edges are the interactions between the active compounds and the target genes. To define the network topology, the degree centrality of each compound, target gene, or pathway was calculated using the Network Analyzer of Cytoscape. Targets that showed the maximum level of interconnectedness were termed 'key targets'.

Protein–Protein Interaction Network Construction

PPIs are essential because they are highly flexible, tunable, and selective processes. The Search Tool for the Retrieval of Interacting Genes/Proteins (STRING) database (31) was then used to search for the functional relationship between the above identified key targets, which requires the combined score to be more than 0.9, while the high confidence score was applied to enhance the reliability of the data. A high threshold was selected to ensure that interactions include all the relevant potential interactions to enhance the reliability of the network interaction.

These interactions involved the use of experimental data such as protein homology, or physical type of interaction, and co-expression data, with the intention to make a more biologically relevant network by employing these additional filters. The obtained PPI network was then subjected to the next step of filtration and analysis using the Cytohubba plugin in Cytoscape to identify essential regulatory genes and potential targets.

Virtual screening

The protein targets identified during the Protein-Protein Interaction Network were then further validated through molecular docking, which is a rapid computational technique. Information about the candidate target was obtained from the X-ray crystal structures offered under the RCSB Protein Data Bank (32). Structural optimization of the complex was done by UCSF Chimera (33), while protein targets and probable binding sites were predicted using the CASTp site mapping tool (34). Virtual screening of the reported compounds was performed using the AutoDock Vina in Ubuntu (35,36) in order to assess the binding of the core targets with the active compounds. The favorable docked conformations were considered in terms of binding energies. Docking scores, which reflect the strength and stability of the compound-target interactions, were used as primary criteria for selecting promising compounds and their targets. The results of the AutoDock vina were validated using the PyRx software to cross-check the predictive score of the ligand and protein interaction. This approach ensures that the docking results are robust using multiple docking methods. Visualization of these interactions was achieved using Discovery Studio (37), highlighting the dynamics of compound-protein interactions in a visual format.

MD simulation

After the virtual screening, the molecular dynamic simulation was performed to assess structural as well as dynamic stability of the ligand-protein complexes for 50 ns using GROMACS software 2024.1 (38). The TIP3P water box was used for solvation, and the CHARMM27, i.e., all-atom force field, was applied. The ligand topologies were generated using the SwissParam software. The system was minimized for 50000 steps to remove the steric clashes using the steepest descent model. Following the energy minimization, the system was equilibrated in two steps, i.e., NVT and NPT ensembles by applying the periodic boundary condition in all directions (36). During the NVT and NPT ensembles, the temperature was maintained at 300 K for 100 ps, while the NPT ensemble was maintained at 100 ps by keeping the pressure at 1 bar. The final MD run was performed for 100 ns, and the

results were analyzed using various dynamical and structural properties (39).

Binding free energy calculations

To assess the binding free energy for all the complexes, MM-PBSA and MM-GBSA were performed (40). The binding free energy was calculated over the 100 ns simulation using MD trajectories, and the per-residue decomposition analysis was performed for both approaches, i.e., MM-PBSA and MM-GBSA, to determine the individual residues' contribution towards the binding energy of the complexes. The binding free energy calculation was performed for 1000 frames (3000-4000), keeping the interval of 2. The various parameters that were assessed include EEL (Electrostatic energy), ESURF (Electrostatic surface potential energy), ENPOLAR (Polar solvation energy), GGAS, Van der Waals, and total energy (40).

Statistical analysis

The experiments were performed three times, and the results are presented as mean ± standard error of the mean. The IC_{50} values were determined using IBM SPSS Statistics 21 software. The data underwent analysis using one-way ANOVA, followed by post hoc Dunnett's multiple comparison test using GraphPad Prism version 8.0.2. The criteria for the statistical significance were chosen as a p-value less than 0.05. Dunnett's post hoc was chosen because it adjusts for multiple comparisons inherently and tries to ensure the family-wise error rate control during multiple group comparisons with a single control while requiring no additional corrections. The effect sizes were applied to all ANOVA calculations for the magnitude effects quantifications. The various tests applied include the Epsilon-squared, Eta-squared, Random-effect, and Omega-Squared calculations with confidence intervals of 95 % to give comprehensive insight into the magnitude of effect.

Results

α-amylase inhibitory assay

The inhibitory efficacy of crude hydro-methanolic extract of *V. unguiculata* and its fractions against α-amylase enzyme was investigated using *in vitro* activity. Various concentrations, including 8, 4, 2, 1, 0.5, 0.25, 0.125, 0.0625, and 0.03125 mg/mL, were used to test the samples and determine their IC_{50} values. The crude extract exhibited a significantly lower IC_{50} value of 0.202 mg/mL compared to the aqueous (0.279 mg/mL), ethyl acetate (0.557 mg/mL), and n-hexane (1.294 mg/mL) fractions. In comparison, Acarbose, used as the standard, demonstrated the highest inhibition of the alpha amylase enzyme with an IC_{50} value of 0.043 mg/ml, as depicted in Figure 1.

α-glucosidase inhibitory assay

The inhibitory potential against α-glucosidase enzyme using *in vitro* activity was examined on the crude hydro-methanolic extract of *V. unguiculata* and its fractions. Various concentrations, including 8, 4, 2, 1, 0.5, 0.25, 0.125, and 0.0625 mg/mL, were used to test the samples, and their IC_{50} values were determined. The crude extract displayed a significantly lower IC_{50} value (0.111 mg/mL) compared to the ethyl acetate (0.135 mg/mL), aqueous (0.243 mg/mL), and n-hexane (0.629 mg/mL) fractions among all the tested samples. Acarbose, used as the standard, exhibited the highest

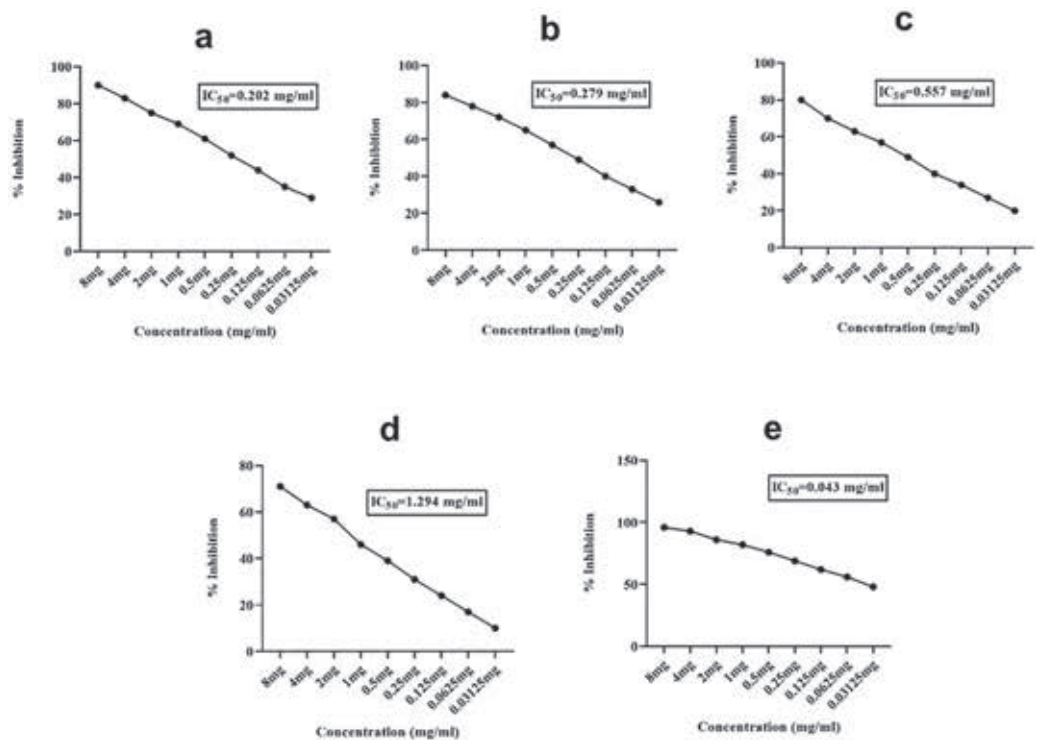

FIGURE 1 - Representing alpha amylase inhibitory activity of (a) Crude extract, (b) Aqueous fraction, (c) Ethyl acetate fraction, (d) n-Hexane fraction, and (e) standard drug, Acarbose.

inhibition of alpha amylase enzyme with an IC_{50} value of 0.034 mg/mL, as depicted in Figure 2.

Aldose reductase inhibitory assay

V. unguiculata crude hydro-methanolic extract and its fractions were examined for their ability to inhibit aldose reductase enzyme through an *in vitro* assay. Various concentrations, including 300, 200, 100, 50, 25, and 10 µg/mL, were tested, and the IC_{50} values were determined. The crude extract displayed the lowest IC_{50} value (15.823 µg/mL) among all the samples tested, followed by ethyl acetate (25.806 µg /mL), aqueous (52.376 µg /mL), and n-hexane (106.857 µg /mL) fractions. Quercetin, used as the standard, exhibited the highest inhibition of alpha amylase enzyme with an IC_{50} value of 8.545 µg /ml, as indicated in Figure 3.

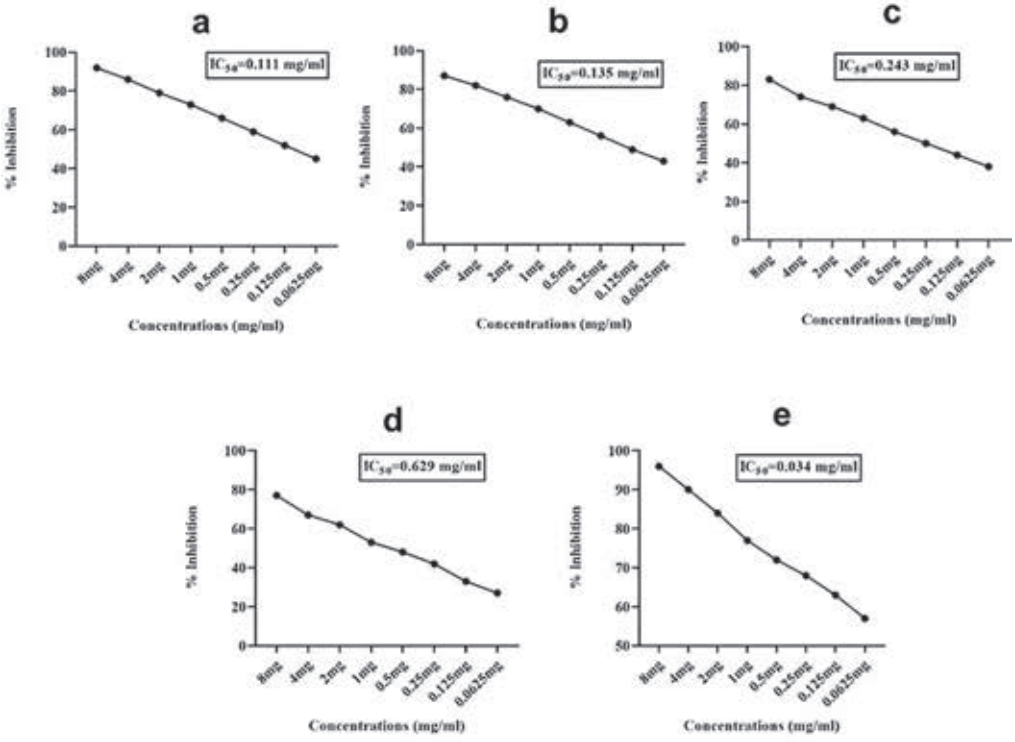

FIGURE 2 - Representing α-glucosidase inhibitory activity of (a) Crude extract, (b) Ethyl acetate fraction, (c) Aqueous fraction, (d) n-Hexane fraction, and (e) standard drug, Acarbose.

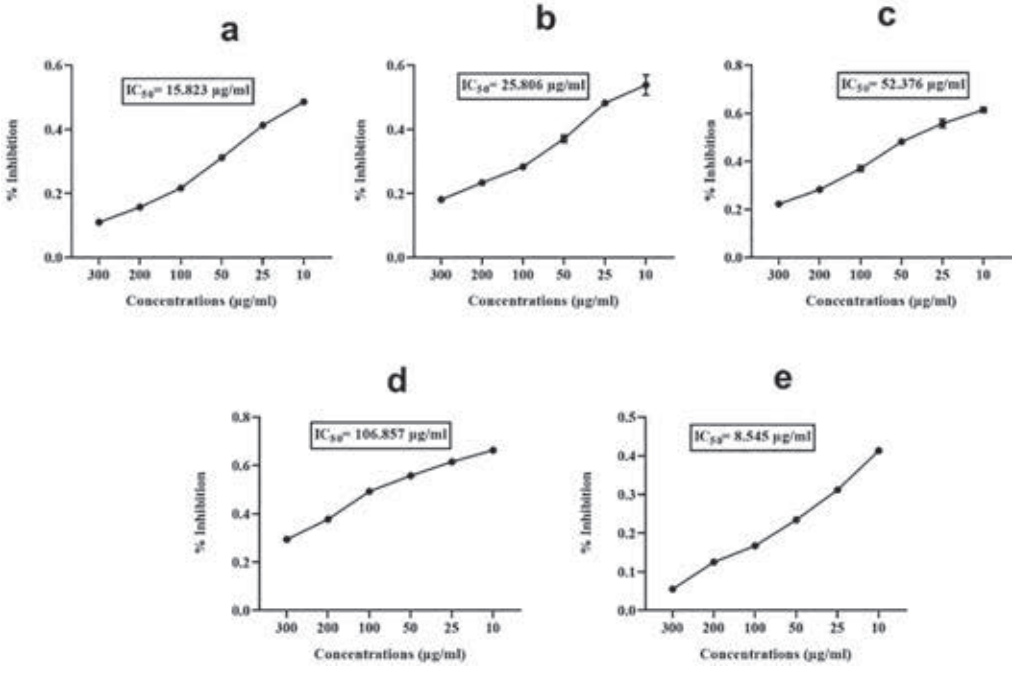

FIGURE 3 - Representing aldose reductase inhibitory activity of (a) Crude extract, (b) Ethyl acetate fraction, (c) Aqueous fraction, (d) n-hexane fraction, and (e) standard drug, Quercetin.

Network Pharmacology

Screening of potential compounds

The screening of potential compounds from *V. unguiculata* identified several candidates with drug-like potential, as summarized in Table 1. The compounds belong to various classes, including flavonoids, phenolic acids, isoflavones, triterpenoids, phytosterols, and alkaloids, each exhibiting different molecular weights, drug likeness (DL), and oral bioavailability (OB). Among the flavonoids, Quercetin, Kaempferol, Catechin, Luteolin, and Apigenin were identified, with molecular weights ranging from 270.24 to 302.23 g/mol. These compounds showed moderate drug likeness scores, with Catechin having the highest DL of 0.64, and all of them exhibited an oral bioavailability of 0.55, indicating their potential for oral administration. Protocatechuic acid, a phenolic acid with a molecular weight of 154.12 g/mol, displayed a lower drug likeness score of 0.23 but a slightly higher oral bioavailability of 0.56, suggesting that while its drug-like properties may be limited, it could still be bioavailable if administered orally. Isoflavones such as Genistein, Daidzein, and Glycitein were also included in the screening. These compounds have molecular weights between 254.24 and 284.26 g/mol and exhibit moderate drug likeness, with Genistein having a DL of 0.44. Like the flavonoids, they all have an oral bioavailability of 0.55. In the category of triterpenoids, Betulinic acid stands out with a significantly higher molecular weight of 456.7 g/mol, a drug likeness score of 0.25, and a notably higher oral bioavailability of 0.85, suggesting its strong potential as an orally administered drug candidate. The phytosterols identified include Beta-sitosterol, Campesterol, and Stigmasterol, with molecular weights around 400 to 414 g/mol. These compounds showed varying drug likeness scores, with Beta-sitosterol achieving the highest DL of 0.78, and all three exhibiting an oral bioavailability of 0.55. Finally, Vicine, an alkaloid with a molecular weight of 304.26 g/mol, demonstrated the highest drug likeness score of 0.84 among the compounds screened, coupled with an oral bioavailability of 0.55, highlighting it as a particularly promising candidate for further drug development. Overall, the screening results indicate that several compounds from *V. unguiculata* possess favorable drug-like properties and oral bioavailability, making them viable candidates for further investigation in drug development efforts. Similarly, the comprehensive pharmacokinetic studies of the selected compounds, including Stigmasterol, Quercetin, Luteoline, and Acarbose, are shown in the Supplementary Table 1.

TABLE 1 - Summarizes the list of compounds obtained from *V. unguiculata* with drug-like potential

Compound	Compound Class	Molecular Weight (MW)	Drug Likeness (DL)	Oral Bioavailability (OB)
Quercetin	Flavonoid	302.23	0.52	0.55
Kaempferol	Flavonoid	286.24	0.5	0.55
Catechin	Flavonoid	290.27	0.64	0.55
Luteolin	Flavonoid	286.24	0.38	0.55
Apigenin	Flavonoid	270.24	0.39	0.55
Protocatechuic acid	Phenolic Acid	154.12	0.23	0.56
Genistein	Isoflavone	270.24	0.44	0.55
Daidzein	Isoflavone	254.24	0.29	0.55
Glycitein	Isoflavone	284.26	0.37	0.55
Betulinic acid	Triterpenoid	456.7	0.25	0.85
Beta-sitosterol	Phytosterol	414.7	0.78	0.55
Campesterol	Phytosterol	400.7	0.59	0.55
Stigmasterol	Phytosterol	412.7	0.62	0.55
Vicine	Alkaloid	304.26	0.84	0.55
Acarbose	Oligosaccharide	645.608		0.17

3.4.2. Microarray Data Analysis

Microarray gene expression data were analyzed using datasets obtained from the GEO database. Additionally, the GSE22435 dataset contained data from 7 affected individuals and 10 healthy controls (Fig. 4A and 4D). Differential expression analysis was conducted using the LIMMA package, resulting in the identification of a significant number of differentially expressed genes (DEGs) across these datasets. Specifically, the analysis of GSE22435 revealed 671 upregulated and 198 downregulated genes, leading to a total of 870 DEGs. In the GSE43950 dataset, 2,133 DEGs were identified (Fig. 4B and 4E), and the GSE92724 dataset yielded 1,160 DEGs (Fig. 4C and 4F). All identified DEGs met the stringent criteria of an adjusted p-value less than 0.05 and an absolute log fold change (|log(FC)|) of greater than or equal to 1. These findings underscore the substantial alterations in gene expression

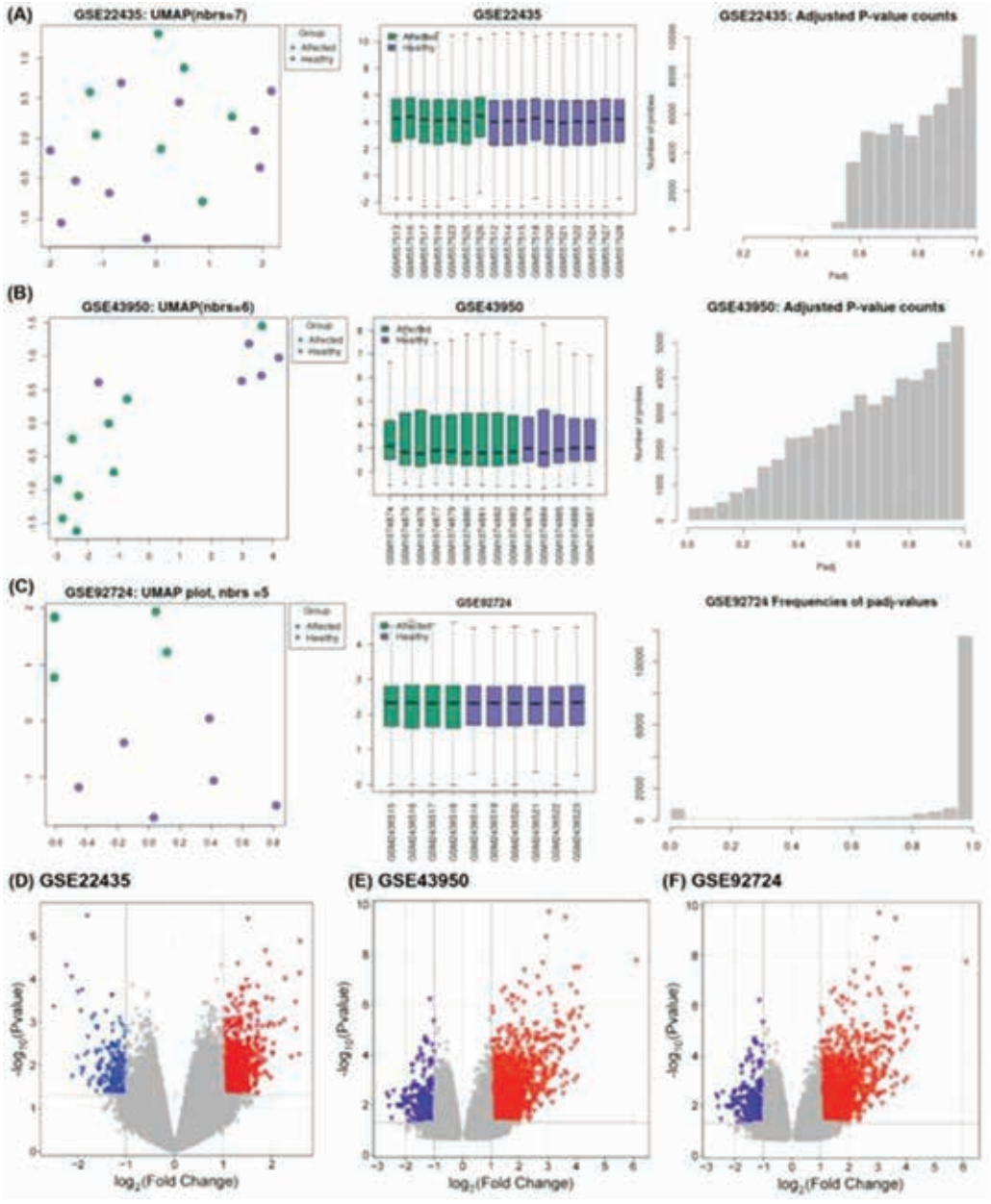

FIGURE 4 - Differential Gene Expression Analysis for GEO Datasets GSE22435, GSE43950, and GSE92724. (A), (B), and (C) show UMAP plots, boxplots of gene expression, and adjusted p-value distributions for each dataset. (D), (E), and (F) present volcano plots highlighting upregulated (red) and downregulated (blue) genes.

between affected individuals and controls, providing a robust basis for further biological interpretation and validation.

Target Identification

A comprehensive target identification process was carried out, resulting in the identification of 1,310 targets for 14 active compounds using the STITCH and SwissTarget Prediction databases. These targets were then cross-referenced with the DEGs identified through the microarray data analysis. This comparison revealed 88 common genes that are implicated in both the disease context and the plant-derived compounds (Fig. 5A). The compound-target network analysis demonstrated that these 88 genes were targeted by multiple compounds, indicating their potential as druggable targets.

Network Analysis

Following the identification of the 88 common genes, a protein-protein interaction (PPI) network was constructed (Fig. 5B). The network consisted of 88 nodes and 144 edges, illustrating the complex interactions among these genes. Further analysis identified the top 10 genes with the highest degree of connectivity within the network (Fig. 5C), which included EGFR (degree score of 43), SRC (41), PTGS2 (39), MMP9 (33), BCL2 (33), TLR4 (29), GSK3B (26), PTPRC (24), KIT (22), and BCL2L1 (20). Due to their high connectivity, these genes may play central roles in the disease mechanism and serve as critical targets for therapeutic interventions.

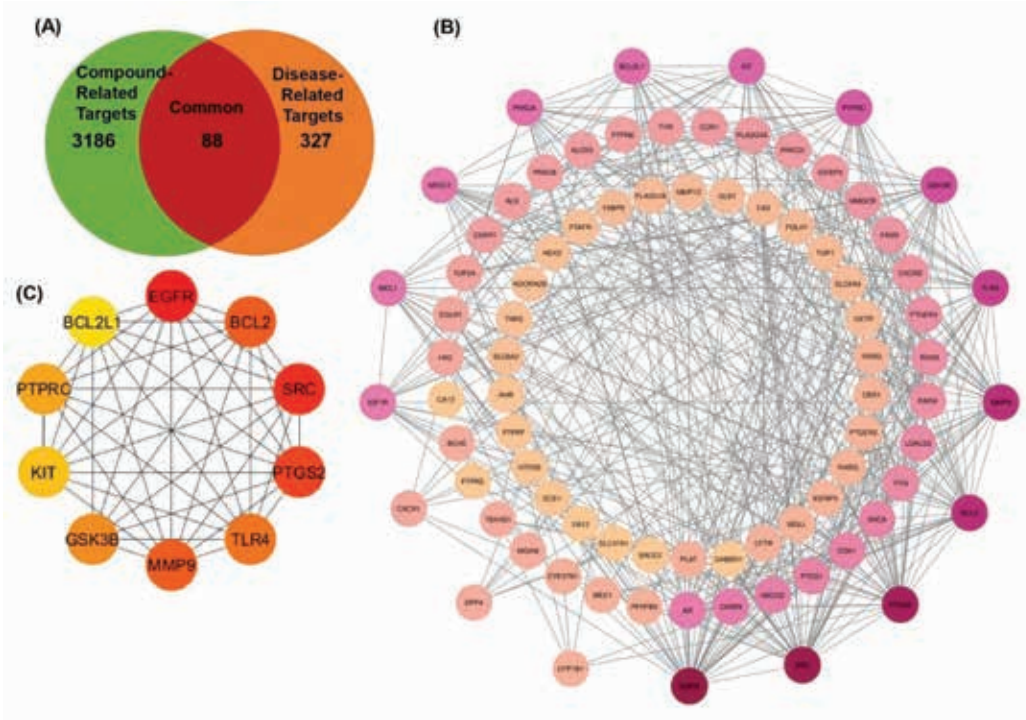

FIGURE 5 - Network and Target Analysis of Common Genes. (A) Venn diagram showing the overlap between compound-related targets (3,186) and disease-related targets (327), identifying 88 common genes. (B) Protein-protein interaction (PPI) network of the 88 common genes, illustrating the complex interactions among these targets. (C) Sub-network highlighting the top 10 genes based on degree of connectivity

Functional Annotation

Later, the functional annotation of these 88 common genes was performed using the DAVID software, which revealed their involvement in multiple diabetes-related pathways. The analysis identified significant clusters of genes associated with key biological processes (Fig. 6), including metabolic pathways such as prostanoid and fatty acid biosynthesis. Specifically, genes were enriched in processes like long-chain fatty acid metabolic processes, organic acid biosynthetic processes, and eicosanoid metabolic processes. Additionally, another cluster highlighted the role of these genes in retinoid metabolic processes and response to retinoic acid, emphasizing their involvement in important signaling pathways. Moreover, a smaller subset of genes was associated with oxidoreductase activity, particularly acting on CH-OH groups of donors and the incorporation of two atoms of oxygen, indicating their role in oxidation-reduction processes.

In terms of molecular function, the common genes were linked to activities such as ligand-activated transcription factor activity and nuclear receptor activity, which are crucial for regulating gene expression, particularly in response to retinoic acid. Other identified functions include protein autophosphorylation, essential for signal transduction, and protein tyrosine kinase activity, which plays a vital role in various cellular signaling pathways. The GO analysis also revealed that these genes are integral components of critical cellular structures, such as the Schaffer collateral-CA1-CA1 synapse, highlighting their role in synaptic transmission and plasticity in the brain. Additionally, other genes were located in the tertiary granule lumen and the intrinsic component of the presynaptic membrane, emphasizing their involvement in neurotransmitter release and synaptic function.

Further KEGG pathway analysis was also performed (Fig. 7). One of the most prominent pathways identified is the Arachidonic acid metabolism, which is crucial for the synthesis of bioactive lipid mediators that play significant roles in inflammation and cellular signaling. Another critical pathway is the HIF-1 signaling pathway, which is essential for cellular responses to hypoxia and is often implicated in cancer progression. The PPAR signaling pathway was also depicted, which plays an important role in regulating fatty acids and glucose homeostasis and is relevant to metabolic diseases. It also marks down pathways that relate to particular diseases, for example, non-small cell lung cancer or Bladder cancer; this means that these genes are involved directly in causing these types of cancer or in their advancement. Moreover, the information about the discovered VEGF signaling pathway, which plays an important role in the formation of new blood vessels and is widely used in cancer treatment. Other pathways under study include NF-kappa B signaling, via which most immune responses are controlled, Th17 cell differentiation during autoimmune diseases, etc. The occurrence of the Adherens junction pathway was also observed for cell-cell adhesion, underlining the importance of these genes in supporting the cell's structure.

In general, the KEGG pathway analysis shows that the common genes are found in various signaling pathways and biological processes that are known to be important for maintaining cellular homeostasis and regulating metabolic and disease processes. This type of analysis is helpful in understanding the possible functions of these genes from a human disease perspective and might inform future directions on treatments and cures. Apparently, the network representation strengthens the claims made with respect to

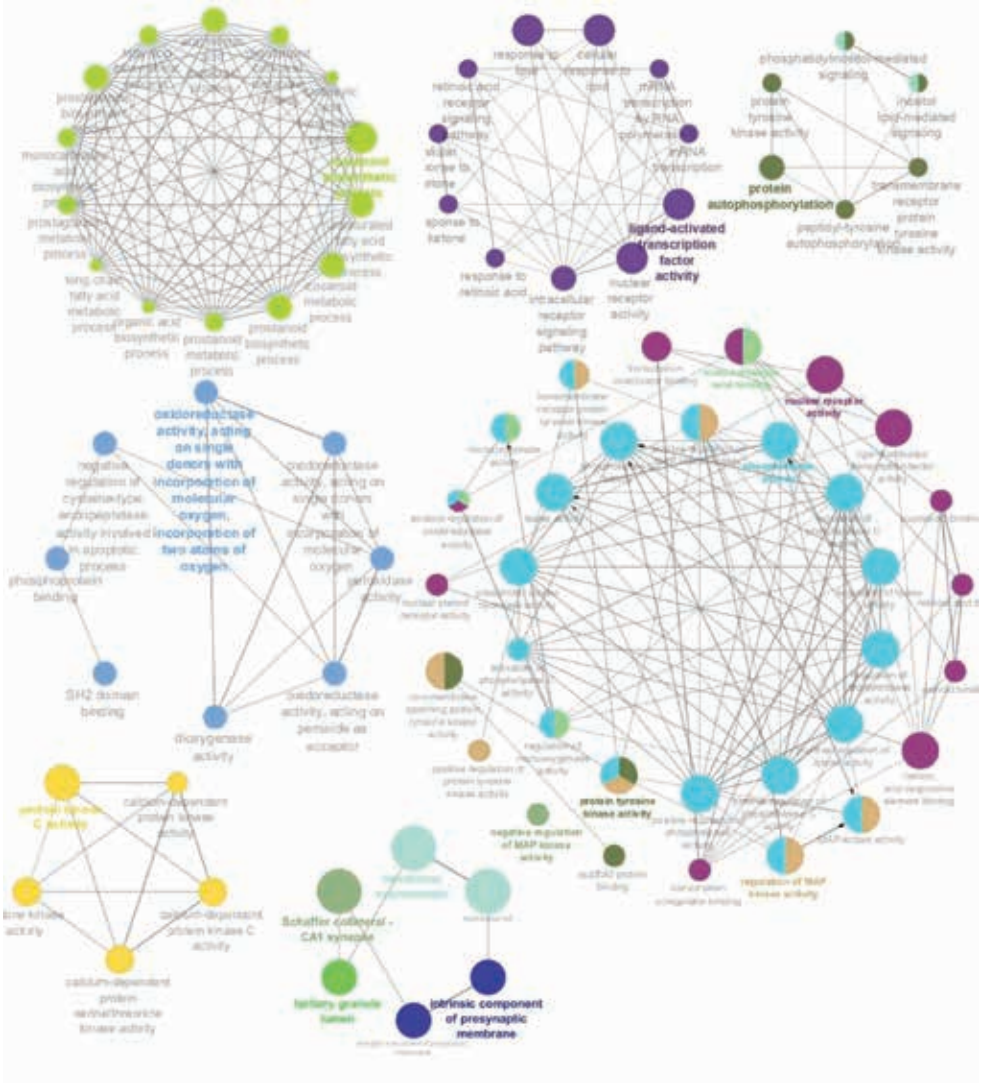

FIGURE 6 - Gene Ontology Analysis of 88 common genes representing their involvement in multiple biological processes, cellular components, and molecular functions.

the connectivity of these genes in the designated GO classes and proves the multifaceted nature of these genes in terms of their functions in various biological processes, molecular functions, and cellular components.

Compound-target pathway network

The compound-target pathway network analysis (Fig. 8) revealed that GSK3B, PTGS2, and TLR4 are the primary target proteins, displaying the highest connectivity within the network and interacting with the most bioactive compounds. The high degree of connectivity values means that these proteins are core to the network and highlight them as potential targets for treatment. Furthermore, the investigation also pointed to the fact that many compounds, including those from *V. unguiculata*, interact with these proteins, making them valuable targets for therapeutic agents. Notably, GSK3B, PTGS2, and TLR4 are known to be associated with type 2 diabetes; GSK3B was reported to be a key protein regulating insulin signaling and glucose homeostasis, PTGS2 participates in inflammation aggravating insulin resistance, and TLR4 was reported to be involved in immune response and chronic inflammation in the development of T2D. These observations indicate that modulating the expression of GSK3B, PTGS2, and TLR4 using the active compounds isolated from *V. unguiculata* may be a potential therapeutic approach for type 2 diabetes.

Molecular docking analysis

The docking results provide insights into the binding affinities of various compounds with three target proteins: GSK3B, TLR4, and PTGS2, as shown in Table 2. These interactions are critical for evaluating the efficacy of these compounds as inhibitors or modulators of these proteins. The Virtual screening results showed Stigmasterol had the highest binding affinity with the 8AV1 (GSK3B), Luteolin exhibited the highest binding affinity with the 4PH9 (PTGS2), while Quercetin showed the highest binding energy with the 3FXI (TLR4). The ligand-protein complexes were further validated using MD simulation and binding free energy calculations. During the virtual screening of the compounds with the 4PH9,

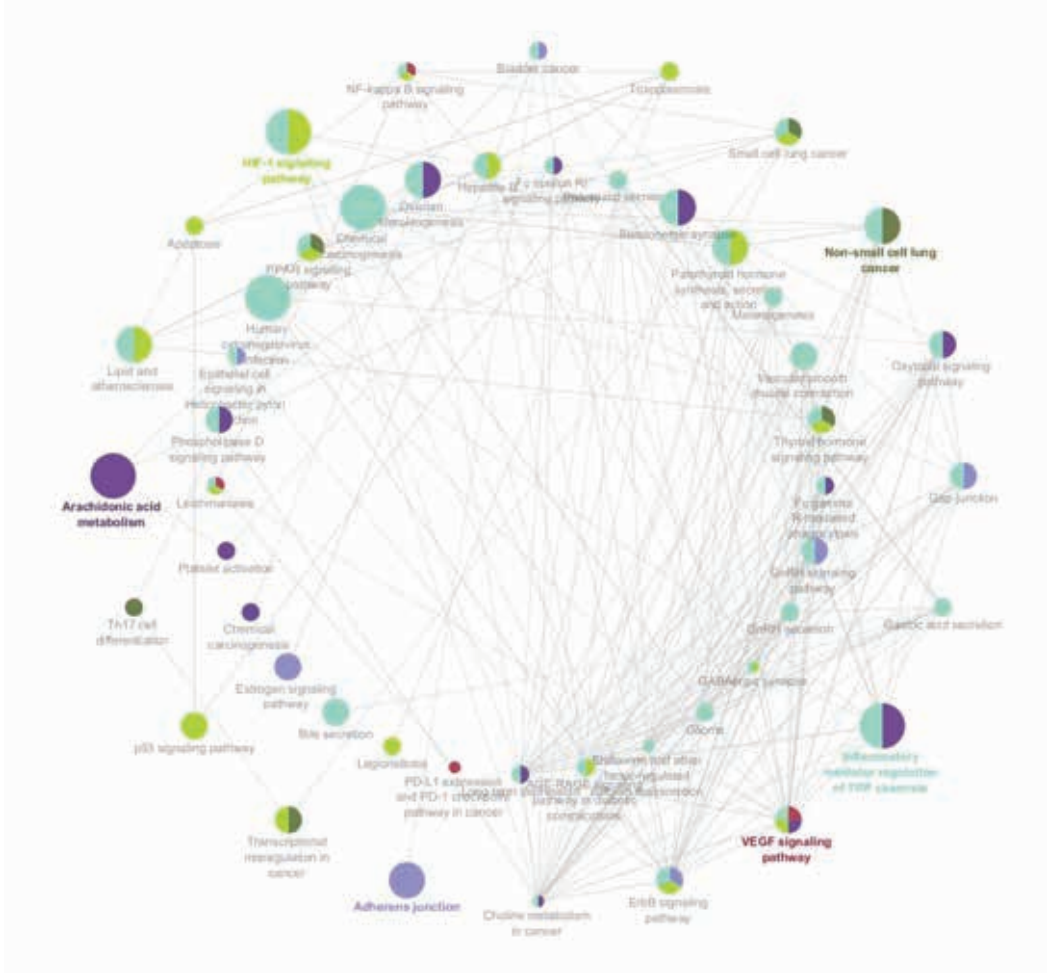

FIGURE 7 - KEGG Pathway analysis demonstrating the involvement of selected genes in diabetes relevant pathways.

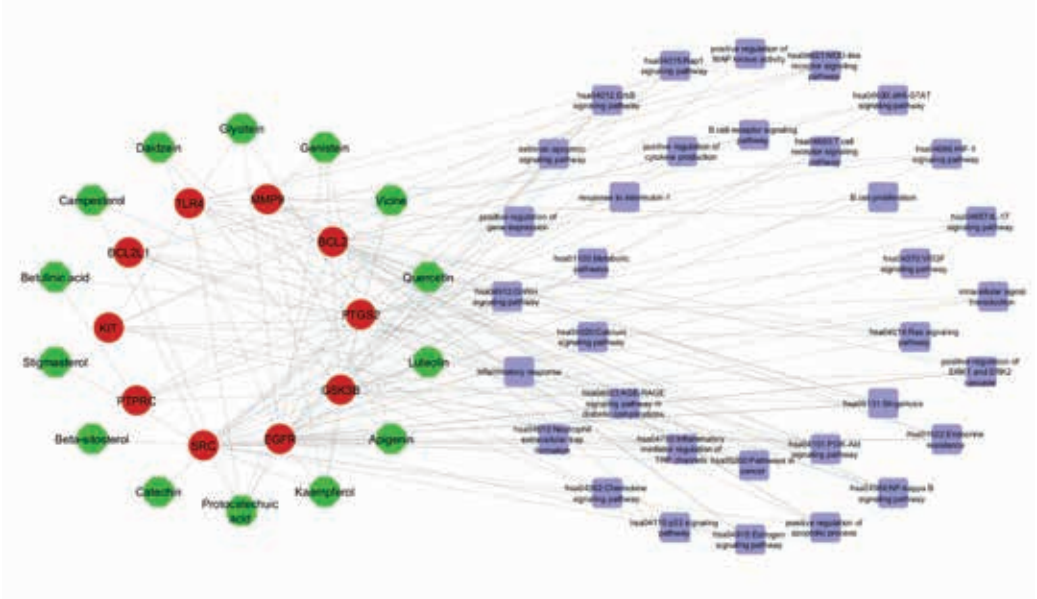

FIGURE 8 - Compound-Target-Pathway network. The green octagon represents the compound, the red circle represents the hub genes, and the blue square represents the pathways targeted by hub genes.

TABLE 2 - Docking results of various compounds with 8AV1 (GSK3B), 3FXI (TLR4), and 4PH9 (PTGS2) proteins. The table summarizes the binding affinities (in kcal/mol)

Compound Name	Binding Affinity (kcal/mol)	Binding Affinity (kcal/mol)	Binding Affinity (kcal/mol)
Stigmasterol	−8.854	−8.679	−7.244
Campesterol	−8.833	−8.062	−7.084
Beta-sitosterol	−8.739	−8.052	−7.149
Daidzein	−8.198	−7.088	−6.667
Quercetin	−8.146	−9.122	−7.237
Apigenin	−8	−8.941	−7.066
Luteolin	−7.982	−9.297	−6.885
Kaempferol	−7.782	−8.619	−6.732
Genistein	−7.685	−8.81	−6.865
Glycitein	−7.645	−7.297	−6.864
Catechin	−7.637	−8.098	−7.159
Vicine	−6.17	−7.04	−6.479
Acarbose	−6.9	−6.7	−8.9

the center of the grid box includes x = 20.685, y = 31.547, and z = 27.584, while the size of the grid box includes x = 80, y = 102, and z = 72. Similarly, the virtual screening of the compounds with the 8AV1, the center of the grid box was kept as x = −3.818, y = 0.936, and z = −2.868, while the size of the grid box was kept as x = 60, y = 64, and z = 72. Furthermore, the virtual screening of the compounds with the 3FXI, the center of the grid box was kept as x = 4.536, y = −17.363, and z = 20.067, while the size of the grid box was kept as x = 60, y = 40, and z = 100. The molecular docking of Luteoline with the 4PH9 showed three hydrogen bonds (ASNA39, GLUA466, and GLYA136), two pi-alkyl bonds (LEUA153 and PROA154), two carbon-hydrogen bonds (CYSA47 and ARGA470), and one unfavorable acceptor-acceptor bond (TYRA131). The molecular docking of the Stigmasterol with the 8AV1 showed seven pi-alkyl bonds (ILEA37, TYRA109, LEUA163, ALAA58, VALA45, LYSA60, and LEUA153), and one carbon-hydrogen bonds (ASPA175). The molecular docking of Quercetin with 3FXI showed one hydrogen bond (LYSA204), two pi-anion bonds (ASPA155 and ASPA183), one carbon-hydrogen bond (HISA153), and one unfavorable acceptor-acceptor bond (SERA183). The molecular docking of Acarbose was conducted against the 8AV1, 3FXI, and 8AV1, and results showed that the binding energy of Acarbose with the 8AV1 is −6.9 kcal/mol, with 3FXI is −6.7 kcal/mol, and with the 4PH9 is −8.9 kcal/mol. The Acarbose showed the highest binding energy against the inflammatory target, i.e., PTGS2; however, against the GSK3B and TLR-4, the Acarbose showed lower binding energy as compared to the other compounds Table 3. The compounds and protein interactions are shown in three-dimensional and two-dimensional views using Discovery Studio visualizer_16 (Fig. 9).

MD simulation analysis

During the entire 100 ns, it was found that all ligand-protein complexes remained stable during the simulation, and no significant deviation in the structural conformation of the ligand-protein complex was noticed. The ligand-protein complex stability was measured using various key parameters such as RMSD, RMSF, RoG, etc., and it was noticed that within the first few ns, the system reached equilibrium and thereafter remained stable. The RMSD values were calculated to assess the convergence of the system to its equilibrium conformation. During the RMSD calculation, initially, the system showed deviation for a few ns due to thermodynamic shock, but thereafter, the RMSD showed no significant fluctuations for all the complexes, as shown in Figure 10. The RMSD analysis showed that the average RMSD of the 3FXI_Quercetin was 0.25828, the average RMSD of the 4PH9_Luteoline was 0.45871, while the average RMSD of the 8AV1_Stigmasterol was 0.28030 nm. The RMSF analysis was conducted to study the behavior, i.e., flexibility of the individual amino acid of the protein following binding with the ligand. The RMSF analysis showed that complexes remain stable during the simulation, and no significant fluctuations were noticed, as shown in Figure 11. The RMSF analysis showed that the average RMSF of the 3FXI_Quercetin was 0.14277, the average RMSF of the 4PH9_Luteoline was 0.10841, while the average RMSF of the 8AV1_Stigmasterol was 0.11547 nm. The compactness of the protein structure following ligand binding was observed using the radius of gyration (RoG). The RoG analysis showed that the complexes remained stable during the entire simulation, which further validated the results of the RMSD and RMSF. Minor fluctuations have been observed in the complexes, which correlate with the small-scale motions and conformational changes associated with the ligand binding with proteins Figure 12. The RoG analysis showed that the average of the 3FXI_Quercetin complex was 3.1447, the average RMSF of the 4PH9_Luteoline was 2.4579, while the average RoG of the 8AV1_Stigmasterol was 2.1969 nm. The changes in the ligand-protein complex surface following exposure to the solvent during the 100 ns simulation were studied using SASA.

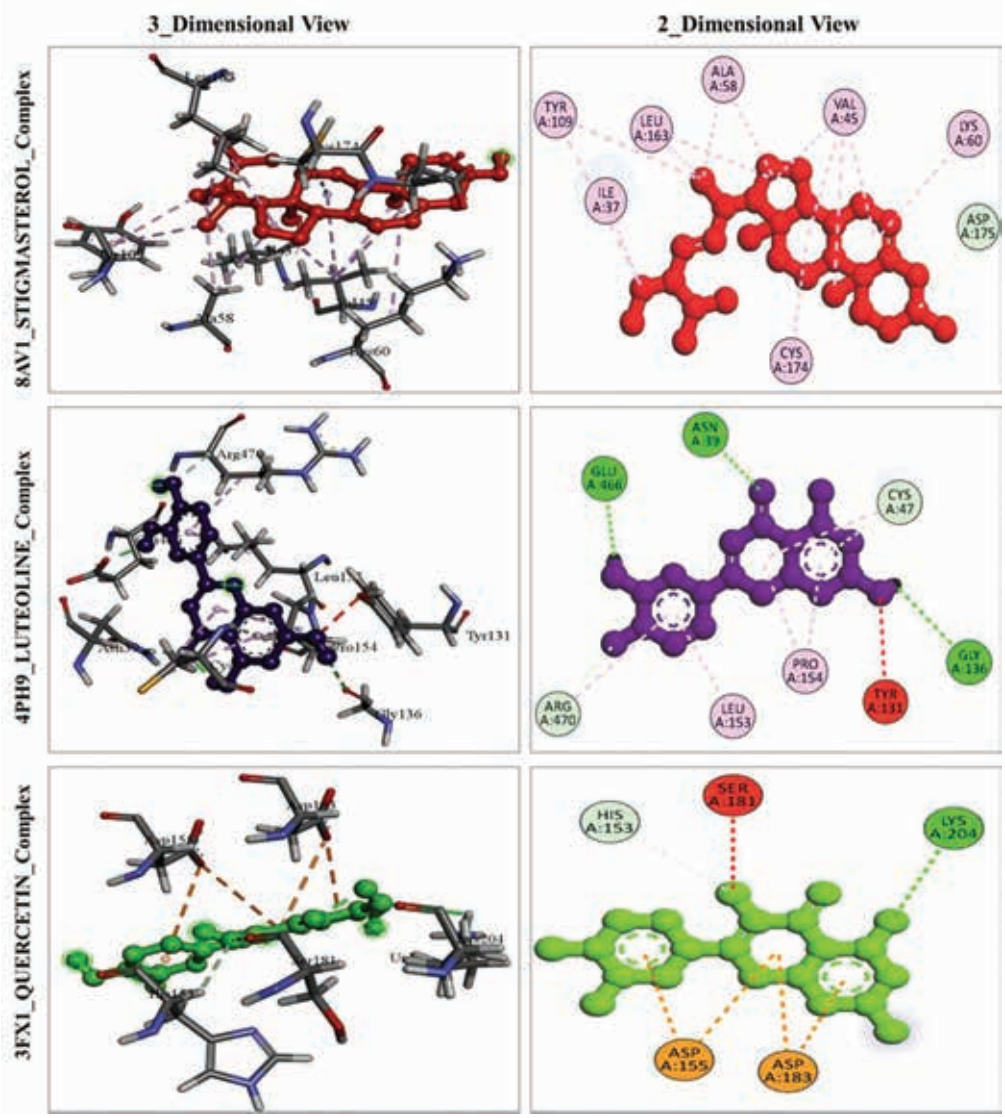

FIGURE 9 - Molecular docking analysis of key compounds with target proteins TLR4 (3FX1), PTGS2 (4PH9), and GSK3B (8AV1). Based on the virtual screening, stigmasterol showed binding affinity with the GSK3B, luteoline exhibited the highest binding energy with the PTGS2, and quercetin showed the highest binding energy with the TLR4. The interaction of the ligands with the target proteins was presented in two-dimensional and three-dimensional views using Discovery Studio Visualizer.

Initially, the SASA showed minor fluctuations, and thereafter the complexes achieved stability as shown in Figure 13. The hydrogen bonds analysis was conducted during the entire simulation to study the stability of ligand-protein complexes. The number of hydrogen bonds fluctuated for all complexes during the course of the simulation; however, the maximum number of hydrogen bonds was retained during the simulation, as shown in Figure 14.

Binding Free Energy parameters

The MM-PBSA and MM-GBSA analyses were performed for all the complexes to determine their stability in terms of binding energy. During the binding free energy calculations of the 8AV1_Stigmastrol using MM-PBSA revealed that the van der Waals energy, EEL, ENPOLAR, and GGAS remain negative and exhibited favorable binding energy. However, EPB energy and GSOLV energy of the system remain positive and indicate unfavorable binding free energy. However, the total energy of the system remains negative and indicates favorable binding energy, as shown in Table 3 and Supplementary Figure 1. Similarly, the MM-PBSA results were validated using the MM-GBSA analysis.

During the binding free energy calculations of the 8AV1_Stigmastrol using MM-GBSA revealed that the van der Waals energy, EEL, ESURF, and GGAS remain negative and exhibited favorable binding energy. However, the EGB energy and GSOLV energy of the system remain positive and indicate unfavorable binding free energy. However, the total energy of the system is negative and indicates favorable binding energy, as shown in Table 4 and Supplementary Figure 2.

The MM-PBSA and MM-GBSA analyses were performed for all the complexes to determine their stability in terms of binding energy. During the binding free energy calculations of the 4PH9_Luteoline using MM-PBSA revealed that the van der Waals energy, EEL, ENPOLAR, and GGAS remain negative and exhibited favorable binding energy. However, EPB energy and GSOLV energy of the system remains positive and indicate unfavorable binding free energy. However, the total energy of the system remains negative and indicates favorable binding

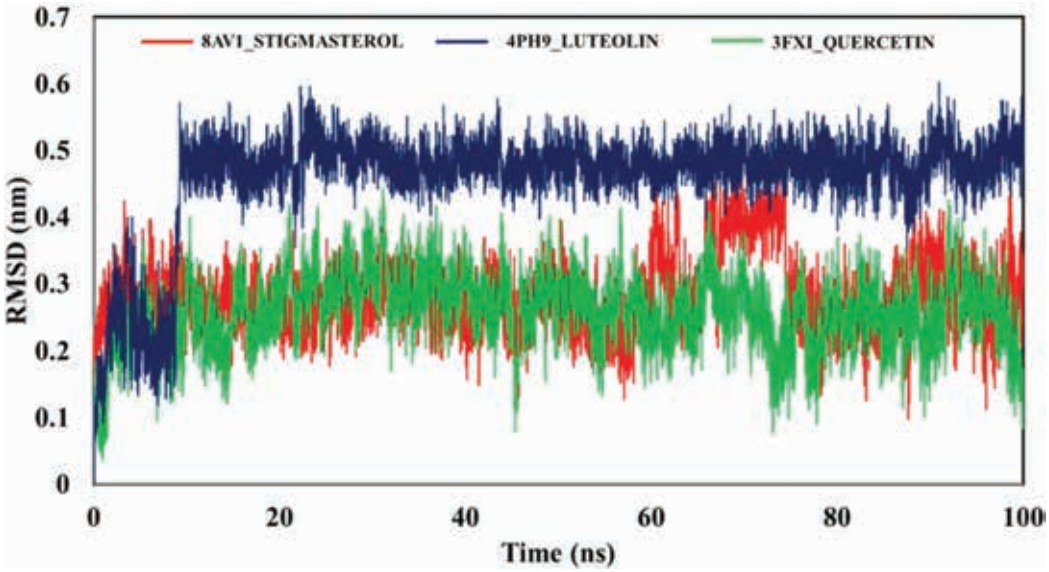

FIGURE 10 - The RMSD parameter following the MD simulation using the compound with the highest binding affinity. The stigmasterol showed the highest binding affinity with the 8AV1, Luteolin with 4PH9, and Quercetin with the 3FXI. The RMSD analysis showed that all complexes showed an acceptable value of RMSD, and no significant changes were observed.

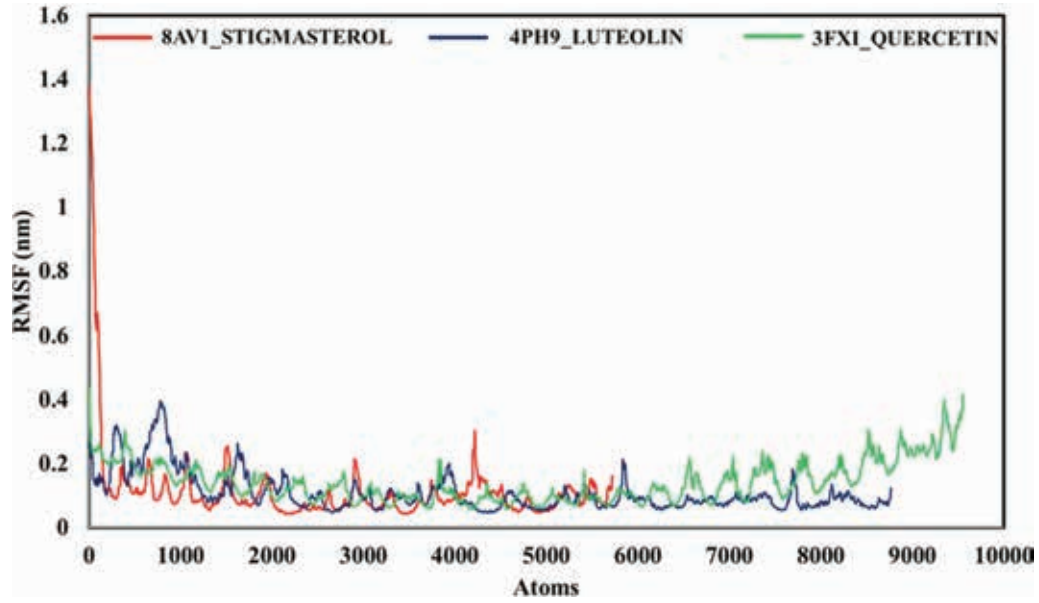

FIGURE 11 - The RMSF analysis was performed for all the complexes following the simulation. The results showed no major fluctuation in the RMSF value, and the results indicate that all complexes remain stable.

energy, as shown in Table 5 and Supplementary Figure 3. Similarly, the MM-PBSA results were validated using the MM-GBSA analysis.

During the binding free energy calculations of the 4PH9_Luteoline using MM-GBSA revealed that the van der Waals energy, EEL, ESURF, and GGAS remain negative and exhibited favorable binding energy. However, the EGB energy and GSOLV energy of the system remains positive and indicate unfavorable binding free energy. However, the total energy of the system is negative and indicates favorable binding energy, as shown in Table 6 and Supplementary Figure 4.

The MM-PBSA and MM-GBSA analyses were performed for all the complexes to determine their stability in terms of binding energy. During the binding free energy calculations of the 3FXI_Quercetin using MM-PBSA revealed that the van der Waals energy, EEL, ENPOLAR, and GGAS remain negative and exhibited favorable binding energy. However, EPB energy and GSOLV energy of the system remains positive and indicate unfavorable binding free energy. However, the total energy of the system remains negative and indicates favorable binding energy, as shown in Table 7 and Supplementary Figure 5. Similarly, the MM-PBSA results were validated using the MM-GBSA analysis.

During the binding free energy calculations of the 3FXI_Quercetin using MM-GBSA revealed that the van der Waals energy, EEL, ESURF, and GGAS remain negative and exhibited favorable binding energy. However, the EGB energy and GSOLV energy of the system remains positive and indicate unfavorable binding free energy. However, the total energy of the system is negative and indicates favorable binding energy,

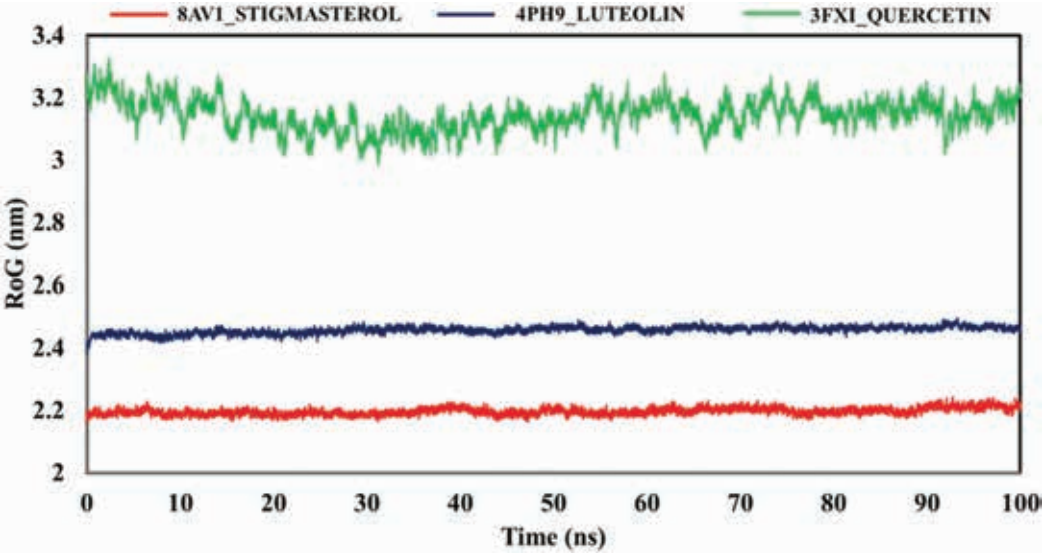

FIGURE 12 - The RoG of all the complexes was determined following the simulation to assess the stability of the complexes. The RoG results showed that 8AV1_Stigmasterol, and 4PH9_Luteolin complexes are lowered as compared to the 3FXI_Quercetin complex.

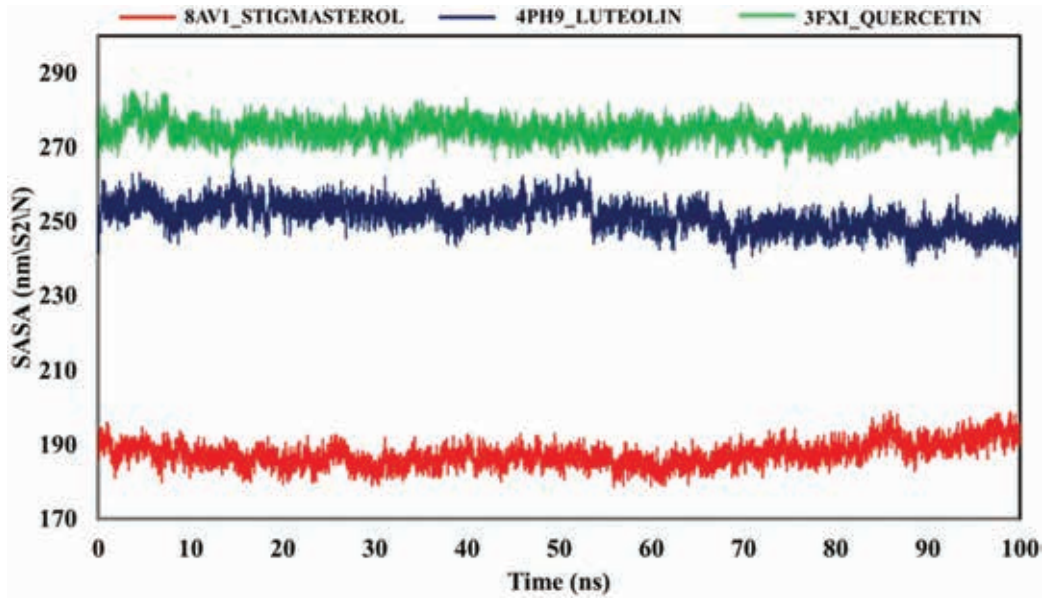

FIGURE 13 - The 8AV1_Stigamsterol result revealed the lowest SASA as compared to the 4PH9_Luteolin and 3FXI_Quercetin complexes.

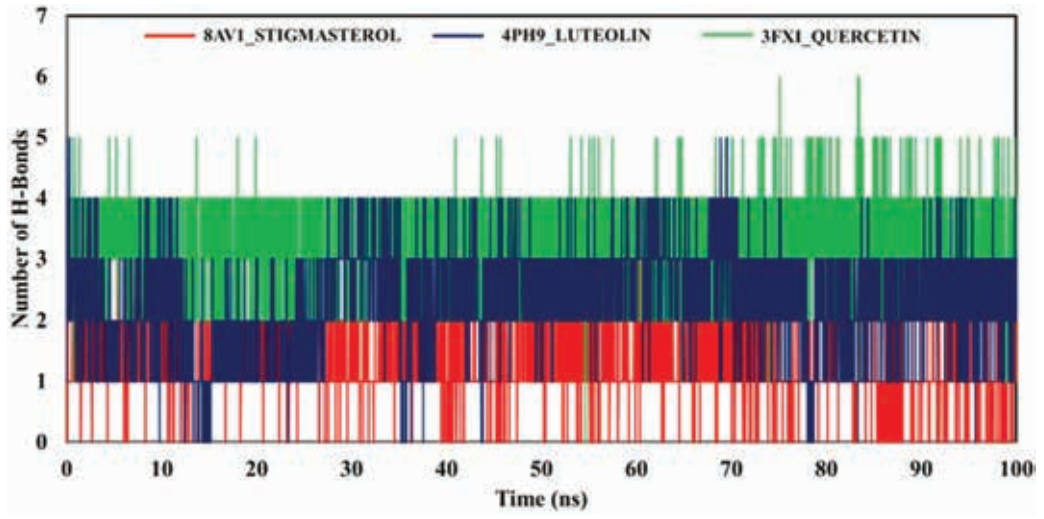

FIGURE 14 - The 3FXI_Quercetin showed the highest number of hydrogen, i.e., five, as compared to the 8AV1_Stigmasterol and 4PH9_Luteolin complex.

TABLE 3 - The MM-PBSA result of the 8AV1_Stigamsterol complex

Frames	VDWAALS	EEL	EPB	ENPOLAR	GGAS	GSOLV	TOTAL
Average	−39.97	−8.1	29.08	−4.52	−48.07	24.56	−23.51
SD	3.34	5.49	4.09	0.21	6.2	4.03	4.8
SEM	0.15	0.25	0.18	0.01	0.28	0.18	0.21

TABLE 4 - The MM-GBSA result of the 8AV1_Stigamsterol complex

Frames	VDWAALS	EEL	EGB	ESURF	GGAS	GSOLV	TOTAL
Average	−39.97	−8.1	21.8	−5.26	−48.07	16.54	−31.52
SD	3.34	5.49	3.5	0.45	6.2	3.36	4.2
SEM	0.15	0.25	0.16	0.02	0.28	0.15	0.19

TABLE 5 - The MM-PBSA result of the 4PH9_Luteolin complex

Frames	VDWAALS	EEL	EPB	ENPOLAR	GGAS	GSOLV	TOTAL
Average	−30.05	−20.24	43.36	−3.45	−50.29	39.91	−10.38
SD	2.24	3.66	4.34	0.07	3.99	4.32	2.78
SEM	0.1	0.16	0.19	0	0.18	0.19	0.12

TABLE 6 - The MM-GBSA result of the 4PH9_Luteolin complex

Frames	VDWAALS	EEL	EGB	ESURF	GGAS	GSOLV	TOTAL
Average	−30.05	−20.24	35.12	−4.74	-50.29	30.38	−19.91
SD	2.24	3.66	3.43	0.17	3.99	3.34	2.03
SEM	0.1	0.16	0.15	0.01	0.18	0.15	0.09

TABLE 7 - The MM-PBSA result of the 3FXI_Quercetin complex

Frames	VDWAALS	EEL	EPB	ENPOLAR	GGAS	GSOLV	TOTAL
Average	−21.08	−46.49	48.11	−2.8	−67.58	45.31	−22.27
SD	2.85	5.84	4.45	0.06	4.95	4.45	2.8
SEM	0.13	0.26	0.2	0	0.22	0.2	0.13

as shown in Table 8 and Supplementary Figure 6. The binding free energy calculations revealed that 8AV1_Stigmaterol showed the highest total binding free energies (MM-PBSA = -23.51, MM-GBSA = −31.52), followed by the 3FXI_Quercetin (MM-PBSA = −22.27, MM-GBSA = −30.56), and the lowest binding free energies were shown by the 4PH9_Luteoline (MM-PBSA = −10.38, MM-GBSA = −19.91).

The contribution of the individual residues was determined using per-residue decomposition analysis for all the complexes. The per-residue decomposition analysis showed that VAL45 and ILE37 were the highest energy contributing amino acids in the 8AV1_Stigmasterol complex using MM-PBSA and MM-GBSA, respectively, Supplementary Figure 7. Meanwhile, in 4PH9_Luteoline complex decomposition analysis, it was revealed that CYS36 and PRO154 were the highest contributing amino acids using MM-PBSA and MM-GBSA parameters, respectively, Supplementary Figure 8. The per-residue decomposition analysis of the 3FXI_Quercetin showed that GLU128 was the highest contributing residue using MM-PBSA and MM-GBSA analysis, as shown in the Supplementary Figure 9.

Discussion

The use of natural remedies as additional treatments alongside conventional therapies for the treatment of

TABLE 8 - The MM-GBSA result of the 3FXI_Quercetin complex

Frames	VDWAALS	EEL	EGB	ESURF	GGAS	GSOLV	TOTAL
Average	−21.08	−46.49	40.85	−3.84	−67.58	37.02	−30.56
SD	2.85	5.84	4.6	0.12	4.95	4.61	2.3
SEM	0.13	0.26	0.21	0.01	0.22	0.21	0.1

diabetes and its associated complications is increasing worldwide, with many plants in different countries known to have effects in lowering blood sugar (41). Indian literature from the past has documented the anti-diabetic properties of more than 800 plants, while ethnopharmacological research has shown that over 1200 plants can be used for their anti-diabetic effects (42). The primary reason for postprandial hyperglycemia is the action of α-amylase and α-glucosidase enzymes, which break down carbohydrates. The process of breaking down carbohydrates starts with α-amylase, which breaks the 1,4-glycosidic bonds in polysaccharides, converting them into disaccharides. Subsequently, α-glucosidase transforms the disaccharides into monosaccharides, resulting in elevated blood glucose levels after meals (43). Delaying the digestion of carbohydrates and reducing postprandial glucose levels, inhibitors of alpha-amylase and alpha-glucosidase aid in controlling high plasma glucose levels. Investigators typically seek out natural substances that can control elevated blood sugar levels by reducing the activity of alpha-glucosidase and alpha-amylase, leading to decreased adverse effects such as diarrhea, nausea, and abdominal pain (44).

During an *in vitro* study, researchers analyzed cowpea protein hydrolysates (PH) and ultrafiltered peptide fractions (UFPF) for their ability to inhibit enzymes like α-amylase, α-glucosidase, and dipeptidyl peptidase IV. The findings indicated that both PH and UFPF demonstrated the most potent inhibitory activity against the enzymes under investigation (45). A different research study found that cowpea seed protein hydrolysates demonstrated greater effectiveness in inhibiting α-amylase (46). The efficacy of sorghum-cowpea composite biscuits in inhibiting starch hydrolysis enzymes like α-amylase and α-glucosidase was examined. This combination could potentially contribute to the reduction of postprandial hyperglycemia by targeting specific enzymes (47). Aldose reductase can be found in almost all mammalian cells, with significantly higher levels in organs such as the cornea, retina, lens, myelin sheath, kidney, and sciatic nerves. These organs are prone to diabetic complications (48). The accumulation of polyol in lens fibers, due to the heightened activity of the polyol pathway, results in the influx of water and the generation of osmotic stress. Consequently, this leads to tissue damage through osmotic swelling, changes in membrane permeability, and oxidative stress. The polyol pathway has garnered considerable focus in the clinical treatment of secondary diabetes complications because of these outcomes (49). The breakdown of glucose through the polyol pathway by enzymes leads to the production of sorbitol, which is a harmful substance for tissues as it increases osmotic pressure and can cause tissue swelling. By inhibiting the activity of aldose reductase, which is mainly present in the lens's epithelial cells, it is possible to prevent the development of cataracts (23). The literature does not contain any data on the *in vitro* anti-diabetic properties, such as the inhibition of α-amylase, α-glucosidase, and aldose reductase activities, of the entire *V. unguiculata* plant. Therefore, our current study aims to assess the ability of the whole *V. unguiculata* plant to inhibit alpha amylase, alpha glucosidase, and aldose reductase enzymes. Among all the samples tested, the crude extract exhibited the most significant inhibitory activity against alpha amylase, alpha glucosidase, and aldose reductase with IC_{50} values of 0.202 mg/mL, 0.111 mg/mL and 15.823 µg/mL, respectively.

Moreover, the current study also used a network pharmacology approach to come up with a complex network connecting the compounds of *V. unguiculata* and the potential protein targets. Unlike most previous studies that focus on single-target drugs, our approach considers multiple targets and their interactions, including those with T2DM. For instance, previous works have defined involvement of proteins such as GSK3B in insulin signaling and glucose metabolism, but this work affords elaborate information to how multiple compounds influence GSK3B, PTGS2, and TLR4 at the same time. This multiple-target approach is in harmony with modern practices in network pharmacology, where the impact of drug candidates on multiple interconnected biological targets is researched. The GO and KEGG study provides insight into important signaling, including PTGS2, GSK3B, and TLR4, which are influenced by the *V. unguiculata* constituents and evidently support the potential multi-target anti-diabetic activity. However, the multi-target analysis conducted in this study increases the likelihood of off-target effects and paves the way for undesired biological responses. Furthermore, the non-specific interactions of the studied protein with multiple signaling protein may alter biological responses and produce adverse effects. This study focused on the computational predictions and *in vitro* analysis; however, to validate the safety and specificity of the compounds, *in vivo* and *in vitro* studies will be required. GSK3B is implicated in insulin signaling and glucose homeostasis. Several studies have revealed that GSK3B knockdown promotes insulin signaling and corrects glucose intolerance in diabetic animal models. Inhibition of GSK3B is important for regulating hyperglycemia and insulin resistance since it is targeted by these inhibitors (50). Similarly, PTGS2, commonly known as COX-2, is an enzyme that plays a significant role in inflammation (51). Inflammatory processes play a crucial role in the evolution and progression of insulin resistance and consequent type 2 diabetes. Select members of the COX-2 enzyme have been

studied as an anti-inflammatory, which may have beneficial effects on other metabolic complications related to diabetes.

In contrast, TLR4 contributes to the immune system, and its overactivation is suggested to induce the inflammation that drives insulin resistance (52). It has been proposed that using specific inhibitors or antagonists of TLR4 may present a useful strategy for the modulation of chronic inflammation and the improvement of insulin resistance in type 2 diabetes. Multi-target therapy in this case entails the identification of a number of pathways or proteins that are related to the disease and treating all of them at once. This is thought to be a better approach to treating various intricate conditions like type 2 diabetes by combating various causes.

In the future, the findings of this study can provide a good foundation for subsequent research into the medical value of compounds of extracts from *V. unguiculata*. *In vivo* studies can also be undertaken to validate the findings made in silico and further examine the PK/PD characteristics of these compounds. We also supposed that the other target proteins may be required for further research, and they may discover the new multi-target drug for the better treatment of T2DM, especially GSK3B, PTGS2, and TLR4. Further insights on how these compounds collectively function might be helpful in designing improved combination therapies, which could be beneficial in patients. Hence, this work not only opens more evidence about network pharmacology as a strategy for searching the targets and new drugs' designs but also shows the application of plant extracts as a treatment for chronic diseases.

Conclusion

In the present study, the *V. unguiculata* was evaluated for anti-diabetic potential using *in vitro*, network pharmacology, and computational approaches. The results of the *in vitro* analysis using *V. unguiculata* phytochemicals showed significant activity against the diabetes targets such as α-amylase, α-glucosidase, and aldose reductase enzymes concerned with glucose metabolism. Furthermore, the network pharmacology studies showed 88 shared target genes associated with T2DM, and the possible drug targets, i.e., GSK3B, PTGS2, and TLR4 were deemed as hub genes in the PPI network. The *in vitro* and network pharmacology studies were followed by the computational studies using virtual screening, MD simulation, and binding free energies calculations. The virtual screening showed the phytochemicals, i.e., Quercetin, Luteolin, and Stigmasterol, with the highest binding energy against the diabetes targets. The MD simulation studies were conducted following the virtual screening to assess the dynamic stability, and the results showed that the complexes remain stable. The binding free energy studies using MM-PBSA, and MM-GBSA exhibited negative and favorable binding energies, hence indicating the stability of the complexes. In conclusion, the study showed that *V. unguiculata* phytochemicals exhibited significant activity against the diabetes targets using *in vitro*, network pharmacology, and comprehensive computational approaches; however, to employ the *V. unguiculata* phytochemicals clinically additional studies such as comprehensive *in-vivo* approaches will be required.

Limitations of the study

The limitations of this study include the lack of *in vivo* validation despite the fact that the present study includes *in vitro* analysis, network pharmacology approaches, and comprehensive computational approaches. In order to validate the results of the study, the *in vivo* studies, including pharmacokinetics, pharmacodynamics, and toxicities associated with the top hits, should be conducted. Furthermore, the study mainly focused on identifying the molecular targets and binding affinities; the stability of the compounds in the *in vivo* system, such as metabolism, protein binding, and solubility, was not studied. Similarly, the computational studies offer key insight into the ligand's interaction with the target protein; however, the computational studies are influenced by various factors such as the type of force field used and the input of the structure provided. Furthermore, the study also lacks *in vitro* and *in vivo* studies to assess the off-target effect and to explore the safety profile of the compounds; thus, to establish the specificity, selectivity, and safety of the studied compounds, comprehensive *in vitro* and *in vivo* studies will be required.

Authors contributors

HS: Data curation, Writing – original draft; Fatima Noor: Data curation, Writing – original draft; SMS: Data analysis, Writing – original draft; JSAO: Data curation, Writing – original draft; AUK: Data curation, Writing – original draft, MD: Data curation, Writing – final draft; HK: Designing, supervision, Writing – final draft

Acknowledgment

The authors are thankful to HEC Pakistan for financial support under project No: (Ref No. 20-16097/NRPU/R&D/HEC/2021 2021). The authors extend their appreciation to the Princess Nourah Bint Abdulrahman University Researchers Supporting Project number (PNURSP2025R13), Princess Nourah Bint Abdulrahman University, Saudi Arabia.

Data availability statement

The data that support the findings of the present study are available from the corresponding authors upon reasonable request.

Disclosures

Conflict of interest: The authors of this article have a conflict of interest

Financial support: This research received no specific grant from any funding agency in the public, commercial, or not-for-profit sectors

References

1. Noor F, Rehman A, Ashfaq UA, et al. Integrating network pharmacology and molecular docking approaches to decipher the multi-target pharmacological mechanism of Abrus precatorius L. acting on diabetes. Pharmaceuticals (Basel). 2022;15(4):414. CrossRef PubMed

2. Ruze R, Liu T, Zou X, et al. Obesity and type 2 diabetes mellitus: connections in epidemiology, pathogenesis, and treatments. Front Endocrinol (Lausanne). 2023;14:1161521. CrossRef PubMed
3. Mishra S, Kumar S, Darokar MP, et al. Novel bioactive compound from the bark of Putranjiva roxburghii Wall. Nat Prod Res. 2021;35(10):1738-1740. CrossRef PubMed
4. Ahmad E, Lim S, Lamptey R, et al. Type 2 diabetes. Lancet. 2022;400(10365):1803-1820. CrossRef PubMed
5. Galicia-Garcia U, Benito-Vicente A, Jebari S, et al. Pathophysiology of type 2 diabetes mellitus. Int J Mol Sci. 2020;21(17):6275. CrossRef PubMed
6. Demir S, Nawroth PP, Herzig S, et al. Emerging targets in type 2 diabetes and diabetic complications. Adv Sci (Weinh). 2021;8(18):e2100275. CrossRef PubMed
7. Reed J, Bain S, Kanamarlapudi V. A review of current trends with type 2 diabetes epidemiology, aetiology, pathogenesis, treatments and future perspectives. Diabetes Metab Syndr Obes. 2021;14:3567-3602. CrossRef PubMed
8. Noor F, Tahir Ul Qamar M, Ashfaq UA, et al. Network pharmacology approach for medicinal plants: review and assessment. Pharmaceuticals (Basel). 2022;15(5):572. CrossRef PubMed
9. Noor F, Asif M, Ashfaq UA, et al. Machine learning for synergistic network pharmacology: a comprehensive overview. Brief Bioinform. 2023;24(3):120. CrossRef PubMed
10. Boukar O, et al., Cowpea (Vigna unguiculata): Genetics, genomics and breeding. 2019;**138**(4):415-424. CrossRef
11. Olopade OB, et al., Glycemic responses of local beans (Vigna unguiculata (Linn Walp) varieties) in persons with Type 2 diabetes mellitus and healthy controls-An experimental study. 2020;**17**(4):100-107. CrossRef
12. Ashraduzzaman M , et al., Vigna unguiculata linn. Walp. Seed oil exhibiting anti-diabetic effects in alloxan induced diabetic rats. 2011;**9**(1):13-23.
13. Wang L, Li J, Di LJ. Glycogen synthesis and beyond, a comprehensive review of GSK3 as a key regulator of metabolic pathways and a therapeutic target for treating metabolic diseases. Med Res Rev. 2022;42(2):946-982. CrossRef PubMed
14. Yehualashet AS. Toll-like receptors as a potential drug target for diabetes mellitus and diabetes-associated complications. Diabetes Metab Syndr Obes. 2020;13:4763-4777. CrossRef PubMed
15. Martín-Vázquez E, Cobo-Vuilleumier N, López-Noriega L, et al. The PTGS2/COX2-PGE_2 signaling cascade in inflammation: pro or anti? A case study with type 1 diabetes mellitus. Int J Biol Sci. 2023;19(13):4157-4165. CrossRef PubMed
16. Cucak H, Mayer C, Tonnesen M, et al. Macrophage contact dependent and independent TLR4 mechanisms induce β-cell dysfunction and apoptosis in a mouse model of type 2 diabetes. PLoS One. 2014;9(3):e90685. CrossRef PubMed
17. Wadhwa P, Jain P, Jadhav HR. Glycogen synthase kinase 3 (GSK3): its role and inhibitors. Curr Top Med Chem. 2020;20(17):1522-1534. CrossRef PubMed
18. Mishra S, Kumar S, Ramdas, et al. Quebrachitol from Putranjiva roxburghii Wall. (Putranjivaceae) a potent antimalarial: preclinical efficacy and its interaction with PfLDH. Parasitol Int. 2023;92:102675. CrossRef PubMed
19. Singh SV, Manhas A, Singh SP, et al. A phenolic glycoside from Flacourtia indica induces heme mediated oxidative stress in Plasmodium falciparum and attenuates malaria pathogenesis in mice. Phytomedicine. 2017;30:1-9. CrossRef PubMed
20. Riyanto S, Rohman A. Antioxidant activities of Rambutan (Nephelium lappaceum L) peel in-vitro. Food Res. 2017;2(1): 119-123. CrossRef
21. Sagbo IJ, van de Venter M, Koekemoer T, et al. In-vitro antidiabetic activity and mechanism of action of Brachylaena elliptica (Thunb.) DC. Evid Based Complement Alternat Med. 2018;2018(1):4170372. CrossRef PubMed
22. Telagari M, Hullatti K. In-vitro α-amylase and α-glucosidase inhibitory activity of Adiantum caudatum Linn. and Celosia argentea Linn. extracts and fractions. Indian J Pharmacol. 2015;47(4):425-429. CrossRef PubMed
23. Patel D, Kumar R, Kumar M, et al. Evaluation of in vitro aldose reductase inhibitory potential of different fraction of Hybanthus enneaspermus Linn F. Muell. Asian Pac J Trop Biomed. 2012;2(2):134-139. CrossRef PubMed
24. Vivek-Ananth RP, Mohanraj K, Sahoo AK, et al. IMPPAT 2.0: an enhanced and expanded phytochemical atlas of Indian medicinal plants. ACS Omega. 2023;8(9):8827-8845. CrossRef PubMed
25. Nakamura Y, Afendi FM, Parvin AK, et al. KNApSAcK metabolite activity database for retrieving the relationships between metabolites and biological activities. Plant Cell Physiol. 2014; 55(1):e7. CrossRef PubMed
26. Daina A, Michielin O, Zoete V. SwissTargetPrediction: updated data and new features for efficient prediction of protein targets of small molecules. Nucleic Acids Res. 2019;47(W1): W357-W364. CrossRef PubMed
27. Kuhn M, Szklarczyk D, Pletscher-Frankild S, et al. STITCH 4: integration of protein-chemical interactions with user data. Nucleic Acids Res. 2014;42(Database issue):D401-D407. CrossRef PubMed
28. Barrett T, Wilhite SE, Ledoux P, et al. NCBI GEO: archive for functional genomics data sets--update. Nucleic Acids Res. 2013;41(Database issue):D991-D995. PubMed
29. Huang DW, Sherman BT, Tan Q, et al. DAVID Bioinformatics Resources: expanded annotation database and novel algorithms to better extract biology from large gene lists. Nucleic Acids Res. 2007;35(Web Server issue)(suppl 2):W169-75. CrossRef PubMed
30. Shannon P, Markiel A, Ozier O, et al. Cytoscape: a software environment for integrated models of biomolecular interaction networks. Genome Res. 2003;13(11):2498-2504. CrossRef PubMed
31. von Mering C, Huynen M, Jaeggi D, et al. STRING: a database of predicted functional associations between proteins. Nucleic Acids Res. 2003;31(1):258-261. CrossRef PubMed
32. Rose PW, Bi C, Bluhm WF, et al. The RCSB Protein Data Bank: new resources for research and education. Nucleic Acids Res. 2013;41(Database issue):D475-D482. PubMed
33. Pettersen EF, Goddard TD, Huang CC, et al. UCSF Chimera—a visualization system for exploratory research and analysis. J Comput Chem. 2004;25(13):1605-1612. CrossRef PubMed
34. Dundas J, Ouyang Z, Tseng J, et al. CASTp: computed atlas of surface topography of proteins with structural and topographical mapping of functionally annotated residues. Nucleic Acids Res. 2006;34(Web Server issue)(suppl 2):W116-8. CrossRef PubMed
35. Sargis Dallakyan, Arthur J Olson. Small-molecule library screening by docking with PyRx. Methods Mol Biol. 2015;1263:243-50. CrossRef
36. Chen M, Chen X, Chen Q, et al. Potential candidates from a functional food Zanthoxyli Pericarpium (Sichuan pepper) for the management of hyperuricemia: high-through virtual screening, network pharmacology and dynamics simulations. Front Endocrinol (Lausanne). 2024;15:1436360. CrossRef PubMed
37. Discovery studio. Accelrys2.1, 2008. 420. Online (Accessed February 2025)

38. Bisht A, Tewari D, Kumar S, et al. Network pharmacology, molecular docking, and molecular dynamics simulation to elucidate the mechanism of anti-aging action of Tinospora cordifolia. Mol Divers. 2024;28(3):1743-1763. CrossRef PubMed
39. Joshi T, Joshi T, Sharma P, et al. Molecular docking and molecular dynamics simulation approach to screen natural compounds for inhibition of Xanthomonas oryzae pv. Oryzae by targeting peptide deformylase. J Biomol Struct Dyn. 2021;39(3):823-840. CrossRef PubMed
40. Rajesh GD, Apte K, Abhirami PV, et al. Comprehensive in silico analysis of flavonoids in breast cancer using molecular docking, ADME, and molecular dynamics simulation approach. Pept Sci (Hoboken). 2025;117(1):24391. CrossRef
41. Shirin Hasani-Ranjbar, Bagher Larijani, Mohammad Abdollahi. A Systematic Review of the Potential Herbal Sources of Future Drugs Effective in Oxidant-Related. Inflam Allergy – Drug Targets. 2009;8(1):2-10. CrossRef.
42. Mishra DSB. An analytical review of plants for anti diabetic activity with their phytoconstituent & mechanism of action. Int J Pharm Sci Res. 2009;1(1):29-46. CrossRef
43. Ouassou H, Zahidi T, Bouknana S, et al. Inhibition of α-glucosidase, intestinal glucose absorption, and anti-diabetic properties by *Caralluma europaea*. Evid Based Complement Alternat Med. 2018 Aug 29;2018:9589472. CrossRef
44. Jhong CH, Riyaphan J, Lin SH, et al. Screening alpha-glucosidase and alpha-amylase inhibitors from natural compounds by molecular docking in silico. Biofactors. 2015;41(4):242-251. CrossRef PubMed
45. Castañeda-Pérez E, Jiménez-Morales K, Quintal-Novelo C, et al. Enzymatic protein hydrolysates and ultrafiltered peptide fractions from Cowpea Vigna unguiculata L bean with in-vitro anti-diabetic potential. J Iran Chem Soc. 2019;16(8):1773-1781. CrossRef
46. Inhibition of the in vitro activities of α-amylase, α-glucosidase and pancreatic lipase by yellow field pea (Pisum sativum L.) protein hydrolysates. International J Food Sci Technol. 2019; 54(6):2021-2034. CrossRef.
47. Oluwafunmilayo OO. Inhibitory effects of sorghum-cowpea composite biscuit on starch-hydrolysing enzymes. Kwara State University; 2019. CrossRef
48. Kim HM, et al. Inhibition of aldose reductase from rat lenses by methanol extracts from Korean folk plants. Nat Prod Sci. 2010;16(4):285-290. CrossRef
49. Halder N, Joshi S, Gupta SK. Lens aldose reductase inhibiting potential of some indigenous plants. J Ethnopharmacol. 2003;86(1):113-116. CrossRef PubMed
50. Jope RS, Johnson GVW. The glamour and gloom of glycogen synthase kinase-3. 2004;**29**(2):95-102. CrossRef
51. Oshima M, et al., Suppression of intestinal polyposis in ApcΔ716 knockout mice by inhibition of cyclooxygenase 2(COX-2). Cell;1996;87(5):803-809. CrossRef
52. Shi H, et al., TLR4 links innate immunity and fatty acid–induced insulin resistance. 2006;**116**(11):3015-3025. CrossRef

DTI
Drug Target Insights 2025; 19: 91-98
ISSN 1177-3928 | DOI: 10.33393/dti.2025.3592
ORIGINAL RESEARCH ARTICLE

Co-occurrence of genes encoding carbapenem resistance and aminoglycoside resistance in clinical isolates of Enterobacterales

Shradha Smriti[1], Gaurav Verma[1], Sujit Pradhan[2], Nipa Singh[1], Subhra Snigdha Panda[1], Ipsa Mohapatra[3], Dipti Pattnaik[1], Rajesh Kumar Dash[1], Liza Das[1]

[1]Department of Microbiology, Kalinga Institute of Medical Sciences, KIIT DU, Bhubaneswar, Odisha - India
[2]Department of Critical Care Medicine, Kalinga Institute of Medical Sciences, KIIT DU, Bhubaneswar, Odisha - India
[3]Department of Community Medicine, Kalinga Institute of Medical Sciences, KIIT DU, Bhubaneswar, Odisha - India

ABSTRACT

Introduction: This study aimed to detect the co-occurrence of carbapenem resistance genes along with aminoglycoside-modifying enzyme (AME) genes in clinical *Enterobacterales* isolates to understand the distribution of multiple resistance genes among clinical isolates.

Methods: This prospective study was conducted for six months (November 2024 to April 2025) in the department of microbiology of a tertiary care hospital. A total of 30 blood culture isolates were identified as resistant to both carbapenem and aminoglycoside antibiotics using the automated VITEK 2 compact system. The genes responsible for carbapenem resistance (bla_{NDM}, bla_{OXA-48}, bla_{KPC}, bla_{IMP}, and bla_{VIM}) were detected by multiplex real-time PCR, and the aminoglycoside-modifying enzyme genes [APH(3')-Ia, APH(2")-Ib, AAC(3)-IIc, AAC(6')-Ib, and ANT(3")-I] were detected by the conventional polymerase chain reaction method. All the clinical data, patient demographics, and molecular findings were entered in an MS Excel spreadsheet version 14.0.4734.1000 and analyzed using GraphPad/PRISM software version 10.5.0.

Results: Of the 30 *Enterobacterales* isolates, *Klebsiella pneumoniae* was the most common isolate (66.7%). Molecular detection revealed bla_{NDM} in 40% isolates and bla_{OXA48} in 10% isolates. The majority of the AME genes were in combination. The most common combination of the AME gene was AAC(6')-Ib+ AAC(3)-IIc+ ANT(3")-I + APH(3')-I detected in 4 (13.3%) isolates. The most common combination of carbapenem and aminoglycoside resistant genes was bla_{NDM} + bla_{OXA48} + AAC(6')-Ib+ AAC(3)-IIc+ ANT(3")-I+ APH(3')-I (13.3%). The bla_{OXA-48} gene had a statistically significant association with AAC(6')-Ib, ANT(3")-I, and APH(3')-I ($p < 0.05$).

Conclusion: The Co-occurence of carbapenem resistance and aminoglycoside-modifying enzyme genes in clinical *Enterobacterales* isolates limits the therapeutic option.

Keywords: Carbapenem resistance, Aminoglycoside-modifying enzymes, mCIM, eCIM, Mortality, Co-occurrence

Introduction

The increasing spread of multidrug-resistant *Enterobacterales* is a major global public health concern (1,2). Carbapenem resistance is caused either by the production of carbapenemase enzymes or by mutation in porin channels, which has led to limited treatment options (3-5). The Centers for Disease Control and Prevention (CDC) defines carbapenem resistance as non-susceptibility to at least one or more carbapenem or production of the carbapenemase enzyme (6). The Clinical and Laboratory Standards Institute (CLSI) recommends the modified carbapenem inactivation method (mCIM), EDTA-modified version (eCIM), and Carba NP for the detection of carbapenemase enzyme production (7). Carbapenemase enzymes are produced by different carbapenemase encoding genes like: Ambler class B metallo-β-lactamases (MBLs)- bla_{NDM}, bla_{VIM}, and bla_{IMP}; Class A serine β-lactamases- bla_{KPC}, and class D oxacillinase- bla_{OXA-48} (8). Aminoglycoside resistance occurs primarily due to the production of aminoglycoside-modifying enzyme genes such as aminoglycoside acetyltransferase (AAC), aminoglycoside nucleotidyltransferase (ANT), and aminoglycoside phosphotransferase (APH), which is encoded by AAC, ANT, and APH genes, respectively (9-11). These resistance genes are frequently present on mobile genetic elements (MGEs) (for example, transposons, plasmids, and integrons), which promote horizontal transfer in bacterial populations (12). Few studies have indicated that clinical isolates with carbapenem resistance genes (i.e., bla_{NDM} and bla_{OXA}) have plasmids that also harbor multiple resistance genes, leading to the limitation of effective treatment options (5,13). This study aimed to evaluate the coexistence of genes

Received: July 8, 2025
Accepted: October 1, 2025
Published online: October 27, 2025

This article includes supplementary materials

Corresponding authors:
Nipa Singh
email: nipa.singh@kims.ac.in

conferring resistance to carbapenems and aminoglycosides in clinical isolates of *Enterobacterales.*

Materials and Methods

This prospective study was conducted for a period of six months from November 2024 to April 2025 in the department of microbiology of a tertiary care hospital.

Inclusion Criteria: All clinical isolates of *Enterobacterales* that were isolated from positive blood culture samples of patients admitted to the main intensive care units (ICUs).

Exclusion Criteria: All non-Enterobacterales isolated from positive blood culture samples, *Enterobacterales* obtained from samples other than blood, or obtained from patients admitted to ICUs other than the main ICU and wards.

Those *Enterobacterales* that were screened to be resistant to both carbapenem and aminoglycoside antibiotics phenotypically, as per CLSI 2024 guidelines, were included in the study (7). Based on the screening, 30 isolates were included, and DNA extraction of the isolates followed by molecular detection of carbapenem-resistant genes and aminoglycoside-modifying enzyme genes was done. Demographic data, clinical parameters, and outcomes of the patients were recorded and analyzed.

Sample collection and processing

Blood samples from patients diagnosed with septicemia were collected in aerobic blood culture bottles (BACT/ALERT FA and FN Plus BC bottles) under aseptic conditions. The culture bottles were incubated inside the BACT/ALERT 3D system (BioMérieux, France) until they flagged positive or upto a maximum of 5 days (14). The blood culture bottle that flagged positive was subcultured on MacConkey and blood agar plates. After incubating the plates overnight at 37°C, the isolated bacterial colony was subjected to identification and antibiotic susceptibility testing.

Identification and Antimicrobial Susceptibility Testing of Clinical Isolates

The identification and AST of the isolates were performed by an automated VITEK 2 compact system (BioMérieux, USA). All the isolates that were identified as *Enterobacterales* and were screened to be resistant to at least one carbapenem antibiotic (ertapenem, imipenem, or meropenem), as well as to any one of the aminoglycoside antibiotics (amikacin, gentamicin, tobramycin, and netilmicin), were included. The interpretation of AST was performed as per the Clinical and Laboratory Standards Institute (CLSI) 2024 M100 guidelines (7).

Phenotypic Detection of Carbapenem Resistance and Aminoglycoside Resistance

All the screened isolates resistant to both carbapenems and aminoglycosides were again phenotypically tested by the Kirby-Bauer disk diffusion method using imipenem 10 µg, ertapenem 10 µg, meropenem µg, amikacin 30 µg, gentamicin 10 µg, tobramycin 10 µg, and netilmicin 10 µg disks (HiMedia, India). *Escherichia coli* (*E. coli*) American Type Culture Collection (ATCC) 25922 was used as the quality control strain.

Phenotypic Detection of Carbapenemase Production

The modified carbapenem inactivation method (mCIM) tests were performed on all the isolates phenotypically resistant to carbapenem antibiotics as per the CLSI 2024 guidelines to detect carbapenemase-producing *Enterobacterales* (CPE) (7). For each strain tested, two tubes were prepared, each containing 2ml of Trypticase Soy Broth (TSB). One tube was EDTA-free, and the other tube was supplemented with 20µl of 0.5M EDTA. A fresh isolated colony from the test organism was inoculated into each tube using an inoculating loop.

A 10 µg meropenem disk (HiMedia, India) was dropped into each tube and incubated aerobically at 35°C for 2-4 hours. Following incubation, meropenem disks were removed from both the tubes and placed onto Mueller-Hinton Agar (MHA) plates that had been freshly inoculated with 0.5 McFarland suspension of carbapenem-sensitive *Escherichia coli* ATCC 25922 indicator strain. Next, the plates were incubated for 16-20 hours at 35 °C. The result of the mCIM test was interpreted as negative when the zone of inhibition was ≥19 mm, positive when it measured between 6 and 15mm, and also considered positive (intermediate) if small, pinpoint colonies appeared within the 16-18 mm zone of inhibition. *E. coli* ATCC 25922 was used as the quality control strain (15,16).

Molecular Detection of Antibiotic Resistance Genes

All the study isolates (n = 30), which were phenotypically confirmed to be resistant to both carbapenem and aminoglycoside antibiotics, were subsequently subjected to DNA extraction by a commercially available spin column, as per the manufacturer's procedure (TRUPCR bacterial nucleic acid extraction kit-3B BlackBio Biotech India Ltd., Bhopal, India) (17). The purity and concentration of the extracted DNA were evaluated by measuring 1 µL of the eluted DNA using a NanoDrop-Multiskan Sky spectrophotometer to measure the optical density at 260 nm and 280 nm with an absorbance ratio of ~1.8-2.0, which is considered a purity indicator of DNA samples (18).

Genes encoding carbapenem resistance (bla_{NDM}, bla_{OXA48}, bla_{KPC}, bla_{VIM}, and bla_{IMP}) were detected using TaqMan hydrolysis probe-based multiplex real-time polymerase chain reaction (PCR) (QuantStudio 5, Applied Biosystems, Waltham, MA, USA) by commercially available TRUPCR UTI AST Panel kit (19). The kit has a two-tube PCR assay, in tube one, primers and probe for bla_{KPC}, bla_{NDM}, and bla_{VIM}, and in the second tube, primers and probe of bla_{OXA-48} and bla_{IMP} were added. The assay was performed by preparing a final volume of 25 µL reaction, consisting of 20 µL Master Mix and 5 µL of DNA template.

The genes encoding aminoglycoside resistance genes [APH(3')-Ia, APH(2")-Ib, AAC(3)-IIc, AAC(6')-Ib, and ANT(3")-I] were detected by the conventional PCR method using previously published primers listed in supplementary Table I. The samples were amplified under different cycling conditions using a thermal cycler (Mastercycler Nexus Gradient PCR, Eppendorf, Germany) [supplementary Table II]. The thermal cycling protocol for AAC(6')-Ib, ANT(3")-I, and APH(3)-Ia was 95°C for 5 mins, followed by 35 cycles of 1 min at 95°C, 45 sec at 55°C, 1 min at 72°C, and final extension for 5 mins at 72°C. The PCR cycling protocol for AAC(3)-IIc and APH(2")-Ib was

95°C for 5 mins, followed by 35 cycles of 1 min at 95°C, 45 sec at 57°C, 1 min at 72°C, and final extension for 5 mins at 72°C. After amplification, 10 µL of the amplified DNA product was separated on 2% tris-Acetate Ethylene diamine tetraacetic acid (TAE) agarose gel electrophoresis and stained with ethidium bromide (final concentration: 0.5 µg/mL). After agarose gel electrophoresis, the amplified DNA band was visualized using the gel documentation system E-Box CX5 (Vilber, France). The different amplified gel products were distinguished using the molecular weight marker in the gel. Each PCR run included *Escherichia coli* ATCC 25922 as a negative control to ensure the absence of non-specific amplification.

Statistical Analysis

All the data (patient demographics, clinical parameters, and outcome) were entered into an MS Excel spreadsheet version 14.0.4734.1000. Analysis of the data was performed using the GraphPad /PRISM software version 10.5.0. A *p*-value of <0.05 was considered statistically significant.

Ethical Clearance

Clinical samples were collected after getting approval from the Institute Ethics Committee (IEC) (Ethics approval number: KIIT/KIMS/ IEC/1857/2024), with a waiver of patient consent provided due to de-identification of collected data.

Results

During the study period, 94 clinical *Enterobacterales* isolates were obtained from positive blood culture samples. Of these, 30 isolates that were phenotypically confirmed to be resistant to both carbapenems and aminoglycosides were subjected to phenotypic and molecular detection of carbapenem and aminoglycoside resistance. Among these, *Klebsiella pneumoniae* was the most prevalent (66.7%, 20/30), followed by *Escherichia coli* (20%, 6/30), *Proteus mirabilis* (6.7%, 2/30), *Enterobacter cloacae* (3.3%, 1/30), and *Providencia rettgeri* (3.3%, 1/30). Most of the isolates were recovered from male patients (66.7%), and the most common age group was 51-60 and 61-70 years (23.3% each).

The carbapenemase production of all the 30 isolates was done by the modified carbapenem inactivation method (mCIM), and 27 (90%) tested positive, indicating that carbapenem resistance was primarily mediated by carbapenemase enzymes.

Molecular Detection of Carbapenem-Resistant Genes

Detection of carbapenem-resistant genes (bla_{NDM}, bla_{OXA48}, bla_{IMP}, bla_{VIM}, and bla_{KPC}) using the multiplex real-time PCR. Only bla_{NDM} and bla_{OXA-48} genes were detected, and all other genes were undetected. The real-time PCR amplification plots of bla_{NDM} and bla_{OXA48} are shown in Figure 1.

Molecular Detection of Aminoglycoside-Modifying Enzyme Genes

Five different aminoglycoside-modifying enzyme (AME) genes, APH(3')-Ia, APH(2")-Ib, AAC(3)-IIc, AAC(6')-Ib, and ANT(3")-I were detected in the 30 isolates using conventional PCR. Representative gel images are shown in Figures 2 (a), (b), and (c).

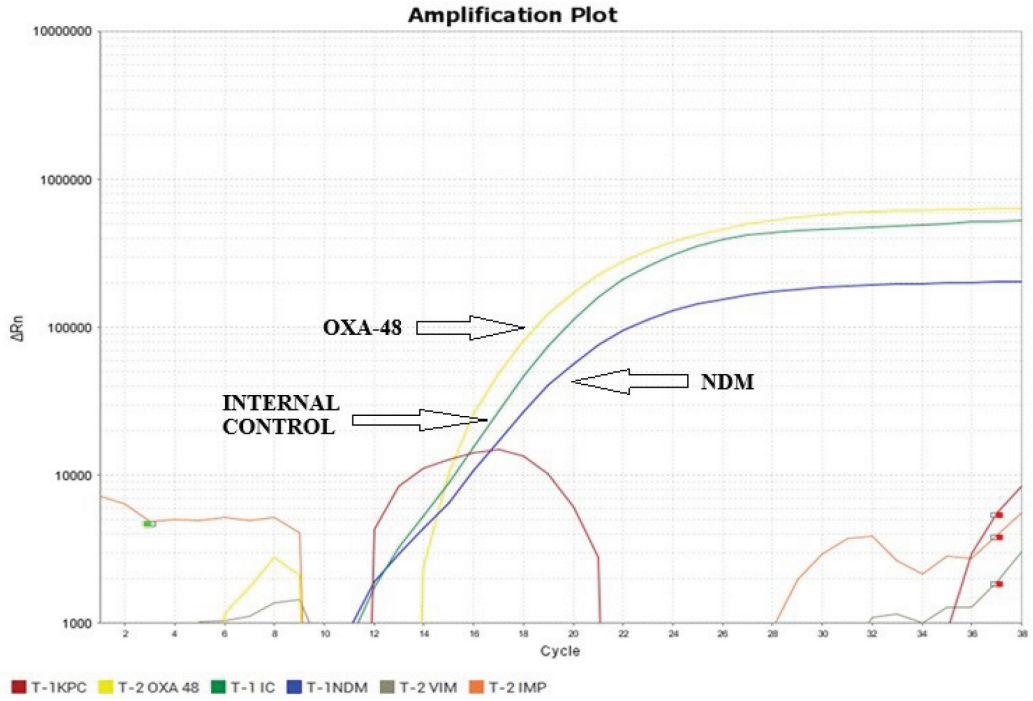

FIGURE 1 - Multiplex real-time PCR amplification plot of bla_{NDM} and bla_{OXA48}.

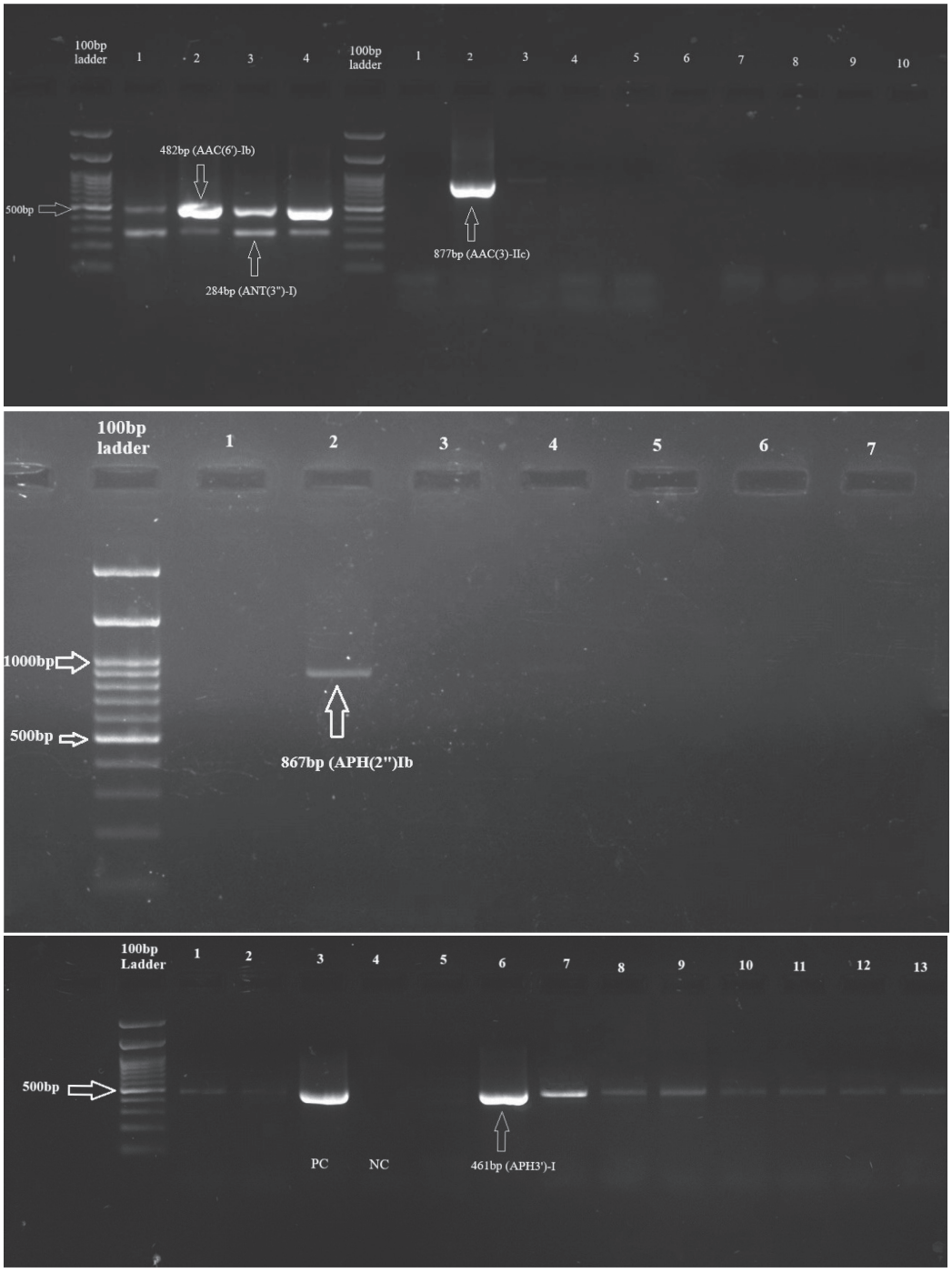

FIGURE 2 - Agarose gel image representing various amplifications of AME genes (a) multiplex PCR of AAC(6')-Ib and ANT(3")-I, lane 6-10: AAC(3)-IIc (b) APH(2")-Ib (c) APH(3')-I.

Detection of carbapenem resistance genes and aminoglycoside resistance genes

Among the carbapenem resistance genes, bla_{NDM} was detected in 12 (40%) isolates, bla_{OXA-48} was found in 3 (10%) isolates, and bla_{NDM} + bla_{OXA48} genes were detected in 13 (43.3%) isolates. In two bacterial isolates bla_{NDM} and bla_{OXA48} genes were undetected.

Detection of AME genes revealed AAC(6')-Ib and APH(3')-I alone were found in 2 (6.7%) isolates each. The most common combination of aminoglycoside resistance genes was AAC(6')-Ib+ AAC(3)-IIc+ ANT(3")-I + APH(3')-I detected in 4 (13.3%) isolates. No isolate harbored the ANT(3")-I gene alone; it was present along with the other AME genes [Figure 3].

Co-occurrence of carbapenem resistance genes and aminoglycoside-resistant genes

Multiple resistance genes were found in various isolates. The most common combination of genes was bla_{NDM}+bla_{OXA48+} AAC(6')-Ib+ AAC(3)-IIc+ ANT(3")-I+ APH(3')-I (13.3%, 4/30), followed by bla_{NDM}+bla_{OXA48}+ AAC(6')-Ib+ ANT(3")-I (10%, 3/30) of the isolates [Table 1].

Association of bla_{NDM} and bla_{OXA-48} genes with aminoglycoside-modifying enzyme genes in clinical isolates

The association between the 5 AME genes and carbapenem-resistant genes was assessed. No significant association was observed between bla_{NDM} and any of the AME genes ($p > 0.05$). The bla_{OXA48} gene showed an association with AAC(6')-Ib ($p = 0.044$), ANT(3'')-I ($p = 0.007$), and APH(3')-I ($p = 0.030$) [Table 2].

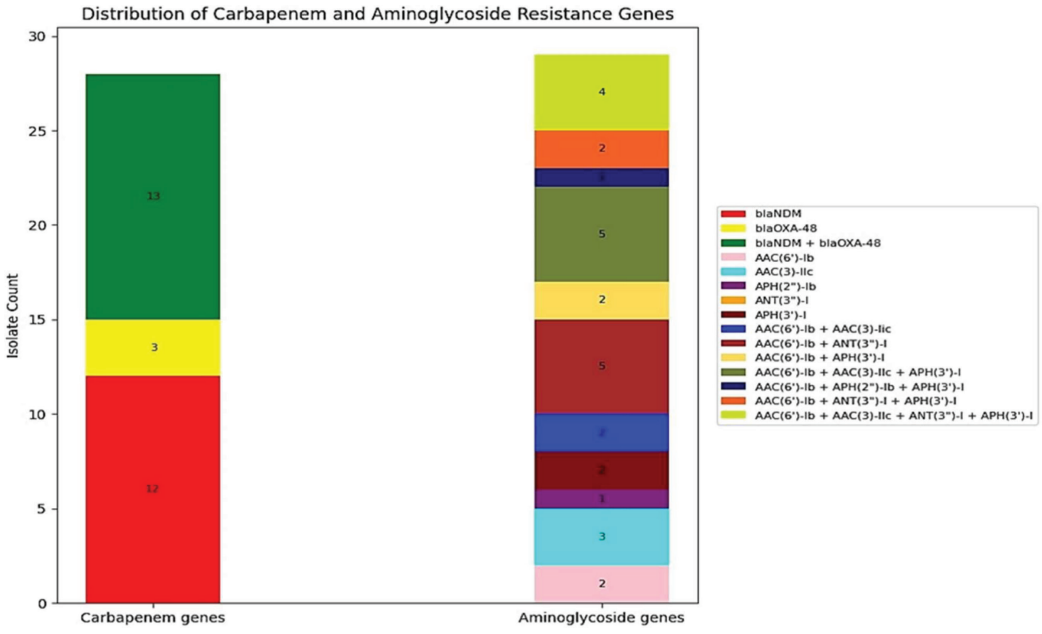

FIGURE 3 - Distribution of the carbapenem and aminoglycoside resistance genes.

TABLE 1 - Distribution of carbapenem resistance genes coexisting with aminoglycoside-modifying enzyme genes

Co-occurrence of genes mediating carbapenem and aminoglycoside resistance							Total Isolates (N = 30)	
Carbapenem resistance genes detected		Aminoglycoside-modifying enzyme genes detected					Number of isolates	Frequency (%)
blaNDM	*blaOXA48*	AAC(6')-Ib	AAC(3)-IIc	APH(2")-Ib	ANT(3")-I	APH(3')-I		
+	–	+	–	–	–	–	**1**	**3.3%**
+	–	–	+	–	–	–	**3**	**10%**
+	–	–	–	+	–	–	**1**	**3.3%**
+	–	–	–	–	–	+	**1**	**3.3%**
+	–	+	–	–	+	–	**1**	**3.3%**
+	–	+	+	–	–	–	**2**	**6.7%**
+	–	+	–	–	–	+	**1**	**3.3%**
+	–	+	+	–	–	+	**2**	**6.7%**
+	–	+	–	–	+	+	**1**	**3.3%**
–	+	–	–	–	–	+	**1**	**3.3%**
–	+	+	–	–	+	–	**1**	**3.3%**
–	+	+	+	–	–	+	**1**	**3.3%**
+	+	+	–	–	+	–	**3**	**10%**
+	+	+	–	–	+	+	**2**	**6.7%**
+	+	+	–	+	–	+	**1**	**3.3%**
+	+	+	+	–	–	+	**2**	**6.7%**
+	+	+	+	–	+	+	**4**	**13.3%**

TABLE 2 - Association of bla_{NDM} and bla_{OXA48} genes with AME genes in clinical *Enterobacterales* isolates

Antibiotic resistance genes	AAC(6')-Ib	AAC(3)-IIc	APH(2")-Ib	ANT(3'')-I	APH(3')-I
bla_{NDM} positive (N = 25)	20	12	11	2	14
bla_{NDM} negative (N = 5)	4	2	1	0	3
***p*-value**	>0.05	0.743	0.512	0.317	0.869
bla_{OXA48} positive (N = 16)	15	7	10	1	12
bla_{OXA48} negative (N = 14)	9	7	2	1	5
***p*-value**	**0.044**	0.732	0.922	**0.007**	**0.03**

In-hospital mortality in patients infected with multiple resistance genes

The rate of in-hospital mortality among patients infected with *Enterobacterales* isolates harboring multiple resistance genes was 43.3%. These isolates carried both carbapenem resistance genes (bla_{NDM} and bla_{OXA48}) along with one or more aminoglycoside-modifying enzymes (AMEs) genes.

Discussion

In this study, we phenotypically detected carbapenemase production in 30 clinical *Enterobacterales* isolates by the modified carbapenem inactivation method (mCIM). Approximately 90% of these isolates were carbapenemase producers, indicating that enzyme production plays a significant role in carbapenem resistance in *Enterobacterales*. This is consistent with the Verma et al. and Gallego et al. studies (16, 23). Furthermore, all mCIM-positive isolates were further tested for the EDTA carbapenem inactivation method (eCIM), and all of them were metallo-β-lactamase producers.

We found that bla_{NDM} was the most common carbapenem resistance gene, detected in 40% of the isolates, either individually or in combination with bla_{OXA48}. The bla_{OXA48} gene was found in 10% of the isolates, while the co-occurrence of bla_{NDM} and bla_{OXA48} was detected in 43.3% of the isolates. The high prevalence of these genes is consistent with reports from other parts of India and European countries, where bla_{NDM} and bla_{OXA48} are the frequent carbapenem resistance genes found in clinical *Enterobacterales* isolates (24-28). Several other studies have also documented the co-carriage of bla_{OXA48} and bla_{NDM} genes, which is in congruence with our findings (29-31). None of the isolates tested positive for the bla_{VIM}, bla_{KPC}, or bla_{IMP} genes in our study. Few Indian studies have similarly identified bla_{NDM} and bla_{OXA48} to be the most common genes detected, while bla_{KPC} remains infrequently detected in *Enterobacterales* (24,25).

Among the aminoglycoside-modifying enzyme (AME) genes, both AAC(6')-Ib and APH(3')-I were detected individually in 6.7 % of the isolates. However, the coexistence of multiple AME genes was more frequent. The most common AME gene combination was AAC(6')-Ib + AAC(3)-IIc + ANT(3")-I + APH(3')-I gene, with a positivity rate of 13.3%. The prevalence of coexisting genes has also been reported by Nie Lu et al. (32). Bacteria can acquire antimicrobial resistance genes (ARGs) through gene mutations under constant antibiotic selection pressure. ARGs are found on mobile genetic elements (MGEs), including plasmids, transposable elements, and bacteriophages (33). The coexistence of multiple resistance genes could be attributed to IncF plasmids, which are well-known carriers of extended-spectrum β-lactamases, carbapenemase, aminoglycoside-modifying enzymes, and plasmid-mediated quinolone resistance (PMQR) genes (34). A study conducted in Spain found that the plasmid conferring aminoglycoside resistance in *Enterobacterales* belongs to the IncF, IncFIA, or IncFIB incompatibility groups (35). Few other studies have also provided evidence suggesting that these plasmids play a crucial role in the dissemination of aminoglycoside resistance genes in drug-resistant bacteria (22).

Importantly, the study demonstrated an increased co-occurrence of carbapenem resistance genes and aminoglycoside resistance genes. The most common co-occurring resistance genes were: bla_{NDM} + bla_{OXA48} + AAC(6')-Ib + AAC(3)-IIc + ANT(3")-I + APH(3')-I, which were detected in 13.3% of the isolates, followed by bla_{NDM} + bla_{OXA48} + AAC(6')-Ib + ANT(3")-I, which were found in 10% of the isolates. Wangkheimayum J et al. reported a high prevalence of carbapenem and colistin resistance in aminoglycoside-resistant *Enterobacterales*. However, they reported that most of the CRE isolates did not carry any carbapenemase genes, indicating an alternative resistance mechanism (22).

The present study investigated the association between all five aminoglycoside-modifying enzyme (AME) genes and carbapenem resistance genes. The bla_{OXA48} gene and three specific AME genes: AAC(6')-Ib (p = 0.044), ANT(3")-I (p = 0.007), and APH(3')-I (p = 0.030) were found to have a statistically significant association. This finding could be due to the co-localization of these resistance genes on conjugative plasmids, like IncF, IncL/M, or other broad-host-range plasmids, which facilitate their horizontal transmission (36,37).

The overall in-hospital mortality was 43.3% among patients harboring multiple resistance genes (bla_{NDM}, bla_{OXA48}, and at least one AME gene). This is in agreement with Baek et al., who reported a 30-day mortality rate of approximately 40.9% in CRE-infected patients harboring multiple carbapenem-resistant genes (38). A systematic review done by Falagas et al. further indicated that CRE-attributable deaths ranged from 26% to 44% (39). There are very limited studies reporting the presence of AME genes attributable to death in patients.

The presence of carbapenem resistance genes along with one or more aminoglycoside-modifying enzyme genes is a

growing concern, as it limits effective treatment options. This co-occurrence of multiple resistance genes could be due to a combination of mutation accumulation or by horizontal transfer of resistance genes via plasmids, transposons, and integrons, ultimately forming clusters of resistance genes known as "antimicrobial resistance islands" (33).

The study has certain limitations; it was conducted in a single tertiary care center with a limited sample size, so the findings cannot be fully generalizable to other regions or healthcare settings. Hence, further multi-centric studies should be conducted to confirm our findings. The sequencing of the resistant genes was not done, which would have provided further confirmation and characterization of those genes. Furthermore, we documented the co-occurrence of carbapenem resistance genes and aminoglycoside-modifying enzyme genes; however, we did not analyze the clinical outcome of the patients harboring multiple resistance genes.

Conclusion

This study highlights the increasing epidemiological risk posed by multidrug-resistant organisms with multiple resistance genes. It specifies the presence of bla_{NDM} and bla_{OXA48} in carbapenem-resistant Enterobacterales, along with circulating aminoglycoside-modifying enzyme genes in the eastern region of India. The coexistence of these genes limits the available therapeutic options, making these infections difficult to manage with an alarming mortality rate.

Acknowledgments

We would like to thank Dr. A Raj Kumar Patro, Ph.D, Consultant, Molecular Biology and Advance Diagnostics, Department of Microbiology, KIMS, for the continuous support and guidance. We would also like to acknowledge Kalinga Institute of Medical Sciences, KIIT DU, for providing financial support for carrying out this work

Disclosures

Conflict of interest: The authors declare no conflict of interest.

Financial support: It was provided by Kalinga Institute of Medical Sciences, KIIT DU, for carrying out this work.

References

1. Noster J, Thelen P, Hamprecht A. Detection of multidrug-resistant Enterobacterales—from ESBLs to carbapenemases. Antibiotics (Basel). 2021;10(9):1140. CrossRef
2. Smith HZ, Hollingshead CM, Kendall B. Carbapenem-resistant Enterobacterales. StatPearls. 2025. Online
3. Morrill HJ, Pogue JM, Kaye KS, et al. Treatment options for carbapenem-resistant Enterobacteriaceae infections. Open Forum Infect Dis. 2015;2(2):ofv050. CrossRef
4. Tompkins K, van Duin D. Treatment for carbapenem-resistant Enterobacterales infections: recent advances and future directions. Eur J Clin Microbiol Infect Dis. 2021;40(10):2053-2068. CrossRef PubMed
5. Lee H, Shin J, Chung YJ, et al. Co-introduction of plasmids harbouring the carbapenemase genes, blaNDM-1 and blaOXA-232, increases fitness and virulence of bacterial host. J Biomed Sci. 2020;27(1):8. CrossRef
6. Centers for Disease Control and Prevention (CDC). About Carbapenem-resistant Enterobacterales. 2024. Online (Accessed July 2025)
7. Clinical and Laboratory Standards Institute (CLSI). Performance standards for antimicrobial susceptibility testing. 34th ed. CLSI supplement M100. 2024. Online (Accessed July 2025)
8. Loqman S, Soraa N, Diene SM, et al. Dissemination of carbapenemases (OXA-48, NDM and VIM) producing Enterobacteriaceae isolated from the Mohamed VI University Hospital in Marrakech, Morocco. Antibiotics (Basel). 2021;10(5):492. CrossRef PubMed
9. Zavascki AP, Klee BO, Bulitta JB. Aminoglycosides against carbapenem-resistant Enterobacteriaceae in the critically ill: the pitfalls of aminoglycoside susceptibility. Expert Rev Anti Infect Ther. 2017;15(6):519-526. CrossRef PubMed
10. Vidal L, Gafter-Gvili A, Borok S, et al. Efficacy and safety of aminoglycoside monotherapy: systematic review and meta-analysis of randomized controlled trials. J Antimicrob Chemother. 2007;60(2):247-257. CrossRef PubMed
11. Shaw KJ, Rather PN, Hare RS, et al. Molecular genetics of aminoglycoside resistance genes and familial relationships of the aminoglycoside-modifying enzymes. Microbiol Rev. 1993;57(1):138-163. CrossRef PubMed
12. Zavascki AP, Carvalhaes CG, Picão RC, et al. Multidrug-resistant Pseudomonas aeruginosa and Acinetobacter baumannii: resistance mechanisms and implications for therapy. Expert Rev Anti Infect Ther. 2010;8(1):71-93. CrossRef PubMed
13. Pitout JD, Nordmann P, Poirel L. Carbapenemase-producing Klebsiella pneumoniae, a key pathogen set for global nosocomial dominance. Antimicrob Agents Chemother. 2015;59(10):5873-5884. CrossRef PubMed
14. BioMérieux. BACT/ALERT® Culture Media Bottles. 2025. Online (Accessed July 2025)
15. Tsai YM, Wang S, Chiu HC, et al. Combination of modified carbapenem inactivation method (mCIM) and EDTA-CIM (eCIM) for phenotypic detection of carbapenemase-producing Enterobacteriaceae. BMC Microbiol. 2020;20(1):315. CrossRef PubMed
16. Verma G, Singh N, Smriti S, et al. Modified carbapenem inactivation method and ethylenediaminetetraacetic acid (EDTA)-carbapenem inactivation method for detection of carbapenemase-producing Enterobacterales and Pseudomonas aeruginosa. Cureus. 2024;16(6):e63340. CrossRef PubMed
17. 3B BlackBio Dx Ltd. TRUPCR® Bacterial DNA Extraction Kit. Online. (Accessed July 2025)
18. Gallagher S. Quantitation of nucleic acids with absorption spectroscopy. Curr Protoc Protein Sci. 2001;4(Appendix):4K. PubMed
19. TRUPCR Europe. TRUPCR® UTI AST Panel Kit. Online (Accessed July 2025)
20. Djagbare P, Nademdega C, Andognaba UW, et al. Detection of aac3-IIc, aac(6')-Ib and armA genes encoding aminoglycoside resistance in Klebsiella pneumoniae in Burkina Faso. Access Microbiology. 2024;6(1):e000669. CrossRef
21. Vakulenko SB, Mobashery S. Versatility of aminoglycosides and prospects for their future. Clin Microbiol Rev. 2003;16(3):430-450. CrossRef PubMed
22. Wangkheimayum J, Majumder TD, Tapadar YB, et al. Occurrence of diverse aminoglycoside modifying enzymes with coexisting extended-spectrum-β-lactamases within Enterobacteriaceae isolated in India. J Glob Antimicrob Resist. 2020;21:369-374. CrossRef PubMed
23. Gallego M, Salazar-Ospina L, Jiménez JN. The modified carbapenem inactivation method (mCIM): highly sensitive and specific tool to assess carbapenemase producing and non-producing in Gram-negative bacilli. Hechos Microbiológicos. 2022;13(2). CrossRef

24. Kazi M, Drego L, Nikam C, et al. Molecular characterization of carbapenem-resistant Enterobacteriaceae at a tertiary care laboratory in Mumbai. Eur J Clin Microbiol Infect Dis. 2015;34(3):467-472. CrossRef PubMed
25. Shanmugam P, Meenakshisundaram J, Jayaraman P. blaKPC gene detection in clinical isolates of carbapenem-resistant Enterobacteriaceae in a tertiary care hospital. J Clin Diagn Res. 2013;7(12):2736-2738. PubMed
26. Remya P, Shanthi M, Sekar U. Prevalence and clonal relatedness of NDM and OXA-48-producing Klebsiella pneumoniae in a tertiary care hospital in South India. J Lab Physicians. 2019;11(4):312-316. CrossRef PubMed
27. Albiger B, Glasner C, Struelens MJ, et al.; European Survey of Carbapenemase-Producing Enterobacteriaceae (EuSCAPE) working group. Carbapenemase-producing Enterobacteriaceae in Europe: assessment by national experts from 38 countries, May 2015. Euro Surveill. 2015;20(45). CrossRef
28. van Duin D, Perez F, Rudin SD, et al. Surveillance of carbapenem-resistant Klebsiella pneumoniae: tracking molecular epidemiology and outcomes through a regional network. Antimicrob Agents Chemother. 2014;58(7):4035-4041. CrossRef PubMed
29. Lascols C, Hackel M, Marshall SH, et al. Increasing prevalence and dissemination of NDM-1 metallo-β-lactamase in India: data from the SMART study (2009). J Antimicrob Chemother. 2011;66(9):1992-1997. CrossRef PubMed
30. Khajuria A, Praharaj AK, Kumar M, et al. Emergence of Escherichia coli co-producing NDM-1 and OXA-48 carbapenemases in urinary isolates at a tertiary care centre in Central India. J Clin Diagn Res. 2014;8(6):DC01-DC04. CrossRef PubMed
31. Das BJ, Singha KM, Wangkheimayum J, et al. Occurrence of blaOXA-48 type carbapenemase in Escherichia coli with coexisting resistance determinants: a report from India. Gene Rep. 2022;26:101459. CrossRef
32. Nie L, Lv Y, Yuan M, et al. Genetic basis of high level aminoglycoside resistance in Acinetobacter baumannii from Beijing, China. Acta Pharm Sin B. 2014;4(4):295-300. CrossRef PubMed
33. Das S, Bombaywala S, Srivastava S, et al. Genome plasticity as a paradigm of antibiotic resistance spread in ESKAPE pathogens. Environ Sci Pollut Res Int. 2022;29(27):40507-40519. CrossRef PubMed
34. Rozwandowicz M, Brouwer MSM, Fischer J, et al. Plasmids carrying antimicrobial resistance genes in Enterobacteriaceae. J Antimicrob Chemother. 2018;73(5):1121-1137. CrossRef PubMed
35. Miró E, Grünbaum F, Gómez L, et al. Characterization of aminoglycoside-modifying enzymes in enterobacteriaceae clinical strains and characterization of the plasmids implicated in their diffusion. Microb Drug Resist. 2013;19(2):94-99. CrossRef PubMed
36. Alousi S, Salloum T, Arabaghian H, et al. Genomic characterization of multidrug-resistant Escherichia coli harboring blaOXA-48 on the IncL/M-type plasmid isolated from bloodstream infection. BioMed Res Int. 2018;2018:3036143. CrossRef PubMed
37. Sabtcheva S, Stoikov I, Georgieva S, et al. Genomic characterization of 16S rRNA methyltransferase-producing Enterobacterales reveals the emergence of Klebsiella pneumoniae ST6260 harboring rmtF, rmtB, blaNDM-5, blaOXA-232 and blaSFO-1 genes in a cancer hospital in Bulgaria. Antibiotics (Basel). 2024;13(10):950. CrossRef PubMed
38. Baek MS, Kim JH, Park JH, et al. Comparison of mortality rates in patients with carbapenem-resistant Enterobacterales bacteremia according to carbapenemase production: a multicenter propensity-score matched study. Sci Rep. 2024;14(1):597. CrossRef PubMed
39. Falagas ME, Tansarli GS, Karageorgopoulos DE, et al. Deaths attributable to carbapenem-resistant Enterobacteriaceae infections. Emerg Infect Dis. 2014;20(7):1170-1175. CrossRef PubMed

DTI
Drug Target Insights 2025; 19: 99-107
ISSN 1177-3928 | DOI: 10.33393/dti.2025.3616
ORIGINAL RESEARCH ARTICLE

Ravulizumab in treatment-naïve patients with atypical hemolytic uremic syndrome: a real-world case series

Livia Maria Sorrentino[1], Candida Iacuzzo[2], Raffaela Sciri[3], Miriam Zacchia[4], Mariarosaria Iannuzzi[1], Paola Marotta[2], Piercarla Vitale[5], Chiara Taglioni[3], Floriana Secondulfo[4], Daniela Palazzetti[6], Rocco Baccaro[7]

[1]Nephrology and Hemodialysis Unit for Elective and Emergency Care, A.O.R.N. Antonio Cardarelli, Naples - Italy
[2]Nephrology, Dialysis, and Transplant Unit, A.O.U. Sangiovanni di Dio e Ruggi d'Aragona, Salerno - Italy
[3]Nephrology, Dialysis, and Kidney Transplant Unit, Azienda Ospedaliera Santa Maria della Misericordia, Perugia - Italy
[4]Nephrology Unit, Department of Translational Medical Sciences, University of Campania L. Vanvitelli, Naples - Italy
[5]Specialization School in Internal Medicine, Università degli Studi di Salerno, Salerno - Italy
[6]Università Cattolica del Sacro Cuore, Rome - Italy
[7]Fondazione Policlinico Universitario Agostino Gemelli IRCCS, Rome - Italy

ABSTRACT

Introduction: Atypical hemolytic uremic syndrome (aHUS) is a potentially life-threatening condition associated with poor clinical outcomes if not treated adequately. Eculizumab has become the standard of care, whereas ravulizumab, a second-generation, high-affinity complement C5 inhibitor, demonstrates comparable efficacy in improving renal function, hematological markers, and dialysis rates. In addition, ravulizumab offers practical advantages, including a longer dosing interval and immediate, complete, and sustained inhibition of free C5, making it a valuable therapeutic option.

Methods: Given the limited real-world experience with ravulizumab, we present a case series of six treatment-naïve aHUS patients who received ravulizumab as first-line therapy.

Results: These cases include one pregnancy-related aHUS, one postpartum case, one related to a urinary tract infection, one associated with hypertension, one with a pneumonia-related trigger, and one kidney transplant patient with a prior verotoxin-producing *E. coli* infection. Altogether, these cases illustrate the challenges in diagnosing aHUS. The choice to administer ravulizumab as first-line treatment was sometimes made in the presence of a clear clinical suspicion, even when not all minor criteria seemed to confirm the diagnosis. In most patients, renal function improved rapidly after ravulizumab administration, followed by recovery of hematological parameters, which were stable in the longer term. As improvements remained sustained over time, the possibility of discontinuing ravulizumab can be evaluated on a case-by-case basis.

Conclusion: These cases highlight the importance of early diagnosis, prompt intervention, and multidisciplinary care in managing aHUS. Ravulizumab as first-line therapy proved effective and well-tolerated, with sustained clinical improvements observed across diverse real-world scenarios.

Keywords: Atypical hemolytic uremic syndrome, Diagnosis, Ravulizumab, Thrombotic microangiopathy, Treatment

Introduction

Atypical hemolytic uremic syndrome (aHUS) is a rare form of thrombotic microangiopathy (TMA) that is characterized by thrombocytopenia, microangiopathic hemolytic anemia, and renal impairment (1,2). In addition, extrarenal manifestations are recognized in up to 20% of cases, involving the central nervous system, lungs, peripheral vasculature, cardiovascular system, skeletal muscle, and gastrointestinal tract (3). The incidence of aHUS is around 0.23-0.42 cases per million (4).

The complement system is an important part of innate immune defense, and aHUS results from an acute, uncontrolled activity of the alternative complement pathway, leading to endothelial cell dysfunction and formation of microvascular thrombi (5,6). Genetic abnormalities in the complement pathway may be in the form of rare variants in complement genes or autoantibodies against specific complement factors (7). In particular, uncontrolled complement activation is caused by gain-of-function variants in complement activation factors (*CFB* and *C3*) or loss-of-function variants in complement regulatory proteins (*CFH, CFHR3, MCP, and CFI*) (8). Genetic or acquired dysregulation of the alternative complement pathway is seen in 40–60% of patients with aHUS, which indicates genetic predisposition in many patients (1,3).

Received: July 28, 2025
Accepted: November 18, 2025
Published online: December 9, 2025

Corresponding author:
Livia Maria Sorrentino
email: liviamaria.sorrentino@aocardarelli.it

Although many variants are implicated in its pathogenesis, the development of aHUS is multifactorial. While an individual may carry a mutation, a trigger (or second-hit) is needed for aHUS to occur (1,2). Such triggers include pregnancy, viral infection, cancer, organ transplantation, and use of certain medications (9). In particular, pregnancy-associated aHUS accounts for about 10-20% of all diagnosed aHUS (10) and post-kidney transplant aHUS for about 10% (9).

It is important to recognize that aHUS remains a clinical diagnosis (11) and, if untreated, a potentially life-threatening condition associated with poor clinical outcomes, high morbidity and mortality, and irreversible renal failure (1,2). In fact, before the availability of effective therapy, one study reported that 56% of adults with aHUS progressed to end-stage renal disease (ESRD) or death within 1 year (4). Plasma exchange was historically the therapy of choice, although in the last decade, due to a greater understanding of complement biology, a complement-inhibiting drug, eculizumab, has become the new standard of care (6,12). This humanized monoclonal antibody binds to the C5 protein in the complement system, preventing the formation of the terminal complement complex C5b-9 and thereby effectively inhibiting cellular hemolysis and autoimmune reactions. The efficacy and safety of treating aHUS with eculizumab are well documented and have become the standard of care (13).

More recently, ravulizumab, a second-generation, specific, high-affinity complement C5 inhibitor, has been developed (14). Ravulizumab was approved by the FDA and EMA for aHUS in 2020. Both eculizumab and ravulizumab are well tolerated and have comparable efficacy in improving renal function, hematological markers, and rates of dialysis (15). However, ravulizumab appears to have several advantages over eculizumab, which include a longer dosing interval (8 weeks vs. 2 weeks) and immediate, complete, and sustained inhibition of free C5 (16). These advantages may be associated with improved quality of life (QoL) for patients and caregivers (6,17,18). However, it has been noted that comparison of ravulizumab and eculizumab is limited by major differences in the characteristics of patients included in the three largest studies with these agents (19). In particular, patients enrolled in the ravulizumab trial were, on average, older and showed a low frequency of complement gene variants, which may not be fully representative of the overall aHUS population. Moreover, the endpoints differed between studies, further limiting the possibility of direct comparison (19,20).

Despite its promising benefits, ravulizumab is a relatively new agent, and there are few reports of clinical experience with the drug in real-world settings (21,22). Herein, we present a real-world case series of 6 treatment-naïve aHUS patients who were treated with ravulizumab. We also include data on its efficacy during the acute phase, which was not addressed in Phase III trials due to their study design.

Case presentations

The following six cases of patients with aHUS were collected from participating centers. In all cases, ravulizumab was administered according to approved clinical practice. The therapeutic regimen included a weight-based intravenous loading dose, followed by the first maintenance dose 14 days later, and subsequent maintenance doses every 8 weeks thereafter. All patients were vaccinated against *Neisseria meningitidis* at least two weeks prior to the first dose of ravulizumab, unless the urgency of treatment outweighed the risk of delaying therapy. Patients who initiated ravulizumab less than two weeks after meningococcal vaccination received appropriate antibiotic prophylaxis until two weeks after vaccination (23).

At our centers, the choice between ravulizumab and eculizumab is patient-specific, guided by internal hospital protocols and in line with international recommendations (6,24).

Case #1

A 38-year-old woman, without chronic disease, was admitted to the Emergency Room at the 25th week of her second pregnancy. The patient complained of abdominal pain and intermittent fever for 3 days (max 40.3°C) that did not respond to paracetamol. Placental abruption was diagnosed due to the onset of profuse metrorrhagia, and the patient was submitted to an emergency C-section with delivery of a dead fetus. A Bakri balloon was inserted in the uterine cavity to achieve hemostasis. Following a sudden worsening of hemodynamic parameters, the patient was admitted to the Intensive Care Unit, needing blood transfusion and treatment with noradrenaline.

Blood tests showed thrombocytopenia (50,000/mm^3), Coombs-negative, normochromic normocytic anemia (Hb, hemoglobin, 7.5 g/dL), increased lactate dehydrogenase (LDH), indirect bilirubin of 1.12 mg/dL, reticulocytes of 7.71%, undetectable haptoglobin, white blood cells 5130/mm^3 with neutrophilia (91%), and increased D-dimer (33,650 ng/mL). Other coagulation test abnormalities showed prolonged prothrombin time and partial thromboplastin time, low fibrinogen, increased serum creatinine (sCr; 1.48 mg/dL), and blood urea nitrogen (BUN; 36 mg/dL). A pregnancy-specific disseminated intravascular coagulation (DIC) score (i.e., fibrinogen concentration, prothrombin time, and platelet count) was used to diagnose DIC, and treatment with fresh frozen plasma, antithrombin III, and prothrombin complex was administered after multidisciplinary consultation.

CT angiography excluded the presence of pulmonary embolism and showed pulmonary infiltrates associated with pleural effusion, while the kidneys were of regular size with reduced bilateral parenchymal and excretory function due to renal damage. Empirical antibiotic therapy with cefazolin was given. Coagulation tests normalized rapidly, but sCr continued to increase, which was associated with oliguria and metabolic acidosis. Continuous renal replacement therapy was started without heparin and citrate, due to contraindications.

Hemolytic anemia and thrombocytopenia persisted, whereas coagulation tests were in the normal range. A peripheral blood smear to evaluate bicytopenia showed schistocytes. Together, these results were indicative of a TMA. Plasma ADAMTS13 activity was normal, neurological symptoms were absent, the patient had no recent history of diarrhea, and *E. coli* was not detected in stool. Thus, TTP and typical HUS were ruled out. The absence of autoantibodies

excluded autoimmune disease, and the persistent hemolytic anemia, thrombocytopenia, and renal failure led to a suspicion of aHUS. Ravulizumab was then started as per the protocol described above (first dose 2700 mg; after two weeks, 3300 mg), in association with vaccination for pneumococcus.

The patient's clinical conditions, hemodynamic parameters, and laboratory markers gradually improved, except for anuria and renal function, and the Nephrology Department was consulted since the patient needed to continue hemodialysis. After 2 weeks, the patient was taken to the cardiac intensive care unit for the sudden onset of respiratory failure, chest pain, and rapid worsening of left ventricular ejection fraction (LVEF, 35% on echocardiogram).

Pulmonary CT showed massive pulmonary infiltrates with pleural and pericardial effusion (Fig. 1), and sputum was positive for *E. coli*, *E. gallinarum,* and *Influenza A* virus. ECG and troponin levels excluded acute coronary syndrome. Non-invasive ventilation and directed antimicrobial therapy were promptly started, and a session of continuous venovenous hemofiltration in combination with CytoSorb led to clinical improvement, with reduction of inflammatory markers, normalization of cardiac and pulmonary function, and induction of diuresis.

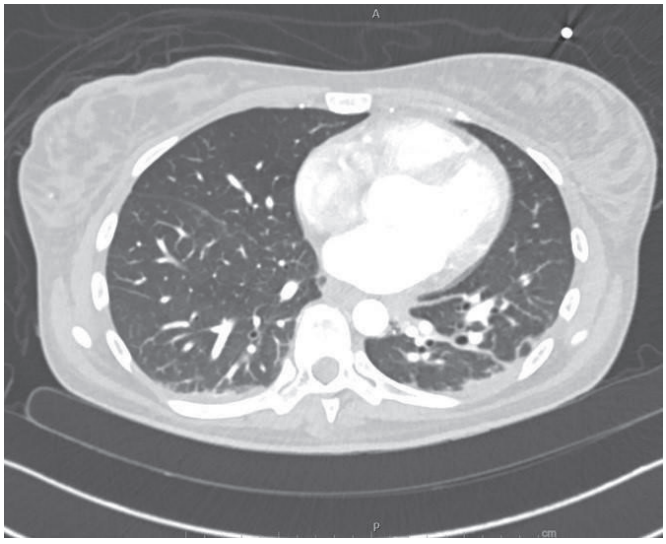

FIGURE 1 - Pulmonary CT scan in patient #1 showing pericardial and bilateral pleural effusion and multiple areas of ground-glass type parenchymal consolidation.

The patient was then transferred to the Nephrology unit, where she gradually suspended hemodialysis. After a few days, she was discharged with a diagnosis of chronic kidney disease (CKD) (eGFR 22 mL/min/1.73 m^2) and an indication to receive ravulizumab every 8 weeks. At the 6-month follow-up visit, the patient was in good clinical condition, asymptomatic, maintaining the same stage of CKD, and with no other laboratory or radiological abnormalities. Blood parameters during treatment with ravulizumab are shown in Table 1. Genetic tests were negative for complement mutations known to be related to aHUS. A final dose of ravulizumab was planned for the patient, after 12 months of treatment, with close specialist outpatient follow-up.

Case #2

A 21-year-old woman with no history of pathology presented to the Emergency Room for profuse diarrhea, reduced diuresis, and the appearance of edema in the lower limbs. Four days earlier, she had delivered her first child with no complications. The patient presented with sensorium intact, BP 185/90 mmHg, no visible bleeding, and mild dyspnea at rest. Chest X-ray showed thickening of lung tissue in the right medio-basal segment with a thickened appearance of the ipsilateral hilar region. Echocardiography indicated volume overload with moderate hemodynamic repercussions (ejection fraction 50%), without evidence of severe ventricular dysfunction or structural abnormalities of cardiac valves. Abdominal ultrasound showed bilateral pleural effusion, which was larger on the right with a thin layer of peritoneal fluid. Renal color Doppler showed kidneys of normal size, with normal cortical thickness and echogenicity, no urinary tract dilation, good vascularization, and both renal arteries and veins well visualized. Laboratory tests revealed severe anemia (hemoglobin 6.8 g/dL), thrombocytopenia (192,000/µL), and hemolysis with markedly increased LDH (1866 IU/L), low haptoglobin (0.07 g/L), and a negative Coombs test. ADAMTS13 activity was normal. Renal function was severely compromised, with serum creatinine of 11 mg/dL, urea of 233 mg/dL, and anuria (~100 mL/24h). Inflammatory markers were elevated, with ferritin of 1734 ng/mL and CRP of 108 mg/L. Immunological screening revealed weakly positive antinuclear antibodies (ANA) (1:160, granular pattern), negative antineutrophil cytoplasmic antibodies (ANCA) and extractable nuclear antigens (ENA), normal immunoglobulin levels, normal complement fractions, and negative lupus anticoagulant (LAC) and antiphospholipid antibodies. Shiga toxin testing was negative. Lymphocyte subsets were normal, and the peripheral smear showed rare schistocytes. Due to severe renal impairment and fluid overload with reduced urine output, urgent dialysis was indicated after placement of a femoral central venous catheter. Blood transfusions were administered.

All data were consistent with a clinical diagnosis of aHUS, and therapy with ravulizumab was initiated as per the protocol described above (2700 mg first dose; 3300 mg maintenance dose). Improvement in hemoglobin was seen at around 3 days after starting ravulizumab (last transfusion required for Hb <7.5 g/dL on 3 days after the first infusion, with progressive improvement). Diuresis resumed immediately, while renal function improved after about 5 days, with a gradual reduction in sCr, resulting in suspension of dialysis.

Upon discharge, one month later, sCr was 2.8 mg/dL, BUN 57 mg/dL, Hb 11.9 mg/dL, platelets (PLT) 223,000, and haptoglobin and LDH were within normal limits, with efficient diuresis, proteinuria 240 mg/24 h, ANA negative, and complement system within normal limits. Genetic testing after the second dose revealed the presence of a genetic variant [c.2383G>A (p.Gly795Arg)] in the *CFH* gene. Early diagnosis and prompt initiation of ravulizumab therapy led to optimal recovery of renal function and restoration of hematological parameters. The treatment was well tolerated, and the 8-week dosing interval allowed for maintenance of high QoL.

TABLE 1 - Laboratory findings in patient #1 during treatment with ravulizumab

Parameter	24 hours	48 hours	1 month	1.5 months	3 months	6 months
sCr (mg/dL)	3.25	3.7	4.33	2.67	2.7	2.71
eGFR (mL/min)	17	15	12	22	21	21
BUN (mg/dL)	95	118	149	153	105	108
Total bilirubin (mg/dL)	2.14	1.83	0.74	0.54	0.49	0.52
Direct bilirubin (mg/dL)	1.12	0.91	0.22	0.14	0.08	0.10
Indirect bilirubin (mg/dL)	1.02	0.92	0.52	0.40	0.41	0.42
LDH (IU/l)	3608	3324	500	525	271	270
Hb (g/dL)	8.1	7.7	11.7	12	11.9	11.2
WBC (x 10^3/µL)	29.99	30.71	7.61	7.27	5.6	4.96
Neutrophils (x10^3/µL)	26.2	26.69	5.17	4.88	3.23	3.13
PLT (x10^3/µL)	21	32	285	263	333	212
PT (sec)	13.6	14.1	16.8	13.6	13.5	13.9
PTT (sec)	22.3	22.4	24.1	23.6	26	24.7
Fibrinogen (mg/dL)	409	394	111	265	257	281
Haptoglobin (mg/dL)	N.A.	N.A.	69.6	180	167	111
D-dimer (ng/mL)	2484	N.A.	1584	N.A.	N.A.	N.A.

Case #3

A 38-year-old woman presented to the Emergency Room with nausea, vomiting, diarrhea, severe hypertension (200/115 mmHg), and headache. She reported a recent course of therapy with amoxicillin/clavulanic acid for a urinary tract infection (UTI) due to *E. coli*. Her medical history included a diagnosis of HELLP syndrome (Hemolysis, Elevated Liver enzymes, Low Platelet count) during pregnancy two years prior in 2021. Laboratory investigations at admission revealed neutrophilic leukocytosis, anemia (Hb 7.6 g/dL), thrombocytopenia (PLT 29,000/µL), and acute kidney injury (sCr 4 mg/dL). After admission, further testing revealed azotemia (110 mg/dL), hyperbilirubinemia (2.33 mg/dL), and markedly elevated LDH (2894 IU/L). Inflammatory markers and arterial blood gas were within normal limits.

The patient was transferred to the Internal Medicine and Vascular Unit with a suspected diagnosis of aHUS; stool cultures and Shiga-like toxin were negative. Laboratory findings included a haptoglobin level of 2 mg/dL, and ADAMTS13 activity was 91.3%. Urinalysis revealed proteinuria (300 mg/dL), hematuria (0.20 mg/dL), and numerous red blood cells in sediment. She was administered a brief cycle of corticosteroids and underwent one session of plasmapheresis. Plasmapheresis was performed as an emergency measure due to the unavailability of complement inhibitors. Corticosteroids were likely given to address thrombocytopenia, although the exact rationale for these treatments cannot be confirmed, as the patient was initially admitted to another ward.

Given the clinical situation and the suspected diagnosis of aHUS, ravulizumab was administered (2700 mg) as per the protocol described above. Laboratory analysis performed on the day of treatment administration showed Hb 8.2 g/dL, PLT 34,000/µL, azotemia 150 mg/dL, sCr 5.78 mg/dL, proteinuria 8.25 g/24h, and low C3 (81 mg/dL; reference range 90-180 mg/dL).

Due to acute kidney injury (AKI), the patient was transferred to the Nephrology department. The patient never required hemodialysis, but received three separate red cell concentrate transfusions on days 1, 3, and 8 after the first infusion of ravulizumab. Antihypertensive therapy with amlodipine and ramipril was initiated, resulting in optimal blood pressure.

Following the first infusion of ravulizumab and consecutive doses, significant improvements in blood parameters were observed (Table 2). Further investigations revealed that the patient carries a heterozygous missense variant [c.3356A>G (p.Asp1119Gly)] in the *CFH* gene, classified as pathogenic. Anti-FH antibodies were negative (11 AU/mL). Induction therapy with ravulizumab, followed by maintenance infusions, enabled the patient to obtain an age-appropriate lifestyle and resume normal work and family activities.

Case #4

A 49-year-old woman presented to the Emergency Department with complaints of asthenia, nausea, and vomiting. Upon evaluation, she exhibited severe hypertension

(200/100 mmHg), anemia (Hb 8.6 g/dL), thrombocytopenia (PLT 63,000/µL), and elevated sCr (3.88 mg/dL). Her medical history was significant for breast carcinoma and a surgically treated cerebral aneurysm following an episode of headache in 2019. In 2022, she was diagnosed with acute iron-deficiency anemia, likely secondary to menometrorrhagia, requiring blood transfusions. At that time, laboratory investigations revealed sCr of 0.7 mg/dL, hemoglobin 5.9 g/dL, and blood pressure of 170/100 mmHg.

Given the patient's present laboratory findings (Hb 7.7 g/dL, PLT 111,000/µL, LDH 626 IU/L) and persistent renal impairment, she was transferred to the Internal Medicine Unit and subsequently to the Nephrology Unit. Peripheral blood smear revealed the absence of schistocytes and the presence of platelet aggregates. ADAMTS13 was mildly reduced (62%), the Coombs test was negative, and complement levels (C3, C4) were within normal range. A comprehensive autoimmune, endocrine, and imaging work-up (including ANA, ANCA, anti-PLA2R, PET-CT, and bone scan) was unremarkable.

The patient underwent two blood transfusions for severe anemia. After excluding other causes of TMA, a first ravulizumab infusion was administered as per the protocol described above, with a planned dose of 2400 mg and a maintenance dose of 3000 mg. Following the placement of a central venous catheter, she initiated replacement hemodialysis. Data on changes in blood parameters are shown in Table 3. A slow acute renal response was noted, whereas the hematologic response was considerably more rapid.

After 6 months, sCr had decreased to 2.9 mg/dL and remained stable at one year (2.59 mg/dL). Genetic analysis was negative. In this patient, ravulizumab improved symptoms and complications due to CKD, leading to less frequent follow-up and a better overall QoL, with no side effects.

Case #5

A 16-year-old girl weighing 29 kg with psychomotor retardation, spasticity, and a congenital solitary kidney, presented to the Emergency Room after being transferred from another hospital for acute renal failure, suspected to be associated with aHUS. Two days earlier, she had visited the Emergency Room with symptoms of drowsiness and hyperglycemia. At previous discharge, the patient had acute renal failure (sCr 5.2 mg/dL) and fever (39°C). She had been treated with intravenous hydration. Despite medical intervention, renal function progressively deteriorated. Additional findings included anemia, thrombocytopenia, positive Coombs test, absence of visible bleeding, lower extremity edema, and mild dyspnea at rest. Laboratory tests upon admission showed Hb 8.7 g/dL, PLTs 141,000 /µL, LDH 633 IU/L, sCr 5.98 mg/dL, BUN 199 mg/dL, anuria, normal aspartate aminotransferase (AST) / alanine aminotransferase (ALT) / gamma-glutamyl transferase (GGT), normal protein electrophoresis, total bilirubin 0.31 mg/dL, prothrombin time in normal range, normal activated partial thromboplastin time (aPTT), fibrinogen 419 mg/dL, and C-reactive protein (CRP) 31 mg/L.

Due to severe renal impairment and the state of overload with reduction in diuresis, urgent dialysis was started following placement of a central venous catheter. Blood transfusions were administered. The next day, the patient had hemoptysis and hematemesis with vomiting, for which she underwent CT angiography and gastroscopy. CT angiography showed bilateral pleural effusion, with lamellar consolidation of the bilateral dorsal basal parenchyma. Areas of parenchymal hyperdensity were observed with acinar involvement affecting both upper lobes. The right kidney was increased in volume, with reduced contrast enhancement and failure to

TABLE 2 - Laboratory investigations following administration of ravulizumab in patient #3

Parameter	Day 3	Day 5	Day 7	Day 10	Week 7	6 months
Hb (g/dL)	7.8	7.9	7.4	7.9	11.4	13.0
Platelets (µL)	91,000	149,000	176,000	222,000	356,000	349,000
sCr (mg/dL)	6.72	5.43	4.70	2.85	0.81	0.88
BUN (mg/dL)	175	149	113	76	47	29
LDH (IU/mL)	1542	1038	780	550	194	182
Haptoglobin (mg/dL)	1	3	3	3	68	104

TABLE 3 - Changes in blood parameters after the first and second dose of ravulizumab in patient #4

Parameter	48 h after 1st infusion	13 days after 1st infusion	20 days after 1st infusion	21 days after 1st infusion	22 days after 1st infusion	24 h after 2nd infusion	72 h after 2nd infusion
sCr (mg/dL)	6.18	5.25	4.83	N.A.	4,48	4.70	4.27
LDH (IU/L)	140	185	259	N.A.	423	405	441
Hb (g/dL)	10.3	9.2	7.9	9.6	N.A.	10.0	11.4
Platelets (µL)	223,000	158,000	291,000	309,000	N.A.	292,000	267,000
Notes		Dialysis	Transfusion				

excrete iodinated urine. Gastroscopy revealed bile material mixed with blood at the bottom of the stomach. The mucosa of the gastric fundus was hyperemic. No obvious lesions or hemorrhagic sources were identified.

Laboratory tests showed Hb 5.4 g/dL, PLTs 77,000/µL, sCr 4.76 mg/dL, BUN 120 mg/dL, LDH 633 IU/L, coagulation time normal, ADAMTS13 58%, haptoglobin 1.47 g/L, Coombs test positive, autoimmune profile with 1:100 ANA positivity with fine granular pattern, anti-dsDNA negative, C3 fraction of complement reduced to 0.66 g/L, C4 fraction and immunoglobulins normal, and ENA negative.

After hematological consultation, aHUS was suspected, and a peripheral blood smear indicated rare schistocytes (3-4 per field). Flow cytometry showed a CD66b+ population of 59%. CD33++ CD14+ monocytes were 10%. The lymphoid component was 15%. B lymphocytes did not show clonality. The patient underwent three consecutive rounds of dialysis and transfusion, and still presented anuria, mild dyspnea, and peripheral edema.

A clinical diagnosis of aHUS was taken into greater consideration, even if not all the data were in agreement, but given the patient's instability and worsening of the clinical situation, it was decided to initiate a therapeutic protocol for aHUS.

In the following days, the patient's respiratory status worsened, and broad-spectrum antibiotic therapy was started. Chest CT showed that the bilateral pleural effusion had increased (max thickness 58 mm vs 37 mm). During bronchoscopy, bronchoscopic aspiration was performed for microbiological analysis, which was positive for *Pseudomonas Aeruginosa* and for *Klebsiella pneumoniae*. Blood cultures were positive for *coagulase-negative Staphylococcus*.

Due to severe oxygen desaturation (SpO_2 85%), mechanical ventilation was initiated, as was renal replacement therapy. After dialysis, the patient was transferred to the intensive care unit (ICU), where she remained under deep sedation and on mechanical ventilation for almost one month. Next, a CT scan was performed, which showed a small pleural collection pouched in the upper right lobe and signs of compensatory hypertrophy in the right kidney. The respiratory situation improved.

Therapy with ravulizumab (900 mg starting dose as per the protocol described above) was included in the treatment plan and contributed to stabilizing the patient's hematological parameters and supporting recovery of renal function. Platelets showed an immediate increase, while hemoglobin improved approximately three days later (last need for transfusion with Hb <7.5 g/dL at 2 days after the first infusion). The day after the initial dose, diuresis resumed, and renal function started to recover after approximately 5 days, with a progressive decrease in sCr and suspension of dialysis. After the second infusion (2100 mg), she presented normal diuresis at approximately 100 mL/h without diuretic stimulation, sCr 0.33 mg/dL, BUN 17 mg/dL, Hb 8.7 g/dL, and PLT 269,000/µL (Table 4). The patient was discharged home from the ICU and currently attends the outpatient clinic for ongoing maintenance therapy with ravulizumab. Genetic testing has been performed, but results are not yet available at the time of writing.

In this case, the clinical diagnosis was complicated because not all minor criteria for TMA were present. While on one hand, the patient presented with life-threatening renal insufficiency and thrombocytopenia, the Coombs test was positive, there was weak ANA positivity, and haptoglobin and bilirubin were normal. Although a negative Coombs test can confirm aHUS, a positive result should not exclude it. The differential diagnosis with TTP was supported by ADAMTS13 activity >10% and normal PTT, while the normal coagulation profile excluded DIC.

Case #6

A 59-year-old woman on hemodialysis since 2018, initiated due to acute renal failure following an infection with verotoxin-producing *E. coli*, was admitted with severe symptoms including comitial seizures, respiratory failure, and worsening renal function, necessitating intensive care. These clinical features led to a diagnosis of typical HUS. As a result of residual ESRD, the patient underwent kidney transplantation. In the postoperative period, the patient experienced hypotension and delayed functional recovery of the kidney, requiring hemodialysis. Subsequently, a gradual improvement in diuresis was observed, with a sCr of 2.94 mg/dL upon discharge.

One month later, the patient was admitted for new onset of acute kidney injury (sCr 4.9 mg/dL), elevated uric acid (11.9 mg/dL), and anemia (hemoglobin 9 g/dL) with a normal platelet count. A graft ultrasound showed the transplanted kidney in the left iliac fossa to be of normal morphology and size, with parenchymal thickness preserved. A cortical cyst of 18 mm in the lower-middle third was seen in the context in which small septa were evident. On Doppler completion, slightly increased intraparenchymal resistance values were seen. A renal biopsy was taken, which, together

TABLE 4 - Clinical course following treatment with ravulizumab in patient #5

Time	Details	Notes
Pre-first infusion	Hb 4.9 g/dL; PLTs 64,000/µL, sCr 4.88 mg/dL, BUN 119 mg/dL	
Day 1 after 1st infusion	Resumption of diuresis	
Day 2 after 1st infusion	Hb <7.5 g/dL	Transfusion
Day 3 after 1st infusion	Hb 11.2 g/dL; PLTs 256,000/µL	
After 2nd infusion	Hb 8.7 g/dL; PLTs 269,000/µL; sCr 0.33 mg/dL; BUN 17 mg/dL	Diuresis ~100 mL/h without stimulation

with the patient's medical history, was suggestive of damage to arterioles and small arteries secondary to TMA (likely reparative phase). Mild tubulo-interstitial scleroatrophy was noted. No features referable to acute rejection are observed. Laboratory testing showed no presence of schistocytes, increased LDH (200 IU/L), consumed haptoglobin levels, C3 in normal range, Coombs tests negative, hemoglobin 8.9 g/dL, and PLT 150,000/µL.

Given the clinical situation, the patient started therapy with ravulizumab (2700 mg; weight 62 kg) as per the protocol described above. The decision to initiate ravulizumab therapy was based on its safety profile, its ability to provide rapid action during the acute phase, and the reassurance of prolonged coverage to prevent potential flare-ups. After 48 h from the first administration, the patient showed improvement in renal function with sCr decreasing to 3.6 mg/dL, hemoglobin increasing to 11 g/dL, and PLT rising to 341,000/µL. After the second dose, recovery of normal haptoglobin levels was seen.

At 10 months of follow-up, renal function improved, with sCr at 2.9 mg/dL, and hemoglobin and PLT were stable. C3 and haptoglobin were in the normal range. Genetic testing is in progress. Table 5 shows the improvement in hemodynamic and renal function after starting therapy with ravulizumab. The patient reported no side effects and only a minimal impact of therapy on social and work life.

TABLE 5 - Laboratory investigations following infusion of ravulizumab in patient #6

	48 h after 1st infusion	10 months
Hb (g/dL)	11.0	11.0
PLTs (uL)	341,000	341,000
sCr (mg/dL)	3.6	2.9

Discussion

Herein, we present six diverse cases of aHUS caused by a variety of triggers. Case #1 demonstrates the difficulty of diagnosing TMAs during pregnancy, especially given the physiological changes of coagulation that occurred. In this case, pregnancy, placental abruption, and infections were all triggering factors. aHUS should be suspected in the presence of hemolytic anemia, thrombocytopenia, and renal failure, and early initiation of anti-C5 treatment, such as ravulizumab in this case, is crucial to minimize complications. Despite prompt treatment, there was unusual cardiac involvement, which was also exacerbated by viral infection. These combined conditions are rare, but can complicate each other and require a multidisciplinary approach. The response to ravulizumab was rapid in terms of hematologic parameters and blood count, while improvement in renal function was delayed in comparison. Dialysis and the underlying causes of renal damage (hemorrhagic shock, sepsis, TMA, and subsequent cardiogenic shock) hindered the drug's effect on renal function. However, renal function gradually improved with discontinuation of dialysis, and stabilization at stage 4 CKD was likely attributable to the positive effects of ravulizumab.

aHUS must always be considered in cases of persistent hemolysis and AKI in the postpartum period, as demonstrated by case #2. Acute renal failure due to pregnancy-associated aHUS often leads to subsequent chronic kidney failure (25,26). This highlights the need for early, specific, and aggressive treatment as advocated by a recent international working group (27). Moreover, a multidisciplinary approach to such cases can greatly aid in achieving a prompt diagnosis and initiating anticomplement therapy as soon as possible (28). This is also in consideration of the finding that many cases of pregnancy-associated aHUS have no identified trigger other than pregnancy (29,30).

In case #5, aHUS was considered even when not all minor criteria were present; in particular, a positive Coombs test should not exclude aHUS diagnosis. Following administration of ravulizumab, there was optimal recovery of diuresis, renal function, and hematological status, despite being in critical condition. Severe pneumonia was probably the trigger for the TMA. Even in the presence of a septic state, the use of ravulizumab should not be delayed for fear of worsening infectious complications.

The present cases also highlight the need for lifelong treatment, at least in some patients. In cases #3 and #6, the reduction in sCr was relatively rapid compared to cases #1 and #4, but in the latter cases, sCr levels continued to improve over time (1.9 mg/dL and 2.04 mg/dL, 12 and 19 months after the initiation of ravulizumab, respectively). In patient #1, given the gradual improvement in sCr and that genetic analyses were subsequently negative, discontinuation of ravulizumab is now being undertaken with careful monitoring. This emphasizes the possibility of discontinuation of anticomplement therapy in patients in whom renal function has recovered and is stable.

In this regard, Wijnsma et al. described the outcomes of restrictive treatment with eculizumab in 20 patients with aHUS (31). Eculizumab was tapered in all patients and discontinued in 17 cases with recurrence of aHUS in 5 patients. However, all patients were closely monitored, recurrence was detected early, and anticomplement therapy was restarted promptly with no clinical sequela or additional kidney dysfunction. Similarly, Ardissino et al. reported on their experience in discontinuation of eculizumab in 10 patients with aHUS (32). Of these, three patients had a relapse within 6 weeks of cessation of anticomplement therapy, but immediately restarted it with complete recovery. These results underline that it is possible to discontinue anticomplement therapy, at least in a proportion of carefully selected patients who achieved stable remission. Furthermore, with close monitoring, it is possible to detect relapses early with no clinical consequences.

Nonetheless, other authors have reported less positive experiences when attempting to discontinue eculizumab in patients with aHUS. In the series by Macia et al., of 52 patients discontinuing therapy, 16 had a subsequent manifestation of TMA; 12 patients had severe complications, 9 of whom restarted eculizumab (33). In an analysis of the available literature, Laurence concluded that discontinuation should be considered on a case-by-case basis with careful monitoring, after 6-12 months of treatment for aHUS and

with at least 3 months of normalization of renal function or stabilization of CKD (34).

Current recommendations include the adoption of an individualized approach to the management of aHUS, and the decision to discontinue therapy should be personalized by evaluating the risk of relapse and the profile of the specific patient, and strict use of close monitoring. As a minimum, patients with pregnancy-associated aHUS and high risk of relapse should be treated for at least 6-12 months. In all cases, the TMA must be resolved before discontinuation of anticomplement therapy is considered (24).

In addition, the potential involvement of multiple organ systems/extrarenal manifestations and complexity of care necessitate specialized interventions and the adoption of a multidisciplinary approach at all stages of management (35). All clinicians must be aware of the complexities of differential diagnosis and the need for early initiation of anticomplement therapy, even when not all minor diagnostic criteria for aHUS are concomitantly present. In this regard, multidisciplinary support can be of significant clinical value, as shown by the cases presented herein.

In conclusion, this real-world case series of treatment-naïve patients with aHUS, presenting with a range of clinical scenarios and underlying triggers, showed that early use of ravulizumab as first-line therapy was consistently associated with rapid and sustained clinical improvements, along with good tolerability. These findings further reinforce its value as a therapeutic option in the management of aHUS and highlight the importance of timely diagnosis and a multidisciplinary approach.

Acknowledgments

The authors thank Patrick Moore, PhD, for medical writing assistance and Alessia Doria for editorial support, provided on behalf of Health Publishing & Services s.r.l. This assistance was funded by Alexion Pharma Italy s.r.l. in compliance with Good Publication Practice (GPP3) guidelines. Alexion Pharma Italy s.r.l. had no role in the conduct of the literature search, in the preparation of the article, in the interpretation of clinical cases, and in the writing of the article for publication.

Disclosures

Conflict of Interest: The authors declare that the research was conducted in the absence of any commercial or financial relationships that could be construed as a potential conflict of interest.

Financial support: This research received no specific grant from any funding agency in the public, commercial, or not-for-profit sectors.

Data availability statement: All data analyzed during this study are included in this article. Further information is available from the corresponding author upon reasonable request.

Statement of Ethics: Written informed consent for publication (including images) has been obtained from the patients. The research was conducted ethically in accordance with the World Medical Association Declaration of Helsinki. The article is exempt from Ethical Committee approval since it is related only to six case reports.

References

1. Raina R, Krishnappa V, Blaha T, et al. Atypical hemolytic-uremic syndrome: an update on pathophysiology, diagnosis, and treatment. Ther Apher Dial. 2019;23(1):4-21. CrossRef PubMed
2. Yoshida Y, Kato H, Ikeda Y, et al. Pathogenesis of atypical hemolytic uremic syndrome. J Atheroscler Thromb. 2019; 26(2):99-110. CrossRef PubMed
3. Loirat C, Frémeaux-Bacchi V. Atypical hemolytic uremic syndrome. Orphanet J Rare Dis. 2011;6(1):60. CrossRef PubMed
4. Fremeaux-Bacchi V, Fakhouri F, Garnier A, et al. Genetics and outcome of atypical hemolytic uremic syndrome: a nationwide French series comparing children and adults. Clin J Am Soc Nephrol. 2013;8(4):554-562. CrossRef PubMed
5. Petr V, Thurman JM. The role of complement in kidney disease. Nat Rev Nephrol. 2023;19(12):771-787. CrossRef PubMed
6. Vivarelli M, Barratt J, Beck LH Jr, et al.. The role of complement in kidney disease: conclusions from a Kidney Disease: Improving Global Outcomes (KDIGO) Controversies Conference. Kidney Int. 2024;106(3):369-391. CrossRef PubMed
7. Stea ED, D'Ettorre G, Mitrotti A, et al. The complement system in the pathogenesis and progression of kidney diseases: what doesn't kill you makes you older. Eur J Intern Med. 2024;124:22-31. CrossRef PubMed
8. Duval A, Frémeaux-Bacchi V. Complement biology for hematologists. Am J Hematol. 2023;98(S4)(suppl 4):S5-S19. CrossRef PubMed
9. Licht C, Al-Dakkak I, Anokhina K, et al. Characterization of patients with aHUS and associated triggers or clinical conditions: a global aHUS registry analysis. Nephrology (Carlton). 2024;29(8):519-527. CrossRef PubMed
10. Meena P, Gala R, Das RR, et al. Kidney and pregnancy outcomes in pregnancy-associated atypical hemolytic uremic syndrome: a systematic review and meta-analysis. Medicine (Baltimore). 2025;104(5):e41403. CrossRef PubMed
11. Laurence J, Haller H, Mannucci PM, et al. Atypical hemolytic uremic syndrome (aHUS): essential aspects of an accurate diagnosis. Clin Adv Hematol Oncol. 2016;14 Suppl 11(11):2-15. PubMed
12. West EE, Woodruff T, Frémeaux-Bacchi V, et al. Complement in human disease: approved and up-and-coming therapeutics. Lancet. 2024;403(10424):392-405. CrossRef PubMed
13. Bouwman HB, Guchelaar HJ. The efficacy and safety of eculizumab in patients and the role of C5 polymorphisms. Drug Discov Today. 2024;29(9):104134. CrossRef PubMed
14. McKeage K. Ravulizumab. First global approval. Drugs. 2019;79(3):347-352. CrossRef PubMed
15. Shahid K, Qayyum S. Eculizumab versus ravulizumab for the treatment of atypical hemolytic uremic syndrome: a systematic review. Cureus. 2023;15(9):e46185. CrossRef PubMed
16. Lee JW, Sicre de Fontbrune F, Wong Lee Lee L, et al. Ravulizumab (ALXN1210) vs eculizumab in adult patients with PNH naive to complement inhibitors: the 301 study. Blood. 2019;133(6): 530-539. CrossRef PubMed
17. Legendre C, Rebecca-Sberro-Soussan, Zuber J. Ravulizumab for the treatment of aHUS in adults: improving quality of life. Kidney Int Rep. 2021;6(6):1489-1491. CrossRef PubMed
18. Mauch TJ, Chladek MR, Cataland S, et al. Treatment preference and quality of life impact: ravulizumab vs eculizumab for atypical hemolytic uremic syndrome. J Comp Eff Res. 2023;12(9):e230036. CrossRef PubMed
19. Fakhouri F, Schwotzer N, Frémeaux-Bacchi V. How I diagnose and treat atypical hemolytic uremic syndrome. Blood. 2023;141(9):984-995. CrossRef PubMed

20. Rondeau E, Scully M, Ariceta G, et al.; 311 Study Group. The long-acting C5 inhibitor, ravulizumab, is effective and safe in adult patients with atypical hemolytic uremic syndrome naïve to complement inhibitor treatment. Kidney Int. 2020;97(6):1287-1296. CrossRef PubMed
21. Schönfelder K, Kühne L, Schulte-Kemna L, et al. Clinical efficacy and safety of switching from eculizumab to ravulizumab in adult patients with aHUS- real-world data. BMC Nephrol. 2024;25(1):202. CrossRef PubMed
22. Schaefer F, Al-Dakkak I, Anokhina K, et al. Global aHUS registry analysis of patients switching to ravulizumab from eculizumab. Kidney Int Rep. 2024;9(9):2648-2656. CrossRef PubMed
23. Ultomiris. Riassunto delle caratteristiche del prodotto. Online (Accessed July 2025)
24. Ávila A, Cao M, Espinosa M, et al. Recommendations for the individualised management of atypical hemolytic uremic syndrome in adults. Front Med (Lausanne). 2023;10:1264310. CrossRef PubMed
25. Cadet B, Meshoyrer D, Kim Z. Atypical hemolytic uremic syndrome: when pregnancy leads to lifelong dialysis: a case report and literature review. Cardiovasc Endocrinol Metab. 2021;10(4):225-230. CrossRef PubMed
26. Mirza M, Sadiq N, Aye C. Pregnancy-associated atypical hemolytic uremic syndrome and life-long kidney failure. Cureus. 2022;14(6):e25655. CrossRef PubMed
27. Fakhouri F, Scully M, Provôt F, et al. Management of thrombotic microangiopathy in pregnancy and postpartum: report from an international working group. Blood. 2020;136(19):2103-2117. CrossRef PubMed
28. Che M, Moran SM, Smith RJ, et al. A case-based narrative review of pregnancy-associated atypical hemolytic uremic syndrome/complement-mediated thrombotic microangiopathy. Kidney Int. 2024;105(5):960-970. CrossRef PubMed
29. Fakhouri F, Scully M, Ardissino G, et al. Pregnancy-triggered atypical hemolytic uremic syndrome (aHUS): a Global aHUS Registry analysis. J Nephrol. 2021;34(5):1581-1590. CrossRef PubMed
30. Rondeau E, Ardissino G, Caby-Tosi MP, et al.; Global aHUS Registry. Pregnancy in women with atypical hemolytic uremic syndrome. Nephron J. 2022;146(1):1-10. CrossRef PubMed
31. Wijnsma KL, Duineveld C, Volokhina EB, et al. Safety and effectiveness of restrictive eculizumab treatment in atypical haemolytic uremic syndrome. Nephrol Dial Transplant. 2018;33(4):635-645. CrossRef PubMed
32. Ardissino G, Testa S, Possenti I, et al. Discontinuation of eculizumab maintenance treatment for atypical hemolytic uremic syndrome: a report of 10 cases. Am J Kidney Dis. 2014;64(4):633-637. CrossRef PubMed
33. Macia M, de Alvaro Moreno F, Dutt T, et al. Current evidence on the discontinuation of eculizumab in patients with atypical haemolytic uraemic syndrome. Clin Kidney J. 2017;10(3):310-319. CrossRef PubMed
34. Laurence J. Defining treatment duration in atypical hemolytic uremic syndrome in adults: a clinical and pathological approach. Clin Adv Hematol Oncol. 2020;18(4):221-230. PubMed
35. Yerigeri K, Kadatane S, Mongan K, et al. Atypical hemolytic-uremic syndrome: genetic basis, clinical manifestations, and a multidisciplinary approach to management. J Multidiscip Healthc. 2023;16:2233-2249. CrossRef PubMed

DTI
Drug Target Insights 2025; 19: 108-115
ISSN 1177-3928 | DOI: 10.33393/dti.2025.3631
ORIGINAL RESEARCH ARTICLE

Antioxidant potential of a new macrocyclic bisbibenzyl and other compounds from *Combretum molle*: *in vitro* and docking analyses

Angele Fanta[1,3], Gaetan Bayiha Ba Njock[1], Amadou Dawe[2], Fawai Yakai[1], Jean Noël Nyemb[3], Herve Landry Ketsemen[4], Vincent Taira[1], Albert Wangso[1], Chantal Doudja[1], Dieudonne Emmanuel Pegnyemb[4], Benoit Loura[3]

[1]Department of Chemistry, Faculty of Science, University of Maroua, Maroua - Cameroon
[2]Department of Chemistry, Higher Teachers Training College, University of Maroua, Maroua - Cameroon
[3]Department of Refining and Petrochemistry, National Advanced School of Mines and Petroleum Industries, University of Maroua, Kaélé - Cameroon
[4]Department of Organic Chemistry, Faculty of Science, University of Yaoundé I, Yaoundé - Cameroon

ABSTRACT

Introduction: Free radicals are key contributors to several diseases, including cancer, inflammation, pain, and neurodegenerative disorders such as Alzheimer's disease. Due to the limitations and adverse effects of synthetic antioxidants, naturally occurring phytochemicals offer safer, more sustainable alternatives. This study investigates the antioxidant potential of twigs of *Combretum molle* R. Br. ex G. Don through integrated experimental and computational approaches.

Methods: Compounds were isolated using chromatographic methods, and their structures established by 1D- and 2D-NMR, HR-ESI-MS, and comparison with reported data. Antioxidant activity was assessed through DPPH radical scavenging and FRAP assays, while molecular docking against xanthine oxidase (PDB: 1FIQ) explored possible mechanisms beyond direct radical scavenging.

Results: A new macrocyclic bisbibenzyl derivative, combrebisbibenzyl A (**1**), was identified along with corosolic acid (**2**), maslinic acid (**3**), a mixture of asiatic acid (**4**) and arjunolic acid (**5**), combregenin (**6**), and *β*-sitosterol glucoside (**7**). The MeOH extract and EtOAc fraction showed notable DPPH scavenging activity (IC_{50} = 170.21 and 197.41 µg/mL) and strong reducing power (65.04 ± 1.07 and 67.42 ± 0.82 mM Vit C/g). Among the isolated compounds, combrebisbibenzyl A (**1**) displayed the strongest radical scavenging effect (IC_{50} = 175.64 µg/mL) and high reducing capacity (57.46 ± 0.42 mM Vit C/g). Docking indicated favorable interactions for all compounds, with combrebisbibenzyl A (**1**) showing the highest affinity (–9.1 kcal/mol), outperforming salicylate (–7.7 kcal/mol).

Conclusion: These findings support the traditional use of *C. molle* and highlight combrebisbibenzyl A (**1**) as a promising natural antioxidant with multi-mechanistic potential.

Keywords: Antioxidant activity, *Combretum molle*, Combrebisbibenzyl A, Macrocyclic bis-bibenzyl, Molecular docking

Introduction

Combretum molle R. Br. ex G. Don, a plant belonging to the Combretaceae family, is widely distributed from tropical to subtropical areas of Africa and Asia (1). Commonly known as soft-leaved *Combretum* in French, *C. molle* has been reported in African folk medicinal practices to treat abdominal disorders, leprosy, fever, snake bites, wounds, worm infections, and convulsions. It is also reported to possess hepatoprotective, antimalarial, antituberculosis, and anti-HIV properties (2-4).

Previous chemical investigations have reported the presence of alkaloids, triterpenes, steroids, tannins, bibenzyls, phenanthrenes, and saponins from some species of the genus *Combretum* (5-7). Several stilbenes, dihydrostilbenes, and their dimers isolated from *Combretum* species have demonstrated strong antioxidant potential (6-8). However, despite these reports, the isolation and investigation of macrocyclic bisbibenzyl derivatives from *C. molle* remain limited, representing a gap in understanding their structural diversity and bioactivity.

As a continuation of our investigation on plants of the Combretaceae family, a new macrocyclic bis-bibenzyl derivative, combrebisbibenzyl A (**1**), was isolated from the twigs of *C. molle*, together with six other known secondary metabolites. Given the reported antioxidant potential of *C. molle*

Received: August 19, 2025
Accepted: November 26, 2025
Published online: December 18, 2025

This article includes supplementary material

Corresponding authors:
Dawe Amadou; Bayiha Ba Njock Gaetan; Jean Noël Nyemb
email: amadoudawe@gmail.com; bayihagaetan@yahoo.fr; nyembjeannoel@gmail.com

extracts and some isolated compounds (3), and the documented activity of related bis-bibenzyl derivatives (4,6,7), we focused on elucidating the antioxidant activity of this newly isolated compound.

To explore potential mechanisms beyond direct radical scavenging, molecular docking studies were conducted targeting xanthine oxidase (XO) inhibition. XO (EC 1.17.3.2) is a molybdenum-containing flavoprotein that catalyzes the terminal steps of purine catabolism, specifically the oxidation of hypoxanthine to xanthine and subsequently to uric acid (9,10). Beyond its metabolic role, XO is a major source of reactive oxygen species (ROS), particularly superoxide anions and hydrogen peroxide, generated as byproducts during the enzymatic reaction with molecular oxygen (11,12). Excessive ROS production by XO contributes to pathological conditions such as ischemia-reperfusion injury, cardiovascular diseases, inflammation, and other oxidative stress-related disorders (11,13,14).

Salicylic acid (salicylate) has been extensively studied as a competitive XO inhibitor and is commonly used as a reference standard in enzymatic assays due to its well-characterized binding mechanism and stabilizing effect on the enzyme (9,15). The crystal structure of bovine milk xanthine oxidase (PDB ID: 1fiq) complexed with salicylate was selected as the target protein because of its high-resolution structural data and the availability of a well-defined active site with a co-crystallized competitive inhibitor (9). This computational approach allows for the prediction of binding affinities and identification of molecular interactions that may contribute to the antioxidant properties of the isolated compounds.

Experimental

General experimental procedures

Bruker MicroTOF was used for Mass spectra analysis. NMR spectra obtained on Bruker Avance DPX-300FT and Bruker Avance III HD 500 NMR spectrometer. Isolation of pure compounds was performed using Column chromatography (CC) on silica gel 60 (Merck, Darmstadt, Germany). Sephadex LH-20 (Merck, Darmstadt, Germany) was used for separation and purification. Thin-layer chromatography (TLC) was performed on Silica gel 60 F254 plates, and TLC spots were detected under UV-254-nm light. Bioactivity was determined using a 96-well microplate reader (SpectraMax 340PC, Molecular Devices, USA). Methanol, ethanol, n-hexane, ethyl acetate, ferrous chloride and copper (II) were obtained from E. Merck (Darmstadt, Germany). 2,2'-Diphenyl-1-picrylhydrazyl (DPPH), 2,4,6-tri-(2-pyridyl)-s-triazine (TPTZ) from Calbiochem. Ascorbic acid, butylhydroxytoluene (BHT) from Sigma Aldrich (Mumbai, India).

Plant material

Combretum molle twigs were harvested around Maroua in Northern Cameroon in October 2023, and the identified was done by comparison with a voucher specimen available in the National Herbarium of Cameroon under the reference number 6518/SRF/CAM.

Extraction and compound isolation

Around 3 kg of the air-dried twigs of *C. molle* were crushed and extracted with 20 L of methanol for 72 H to yield 167 g of crude extract. 150 g of this extract was dissolved in 10 L of water and partitioned with 5 L of EtOAc to afford 62 g of EtOAc extract (62 g). 55 g of the resulted EtOAc extract was subjected to column chromatography (CC) using silica gel and eluted with a gradient n-hexane-EtOAc (100:0 to 0:100, v/v) and EtOAc-MeOH gradient (100:0 to 0:100, v/v) to afford 156 fractions of 300 mL each, which were combined into 7 major fractions (A- G) based on their TLC profiles. Fraction E (2 g) was subjected to repeated silica gel CC using a gradient elution of n-hexane-EtOAc (100:0 to 0:100, v/v) to yield compound **1** (17.2 mg). Fraction F (8.6 g) was subjected to silica gel CC using a gradient elution of n-hexane-EtOAc (100:0 to 0:100, v/v), followed by CC over Sephadex LH-20 eluting with CH_2Cl_2-CH_3OH 50:50, v/v to afford compounds **2** (19.4 mg), **3** (15.8 mg) and a mixture of **4** and **5** (23.8 mg). Compound **7** (21.3 mg) precipitated from fraction G (1.5 g). The residue of fraction G (1.12 g) was subjected to silica gel CC and eluted with a gradient of CH_2Cl_2-CH_3OH to afford compound **6** (21.3 mg).

Spectroscopic data of Combrebisbibenzyl A (1)

$C_{32}H_{32}O_{10}$, White powder; ^{1}H NMR (500 MHz, $CDCl_3$): δ_H 7.73 (2H, s, H-6 and H-13'), 6.83 (2H, s, H-3 and H-14'), 6.44 (2H, d, *J* = 2.5 Hz, H-12 and H-1'), 6.33 (2H, d, *J* = 2.5 Hz, H-10 and H-5'), 5.62 (2H, s, 2, 13'-OH), 5.33 (2H, s, 13, 2'-OH), 3.91 (6H, s, 1,2'– OCH_3), 3.80 (6H, s, 11,6'– OCH_3), 2.72 (4H, m, H-8 and H-8') and 2.70 (4H, m, H-7 and H-7'). ^{13}C NMR (125 MHz, $CDCl_3$): δ_C 158.7 (C-11 and C-6'), 153.1 (C-13 and C-2'), 144.9 (C-1 and C-12'), 143.8 (C-2 and C-13'), 141.5 (C-14 and C-3'), 131.7 (C-5 and C-10'), 124.6 (C-4 and C-9'), 115.2 (C-9 and C-4'), 114.3 (C-3 and C-14'), 109.9 (C-6 and C-11'), 101.2 (C-10 and C-5'), 106.7 (C-12 and C-1'), 56.3 (1, 12'-OCH_3), 55.4 (11, 6'-OCH_3), 31.0 (C-8 and C-8') and 29.2 (C-7 and C-7'). HR-ESI-MS m/z 575.1930 $[M-H]^-$ (Calcd for $C_{32}H_{31}O_{10}$ 575.1917).

Antioxidant and molecular docking activities

DPPH radical scavenging activity

The DPPH radical scavenging activity was evaluated following a slightly modified version of the method reported by (16). In brief, 5 µL of each sample (at concentrations between 62.5 and 500 µg) was added to 95 µL of a 0.3 mM ethanolic DPPH solution in a 96-well microplate (Costar). The mixture was then incubated at 37°C for 30 minutes in the dark. After incubation, the absorbance was recorded at 515 nm using a microplate reader, with ethanol-treated wells serving as the control. Each sample was analyzed in triplicate. Butylhydroxytoluene (BHT) was employed as the positive control, while the ethanol-treated wells were used as the negative control. The percentage of DPPH radical scavenging activity was calculated using the following equation (17,18):

$$\text{DPPH}\cdot \text{ scavenging effect (\%)} = \frac{(\text{Ac} - \text{As}) \times 100}{\text{Ac}}$$

Where Ac = absorbance of control and As = absorbance of sample.

Ferric reducing power (FRAP) activity

In the presence of an oxidizing agent, the ferric-tripyridyltriazine complex ([Fe^{3+}–TPTZ]) is reduced to its ferrous form ([Fe^{2+}–TPTZ]) (19). The ferrous ion–chelating capacity was determined according to the method described by Benzie (20), with slight modifications. In brief, 3 mL of freshly prepared FRAP reagent was mixed with 100 µL of the sample solution (500 µg/mL in DMSO) and incubated at 37°C for 10 minutes. The absorbance of the resulting mixture was measured at 593 nm using a UV–visible spectrophotometer. Ascorbic acid, a well-established natural antioxidant, served as the positive control. The FRAP reagent was prepared by combining 5 mL of TPTZ solution (10 mM in 40 mM HCl), 50 mL of acetate buffer (0.3 M, pH 3.6), and 5 mL of freshly prepared $FeCl_3$ solution (20 mM). All assays were performed in triplicate, and results were expressed as millimoles of Vitamin C equivalents per gram of sample (mM Vit C/g).

Molecular Docking Analysis

Preparation of Ligands

The three-dimensional structures of all isolated compounds were constructed using Chem3D Pro 15.0 software (PerkinElmer, USA). The molecular structures were drawn based on their elucidated NMR and mass spectrometric data, and all ligands were energy-minimized using the MM2 force field to obtain stable conformations prior to docking calculations. The optimized structures were saved in Protein Data Bank (.pdb) format for subsequent molecular docking studies.

Preparation of Target Protein

The crystal structure of bovine milk xanthine oxidase complexed with salicylate (PDB ID: 1FIQ) was obtained from the Protein Data Bank (Online) (9). This particular structure was chosen as it represents the oxidase form with a well-defined active site geometry and contains salicylate as a competitive inhibitor, serving as an appropriate reference for comparative analysis. Protein preparation was carried out using AutoDockTools (ADT) version 1.5.6 (21). Prior to docking, all water molecules, ions, and the co-crystallized salicylate ligand were removed. Polar hydrogens were added, and Gasteiger and Kollman partial charges were assigned to all atoms. The protonation states of ionizable residues were adjusted to reflect physiological pH (7.4), followed by energy minimization to eliminate steric conflicts.

Molecular Docking Procedure

Molecular docking simulations were conducted using AutoDock Vina version 1.2.7 (22), which utilizes an advanced scoring function to evaluate intermolecular interactions, including hydrogen bonds, hydrophobic contacts, van der Waals forces, and electrostatic interactions. The docking grid was centered on the molybdenum-containing active site originally occupied by salicylate, with coordinates set at x = 24.642, y = 15.264, z = 108.210 and grid dimensions of 40 × 40 × 40 Å. This configuration encompassed both the salicylate binding pocket and the surrounding molybdopterin active site, allowing comprehensive exploration of potential ligand binding modes. To validate the docking protocol, salicylate was re-docked into the active site, confirming the reliability of the procedure. For each compound, 50 independent docking runs were performed to ensure thorough sampling of conformational space. Binding poses were ranked according to their predicted binding energies (kcal/mol), and the conformation with the lowest energy was selected for detailed interaction analysis.

FIGURE 1 - Xanthine oxidase RCSB: 1FIQ, in complex with salicylate (co-crystallized ligand shown in green) and its cofactors (shown in yellow).

Analysis of Molecular Interactions

Intermolecular interactions between the docked ligands and xanthine oxidase were analyzed and visualized using Discovery Studio Visualizer 2021 (Dassault Systèmes BIOVIA, USA). The analysis encompassed hydrogen bonds, hydrophobic interactions, π–π stacking, π–alkyl interactions, salt bridges, and other non-covalent contacts. Hydrogen bonds were defined as interactions with donor–acceptor distances ≤3.5 Å and angles ≥120°. Binding affinities were reported as binding energies (kcal/mol), with more negative values indicating stronger interactions. All observed interactions were

compared with those of the reference inhibitor salicylate to evaluate the relative binding potential of the test compounds.

Statistical analysis

Results expressed as mean ± SD (n = 3). The analysis was done by one-way ANOVA followed by a Newman-Keuls Multiple Comparison post-test using the Graph Pad Prism 6.0 software (Microsoft, USA). Differences at $p < 0.05$ were considered statistically significant.

Results and discussion

Compounds identification

Air-dried twigs of *C. molle* (3 kg) were extracted by maceration in methanol (20 L), yielding 167 g of crude extract. This extract was suspended in water and subsequently partitioned with ethyl acetate. From the resulting EtOAc fraction, 62 g was subjected to sequential column chromatography on silica gel and Sephadex LH-20, using gradients of n-hexane/EtOAc followed by EtOAc/MeOH, which led to the isolation of seven compounds (**1**–**7**). Compound **1**, designated combrebisbibenzyl A, was characterized as a new macrocyclic bisbibenzyl. The remaining six compounds were identified as corosolic acid (**2**), maslinic acid (**3**), a mixture of asiatic acid (**4**) and arjunolic acid (**5**) (23), combregenin (**6**) (24), and *β*-sitosterol glucoside (**7**) (25,26) (Fig. 2). The structures of all isolated compounds were determined through spectroscopic techniques and by comparison with previously reported data.

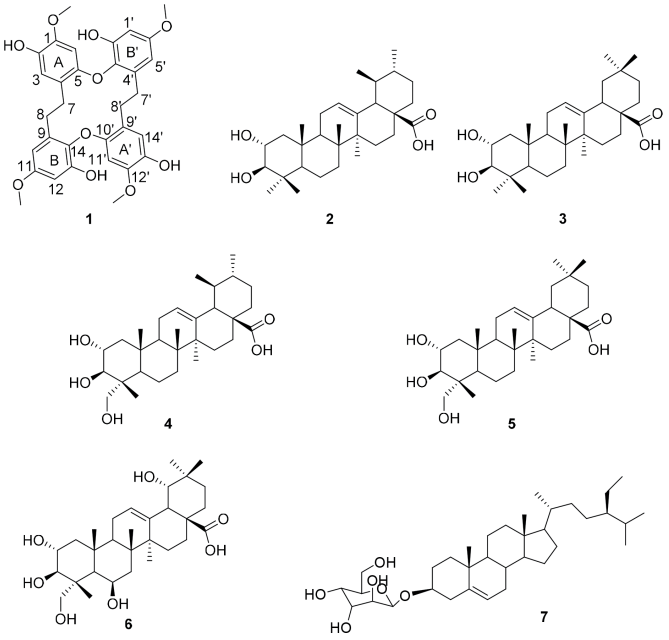

FIGURE 2 - Chemical structures of compounds **1-7** isolated from the twigs of *Combretum molle*.

Compound **1** was isolated as a white amorphous powder, and its molecular formula was determined to be $C_{32}H_{32}O_{10}$ based on its HR-ESI-MS data (Fig. S1), showing $[M-H]^-$ at *m/z* 575.1930 (calcd 575.1917 for $C_{32}H_{31}O_{10}$), which corresponds to seventeen degrees of unsaturation. The structure of compound **1** closely resembles a previously reported combrebisbibenzyl (27), with the primary distinction being that combrebisbibenzyl contains additional methoxy substituents compared to compound **1**. The ^{1}H NMR spectrum (Fig. S2) exhibited characteristic signals of two benzylic methylene groups, presenting as four aliphatic protons in multiplet patterns at δ_H 2.70 (2H) and 2.72 (2H) (28). Aromatic proton signals were observed at δ_H 6.33 (1H, d, *J* = 2.5 Hz) and 6.44 (1H, d, *J* = 2.5 Hz), indicative of a *meta*-coupled AB pattern on the B ring, along with δ_H 6.83 (1H, s) and 7.73 (1H, s) corresponding to *para*-substituted protons on the A ring (29). Two methoxy groups were detected at δ_H 3.80 (3H, s) and 3.91 (3H, s), and phenolic hydroxyl protons appeared at δ_H 5.33 (1H, s) and 5.62 (1H, s).^{13}C NMR and APT analyses (Figs S3 and S4) revealed 16 distinct carbon signals, including two aliphatic methylenes at δ_C 29.2 (C-7) and 31.0 (C-8), four methines at δ_C 114.3 (C-3), 109.9 (C-6), 101.2 (C-10), and 106.7 (C-12), and eight quaternary carbons, six of which were oxygenated, at δ_C 144.9 (C-1), 143.8 (C-2), 124.6 (C-4), 131.7 (C-5), 115.2 (C-9), 158.7 (C-11), 153.1 (C-13), and 141.5 (C-14). The two methoxy carbons resonated at δ_C 55.4 (11-OCH_3) and 56.3 (1-OCH_3). The relative positions of methoxy and hydroxyl groups were elucidated through HMBC correlations (Fig. S5). Cross-peaks between the hydroxyl proton at δ_H 5.62 (2-OH) and carbons C-1 (δ_C 144.9) and C-3 (δ_C 114.3), as well as between the methoxy protons at δ_H 3.91 (1-OMe) and C-1, confirmed their locations on the A ring. On the B ring, correlations of δ_H 5.33 (13-OH) with C-13 (δ_C 153.1) and δ_H 3.80 (11-OMe) with C-11 (δ_C 158.7) established the positions of the respective substituents. Additional HMBC correlations of aromatic protons further supported these assignments: H-3 (δ_H 6.83) correlated with C-1, C-2, C-4, and C-7, while H-6 (δ_H 7.73) showed correlations with C-1, C-2, C-4, and C-5 on the A ring. On the B ring, H-10 (δ_H 6.33) correlated with C-8, C-9, C-11, and C-12, and H-12 (δ_H 6.44) with C-10, C-11, and C-13. The HMBC correlations of H-7 (δ_H 2.70) with C-3, C-4, C-5, and C-8, and H-8 (δ_H 2.72) with C-7, C-9, and C-14, confirmed the linkage between the two benzene rings and established the dihydrostilbene skeleton (30). Accordingly, the dihydrobibenzyl moiety (**1a**) was deduced (Fig. 3), similar to combrebisbibenzyl. The seventeen degrees of unsaturation correspond to four aromatic rings and one additional unsaturation attributed to a symmetric macrocyclic junction between the two monomeric units of **1a** (31).

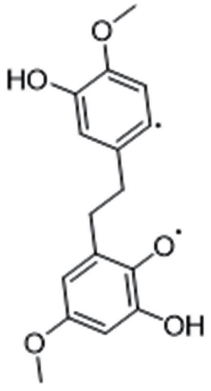

FIGURE 3 - Substructure **1a**.

Long-range HMBC correlations (27,31,32) (Fig. S6) between the proton signals H-6/H-11' (δ_H 7.73) and the quaternary carbon atoms C-4'/C-9 (δ_C 115.2) revealed the symmetric linkages between the two bibenzyl units at C-5–O–C-3' and C-14–O–C-10'. Based on these spectral data, the structure of compound **1** was identified as a novel bisbenzyl derivative, for which the name combrebisbibenzyl A has been proposed.

Antioxidant and molecular docking results

To establish a comprehensive antioxidant profile, we employed complementary approaches including the 2,2-diphenyl-1-picrylhydrazyl (DPPH) and Ferric Reducing Antioxidant Power (FRAP) assays, evaluating direct free-radical scavenging and metal-reduction capacities, respectively, combined with molecular docking against Xanthine oxidase (XO) to explore potential inhibition of enzymatic ROS production. The DPPH assay is widely used to evaluate antiradical activity through the ability of extracts or compounds to reduce the DPPH radical to its non-radical form (DPPH–H) and thus estimate their free-radical neutralizing potential in human-related systems (33). The FRAP assay, meanwhile, measures the capacity of antioxidants to donate electrons and reduce Fe^{3+} to Fe^{2+}, reflecting reducing power which complements radical-scavenging behavior, especially given that free radicals are often generated via redox-active metal catalysis (33). A positive correlation between DPPH and FRAP results has been well-documented, indicating that compounds able to donate hydrogen atoms (DPPH) also tend to act as efficient electron donors (FRAP) and thus share a common mechanistic basis (33,34). Inclusion of the XO assay further extends the evaluation from non-enzymatic antioxidant mechanisms to enzymatic ROS generation: XO catalyzes the oxidation of hypoxanthine/xanthine to uric acid with concomitant generation of superoxide radicals and hydrogen peroxide, so inhibition of XO represents a way to curb ROS at their source (35). Furthermore, compounds exhibiting strong radical-scavenging and reducing capacities often demonstrate XO inhibitory activity, suggesting a mechanistic link between non-enzymatic antioxidant potential and enzymatic ROS suppression (36,37). Thus, the combined use of DPPH, FRAP and XO-inhibition (or molecular docking thereof) provides a multi-faceted understanding of antioxidant mechanisms—covering hydrogen-atom transfer, electron-transfer/reduction power, and suppression of ROS-generating enzymes—and justifies our selection of these assays for the present study.

DPPH radical scavenging assay

In this study, the DPPH assay (Table 1) showed that the MeOH extract exhibited the highest free radical scavenging activity, with an IC_{50} value of 170.21 ± 1.12 µg/mL. This high activity can be attributed to its ability to extract phytochemical constituents, such as phenolic compounds and flavonoids, which are known to contribute to antioxidant effects. Statistically, there was no significant difference ($p < 0.05$) between the DPPH scavenging activity of the MeOH extract and the standard antioxidant BHT (IC_{50} = 170.86 ± 0.95 µg/mL). In contrast, the EtOAc extract showed weaker activity (IC_{50} = 197.41 ± 2.47 µg/mL), likely due to its lower content of phenolic compounds.

Among the isolated compounds, combrebisbibenzyl A (**1**) exhibited the highest scavenging activity (IC_{50} = 175.64 ± 1.36 µg/mL), followed by compound **7** (IC_{50} = 190.56 ± 1.42 µg/mL) and compound 6 (IC_{50} = 200.25 ± 1.51 µg/mL). The superior activity of compound **1** is likely related to the presence of phenolic hydroxyl groups in its structure, consistent with previous reports (12,14,27,38).

Ferric reducing power (FRAP) assay

The antioxidant reducing power of the samples was expressed as mmol vitamin C equivalents per gram of dry extract (mME Vit C/g). The calibration equation obtained from the vitamin C standard curve was $y = –0.001x + 2.605$ ($R^2 = 0.9976$), where y represents the absorbance measured at 593 nm and x denotes the concentration of vitamin C (µg/mL). The high correlation coefficient ($R^2 = 0.9976$) indicates excellent linearity and confirms the reliability of the calibration curve for quantifying the ferric-reducing antioxidant power (FRAP) of the test samples (20). The FRAP values of extracts and isolated compounds were calculated by interpolating their absorbance readings into this standard equation. This method is widely accepted for comparing the reducing potential of various antioxidant samples based on their equivalence to a standard electron donor such as vitamin C (39).

As shown in Table 1, the ethyl acetate (67.42 mME Vit C/g) and methanol (65.04 mME Vit C/g) extracts exhibited the highest metal-reducing capacities, suggesting that these extracts possess strong electron-donating abilities. Such activity may be attributed to the synergistic effects of phenolic and other redox-active phytochemicals capable of transferring electrons to reduce Fe^{3+} ions. Compounds **1** (57.46 mME Vit C/g) and **6** (59.79 mME Vit C/g) also demonstrated significant ferric-reducing potential compared to compound **7** (50.43 mME Vit C/g). The relatively higher reducing power of compounds **1** and **6** could be associated with the presence of free hydroxyl groups in their molecular structures, which facilitate electron transfer during redox reactions (20,39).

TABLE 1 - Variation of antioxidant activities of extracts and isolated compounds according to DPPH and FRAP test

Sample	DPPH		FRAP
	% inhibition	IC_{50} (µg/mL)	mMEVitC/g
1	67.42 ± 0.48^{c}	175.64 ± 2.87^{d}	57.46 ± 0.42^{d}
6	48.78 ± 0.58^{e}	200.25 ± 3.44^{a}	59.79 ± 0.65^{c}
7	62.29 ± 0.32^{d}	190.56 ± 2.61^{b}	50.43 ± 0.72^{e}
AcOEt Ex	63.42 ± 0.62^{d}	197.41 ± 2.47^{c}	67.42 ± 0.82^{a}
MeOH Ex	70.77 ± 0.55^{b}	170.21 ± 4.22^{e}	65.04 ± 1.07^{b}
BHT	74.12 ± 0.92^{a}	170.86 ± 2.19^{e}	-

AcOEt Ex: Ethyl Acetate Extract, MeOH Ex: Methanol Extract, BHT: Buthylhydroxytoluene. Values are expressed as Mean ± ET of 3 replicates per extracts and isolates. Means with different letters (a, b, c, d, e) in the same column are significant at P < 0.05

Molecular Docking Analysis

Molecular docking was performed to complement the experimental antioxidant assays by investigating a potential mechanism involving xanthine oxidase inhibition, while DPPH and FRAP measure direct antioxidant capacity, XO inhibition provides an indirect pathway by reducing the enzymatic generation of superoxide radicals. All tested compounds from Combretum molle exhibited favorable binding affinities to the XO active site, ranging from –8.0 to –9.1 kcal/mol (Table 2). Notably, the novel macrocyclic bisbibenzyl derivative combrebisbibenzyl A (compound 1) demonstrated the highest binding affinity (–9.1 kcal/mol), considerably superior to the reference inhibitor salicylate (–7.7 kcal/mol). A detailed comparative analysis reveals clear differences in binding modes between salicylate and compound **1**. While salicylate primarily interacts with ARG880 and PHE914 within the molybdopterin active site, compound **1** establishes a more extensive interaction network, engaging TYR592, LEU744, PHE798, and GLN1194 (Fig. 4). Its phenolic hydroxyl groups are optimally positioned for multiple hydrogen bonds. This broader and more deeply embedded interaction profile provides a plausible molecular basis for the superior binding affinity of compound **1**. Previous structure–activity relationship (SAR) studies of phenolic and polyphenolic inhibitors of XO underscore the importance of hydroxylation pattern (e.g., C5, C7 positions) and hydrogen-bonding with key residues in the enzyme for high inhibitory potency (40,41).

The consistent binding pattern across all compounds suggests competitive inhibition, as they occupy overlapping regions within the enzyme's active site. TYR592 emerges as a critical residue, forming hydrogen bonds with multiple compounds (**1**, **3**, **5**, **6**, **7**) in our series, supporting its mechanistic importance in XO inhibition. Importantly, the computational results correlate with experimental antioxidant activities: compounds **1** and **7**, both showing the strongest DPPH radical scavenging (IC_{50} = 175.64 and 190.56 µg/mL, respectively) and FRAP values (57.46 and 50.43 mmol Vit C-equivalents/g, respectively), also exhibit the highest XO binding affinities (–9.1 and –8.0 kcal/mol, respectively). This dual performance supports that combrebisbibenzyl A may exert antioxidant effects via multiple mechanisms: direct radical scavenging, metal-ion reduction, and suppression of enzymatic ROS generation. The macrocyclic structure of compound 1 appears to provide optimal geometry for engaging multiple key residues in XO's active site, while its phenolic hydroxyl groups facilitate crucial hydrogen bonding interactions in line with documented SAR of XO inhibitors (42,43).

Given this evidence, compound **1**'s high binding affinity supports its observed superior antioxidant activity and suggests that XO inhibition may play a significant role in its *in vitro* antioxidant profile. The comprehensive interaction network, favorable binding energy, and correlation with phenolic structural features position combrebisbibenzyl A as a promising multi-target antioxidant agent with scientific superiority over the reference compound salicylate.

TABLE 2 - Molecular docking results and binding interactions of isolated compounds with xanthine oxidase (PDB ID: 1fiq)

Compounds	Binding Energy (kcal/mol)	Key Interacting Residues and Interaction Types
SAL	–7.7	Salt Bridge - C chain: ARG880
		Conventional Hydrogen Bond - C chain: ARG880, THR1010
		Pi-Pi Stacked and Pi-Pi Shaped- C chain: PHE914, PHE1009
		Pi-Alkyl - C chain: ALA1079
1	–9.1	Conventional Hydrogen Bond - C chain: TYR592, LEU744
		Carbon and Pi-Donor Hydrogen Bond - C chain: GLN1194, GLU1196
		Pi-Sigma - C chain: LEU744
		Pi-Pi Shaped- C chain: PHE798
		Pi-Alkyl - C chain: TYR592, PHE798
2	–8.8	Conventional Hydrogen Bond - C chain: GLN1201
3	–8.2	Conventional Hydrogen Bond - C chain: TYR592, GLY1197
4	–8.0	Conventional Hydrogen Bond - C chain: PRO1230
		Unfavorable Donor-Donor - C chain: GLN1194
		Pi-Sigma - C chain: PHE1232
5	–8.0	Conventional Hydrogen Bond - C chain: GLN585, TYR592, MET794
		Carbon Hydrogen Bond - C chain: MET1038
6	–8.2	Conventional Hydrogen Bond - C chain: TYR592, MET1038
7	–8.0	Conventional Hydrogen Bond - C chain: GLN585, TYR592
		Alkyl - C chain: LEU744, VAL1200

Conclusion

This study reports the isolation of one novel macrocyclic bisbibenzyl derivative, combrebisbibenzyl A (**1**), along with six known triterpenoids from the twigs of *Combretum molle*. Experimental evaluation of antioxidant activity demonstrated that the EtOAc and MeOH extracts, as well as compounds **1**, **6**, and **7**, possess significant radical scavenging and metal-reducing capacities. Notably, combrebisbibenzyl A (**1**) exhibited the strongest activity, highlighting its potential as a bioactive natural antioxidant. These findings provide empirical evidence supporting the traditional use of *C. molle* in managing oxidative stress-related conditions, including infections and degenerative diseases. Molecular docking studies further suggest that combrebisbibenzyl

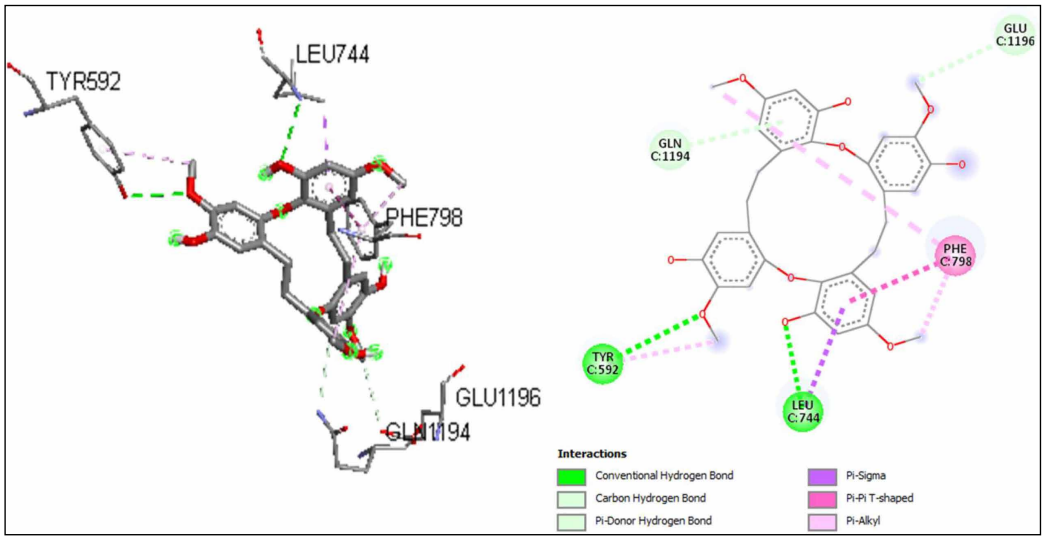

FIGURE 4 - 3D and 2D conformations of Combrebisbibenzyl A **(1)** in complex with 1fiq.

A may act as an effective xanthine oxidase inhibitor, with strong binding interactions involving key active site residues (TYR592, GLN1194, LEU744, ARG880). The complementary experimental and computational results indicate that the antioxidant potential of *C. molle* constituents may arise from both direct radical scavenging and inhibition of enzymatic reactive oxygen species generation. Overall, the data position *C. molle* extracts and isolated compounds as promising candidates for the development of natural antioxidant agents with potential applications in nutraceuticals, functional foods, and therapeutic interventions targeting oxidative stress-related disorders. Future research should focus on the detailed identification of specific bioactive phytochemicals, optimization of their bioavailability, and *in vivo* evaluation to advance their potential for drug development or dietary supplementation.

Acknowledgements

All the authors are grateful to the Laboratory of Biology, Faculty of Science, University of Maroua (Cameroon) for the biological experiments and the Department of Chemistry, Organic and Bioorganic Chemistry, Bielefeld University, Bielefeld, P.O. Box 100131, 33501 Bielefeld, Germany, for spectroscopic analysis of isolated compounds.

Disclosures

Conflict of interest: The authors declare that they have no known competing financial interests or personal relationships that could have appeared to influence the work reported in this paper.

Financial support: This research received no funding.

Data availability statement: The research data associated with this article are included within the article and in the supplementary material of this article.

Authors contribution: Conceptualization, A.D. and G.B.b.N.; Methodology, A.F. and A.D.; Software, J.N.N., H.L.K. and A.W.; Formal analysis, A.D., C.D., A.W. and G.B.b.N.; Investigation, A.F., G.B.b.N., A.W. and F.Y.; Data curation, A.D., C.D. and J.N.N.; Writing-original draft preparation, A.F., T.V., F.Y. and J.N.N.; Writing-review & editing, A.D. and J.N.N.; Project administration, D.E.P. and B.L.; Supervision, D.E.P. and A.D. All authors have read and agreed to the published version of the manuscript.

References

1. Viau CM, Moura DJ, Pflüger P, et al. Structural aspects of antioxidant and genotoxic activities of two flavonoids obtained from ethanolic extract of *Combretum leprosum*. Evid Based Complement Alternat Med. 2016;2016(1):9849134. CrossRef PubMed
2. Parusnath M, Naidoo Y, Singh M, et al. Antioxidant and antibacterial activities of the leaf and stem extracts of *Combretum molle* (R. Br. ex G. Don.) Engl. & Diels. Plants. 2023;12(9):1757. CrossRef PubMed
3. Dawe A, Saotoing P, Tsala DE, et al. Phytochemical constituents of *Combretum loefl*. (Combretaceae). Pharm Crop. 2013;4(1):38-59. CrossRef
4. Silén H, Salih EYA, Mgbeahuruike EE, et al. Ethnopharmacology, antimicrobial potency, and phytochemistry of African *Combretum* and *Pteleopsis* species (Combretaceae): a review. Antibiotics. 2023; *12*(2), 264. CrossRef
5. Ali IJ, Adonu CC, Okorie NH, et al. Phytochemical analysis, antioxidant and antimicrobial activities of the leaves of *Combretum bauchiense* Hutch & Dalziel (Combretaceae). SARJNP. 2023;6(3):248-260.
6. Asmaa SAE, Hanan AAT. Characterization of flavonoids from *Combretum indicum* L. growing in Egypt as antioxidant and antitumor agents. Egypt J Chem. 2023;66(13):2291-2305.
7. Silvère Gade I, Nyemb JN, Mahamat A, et al. A novel pentacyclic triterpene acid from the stem barks of *Combretum fragrans* F. Hoffm (Combretaceae). Nat Prod Res. 2024;38(8):1294-1301. CrossRef PubMed
8. Mathipa MM, Mphosi MS, Masoko P. Phytochemical profile, antioxidant potential, proximate and trace elements composition of leaves, stems and ashes from 12 *Combretum* spp. Used as Food Additives. Int J Plant Biol. 2022; 13(4), 561-578; CrossRef
9. Enroth C, Eger BT, Okamoto K, et al. Crystal structures of bovine milk xanthine dehydrogenase and xanthine oxidase: structure-based mechanism of conversion. Proc Natl Acad Sci USA. 2000;97(20):10723-10728. CrossRef PubMed

10. Rastelli G, Costantino L, Albasini A. A model of the interaction of substrates and inhibitors with xanthine oxidase. J Am Chem Soc. 1997; 119(13): 3007–3016. CrossRef
11. Battelli MG, Polito L, Bortolotti M, et al. Xanthine oxidoreductase-derived reactive species: physiological and pathological effects. Oxid Med Cell Longev. 2016;2016(1):3527579. CrossRef PubMed
12. Apak R, Özyürek M, Güçlü K, et al. Antioxidant activity/capacity measurement. 1. Classification, physicochemical principles, mechanisms, and electron transfer (ET)-based assays. J Agric Food Chem. 2016;64(5):997-1027. CrossRef PubMed
13. McCord JM. Oxygen-derived free radicals in postischemic tissue injury. N Engl J Med. 1985;312(3):159-163. CrossRef PubMed
14. Niccoli T, Partridge L. Ageing as a risk factor for disease. Curr Biol. 2012;22(17):R741-R752. CrossRef PubMed
15. Bergel F, Bray RC. Stabilization of xanthine oxidase activity by salicylate. Nature. 1956;178(4524):88-89. CrossRef PubMed
16. Gulcin I, Alwasel SH. DPPH radical scavenging assay. Processes (Basel). 2023;11(8):2248. CrossRef
17. Baliyan S, Mukherjee R, Priyadarshini A, et al. Determination of antioxidants by DPPH radical scavenging activity and quantitative phytochemical analysis of *Ficus religiosa*. Molecules. 2022;27(4):1326. CrossRef PubMed
18. Parusnath M, Naidoo Y, Singh M, et al. Phytochemical composition of *Combretum molle* (R. Br. ex G. Don.) Engl. & Diels leaf and stem extracts. Plants. 2023;12(8):1-19. CrossRef PubMed
19. Yaya JAG, Nyemb JN, Olboungou NM, et al. Antiradical, antibacterial activities and in silico molecular docking of ethyl-*β*-D-fructofuranoside from hydro-ethanolic crude extract of *Erythrina excelsa* stem bark. Plant Biosyst. 2025;159(4): 768-777. CrossRef
20. Benzie IFF, Strain JJ. The ferric reducing ability of plasma (FRAP) as a measure of "antioxidant power": the FRAP assay. Anal Biochem. 1996;239(1):70-76. CrossRef PubMed
21. Morris GM, Huey R, Lindstrom W, et al. AutoDock4 and AutoDockTools4: automated docking with selective receptor flexibility. J Comput Chem. 2009;30(16):2785-2791. CrossRef PubMed
22. Trott O, Olson AJ. AutoDock Vina: improving the speed and accuracy of docking with a new scoring function, efficient optimization, and multithreading. J Comput Chem. 2010;31(2):455-461. CrossRef PubMed
23. Facundo VA, Rios KA, Medeiros CM, et al. Arjunolic acid in the ethanolic extract of *Combretum leprosum* root and its use as a potential multi-functional phytomedicine and drug for neurodegenerative disorders: anti-inflammatory and anticholinesterasic activities. J Braz Chem Soc. 2005; 16 (6b). CrossRef
24. Ponou B, Barboni L, Teponno R, et al. Polyhydroxyoleanane-type triterpenoids from *Combretum molle* and their anti-inflammatory activity. Phytochem Lett. 2008;1(4):183-187. CrossRef
25. De Leo M, De Tommasi N, Sanogo R, et al. Triterpenoid saponins from *Pteleopsis suberosa* stem bark. Phytochemistry. 2006;67(24):2623-2629. CrossRef PubMed
26. Nyemb JN, Djankou MT, Talla E, et al. Antimicrobial, *α*-glucosidase and alkaline phosphatase inhibitory activities of bergenin, the major constituent of *Cissus populnea* roots. Med Chem (Los Angeles). 2018;8(2):426-430. CrossRef
27. Yakai F, Dawe A, Manshuk I, et al. Antioxidant and antibacterial effects of a new macrocyclic bis(bibenzyl) ether from *Combretum molle* (Combretaceae). Z Naturforsch C J Biosci. 2024;79(11-12):377-385. CrossRef PubMed
28. Cioffi G, Montoro P, De Ugaz OL, et al. Antioxidant bibenzyl derivatives from Notholaena nivea Desv. Molecules. 2011;16(3):2527-2541. CrossRef PubMed
29. Chaofeng Z, Min W, Ping L, et al. A new bibenzyl compound from *Dendrobium gratiosissmum*. ChemInform. 2008;39(19). CrossRef
30. Karatoprak GŞ, Küpeli Akkol E, Genç Y, et al. Combretastatins: an overview of structure, probable mechanisms of action and potential applications. Molecules. 2020;25(11):1-33. CrossRef PubMed
31. Asakawa Y, Toyota M, Tori M, et al. Chemical structures of macrocyclic bis(bibenzyls) isolated from liverworts (Hepaticaea). J Spectrosc. 2000;14(4):149-175. CrossRef
32. Araya-Maturana R, Pessoa-Mahana H, Weiss-López B. Very long-range correlations ($^{n}J_{C,H}$ n > 3) in HMBC spectra. Nat Prod Commun. 2008;3(3):445-450. CrossRef
33. Clarke G, Ting KN, Wiart C, et al. High correlation of 2,2-diphenyl-1-picrylhydrazyl (DPPH) radical scavenging, ferric reducing activity potential and total phenolics content indicates redundancy in use of all three assays to screen for antioxidant activity of extracts of plants from the Malaysian rainforest. Antioxidants (Basel). 2013;2(1):1-10 CrossRef PubMed
34. Han C, Shi H, Cui C, et al. Strain-specific benefits of *Bacillus* on growth, intestinal health, immune modulation, and ammonia-nitrogen stress resilience in hybrid grouper. Antioxidants (Basel). 2024;13(3):317. CrossRef PubMed
35. Noda M, Kikuchi C, Tarui R, et al. Effects of xanthine oxidoreductase inhibitors on reactive oxygen species produced in vitro from xanthine oxidase. BPB Reports. 2023;6(6):189-192. CrossRef
36. Ahmad AR, Elya B, Mun'im A. Antioxidant activity and isolation of xanthine oxidase inhibitor from *Ruellia tuberosa* L. leaves. Pharmacogn J. 2017;9(5):607-610. CrossRef
37. Ozyürek M, Bektaşoğlu B, Güçlü K, et al. Measurement of xanthine oxidase inhibition activity of phenolics and flavonoids with a modified cupric reducing antioxidant capacity (CUPRAC) method. Anal Chim Acta. 2009;636(1):42-50. CrossRef
38. Nyemb JN, Ndoubalem R, Talla E, et al. DPPH antiradical scavenging, anthelmintic and phytochemical studies of *Cissus poulnea* rhizomes. Asian Pac J Trop Med. 2018;11(4):280-284. CrossRef
39. Apak R, Güçlü K, Ozyürek M, et al. Novel total antioxidant capacity index for dietary polyphenols and vitamins C and E, using their cupric ion reducing capability in the presence of neocuproine: CUPRAC method. J Agric Food Chem. 2004;52(26):7970-7981. CrossRef PubMed
40. Liu X, Wu D, Liu J, et al. Characterization of xanthine oxidase inhibitory activities of phenols from pickled radish with molecular simulation. Food Chem X. 2022;14:100343. CrossRef PubMed
41. Li X, Wang J. Structure–activity relationships and changes in the inhibition of xanthine oxidase by polyphenols: a review. Food Chem Adv. 2022;15:100121.
42. Mehmood A, Li J, Rehman M, et al. Xanthine oxidase inhibitory study of eight structurally diverse phenolic compounds. Front Nutr. 2022;9:966557. CrossRef
43. Chen Y, Gao F, Wu X, et al. Computationally exploring novel xanthine oxidase inhibitors using docking-based 3D-QSAR, molecular dynamics, and virtual screening. New J Chem. 2020;44(44):19276-19287. CrossRef

Drug Target Insights

www.aboutscience.eu

ISSN 1177-3928

ABOUTSCIENCE